NANYANG
TECHNOLOGICAL
UNIVERSITY

Transport Phenomena in Multiphase Microfluidics

Che Zhizhao

SCHOOL OF MECHANICAL AND AEROSPACE ENGINEERING

2012

Transport Phenomena in Multiphase Microfluidics

Che Zhizhao

School of Mechanical and Aerospace Engineering

A thesis submitted to the Nanyang Technological University

in partial fulfilment of the requirement for the degree of

Doctor of Philosophy

2012

Abstract

Multiphase microfluidics offers a great number of opportunities in different applications ranging from analytical chemistry, chemical engineering, pharmaceutical and biomedical sciences, to life science. The present work builds models of flow fields in liquid plugs moving in microchannels, and implements these models to investigate the transport phenomena in multiphase microfluidics.

To understand the flow fields within liquid plugs in microchannels, four models of flow fields are developed for plugs in different channel geometries, such as microcapillaries/microchannels with circular cross section, two-dimensional microchannels, curved microchannels, and plug trains in two-dimensional microchannels. These models offer conveniences for subsequent analyses since transport phenomena can be analyzed directly with the known flow fields. Different applications are demonstrated with the proposed models, such as the flow resistance, the heat transfer in plugs, and the chaotic mixing in plugs moving in meandering microchannels.

Based on the results provided by the model, some ideas are proved to utilize and to manipulate multiphase microfluidics. A method to split droplets mediated by hydrodynamic focusing is proposed and investigated. The number and the size of the daughter droplets are controllable by varying the splitting flow rate and

the size of the mother droplet. This method of droplet splitting is proved robust, reliable, and flexible. The studies of liquids and gas-liquid plugs at the outlet of microcapillaries are performed. For a liquid, it leaves a capillary in the form of pendant drop. During the growth and breakup of pendant drops, with a fixed flow rate at the inlet of the capillary, upstream pressure fluctuation is produced by the size variation of the pendant drop. The pressure fluctuation can be used to measure the surface tension of the fluid by measuring the period of the pressure fluctuation. For gas/liquid plug flow, fluids leave a microcapillary in the form of compound pendant drops. With a fixed upstream pressure, velocity fluctuation in the upstream is caused by the formation and breakup of compound pendant drops. Experimental investigation shows that the velocity fluctuation is reduced by adding surfactant into the liquid.

Acknowledgements

First and foremost, I would like to express my sincere gratitude to my supervisors Associate Professor Wong Teck Neng and Associate Professor Nguyen Nam-Trung for their continuous support of my PhD research. They are patient, inspiring, encouraging, and of immense knowledge. This thesis would not have been possible without their guidance and support.

I would like to thank Professor John Chai and Dr. Yap Yit Fatt for their invaluable advices on the numerical simulation, which is of great value to this study.

I would like to thank technical staffs Mr. Yuan Kee Hock in Thermal and Fluid Research Laboratory, Mr. Yap Pow Khim in Fluid Mechanics Laboratory, Mr. Cheong Yuen Kong, and Mr. Foo Jong Hin in Heat Transfer Laboratory for their help in experiments.

I greatly appreciate my fellow research students and staffs, Ms. Liu Jing, Mr. Li Haiwang, Mr. Shen Yi, Ms. Li Hongying, Mr. Zhao Cunlu, Ms. Wang Shasha, Mr. Song Chaolong, Mr. Tan Say Hwa, Mr. Xu Bin, Mr. Yan Zhibin, Dr. Zhao Rui, Mr. Tan Yunn Boon, Mr. Xie Jinglong, Mr. He Bin, Mr. Phan Vinh Nguyen, Ms. Tan Hsih Yin, and other friends in Thermal and Fluid Research Laboratory for sharing their experiment and simulation skills.

Last but not least, I would like to thank my family for their supports and encouragement. This thesis is impossible without their love.

Che Zhizao

July 2011, Singapore

Contents

List of Figures

List of Tables

Nomenclature

Romans

A, C, D	Constant coefficient, [-]
A, B	Vortex near the top/bottom (outer/inner) wall, [-]
Bo	Bond number, [-]
C	Molar concentration of species, [mol/m^3]
Ca	Capillary number, [-]
C_f	Plug resistance coefficient, [-]
c	Number of particles in statistical bins, [-]
c_p	Specific heat capacity, [J/(kg·K)]
D	Diameter, [m]
	Diffusivity, [m^2/s]
De	Dean number, [-]
D_H	Hydraulic diameter of the channel, [m]
F	Force, [N]
f	Moody friction factor, [-]
	Volume fraction in compound pendant drops, [-]
g	Gravitational acceleration, [m/s^2]
H	Smoothed Heaviside function, [-]

h	Half width of the microchannel, [m]
	Heat transfer coefficient, [W/(m^2·K)]
I	Modified Bessel function, [-]
$\mathbf{I}$	Identity matrix of size three, [-]
k	Thermal conductivity, [W/(m·K)]
L	Length (half length in Chapter 6) of the plug, [m]
M	Moment of force for plugs in 2D curved channels in Chapter 5, [N·m]
	Number of bins used to calculate mixing index in Chapter 6, [-]
N	Number of plugs in the plug train in Chapter 6, [-]
	Number of fronts and rears of the air plugs in the observing window in Chapter 9, [-]
NP	Number of particles in the particle tracking simulation, [-]
Nu	Nusselt number, [-]
$\mathbf{n}$	Unit direction vector normal to a surface, [-]
p	Pressure, [Pa]
Pe	Peclet number for heat transfer, [-]
Pe_D	Peclet number for mixing, [-]
Q	Volumetric flow rate, [m^3/s]
	Energy transfer, [J]
q	Heat flux, [W/m^2]
R	Radius, [m]
Re	Reynolds number, [-]
r, θ	Coordinates in cylindrical coordinates systems, [m], [rad]
S	Sliding velocity of the channel wall, [m/s]
S-S	Zero stream function line, [-]

T	Temperature, [K]
	Period of pressure fluctuation, [s]
T_c	Characteristic temperature, [K]
T_w	Wall temperature, [K]
t	Time, [s]
u	Velocity component, [m/s]
V	Speed of the plug unit, [m/s]
w	Width of the microchannel, [m]
We	Weber number, [-]
X	Distance from the entrance of the heated microchannel, [m]
X, Y	Constant coefficients, [-]
X-X	Middle cross section of the plug, [-]
x	Radial position of vortex centre, [-]
x, y	Coordinates in Cartesian coordinate systems, [m]
z, r	Coordinates in cylindrical coordinate systems, [m]

Greeks

α	Thermal diffusivity, [m^2/s]
α, β	Eigenvalues, [-]
η	Heat transfer index in Chapter 4, [-]
	Mixing index in Chapter 6, [-]
κ	Curvature of interface, [m^{-1}]
μ	Dynamic viscosity of fluid, [Pa·s]
ω	Angular speed of the plug unit, [rad/s]
ϕ	Level set function, [m^2/s]
ρ	Density of fluid, [kg/m^3]

σ	Surface tension, [N/m]
	Standard deviation of particle numbers in bins, [-]
τ	Characteristic time, [s]
τ	Stress, [Pa]
θ	Contact angle, [rad]
φ	Stream function, [m^2/s]
ξ	Dimensionless sliding velocity of the wall, [-]
ζ	Polydispersity, [-]
δ_T	Thickness of thermal boundary layer, [m]

Superscripts

$'$	Absolute velocity.
$+$, $-$	Instant before/after the pinch-off of the pendant drop.
e, o	Even/odd function.

Subscripts

i	Index of plug in a plug train.
i, o	Inner/outer (diameter).
j	Index of statistical bins.
k	Index of tracer particles.
q	Constant-surface-heat-flux condition.
$R1$, $R2$	Outer/inner wall of the curved microchannels.
T	Constant-surface-temperature condition.
1, 2	Top/bottom (or outer/inner) walls of the microchannel.
adv, rec	Advancing/receding (front/rear) end of the plug.
asymp	Asymptotic value.
c1, c2, c3	First, second, and third critical value.

centre	Vortex centre in plugs.
friction	Friction contribution to plug resistance.
long	Long plugs.
max, min	Maximum/minimum.
oA, oB	Oil inlet A/B.
pixel	Dimension by pixel in image.
plug	Plug flow.
sp	Single phase flow.
tip	Capillary tip.
w	Water.

Overscripts

ˆ	Dimensionless variable.
-	Average value.

Abbreviations

µPIV	Micro particle image velocimetry.
1D	One-dimensional.
2D	Two-dimensional.
3D	Three-dimensional.
AC	Alternating current.
CCD	Charge-coupled device.
CPD	Compound pendant drop.
CS-i	Coordinate system for plug-i.
DI	Deionized (water).
EWOD	Electro wetting on dielectrics.
FFT	Finite Fourier transform.

fps	Frame per second.
FVM	Finite volume method.
LSM	Level set method.
MEMS	Micro-electromechanical systems.
PDMS	Polydimethylsiloxane.
PMMA	Polymethylmethacrylate.
RK	Runge-Kutta (scheme).
SDS	Sodium dodecyl sulfate.
TBL	Thermal boundary layer.
TVD	Total variation diminishing.
WENO	Weighted essentially non-oscillatory (scheme).

Chapter 1

Introduction

1.1 Background

Microfluidics involves studying fluid properties, flow behaviours, mass and energy transfer, and manipulation of fluids at a length scale less than a millimetre. The interest in microfluidics has grown fast in the past decades due to its wide promising applications and opportunities in different areas.

The development of microfluidics is a requirement of micro/nanotechnologies, in which areas, microdevices, such as micro-valves, micro-pumps, micro-actuators, micro-switches, micro-sensors, micro-dispensers, micro-mixers, micro-filters, micro-separators, micro-heaters, are expected to cope with the dimension requirements of micro-electro-mechanical systems (MEMS). Hence, it is necessary to understand flow conditions, interactions between the fluids and the devices, interactions between different fluids, and mass and energy transfer processes.

Microfluidics has tremendous potential to offer in the area of drug delivery, point-of-care diagnostics, microreactors, organic synthesis, DNA microarrays, gene-expression analysis, drug screening, etc. In these areas, the reagents are usually

expensive, or only available in a limited amount, while microfluidic systems only require samples of several microlitres or nanolitres. Using microfluidic techniques, the processes can achieve fast reactions, less sample requirements with low-cost microfluidic devices.

Droplet-based microfluidics deals with the manipulation of discrete droplets in the microfluidic systems (Teh et al., 2008). It has many advantages over the traditional continuous-flow microfluidics, such as

(1) Each droplet can be controlled independently. By manipulating an individual droplet, actuation, manipulation, heat and mass transfer, and analysis can be carried out independently and precisely.

(2) Droplets can be transported without contamination. Droplets can be used as micro-vesicles. The reagents in them are protected by the interface and the mass transport between droplets can be decreased effectively, or even eliminated. The residence time distribution can be narrowed, which is significant for mixing, reactions and syntheses.

(3) Less amount of reagents and short reaction time are required. In droplet-based microfluidics, the reagents are confined in different droplets, which have volume much less than that for continuous-flow microfluidics.

(4) Droplet-based microfluidic chips are easy to scale and to integrate. As dispersion and contamination are decreased, the influence of a process on subsequent processes can be decreased. Therefore, the systems are easy to integrate and to achieve complex functions and high throughput.

1.2 Objectives and scopes

Transport phenomena in multiphase microfluidics play an important role in the applications of multiphase microfluidics. The objective of the present study aims to develop practical models which can be used to deepen the understanding of the physics in multiphase microfluidics, to implement these models for various applications of transport phenomena, and to investigate the role of the flow pattern in the transport phenomena.

The scope of the current study includes:

(1) To study the recirculating flow in plugs moving in microchannels, and to study the factors influencing the flow pattern, such as the plug length, the channel geometry, and the viscosity.

(2) To study the effects of the recirculating flow on the transport phenomena in plugs, such as flow resistance, heat transfer, and micromixing.

(3) To study droplet manipulation methods based on the recirculating flow in plugs.

(4) To study the leaving of liquids or gas-liquid plugs at the outlets of microcapillaries, and their effects on the upstream.

1.3 Outline of the thesis

Chapter 1 briefly introduces droplet-based microfluidics and continuous-flow microfluidics. The advantages of droplet-based microfluidics over continuous-flow microfluidics are discussed.

Chapter 2 reviews the development of the droplet-based microfluidics, including droplet manipulation methods and transport phenomena associated with droplet-based microfluidics, such as flow field, heat transfer, and micromixing.

Chapters 3–6 provide four models for plug flow in microchannels or microcapillaries. Plugs refer to droplets which occupy the entire cross section of the microchannels/microcapillaries. Chapter 3 provides a model for plug flow in microcapillaries with circular cross section. This model is used to study the flow resistance of liquid plugs, which shows that the resistant is (i) plug length dependent, and (ii) much higher than that of single phase flow. Chapter 4 provides a model for plug flow in two-dimensional (2D) microchannels. This model is used to study the heat transfer in plugs. The results show that as compared to single phase flow, the heat transfer in plugs can be significantly enhanced by the recirculating vortices. Chapter 5 provides a model for plug flow in 2D curved microchannels. This model shows that the vortex pair in the plug is asymmetric due to the channel curvature, and the vortex sizes can be manipulated by the channel curvature and the plug length. Chapter 6 provides a model for plug train flow in 2D microchannels. Plug train refers to a series of consecutive different plugs which repeat periodically in microchannels. This model is used to study the chaotic mixing in plugs moving in meandering microchannels. The results show that the mixing process in plugs can be enhanced by increasing the channel curvature, reducing the Peclet number, and selecting a proper viscosity ratio and a proper plug length.

Based on the results provided in Chapters 3–6, some ideas are generated in manipulating multiphase flow in microfluidics. Chapter 7 experimentally

demonstrates a method to split droplets in microchannels. Chapter 8 numerically investigates the behaviour of liquids leaving from a microcapillary in the form of pendant drops. If a constant flow rate of the liquid is maintained at the inlet of the capillary, the growth and breakup of pendant drops at the capillary tip causes upstream pressure fluctuation, which can be utilized to measure the surface tension of the liquid. Chapter 9 experimentally studies the leaving of gas/liquid plugs from a microcapillary in the form of compound pendant drops. If a constant pressure is maintained at the inlet of the capillary, the growth and breakup of compound pendant drops at the capillary tip causes upstream velocity fluctuation.

The thesis is concluded in Chapter 10 with suggestions of future works.

Chapter 2

Literature Review

Droplet-based microfluidics attracted many researchers' interests due to its wide applications in chemical reactions, particle syntheses, biological analyses, etc. It gains rapid development in the last decades (Belder, 2005; Chiu et al., 2009; Günther and Jensen, 2006; Lorber et al., 2011; Tabeling, 2009, 2010; Theberge et al., 2010). In this chapter, the development of droplet-based microfluidics is reviewed. Droplet manipulation techniques, such as coalescence, splitting, and injection, are reviewed in Section 2.1. Transport phenomena in droplets, including the flow field, mixing, and heat transfer, are reviewed in Section 2.2.

2.1 Droplet manipulation

2.1.1 Droplet generation

Droplet generation in microfluidic devices is a crucial step for droplet-based lab-on-a-chip platforms. As compared to traditional methods to generate droplets in large scales such as atomization and sprays, droplets generation in microchannels is more controllable over the droplet size and the polydipersity. the polydipersity

of droplets refers to the normalized standard deviation of the size distribution of droplets (Christopher and Anna, 2007), and monodisperse droplets are of crucial importance for many applications. As the dimension of microfluidic devices shrinks to micrometre scale, the flow in microchannels is characterized by low Reynolds numbers. Therefore, instability and nonlinearity usually cannot be produced by the small inertial force. However, the viscous force and the surface tension force dominate the flow, and their competition may result in instability and can be used to produce droplets in microchannels (Thorsen et al., 2001). The droplet generation methods can be categorized into two groups, passive and active, according to whether external energy is used to assist the breakup process (Christopher and Anna, 2007). T-junction and flow focusing geometry are two passive techniques widely used in lab-on-a-chip platforms.

2.1.1.1 T-junction

Using a T-junction to generate droplets was first proposed by Thorsen et al. (2001), as shown in Figure 2.1. Two immiscible phases are introduced separately into a microchannel, normally an aqueous phase and an organic phase. One phase, such as oil, which wets the wall of the microchannel, serves as the continuous phase. The other phase, such as water, which does not wet the wall, serves as the dispersed phase (droplet). The oil is introduced through the main channel, while the water is introduced through the side channel, and the two phases meet at the T-junction, as shown in Figure 2.1. The competition between the surface tension force and the viscous force results in three regimes of droplet generation: squeezing, dripping, and jetting. The capillary number (Ca) is an important factor influencing the process of

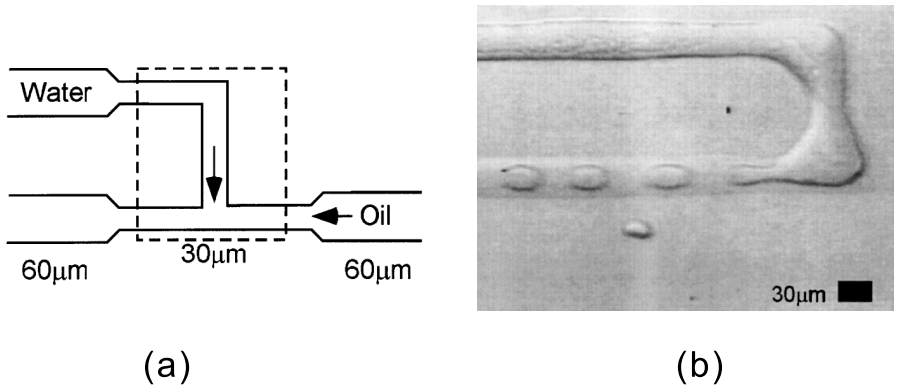

Figure 2.1: A T-junction for generation of monodisperse droplets (Thorsen et al., 2001).

droplet generation. It characterizes the relative effect between the viscous force and the surface tension force, and is defined as $Ca = \mu V/\sigma$, where μ is the characteristic viscosity, V is the characteristic velocity, and σ is the interfacial tension.

When the capillary number is small, $Ca < 10^{-2}$, the surface tension force dominates the flow, and the T-junction works in a *squeezing* regime, as shown in Figure 2.2**a**. A liquid thread of the dispersed phase enters the main channel and grows to almost occupy the entire cross section of the main channel. The breakup of a droplet in the squeezing regimes includes two stages: *filling* and *squeezing* (Garstecki et al., 2006; van Steijn et al., 2009, 2010). At the filling stage, the thread of the dispersed phase gradually grow until it approaches the wall opposite to the side channel, which initiates the beginning of the squeezing stage. At the squeezing stage, the presence of the dispersed phase in the main channel blocks the flow of the continuous phase, and results in gutters between the wall and the dispersed phase for the flow of the continuous phase. Therefore, the continuous phase squeezes the shape of the dispersed phase until pinch-off occurs. Van Steijn et al. (2009) found that the breakup of bubbles in the squeezing regime is initiated by the flow of the liquid from the tip of the thread to the neck where pinch-off

occurs. They proposed a simple model to predict the size of bubbles/droplets by separately considering the volumes during the filling and squeezing stages (van Steijn et al., 2010). Schneider et al. (2011) through numerical simulation found that the model proposed by van Steijn et al. (2010) is applicable in a limited range of surface tensions because the model excluded interfacial effects which governs the curvature of the droplet when using the flow rates necessary to achieve similar droplet sizes.

Dripping of droplets occurs as the capillary number increases (Christopher et al., 2008), as shown in Figure 2.2**b**. The viscous force plays an important role as the capillary number increases, and it applies a shear force to the dispersed phase during the growth of the water thread. The shear force increases as the thread grows, and causes the pinch-off of a droplet when the surface tension is not able to balance the shear force. Until the breakup of the droplet, the buildup of the upstream pressure is not negligible, unless the droplet size is much smaller than the width of the channel (De Menech et al., 2008; Sivasamy et al., 2011).

As the capillary number increases further, dripping gives way to *jetting*, during which the thread of the dispersed phase is extended to the downstream, and breakup of droplets happens at the end of a long column of the dispersed phase (De Menech et al., 2008), as shown in Figure 2.2**c**.

The process of droplet generation and the resultant size of droplets depend on the flow rates of the two immiscible phases (Thorsen et al., 2001), the geometry of the channel (Abate et al., 2009; Fries and Rudolf von Rohr, 2008; Ménétrier-Deremble and Tabeling, 2006), the viscosities of the two phases (Liu and Zhang, 2009; Sang et al., 2008), and the interfacial tension (Garstecki et al., 2006).

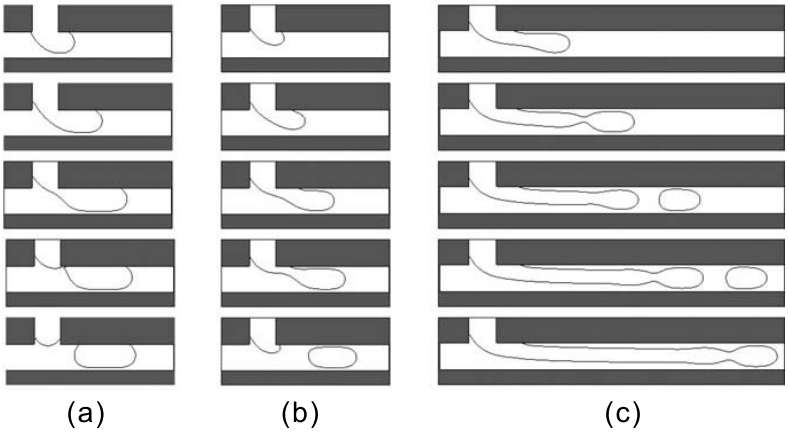

Figure 2.2: Droplet generation at a T-junction at different regimes: (a) squeezing, $Ca = 0.004$, (b) dripping $Ca = 0.035$, and (c) jetting $Ca = 0.05$ (De Menech et al., 2008).

Different active methods to change these factors have been reported to control the droplet generation process, such as changing the surface tension and viscosity by heat (Murshed et al., 2009), or changing of the channel geometry by pneumatic valves (Choi et al., 2010a).

Y-junction is a geometrical variation of the T-junction (Steegmans et al., 2009) for droplet generation. Through experimental investigations, Steegmans et al. (2009) found that the flow rate and the viscosity of the dispersed phase have no effect on the droplet size in droplet generation at a Y-junction. Another variation of the T-junction is a head-on geometry (Shui et al., 2008, 2009), in which, droplets can be produced at an extremely low capillary number $Ca \sim 10^{-5}$.

2.1.1.2 Flow focusing geometry

Droplet generation using a flow focusing geometry in microchannels was first proposed by Anna et al. (2003), as shown in Figure 2.3. The dispersed phase (water) is introduced into the centre channel, while the continuous phase (oil) is

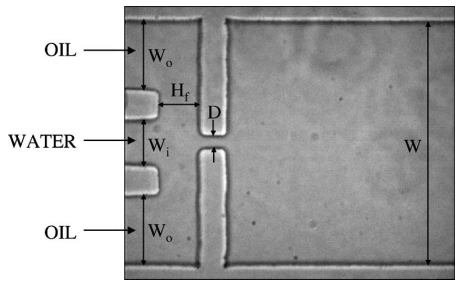

Figure 2.3: Flow focusing geometry for generation of monodisperse droplets (Anna et al., 2003).

introduced symmetrically from the two side channels. The interplay of the viscous force, the surface tension force, and the inertial force results in four regimes of droplet generation at a flow focusing geometry (Anna and Mayer, 2006), namely squeezing, dripping, jetting, and threading regimes.

(1) Squeezing regime [Figure 2.4**a**]: For a small capillary number, the interfacial tension force dominates the flow at the flow focusing geometry. As the dispersed phase is pushed into the orifice, the dispersed phase forces the continuous phase into narrow gutters between the interface and the orifice. The pressure drop of the continuous phase across the orifice squeezes the dispersed phase at the neck and causes the finger of the dispersed phase to break up. After the detachment of a droplet, the dispersed phase retreats upstream, and a new cycle of droplet generation starts. The droplets generated in this regime are monodisperse (Garstecki et al., 2005).

(2) Dripping regime [Figure 2.4**b**]: As the capillary number increases, after the detachment of a droplet, the interfacial tension force is insufficient to restore the finger of the dispersed phase to nearly sphere. Hence, the finger of the dispersed phase does not retreat in the dripping regime. The droplets produced in the

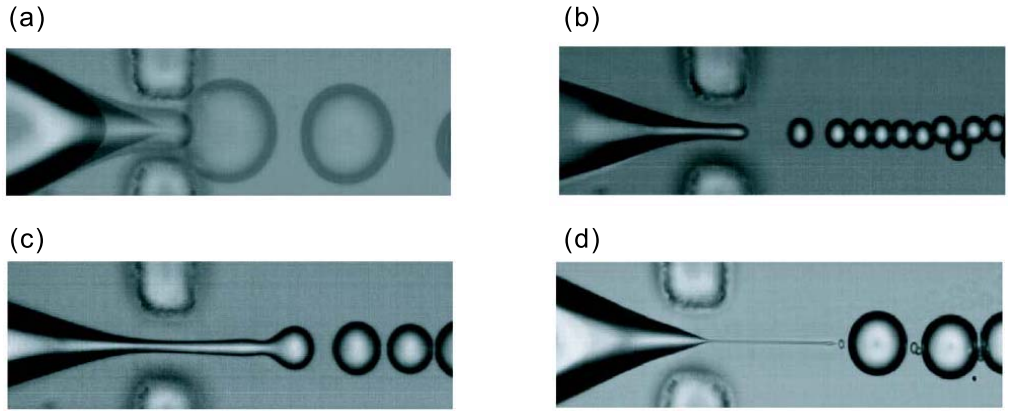

Figure 2.4: Four regimes of droplet generation at a flow focusing geometry (Anna and Mayer, 2006). (a) squeezing, (b) dripping, (c) jetting, (d) threading.

dripping regime are still monodisperse.

(3) Jetting regime [Figure 2.4**c**]: As the capillary number increases further, the finger of the dispersed fluid will be extended beyond the orifice. The finger breaks up due to the Plateau-Reynolds instability. The droplets produced in the jetting regime are polydisperse.

(4) Threading regime [Figure 2.4**d**]: If the flow rates and the surfactant concentration are well controlled, another regime of droplet generation, threading regime, can be founded, as reported by Anna and Mayer (2006). In the threading regime, subsequent to the breakup of each large droplet, a thin thread is drawn out from the finger of the dispersed phase.

The size, the frequency, and the polydipersity of the droplets are highly dependent on the geometry of the microchannel, the flow rates of the two immiscible phases, and the fluid properties such are viscosity (Lee et al., 2008b; Nie et al., 2008) and interfacial tension. Using a flow focusing geometry, monodisperse *bubbles* can also be generated (Garstecki et al., 2004). Surfactants (Anna and Mayer, 2006),

electric fields (Kim et al., 2007; Link et al., 2006), heat (Tan et al., 2008), and moving walls by pneumatic chamber (Lee et al., 2008a) can be utilized to control the process of droplet generation at flow focusing geometries. Both experimental investigations (Anna and Mayer, 2006; Lorenceau et al., 2006) and numerical simulations (Ong et al., 2007; Weber and Shandas, 2007; Zhou et al., 2006) have been widely performed.

2.1.1.3 Double emulsion

Double emulsions refer to droplets having smaller droplets/bubbles within them. The shell fluid serves as a barrier between the core fluid and the outer fluid, as shown in Figure 2.5**a**. Double emulsions have wide potential applications such as particle syntheses, drug delivery and release, nutrient encapsulation, and personal care products. Series combination of droplet generation units can be used to produce double emulsions in microfluidic devices at a highly controllable manner over their polydispersity and contents. One issue associated with the combination of droplet generation units is the wettability. Since the wettability of the channels determines the type of droplets prepared, such as water-in-oil droplets in hydrophobic channels or oil-in-water droplets in hydrophilic channels, the two units for the generation of double emulsions should have opposite wettability. Therefore, there are two types of devices reported in the literature depending on whether the two units are fabricated in one or two chips. In the two-chip design, the core droplets are firstly generated in one chip and then they are re-injected into a second chip, as shown in Figure 2.5**b**. Therefore, different materials with opposite wettability can be used for the two chips, and the interaction between the two junctions is

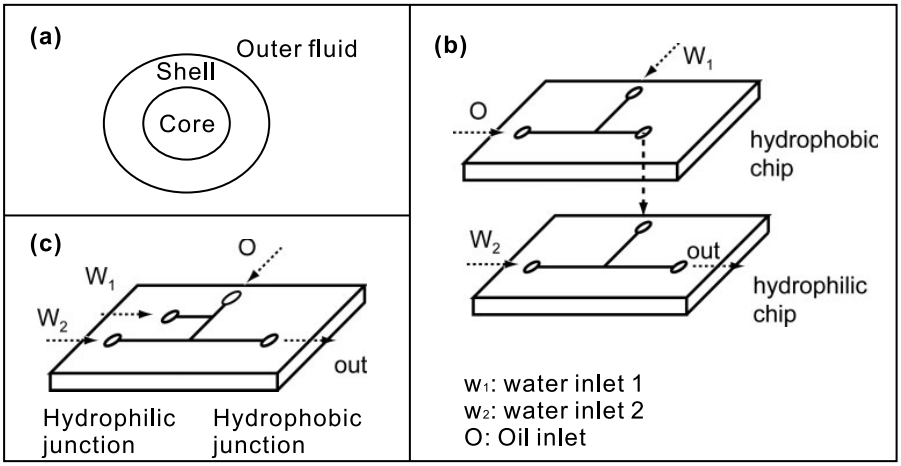

Figure 2.5: (a) Schematic diagram of double emulsions with a core (inner) fluid and a shell (middle) fluid surrounded by an outer fluid. The generation of double emulsions in microchannels normally in two types of devices: (b) two-chip design, and (c) one-chip design (Nisisako, 2008).

minimized (Okushima et al., 2004). In contrast, the one-chip design [Figure 2.5**c**], normally requires modifying the wettability of one unit. There are several methods to modify the surface wettability, such as plasma polymerization (Barbier et al., 2006), laminar flow (Zhao et al., 2001), flow confinement (Abate et al., 2010b), and photolithography (Zhao et al., 2002). Interested readers are referred to a review by Priest (2010).

When forming the core or the shell of double emulsions, two T-junctions in serial (Nisisako et al., 2005; Okushima et al., 2004), or two flow focusing geometries (Abate and Weitz, 2009; Hennequin et al., 2009; Wan et al., 2008) can be used. The sizes of the cores, the thickness of the shells, and the number of cores are controllable by their respective flow rates.

To produce monodisperse double emulsions, the flow rates of different phases must be controlled that both droplet generation units work in the dripping regime.

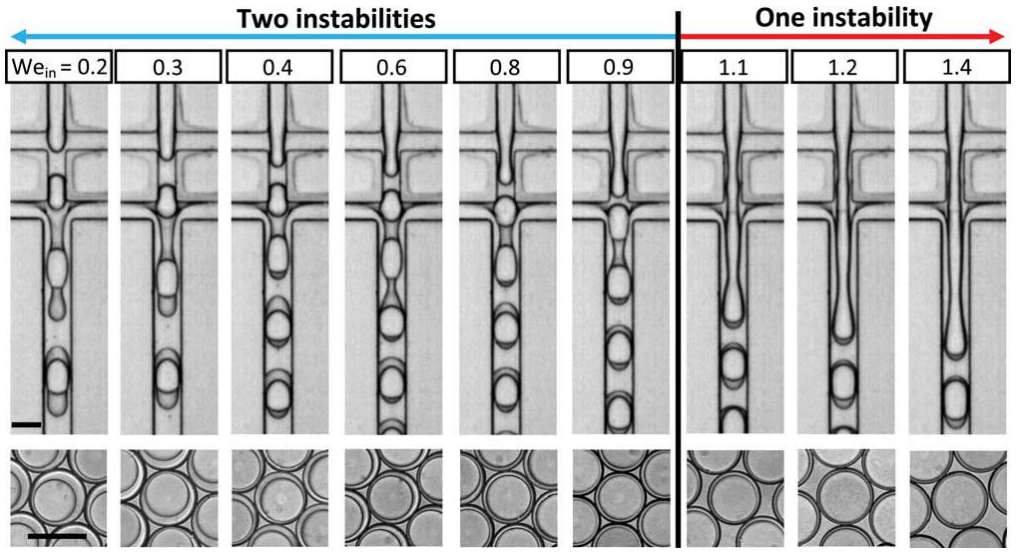

Figure 2.6: Generation of double emulsions with the two-step method and the one-step method. In the two-step method, the two units both work in dripping regimes, and the generation requires two instabilities to form double emulsions. As the increase in the Weber number of the inner phase, the first instability is removed, and a liquid jet is extended to the second unit. Therefore, the pinch-off at the second unit results in double emulsions (Abate et al., 2011).

To obtain double emulsion with thin shells, Abate et al. (2011) reported a one-step method by replacing the first dripping unit with a jetting unit, which results in a liquid jet of the inner fluid extended to the second unit. Dripping at the second unit causes the breakup of the inner phase, as shown in Figure 2.6. Therefore, it can effectively reduce the shell thickness, and successively generated droplets from viscoelastic fluids which are difficult to emulsify controllably.

Utada and coworkers (Lorenceau et al., 2005; Utada et al., 2005) designed a capillary device to form double emulsions by combining a co-flowing geometry and a flow focusing geometry, as shown in Figure 2.7. The inner fluid (core fluid) is introduced from the inner capillary on the right hand side, while the middle fluid

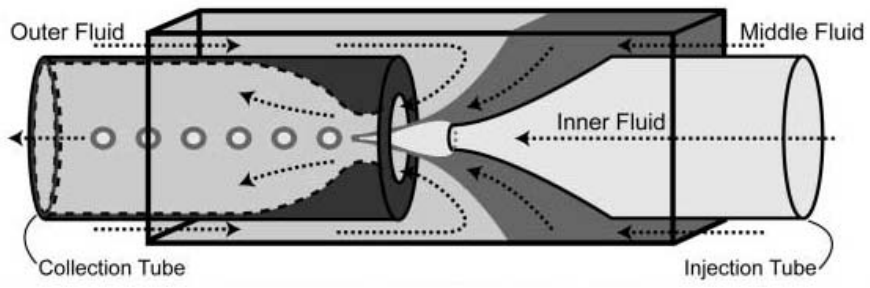

Figure 2.7: Generation of double emulsions using a microcapillary device (Utada et al., 2005).

(shell fluid) is introduced from the outer capillary on the right hand side. The inner and outer capillaries together function as a co-flowing geometry to generate droplets. The produced droplets enter the inner capillary on the left, where the outer fluid (carrier fluid) focuses the middle fluid to produces the shell of the double emulsions. The size of the double emulsions, the fraction of each phase, and the formation frequency are controllable by varying the flow rates of different phases.

2.1.2 Droplet splitting

Droplet splitting refers to the splitting a big droplet into two (or more) daughter droplets in a controllable manner. In some applications such as microreactors (Song et al., 2006a), drug delivery capsules, and micromixers, droplets of identical contents are needed to satisfy the follow-up reaction (Adamson et al., 2006). One way to produce this type of droplets is by splitting a larger droplet into two (or more) daughter droplets. Splitting of droplets at a T-junction was proposed by Link et al (2004), as shown in Figure 2.8. Asymmetric splitting can be achieved by making the asymmetry of (i) the lengths of the branch channels (Link et al., 2004) or (ii) the temperature difference at the branch channels (Ting et al., 2006).

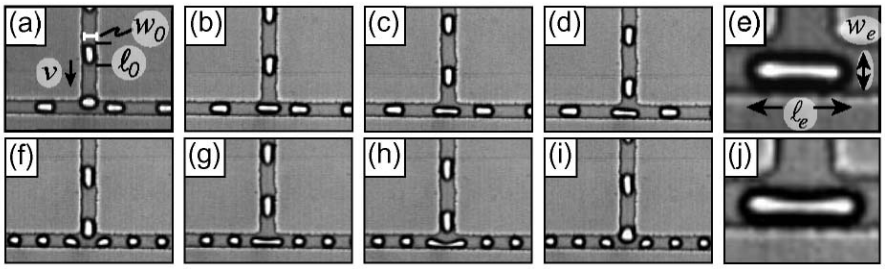

Figure 2.8: Droplet splitting at a T-junction (Link et al., 2004).

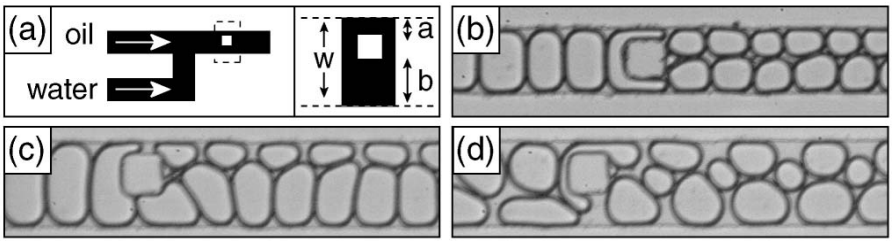

Figure 2.9: Droplet splitting in a microchannel with an obstacle (Link et al., 2004).

If a pulsing pressure is added at the T-junction, the splitting symmetry can be controlled by the position of the pulsing pressure, or even obtain more daughter droplets (Köhler et al., 2004).

Splitting of droplets can also be achieved by letting the droplets pass a channel with an obstacle, as shown in Figure 2.9 (Link et al., 2004). The sizes of the daughter droplets can be controlled by adjusting the position of the obstacle. An alternation of the obstacle is a micromesh structure. A droplet is fragmented into many small droplets when passing a three-dimensional (3D) micromesh in microchannels, as reported by Sato et al. (2006).

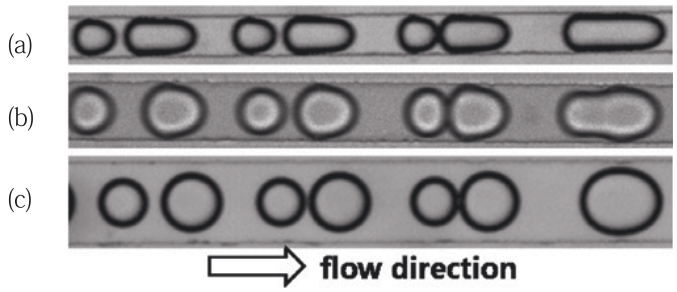

Figure 2.10: A method to bring droplets of different sizes together for coalescence relying on their velocity difference in microchannels (Jin et al., 2010).

2.1.3 Droplet coalescence

Droplet coalescence refers to fuse two (or more) droplets into a larger droplet in a controllable manner. In droplet-based microractors and micromixers, droplet coalescence can be used to initiate or quench a reaction at a well-defined instant and location.

The coalescence process of droplets requires three stages: (1) collision of two droplets, (2) drainage of the liquid film between the droplets, and (3) rupture of the liquid film. The difficulties in coalescence of droplets are how to bring two droplets together in a microchannel, and how to drain the liquid film. Droplets of different sizes can be brought together by size-dependant flow in microchannels, as reported by Ahn et al. (2006a) and by Jin et al. (2010). Smaller droplets move faster than larger droplets in microchannels due to the Poiseuille velocity profile. Therefore, smaller droplets can catch up larger ones for coalescence, as shown in Figure 2.10.

For droplets of equal size, however, it is relatively difficult to bring them together for coalescence because they experience the same flow resistance and the

same flow speed. Several methods to bring two droplets together for coalescence in microchannels have been reported, as shown in Figure 2.11. Tan et al. (2007) used a trifurcation junction to bring droplets together, as shown in Figure 2.11**a**. At the trifurcation junction, the drainage of the continuous phase to the side channel allows a droplet to be hydrodynamically trapped. Therefore, this droplet waits until the subsequent droplet comes to coalesce. In addition, circular chambers (Liu et al., 2007) [Figure 2.11**b**] or diverging structures (Hung et al., 2006) [Figure 2.11**c**] also can slow down a droplet, and allow the subsequent drop to catch up and coalesce. However, the deceleration of the droplet caused by chambers or diverging structures is not significant, and the speed of the continuous phase also slows down, creating flow resistance for the subsequent droplet. To pin the droplets while allow the continuous phase to flow, Niu et al. (2008) proposed a pillar structure to induce a large shear resistance to the droplets, as shown in Figure 2.11**d**. When the first droplet arrives at the pillar section, it is pinned by the pillars, allowing time to wait for the subsequent droplet to merge. The merging also causes the flow resistance to increase. Hence, the pressure drop across the large droplet is built up until it overcomes the flow resistance to push the large droplet downstream.

To pin a droplet in microchannels, Fidalgo el al. (2007) proposed another method which uses a wetting section, as shown in Figure 2.11**e**. In this method, a droplet which does not wet the wall when travelling in a microchannel, may be trapped when passing a wetting section. Once the droplet is trapped at the wetting section, the continuous phase may not have enough energy to push the trapped dispersed fluid away. Arriving of more droplets at the wetting section will result in the accumulation of the dispersed fluid at the wetting section, which increases

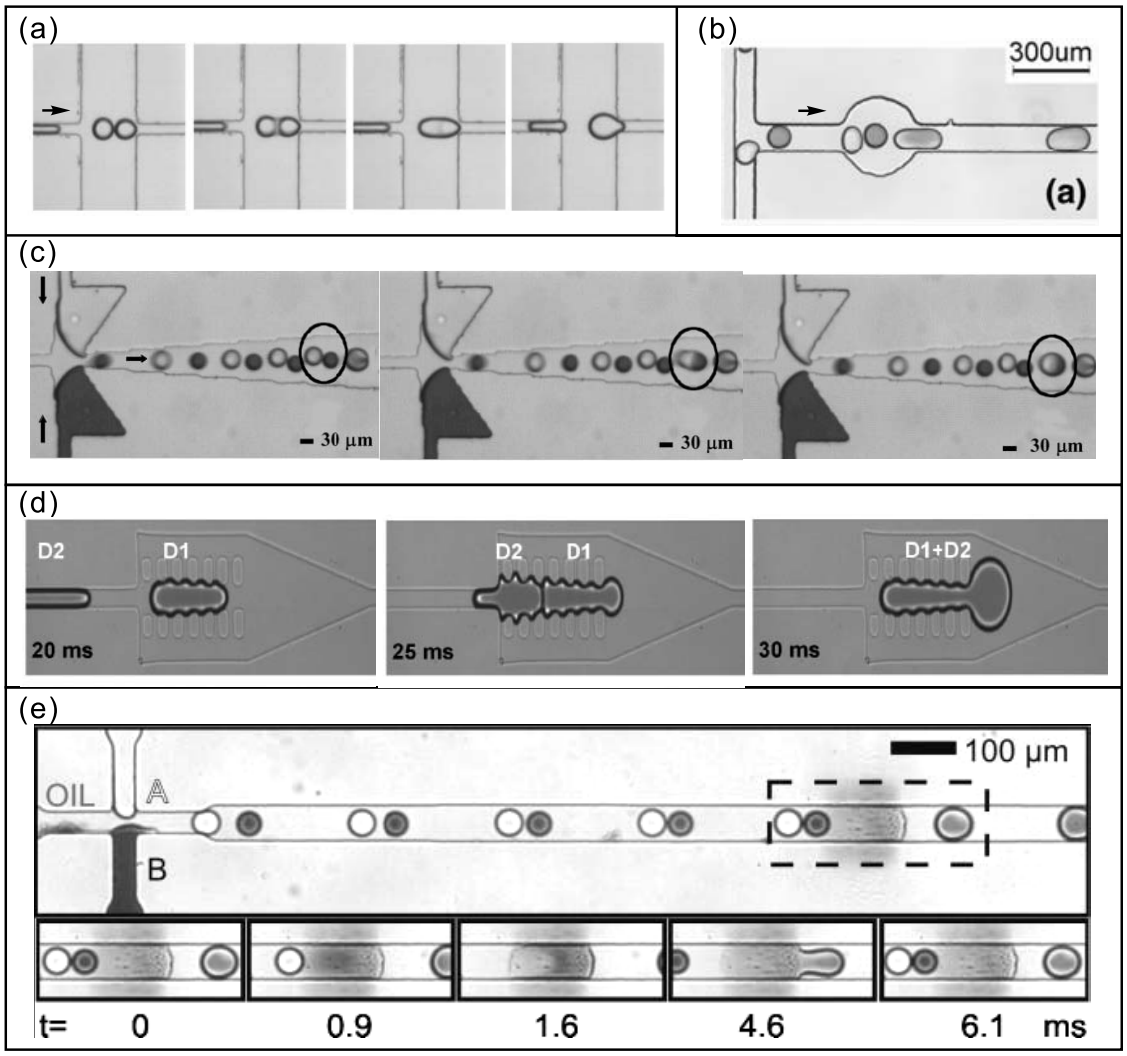

Figure 2.11: Different passive methods to bring droplets together for passive coalescence of droplets in microchannels: (a) Trifurcation junction (Tan et al., 2007). (b) Circular chamber (Liu et al., 2007), (c) Diverging structure (Hung et al., 2006), (d) Pillars (Niu et al., 2008), (e) Wetting section (Fidalgo et al., 2007).

the flow resistance. Hence, the pressure builds up and pushes the dispersed fluid away to form a larger droplet. This trapping and detaching mechanism does not require active elements and nor accurate synchronization of droplets. However, it may cause cross contamination between droplets, which is a disadvantage of this method.

External forces can be used to bring droplets together in microchannels, as shown in Figure 2.12. An active method is to charge the two to-be-fused droplets with opposite charges, as reported by Link et al. (2006) and by Gu et al. (2011) [Figure 2.12**a**]. Charging can be achieved upon the formation of droplets. With opposite charges, the electrostatic force can drive the droplets to traverse the streamlines and contact each other to coalesce.

Zagnoni and Cooper (2009) found that an electric field, if strong enough (2–10 kV/cm), can be used to trap moving droplets of velocity up to 30 mm/s. They used this method to bring droplets together for coalescence, as shown in Figure 2.12**b**. When a droplet passes through the electrode section, it is deformed and trapped. The deformation of the droplet results in a path for the continuous phase. The second droplet, when passing through the electrode section, merges with the first droplet. Being similar to the droplet coalescence at a wetting section, the resultant droplet increases in size until the upstream pressure builds up and pushes the big droplet to the downstream.

To bring the droplets together is not sufficient for the success of the coalescence. During the process of droplet generation, surfactants are widely added to the continuous phase to increase its wettability to the channel and to reduce its interfacial tension with the dispersed phase. The presence of the surfactant at the interface can stabilize the thin liquid film between droplets and hinder the coalescence. To promote the drainage of the thin film between droplets for coalescence, several methods have been proposed, as shown in Figure 2.13.

Through experimental investigations with a high speed imaging system, Bremond et al. (2008) found that coalescence happens at a separation stage instead

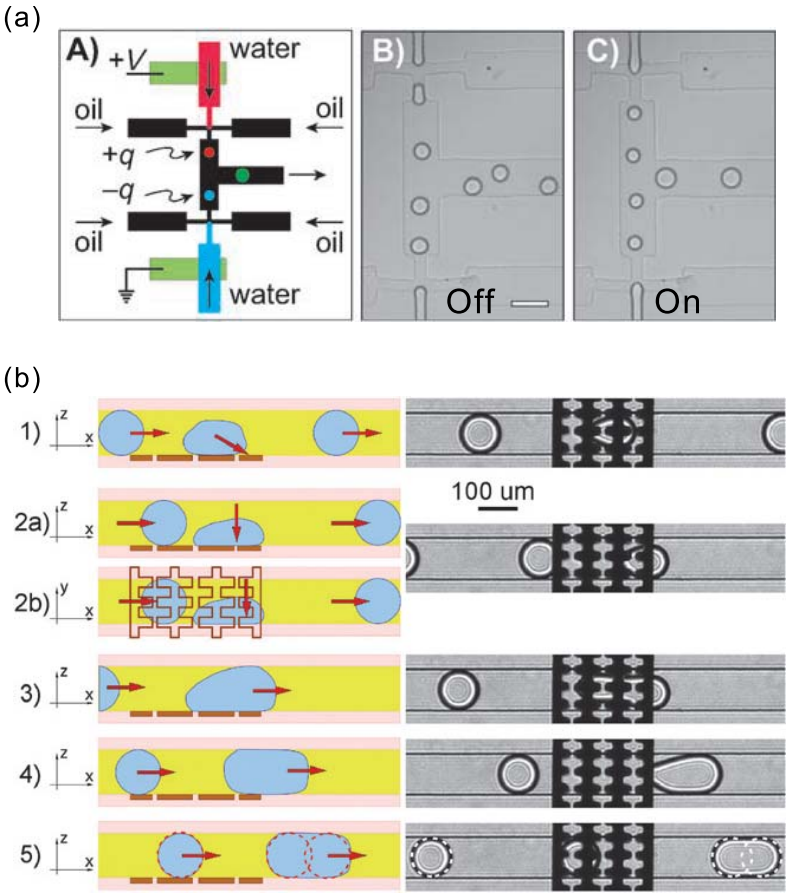

Figure 2.12: Active methods to bring droplets together for coalescence in microchannels: (a) Droplets with opposite charges (Link et al., 2006); (b) Strong electric field (Zagnoni and Cooper, 2009).

of an impact stage, as shown in Figure 2.13**a**. During the separation stage, two nipples in the contact area are formed to destabilize the liquid and accelerate the coalescence. Lai et al. (2009) proposed a 2D model using the lubrication theory and found the approximate shape of the droplet deformation. For two droplets moving apart according to $h_0(t) = h_0(0) + \alpha t^2$, where $2h_0(t)$ is the separation distance and α is a separation parameter, they established a critical value of the dimensionless number $A = 4C\mu R^2\alpha^{1/2}/\pi\sigma[h_0(0)]^{3/2} = 16/3^{3/2}$, below which the separation is unlikely to promote coalescence, where C depends on the viscosities of the two

phases, μ is the viscosity of the continuous phase, R is the radius of droplets, σ is the interfacial tension, and $h_0(0)$ is the initial separation distance.

To promote coalescence of droplets in microchannels, electrocoalescence can be used as an active method by destabilizing the interface (Chabert et al., 2005). When there is a difference in conductivity or permittivity between the dispersed phase and the continuous phase, an electric field results in polarization of the droplets, accumulation of charges at the droplet interfaces, and deformation of droplet shapes. If the two to-be-fused droplets are sufficient close to each other, their interaction may lead to destabilization of the interface, and then coalescence. In an alternating current (AC) electric field, coalescence of droplets occurs in a certain range of amplitude of the electric field (Chabert et al., 2005). Below this range, the two droplets fail to approach each other, whereas above this range, the two droplets repel each other and form small satellite droplets between them even when they are close to contact. This is because of the Taylor cone caused by a strong field, which results in an unstable liquid bridge between the droplets.

Priest et al. (2006) introduced the electrocoalescence method into the droplet coalescence in microchannels. They applied a low potential pulse to induce the electrocoalescence of droplets with different structures, such as bamboo and zigzag shapes. This method can accurately induce the rupture of a single lamella, as shown in Figure 2.13**b**. Ahn et al. (2006a) used the electrocoalescence method to fuse droplet pairs in microchannels, which are synchronized by a size-dependent flow. They demonstrated the application of the electrocoalescence in determining the kinetic constants of the enzyme β-galactosidase from E. coli which requires precise initiation timing.

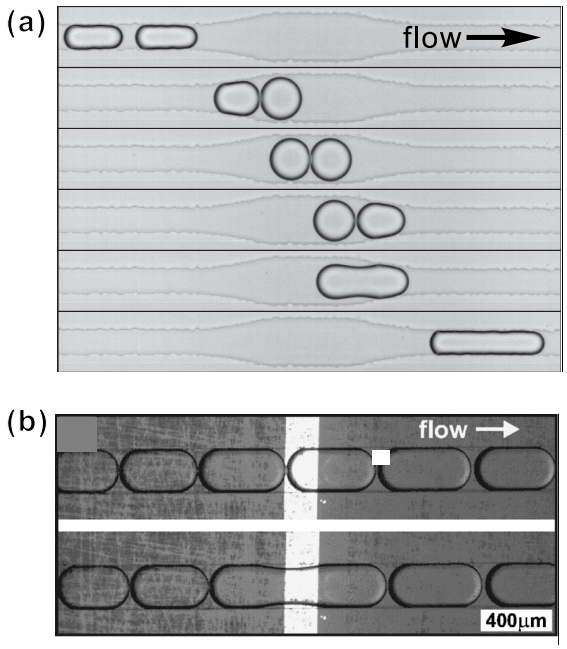

Figure 2.13: Different methods to promote the drainage and destabilization of the thin liquid films between droplets: (a) Separation flow of droplets (Bremond et al., 2008), (b) Electrocoalescence (Priest et al., 2006).

2.1.4 Droplet injection

Adding reagents into droplets is an important function for droplet-based microfluidics. Besides using methods of droplet coalescence to initiate a reaction within the droplet, injection is another way to introduce reagents into droplets and initiate chemical reactions. For this purpose, the reliability, the injection rate, and the controllability over injection amount are essential requirements of droplet injection systems.

Henkel et al. (2004) reported a method to inject reagents using a T-junction in a microchannel, as shown in Figure 2.14**a**. Before the arriving of the droplet from the main channel, a small liquid finger of the dispersed phase is formed at the tip of the side channel. The liquid finger coalesces with the coming droplet when

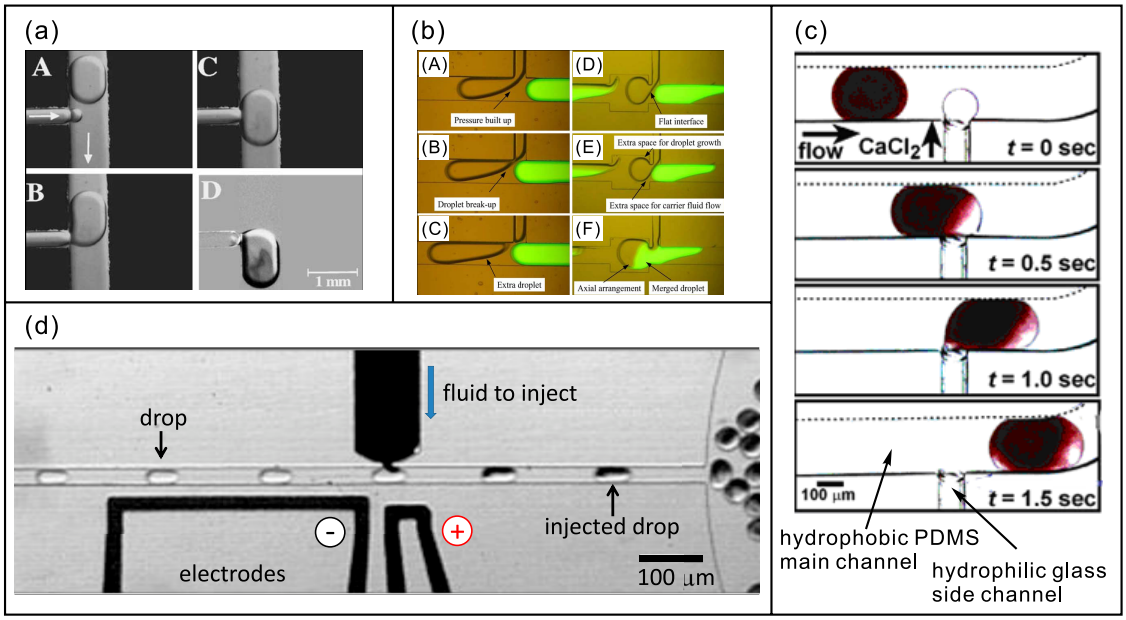

Figure 2.14: Various techniques of droplet injection in microchannels. (a) Droplet injection at a T-junction (Henkel et al., 2004); (b) Droplet injection with an extra space to prevent breakup before coalescence (Sivasamy et al., 2010); (c) Droplet injection with a hydrophilic side channel to prevent breakup before coalescence (Song et al., 2006b); (d) Droplet injection using an electric field to destabilize the interface and promote the injection (Abate et al., 2010a).

the droplet passes the T-junction. Then the neck connecting the droplet and the side stream is torn off by the upstream pressure which is built up due the blockage of the main channel. Using this device, the injection amount up to 250 nL at a rate of 2000 droplets per hour with relative errors below 6% were reached. Shestopalov et al. (2004) used this method to initiate a reaction in droplets, and quench the reaction in droplets during nanoparticle syntheses.

Droplet injection at a T-junction is not reliable because the injected fluid might break up into droplets before merging with the coming droplet, which fails the injection process. Sivasamy et al. (2010) proposed a method to prevent the

breakup before the coalescence by introducing extra space for the growth of the injection fluid, as shown in Figure 2.14**b**. Another method to avoid the breakup before coalescence is by changing the wettability of the side channel for injections (Song et al., 2006b), as shown in Figure 2.14**c**. If the side channel is preferentially wetted by the to-be-injected fluid, such as a hydrophilic side channel and an aqueous reagent, breakup can be prevented until the passing by of the droplet.

Injecting reagents using a T-junction is not reliable when a small amount of fluid is to be injected, or when the droplet passes the junction at a high speed, because the thin film between the to-be-injected finger and the droplets may not rupture. In this case, the droplet slides over the bulged to-be-injected finger without injection, because surfactants prevent merging. Abate et al. (2010a) introduced an electric field at the injection junction, which destabilizes the interface and allows the coalescence with the droplets, as shown in Figure 2.14**d**. By switching the electric field on and off, injection can be achieved selectively at a rate of kilohertz, which is several thousand times higher than simple T-junction injectors. Meanwhile, the injection amount may be low to sub-picolitre scale.

2.2 Transport phenomena

2.2.1 Flow fields

Knowing the flow field within droplets is an important task to understand the flow phenomena by paving the way for related applications. Various methods have been reported in the literature to study the flow field within droplets.

Particle image velocimetry (PIV) is an optical method to measure the

instantaneous flow field in fluids (Adrian, 1991). The fluid is seeded with tracer particles which are assumed to faithfully follow the flow field. The locations of the particles are recorded by a camera and used to calculate the velocity field. For micro particle image velocimetry (μPIV) (Santiago et al., 1998), epifluorescent microscopes are generally used to cope with the small dimension of microfluidic devices. Due to the dimensional requirement, the traditional intrusive velocity measurement methods are not suitable for microfluidic systems. On the contrary, μPIV is a powerful tool as it is a nonintrusive technique by providing instantaneous velocity measurements with a high resolution. However, for multiphase microfluidic systems, special care should be taken during the μPIV measurement. (i) Refractive indices of different phases should be matched to ensure optical access without distortions at the fluid interface (Kim et al., 2004; Oishi et al., 2009). (ii) Particles should be carefully selected to guarantee a homogeneous and optimum solvability in either of the phases and to prevent agglomeration at the interface (Miessner et al., 2008). Measurements of velocity fields in multiphase flow using μPIV have been reported in the literature (Günther et al., 2005, 2004; King et al., 2007; Nguyen et al., 2006). Using a confocal camera and a high speed scanner, Kinoshita et al. (2007) measured the 3D velocity field of a droplet moving in a microchannel. The out-of-plane velocities were determined from the in-plane velocities according to the continuity equation.

Numerical simulation of the multiphase flow is an old topic in computational fluid dynamics (CFD), however, it is still difficult to solve the full Navier-Stokes equations in the presence of a deforming interface. As the dimension of the flow domains shrink to micrometre scale, the simulation of droplets in microchannels

is even more difficult due to the effects of large surface tension forces. There are several methods to predict the interface shape and the evaluation.

Moving mesh method: In the moving mesh method, simulation is performed with a mesh moving with the flow. There are two subgroups of this method. The first subgroup uses boundary fitted grid with each phase (Ryskin and Leal, 1984). The other subgroup uses the Lagrangian grid, i.e., grid following the fluid (Bozzi et al., 1997). The first approach has been applied to study plug flow in microchannels by Grotberg's research group (Fujioka and Grotberg, 2004, 2005; Fujioka et al., 2008; Zheng et al., 2007).

Front tracking method: The front tracking method is a Lagrangian method for the propagation of a moving interface (Tryggvason et al., 2001; Unverdi, 1992). It uses moving marker particles to represent the interface on a fixed computational grid. This approach was utilized to compute the flow of droplets in straight microchannels (Sarrazin et al., 2008), particle dispersion process with droplets in straight microchannels (Muradoglu et al., 2007), and chaotic mixing in droplets moving in meandering microchannels (Muradoglu and Stone, 2005).

Volume of fluid method: The volume of fluid method employs a fraction function C, which is defined as the integral of fluid's characteristic function in the control volume (Scardovelli and Zaleski, 1999). When there is no traced fluid in the control volume, the value of C is zero. When the control volume is full, the value of C is 1. When the interface crosses the control volume, the value of C satisfies $0 < C < 1$. Then the following equation of the fraction function C is solved numerically to predict the interface.

$$\frac{\partial C}{\partial t} + \mathbf{u} \cdot \nabla C = 0 \tag{2.1}$$

This method is widely used in multiphase microfluidics. Utilizing this approach, plug flow in capillaries with circular (Taha and Cui, 2004) and non-circular (Liu and Wang, 2008; Taha and Cui, 2006b) cross section were studied. The effect of gravity on plug flow (Taha and Cui, 2006a), the resistant distribution time (Wöner et al., 2007) were investigated.

Level set method: The level set method (LSM) computes the moving interfaces on a fixed grid (Osher and Fedkiw, 2001, 2003). As compared to other methods for interface tracking or capturing, the LSM is comparatively easy to implement. Topological changes, such as breakup and coalescence, are handled automatically. Besides, it offers the ease of calculating geometrical properties, e.g. volume, surface area and curvature. It solves a level set function as follows

$$\frac{\partial \phi}{\partial t} + \mathbf{u} \cdot \nabla \phi = 0 \tag{2.2}$$

where ϕ is the signed distance function from the point to the interface. The LSM has been used in microfluidics to model processes of droplet generation (Nguyen et al., 2007), splitting (Ting et al., 2006), transport and deformation under electrophoresis (Singh and Aubry, 2007), and actuation and splitting under electrowetting on dielectric (EWOD) (Walker and Shapiro, 2006).

Other approaches of predicting the interface of multiphase flow, such as marker-and-cell method (Harlow and Welch, 1965), constrained interpolation profile method (Yabe et al., 2001), phase-field method (Jacqmin, 1999), will not be covered here due to their less significant applications in droplet-based microfluidics.

Although all of the above methods can give a good result of flow flied, they have common disadvantages that they need complex algorithms to predict the interface and need a large computation time. For simplicity, another type of

methods for computing the flow field in the droplet is to assume the interface shape, such as a curved (Fries and von Rohr, 2009; Kashid et al., 2007) or flat interface (Harries et al., 2003), or even static wall with no-slip boundary condition (Tanthapanichakoon et al., 2006). This type of methods can save computation time, and obtain reasonable results.

Analytical methods for droplet flow are favourable especially for applications in which additional processes need to be analyzed, such as chaos analyses in mixing process (Aref, 2002; Ottino, 1989; Song et al., 2003b). With explicit fully analytical models, analyses is much more convenient, as they can be performed directly on the known flow fields. The flow of droplets moving in microchannels can be approximated as fully developed Poiseuille flow when the droplet is sufficiently long (Handique and Burns, 2001). However, this approximation is invalid when the plug is relatively short. Another analytical approach for droplet flow in microchannels is to approximate droplets as spherical shapes (Kroujiline and Stone, 1999; Stone and Stone, 2005). However, this approach is not practical for confined droplets, or plugs, which refers to droplets occupying the entire cross section of the microchannel.

2.2.2 Micromixing

Rapid mixing is an important task in numerous microfluidic applications such as chemical reactions (Song et al., 2006a), particle syntheses (Dendukuri and Doyle, 2009; Theberge et al., 2010), protein crystallization (Li and Ismagilov, 2010), and drug delivery (Choi et al., 2010b; Yeo et al., 2011). However, when the dimensions of the fluidic devices shrink to micrometre scale, the mixing in microchannels is difficult to achieve because it is hindered by the low Reynolds number (Nguyen and

Wu, 2005; Nguyen, 2008; Squires and Quake, 2005). Without stirring by turbulence due to the low Reynolds number, mixing occurs mainly via molecular diffusion. In addition, mixing in biological applications is even more difficult because of the low diffusivities of the large molecules such as proteins ($D \sim 10^{-11}\mathrm{m}^2/\mathrm{s}$). Numerous methods to enhance mixing in microfluidic devices have been reported (Nguyen and Wu, 2005). A common idea of these methods is to increase the contact area between the liquid filaments. These methods can be categorized into two groups depending on whether external activation is required to stir the fluid filaments: passive and active mixers. The active mixers require external forces, such as electroosmosis (Ng et al., 2009), magnetism (Lee et al., 2009), acoustics (Ahmed et al., 2009), thermocapillarity (Vainchtein et al., 2007), pulsating flow (Nguyen and Huang, 2005), or moving parts. These methods can effectively enhance the mixing process. However, the actuation parts increase the complexity and reduce the robustness of the microdevices. The other group of micromixers, passive mixers, requires no external energy to stir the fluid filaments except the force to deliver the fluids in the devices. Without moving parts in the devices, these methods are usually robotic and reliable. Various passive mixing techniques have been reported such as multi-lamination (Bessoth et al., 1999; Hessel et al., 2003), injection (Miyake et al., 1993), hydrodynamic focusing (Knight et al., 1998), and droplet mixing (Burns and Ramshaw, 2001; Handique and Burns, 2001; Rhee and Burns, 2007; Teh et al., 2008; Tice et al., 2003). The droplet mixing utilizes the internal recirculating vortices in a moving droplet.

Chaotic advection enhances mixing by exponentially increase the interfacial area between two initially segregated fluids (Aref, 1984; Ottino, 1989). It can

be generated in a 3D microchannel by producing transverse flow with patterned grooves on the wall (Stroock et al., 2002). In addition, active mixers can produce transverse flows for chaotic advection using pulsating pressure (Niu and Lee, 2003), electroosmosis (Qian and Bau, 2002; Stroock and Whitesides, 2003), magnetism (Oh et al., 2007), etc.

Although transverse flow is generated in droplets moving in a straight microchannel passively by interface, chaotic advection is not formed because the pair of vortices in the droplet are symmetrical. The vortices are steady in a frame of reference moving together with the droplet. The species in the droplet are mixed within each vortex, but not between the two vortices, as shown in Figure 2.15**a**. Therefore, the effect of the recirculating vortices in a straight microchannel on the mixing is moderate. To produce chaotic advection in the plugs, Song et al. (2003b) proposed a simple and effective method using meandering microchannels, as shown in Figure 2.15**b**. The vortices in droplets become asymmetrical by introducing curvature, and become unsteady by changing direction of the curvature, i.e., using a meandering microchannel. Being a passive and efficient mixing method, droplets moving in meandering microchannels have extra advantages. The axial dispersion is reduced by confining the species in the droplet (Teh et al., 2008; Trachsel et al., 2005). The actuation time in the droplet can be accurately controlled in millisecond scale (Song et al., 2003b). Song et al. (2003a) conducted a series of mixing experiments in droplets moving in meandering microchannels and verified the scaling of mixing time. However, as they stated, "this scaling argument is too simple to predict the geometry of the microchannels that produces the most rapid mixing, and more theoretical and experimental work towards this goal will be

required."(Song et al., 2003a). Tung et al. (2009) investigated the droplet mixing in a meandering microchannel with square turns, and they found that mixing index can be increased eight times compared to that in a straight microchannel. They addressed the droplet deformation at the turns, which contributes the mixing process. Fries and von Rohr (2009) investigated the mixing in liquid plugs and found that the mixing length could be decreased to 12% compared to that in the straight channel design.

Numerical investigations on flow fields or mixing in droplets moving in straight (Harries et al., 2003; Kashid et al., 2005; Muradoglu et al., 2007), or meandering microchannels (Dogan et al., 2009; Fries and von Rohr, 2009; Muradoglu and Stone, 2005) have been reported. Some simulations were carried out with interface prediction methods to predict the interface shape (Dogan et al., 2009; Muradoglu et al., 2007; Muradoglu and Stone, 2005; Tung et al., 2009), while others assumed reasonable interface shapes (Fries and von Rohr, 2009; Harries et al., 2003; Kashid et al., 2005). Most of the simulations were performed in two-dimension. One main reason for the lack of 3D simulation is that the simulation is computation-time demanding. The interface prediction part and the analysis of mixing also increase the complexity and the requirement of computation time.

The transfer of species is an advection-dominated process as the Peclet number is high due to the low diffusivity of the species, particularly for large molecules in various lab-on-a-chip applications. In these situations, numerical methods to solve the mass transfer equation may fail, because false diffusion may be a problem which over-estimates the diffusion effect (Versteeg and Malalasekera, 2007). The particle tracking method is often used to consider the chaotic mixing

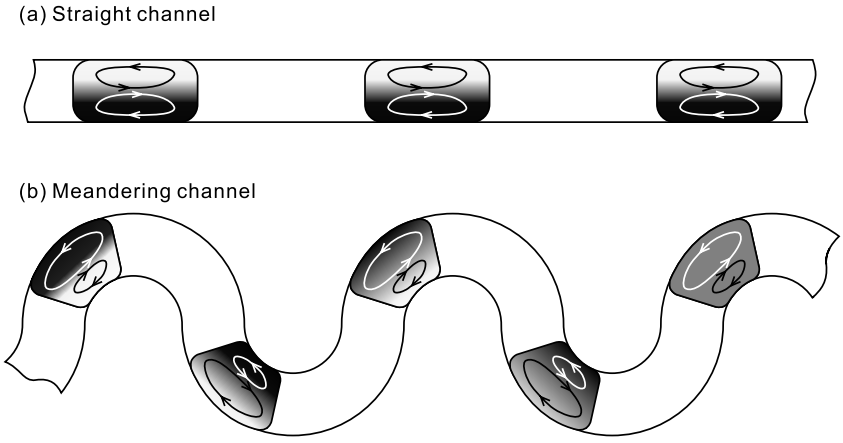

Figure 2.15: Micromixing in droplets moving in microchannels (Song et al., 2003b). (a) Nonchaotic mixing in a straight microchannel; (b) Chaotic mixing in a meandering microchannel.

of species (Chang and Yang, 2006; Kang and Kwon, 2004; Muradoglu et al., 2007; Muradoglu and Stone, 2005). However, to evaluate the results of mixing using the particle tracking method, spatial statistics is often used, which extracts some quantitative variables from the locations of the particles. Therefore, a sufficiently large number of tracer particles is required to be distributed into the flow, which results in a very large computation time for the particle tracking method.

2.2.3 Heat transfer

Heat can be transported in fluids with the help of vortices. With a recirculating flow, heat or mass can be advected by the flow even in the Stokes regime, during which the Reynolds number is so small that the inertial force is negligible (Happel and Brenner, 1983). Liquid filaments can be continuously stretched and folded by recirculating flow, and interfacial area between liquid filaments can be greatly increased. If vortices are of sufficient size and strength, their enhancement of heat

or mass transfer can be significant (Aref, 1984; Ottino, 1989).

Many methods to enhance heat transfer reported in the literature can be categorized into the group of promoting vortices. For example, curved channels have been used to produce Dean vortices (Dean, 1927, 1928b) to enhance heat transfer (Berger et al., 1983; Naphon and Wongwises, 2006; Liu and Wang, 2009). The Dean vortices are a type of secondary flow consisting of a pair of counter-rotating vortices resulted from the imbalance between the centrifugal force and the radial pressure difference when the fluid passes through a curved channel. The vortices get stronger when the Dean number increases, which characterizes the relative effect of centrifugal force with the viscous force, $De \equiv \frac{\rho V D_H}{\mu}\sqrt{\frac{D_H}{2R}}$, where ρ and μ are, respectively, the density and the dynamic viscosity of the fluid, V is the axial velocity, D_H is the hydraulic diameter of the channel, and R is the radius of the curved channel path. In microchannels, however, due to the low velocity, the centrifugal force and the Dean number are small. Consequently, the Dean vortices are much weaker than those in channels of large scale.

Another way to promote vortices in microchannels is to use vortex promoters (Meis et al., 2010), which are usually one or arrays of built-in obstacles in microchannels. Vortex promoters of different shapes (such as square (Rahnama and Hadi-Moghaddam, 2005; Turki et al., 2003), rectangular (Icoz and Jaluria, 2006), triangular (Abbassi et al., 2001), and circular (Meis et al., 2010; Valencia and Sen, 2003)) can produce transverse flow by flow separation on the surface of the vortex promoters, which results from the interplay between the inertial force and the viscous force. The vortex strength increases with increasing the Reynolds number ($Re = \rho V D_H/\mu$), which enhances the heat transfer process. In

microchannels, however, the transfer of momentum, mass, and energy takes place in the laminar regime and is characterized by low Reynolds numbers (Squires and Quake, 2005), which restricts the applications of vortex promoters to enhance heat transfer. Moreover, the cost to fabricate the obstacles in microchannels is much higher than that to fabricate simple smooth channels.

A simple and effective method to induce vortices in microchannels is by introducing interfaces into the flow. When a second immiscible fluid is introduced into a microchannel, interfaces of different shapes are formed which correspond to different flow patterns, such as bubble/droplet flow, plug flow, annular flow, and stratified flow (Kawahara et al., 2002; Triplett et al., 1999). Plug flow can be formed by continuously generating droplets/bubbles in microchannels (Anna et al., 2003; Christopher and Anna, 2007; Thorsen et al., 2001). As the size dispersity of the droplets/bubbles can be as low as 2%, this ordered structure makes it possible to manipulate the flow and transport phenomena in droplets/plugs accurately. In the presence of the interface, vortices are formed in liquid plugs (Günther et al., 2004; Handique and Burns, 2001). Unlike vortex promoters, in which vortices are formed locally in the region behind the obstacles, vortices produced by plug flow occupy the whole plug. Therefore, it possesses the advantage that the vortices in plugs can be used to enhance heat transfer in microchannels.

Plug flow shows promising opportunities in heat exchangers by inducing vortices (Baird and Mohseni, 2008), and the flow can be induced by pressure using pumps (Walsh et al., 2010) or electrowetting on dielectric (EWOD) (Baird and Mohseni, 2008, 2009) method. However, systematic investigations of heat transfer enhancement in plugs are few, and heat transfer in two phase flow in microchannels

has not been studied as extensively as single phase flow (Palm, 2001). A possible reason is that two phase flow is much more complex than single phase flow. Some previous work dealing with heat transfer of multiphase flow in microchannels mainly contributed to boiling (Peng and Wang, 1993; Thome, 2004) and condensation (Chen and Cheng, 2005). The effects of phase change on the Nusselt number or convective heat transfer coefficient were investigated, while the effects of the vortices on heat transfer were not quantified.

To experimentally investigate the effect of the vortices in droplets/plugs on the heat transfer process, it is necessary to characterize the interaction between the velocity field and the temperature field. μPIV is a tool widely used to assess the flow field in microchannels; while laser induced fluorescence (LIF) method is a technique to measure the temperature field in microchannels. Both methods require the refractive indices of different phases to match to ensure the optical access without distortion at fluid interfaces (Kim et al., 2004; Oishi et al., 2009). Moreover, most materials used for heat exchangers are not transparent to visible light, which increases difficulties in using these optical methods (μPIV and LIF). In the experimental investigations of heat transfer in a stainless steel tube (1.5 mm internal bore) done by Walsh et al. (2010), the surface temperature on the tube was obtained using a high resolution infrared thermography system, but the temperature field in the liquid plug could not be measured.

To numerically and analytically model the heat transfer process of plug flow in microchannels, both the flow field and the temperature field should be considered. Muzychka et al. (2010) proposed a simplified model to consider the heat transfer in plugs in microchannels of different cross-sectional shapes. The heat transfer process

was considered as a Graetz problem with a steady state condition. The problem was solved analytically by assuming a uniform velocity profile throughout the liquid plug. A better way is to incorporate the recirculating flow in the liquid plug into the model of heat transfer and to investigate how the recirculating vortices affect the heat transfer process.

To numerically simulate the heat transfer process of plug flow in microchannels, numerical methods to predict the location and shape of the interface are often necessary. These methods, as discussed in Section 2.2.1, are usually complex and computation-time consuming, which are unfavourable for heat transfer analysis in plug flow in microchannels.

2.3 Summary

Droplet-based microfluidics gained rapid development in the last decade. Many techniques to manipulate droplets in microchannels have been developed, such as generation, splitting, coalescence, and injection. The complex behaviours of droplets have motivated a large number of studies aiming to extract the essential physics that governs the droplet-based microfluidics. However, current methods studying the transport phenomena have their advantages and disadvantages. The numerical methods to predict the evolution of the interface are too complex and computation-time consuming, and make the understanding of transport phenomena in droplets more difficult. The available analytical approaches are not suitable for plug flow in microchannels. Simple yet effective models for plugs in microchannels are necessary, because (i) they can provide insight information of the flow, and (ii) they can be used directly and easily to study subsequent processes such as

mixing or heat transfer.

Chapter 3

Plug Flow in Microcapillaries with Circular Cross Section [†]

3.1 Introduction

In this chapter, an analytical model is proposed for plug flow in microcapillaries or microchannels with circular cross section. The flow is rotationally symmetric in a translating cylindrical coordinate system. In Section 3.2, the Stokes flow is modelled with a fourth-order partial differential equation. Series solution is obtained and the associated boundary conditions are satisfied. In Section 3.3, the flow field is calculated and compared with experimental results. The effect of plug length on the flow pattern is investigated. In Section 3.4, the analytical model is used to calculate the flow resistance. The comparison of the flow resistance with experimental results shows good agreement.

[†]This work has been published in *International Journal of Heat and Fluid Flow 32 (5) 935-943.*

3.2 Mathematical modelling of flow field

3.2.1 Problem description and assumptions

Figure 3.1 shows liquid plugs in a microcapillary with circular cross section. Water plugs are separated by an immiscible phase such as air. The inner radius of the capillary is R. The plug, with its length L, is moving to the right at a constant speed of V.

In the analysis, the following assumptions are made:

(1) Stokes flow exists within the plug due to the low Reynolds number. The transient term and the convection term in the momentum equation are neglected.

(2) No body force is considered. The gravity is neglected and there is no other body force for the liquid plug.

(3) The interface is flat and is perpendicular to the wall of the capillary. Numerical simulations were performed to validate the flat-interface assumption and to examine the effects of the contact angle and the curvature on the flow pattern in liquid plugs, and they are provided in Appendix A.

(4) The liquid plug does not slip on the wall of the capillary. This is a reasonable assumption for liquid flow in microcapillaries/microchannels at micrometre scales. Some recent investigations showed that the wettability of the solid wall affects the slip length (Squires and Quake, 2005). Wetting (hydrophilic) surfaces obey the no-slip boundary condition as expected, whereas clean

nonwetting (hydrophobic) surfaces exhibit apparent slip (Lumma et al., 2003; Priezjev et al., 2005). However, the slip length is still in the nanometre scale. For water flows over hydrophobic walls, the typical slip lengths that are observed in the range between 10 and 30 nm (Tabeling, 2009). For liquid flow in microchannels/microcapillaries (normally tens to hundreds of micrometres), the liquid can be treated as a continuum and the no-slip condition applies.

(5) The viscosity of the adjacent immiscible phase is neglected, and there is no shear stress on the free surface of the plug. This is a reliable assumption if the immiscible phase has a much lower viscosity than the liquid plug, such as a gas.

(6) The liquid is an incompressible Newtonian fluid.

3.2.2 Governing equation and boundary conditions

A translating cylindrical coordinate is built on the plug, as shown in Figure 3.2. The plug takes the region of $0 \leq z \leq L$, $0 \leq r \leq R$. The coordinate system is translating together with the plug at a speed of V. In this way, the plug unit is relatively stationary with respect to the coordinate system, while the wall of the microcapillary is translating at a speed of V to the left. The middle cross section **X**-**X** is indicated in Figure 3.2.

For the plug in the Stokes flow regime moving in a microcapillary with circular cross section, the governing equation is a fourth-order partial differential equation

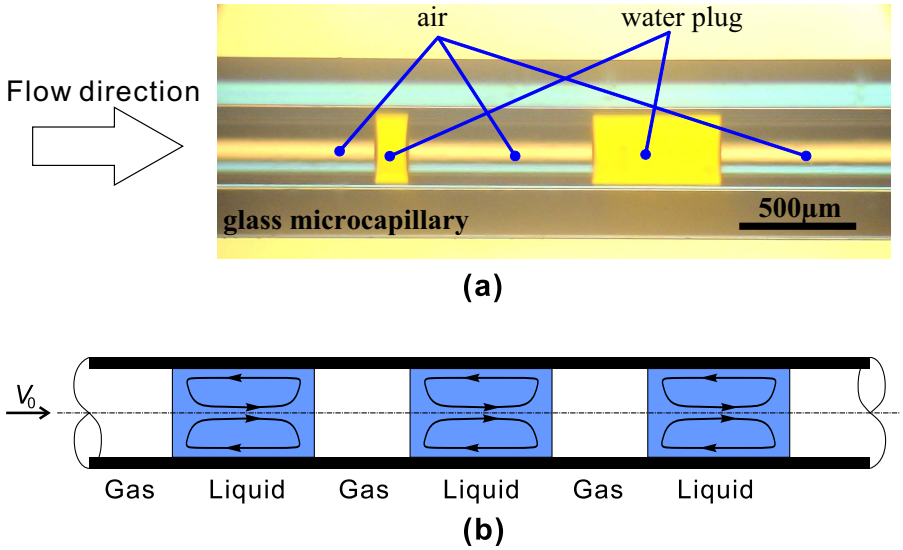

Figure 3.1: (a) Typical liquid plugs in a microcapillary with circular cross section. The liquid plugs of deionized (DI) water are separated by air in a glass microcapillary of inner radius 176 μm (Sigma-Aldrich, P0549) viewed under an inverted microscope. (b) Schematic diagram of plug flow in a microcapillary with circular cross section.

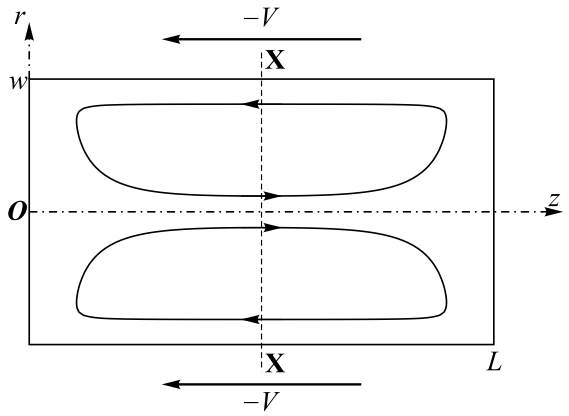

Figure 3.2: Mathematical modelling of a plug moving in a microcapillary. With the translating frame of reference fixed on the plug unit, the wall is moving to the left at a speed of V.

(Deen, 1998; Duda and Vrentas, 1971; Shankar, 2007; Meleshko, 2003)

$$\left(\frac{\partial^2}{\partial^2 r}-\frac{1}{r}\frac{\partial}{\partial r}+\frac{\partial^2}{\partial z^2}\right)\left(\frac{\partial^2}{\partial^2 r}-\frac{1}{r}\frac{\partial}{\partial r}+\frac{\partial^2}{\partial z^2}\right)\varphi=0 \tag{3.1}$$

where φ is the stream function defined as

$$u_r=-\frac{1}{r}\frac{\partial\varphi}{\partial z},\quad u_z=\frac{1}{r}\frac{\partial\varphi}{\partial r} \tag{3.2}$$

According to the boundary condition on the walls of the microcapillary, as shown in Figure 3.2, we have

$$\frac{1}{R}\frac{\partial\varphi\left(R,z\right)}{\partial r}=-V \tag{3.3}$$

The two ends of the plug are free surfaces, as the shear effect of the adjacent gas is negligible

$$\frac{\partial^2}{\partial z^2}\varphi\left(r,0\right)=0,\quad \frac{\partial^2}{\partial z^2}\varphi\left(r,L\right)=0 \tag{3.4}$$

According to the definition of the stream function, the value of the stream function φ is the same along the streamline. As the control volume of the liquid plug is closed with no fluid flowing in or out of the plug, the stream function is constant along the boundary of the plug. Here it is set to be zero.

$$\varphi(0,z)=0,\quad \varphi(R,z)=0 \tag{3.5}$$

$$\varphi(r,0)=0,\quad \varphi(r,L)=0 \tag{3.6}$$

Since the flow is rotational symmetric, and the radial velocity component u_r is zero along the axis

$$u_r\left(0,z\right)=\lim_{r\to 0}\left(-\frac{1}{r}\frac{\partial\varphi}{\partial z}\right)=0 \tag{3.7}$$

The fourth-order partial differential equation (3.1) and its boundary conditions Eqs. (3.4)–(3.7) represent a system of equations describing the spatial variation of the stream function in the liquid plug. Once the expression of the stream function

is determined, the velocity, the vorticity, and the stress can be determined from the stream function.

3.2.3 Nondimensionalisation

The governing equation (3.1) and the associated boundary conditions Eqs. (3.4)–(3.7) can be nondimensionalised for the convenience of modelling and analysis. The radius of the microcapillary R is set as the characteristic length

$$\hat{r} \equiv \frac{r}{R}, \quad \hat{z} \equiv \frac{z}{R}, \quad \hat{L} \equiv \frac{L}{R} \tag{3.8}$$

where $\hat{L}$ is the dimensionless plug length. The velocity of the liquid plug V is set as the characteristic speed. Hence, the dimensionless velocity components in the r and z directions are, respectively:

$$\hat{u}_r \equiv \frac{u_r}{V}, \quad \hat{u}_z \equiv \frac{u_z}{V} \tag{3.9}$$

According to the definition of the stream function in Eq. (3.2), the dimensionless stream function can be defined as

$$\hat{\varphi} \equiv \frac{\varphi}{VR^2} \tag{3.10}$$

Therefore, the dimensionless governing equation can be obtained from Eq. (3.1)

$$\left(\frac{\partial^2}{\partial \hat{r}^2} - \frac{1}{\hat{r}}\frac{\partial}{\partial \hat{r}} + \frac{\partial^2}{\partial \hat{z}^2}\right)\left(\frac{\partial^2}{\partial \hat{r}^2} - \frac{1}{\hat{r}}\frac{\partial}{\partial \hat{r}} + \frac{\partial^2}{\partial \hat{z}^2}\right)\hat{\varphi} = 0 \tag{3.11}$$

The corresponding dimensionless boundary conditions can be obtained from Eqs. (3.4)–(3.7)

$$\frac{\partial \hat{\varphi}}{\partial \hat{r}}(1, \hat{z}) = -1 \tag{3.12}$$

$$\frac{\partial^2}{\partial \hat{z}^2}\varphi(\hat{r}, 0) = 0, \quad \frac{\partial^2}{\partial \hat{z}^2}\hat{\varphi}\left(\hat{r}, \hat{L}\right) = 0 \tag{3.13}$$

$$\hat{\varphi}\left(0,\hat{z}\right)=0,\quad \hat{\varphi}\left(1,\hat{z}\right)=0 \tag{3.14}$$

$$\hat{\varphi}\left(\hat{r},0\right)=0,\quad \hat{\varphi}\left(\hat{r},\hat{L}\right)=0 \tag{3.15}$$

3.2.4 Analytical solution

According to the fact that the governing equation (3.11) is linear and the domain is rectangular, a tentative solution is of a series form (Deen, 1998; Duda and Vrentas, 1971; Shankar, 2007). We can construct the format of the solution of the governing equation (3.11) as

$$\hat{\varphi}\left(\hat{r},\hat{z}\right)=\sum_{n=1}^{\infty}\sin\left(n\pi\frac{\hat{z}}{\hat{L}}\right)A_nF_n \tag{3.16}$$

where

$$F_n\left(\hat{r}\right)=\frac{\hat{r}I_1\left(n\pi\hat{r}/\hat{L}\right)I_2\left(n\pi/\hat{L}\right)-\hat{r}^2I_1\left(n\pi/\hat{L}\right)I_2\left(n\pi\hat{r}/\hat{L}\right)}{I_2^2\left(n\pi/\hat{L}\right)} \tag{3.17}$$

where I_n is the modified Bessel function of the first kind of order n. This format of solution in Eq. (3.16) satisfies the dimensionless governing equation (3.11), the boundary conditions of $\hat{\varphi}=0$ in Eqs. (3.14)–(3.15), and the free surface boundary conditions in Eq. (3.13). Hence, the coefficient A_n can be obtained which lets Eq. (3.16) satisfy the boundary velocity on the wall. From Eq. (3.12), we have

$$-1=\sum_{n=1}^{\infty}\sin\left(n\pi\frac{\hat{z}}{\hat{L}}\right)A_nF_n^{'}\left(1\right) \tag{3.18}$$

where

$$F_n^{'}\left(\hat{r}\right)=\frac{-n\pi\hat{r}^2I_1\left(n\pi/\hat{L}\right)I_1\left(n\pi\hat{r}/\hat{L}\right)+n\pi\hat{r}I_0\left(n\pi\hat{r}/\hat{L}\right)I_2\left(n\pi/\hat{L}\right)}{\hat{L}I_2^2\left(n\pi/\hat{L}\right)} \tag{3.19}$$

Multiplying $\sin(n\pi\hat{z}/\hat{L})$ on both sides of Eq. (3.18) and integrating with respect to z from 0 to $\hat{L}$, we can obtain the coefficient A_n through the Fourier transform

$$A_n=\frac{2\left[(-1)^n-1\right]}{F_n^{'}\left(1\right)n\pi} \tag{3.20}$$

In this way, the stream function field is established. The velocity field can also be obtained from the stream function accordingly

$$\hat{u}_r \equiv -\frac{1}{\hat{r}}\frac{\partial}{\partial z}\hat{\varphi}\left(\hat{r},\hat{z}\right) = -\sum_{n=1}^{\infty}\frac{n\pi}{\hat{L}}\cos\left(n\pi\frac{\hat{z}}{\hat{L}}\right)A_n\frac{F_n}{\hat{r}} \tag{3.21}$$

$$u_z \equiv \frac{1}{\hat{r}}\frac{\partial}{\partial \hat{r}}\hat{\varphi}\left(\hat{r},\hat{z}\right) = \sum_{n=1}^{\infty}\sin\left(n\pi\frac{\hat{z}}{\hat{L}}\right)A_n\frac{F_n{}'\left(\hat{r}\right)}{\hat{r}} \tag{3.22}$$

3.3 Results and discussion

3.3.1 Comparison with experimental results

When a liquid plug moves in a microcapillary, in the presence of the interfaces at the front and rear ends of the liquid plugs, the flow pattern is much different from that of the continuous flow. For a typical dimensionless plug length $\hat{L} = 2.45$, the vortices of toroidal shapes are shown in Figure 3.3**a**, and the streamlines and the velocity vectors on a longitudinal section are shown in Figures 3.3**b** and **c**, respectively. When the liquid in the plug is moving towards the front end, it is blocked by the front interface and moves towards the wall of the microcapillary. Due to the presence of the rear interface, the liquid moves from the wall of the microcapillary towards the centre of the plug. This movement of the fluid produces recirculating flow in the liquid plug with respect to the translating frame of reference, which is clearly shown Figures 3.3**a**–**c**. A streamline **S**-**S** along the z-axis works as the axis of the toroidal-shaped vortex. The comparison of velocity component between the analytical result and the measured flow field by Ahn et al. (2006b) is shown in Figures 3.3**d** and **e**, respectively. The measured flow field is obtained with frequency domain optical coherence tomography. Figures 3.3**d** and

e show the velocity components projected in the direction which is tilted 1.5° away from the cross-sectional plane of the microcapillary. The dimensionless plug length $\hat{L} = 2.45$ is obtained in pixels from the image by a MATLAB program as

$$\hat{L} \equiv \frac{L_{\text{pixel}}}{R_{\text{pixel}}} = \frac{A_{\text{pixel}}}{R_{\text{pixel}}^2} \tag{3.23}$$

where L_{pixel}, R_{pixel}, and A_{pixel} are the length of the plug, the radius of the capillary, and the area of the plug in pixels, respectively. The comparison with the experimental result shows that the analytical model can offer a reasonable good prediction of the flow field within liquid plugs.

3.3.2 Vortex centres

As the stream function at the boundary is zero, the maximum/minimum points of the stream function ($\hat{\varphi}_{\max}$ or $\hat{\varphi}_{\min}$) within the plug correspond to the vortex centres, and the magnitude of the stream function reflects the strength of the vortex. Hence the location of the vortex centre and the value of the stream function at the vortex centre are important parameters to quantify the vortex pattern in the plug. As the stream function is symmetric with respect to the cross section **X**-**X** (shown in Figure 3.2), the vortex centres are located along **X**-**X**. The radial position of the vortex centre ($\hat{r}_{\text{centre}}$) for different dimensionless plug lengths ($\hat{L}$) and the corresponding dimensionless stream function ($\hat{\varphi}_{\text{centre}}$) are shown in Figure 3.4. The location of the vortex centres and the strength of vortices strongly depend on the dimensionless plug length ($\hat{L}$). The vortex centre moves in the direction towards the axis of the microcapillary, while $\hat{\varphi}_{\text{centre}}$ increases with increasing $\hat{L}$. This effect can be observed in Figure 3.5. Initially, with increasing the plug length, the vortices increase in size and strength, and the vortex centres move rapidly in

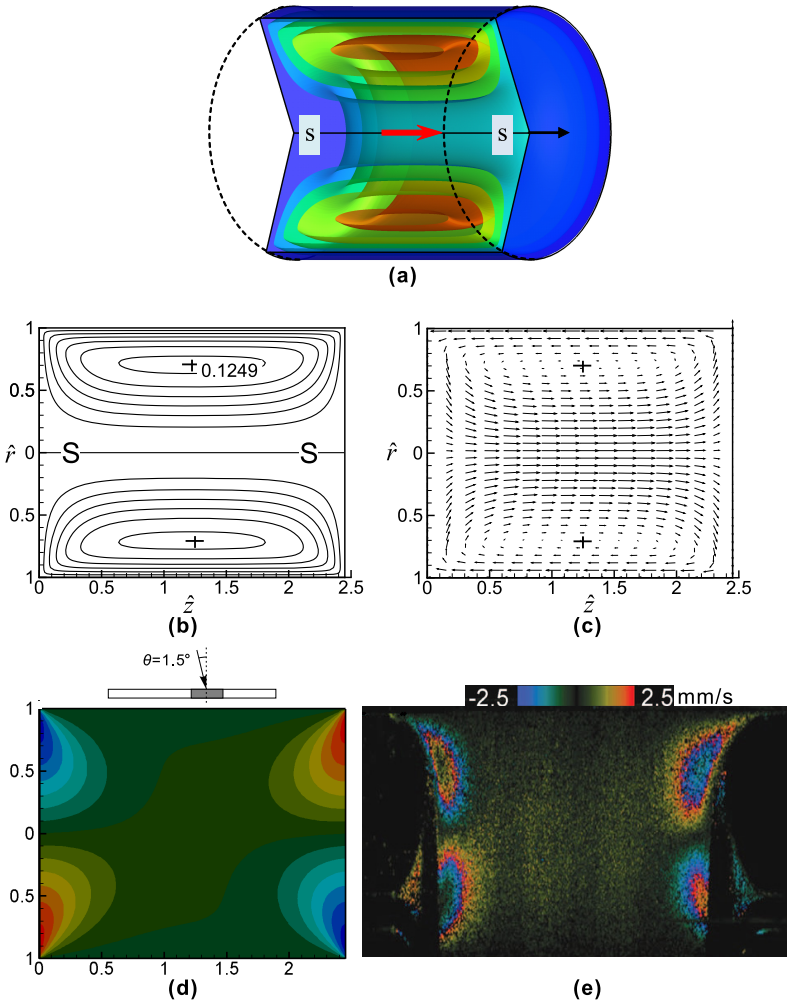

Figure 3.3: Flow pattern within a liquid plug of dimensionless plug length $\hat{L} = 2.45$: (a) 3D view of the vortices of toroidal shape within a liquid plug in a capillary of circular cross section. The fluid flows along the iso-surfaces of stream function, and forms vortices of toroidal shape. (b) Stream function contours, the increment between two consecutive contours is $\Delta\hat{\varphi} = 0.02$. The crosses and the corresponding values indicate the locations and stream functions of the vortex centres, respectively. (c) Velocity vectors. (d) Dimensionless velocity projected in the direction $\theta = 1.5°$ from the model. (e) Experimental result of velocity projected in the direction $\theta = 1.5°$ (Ahn et al., 2006b).

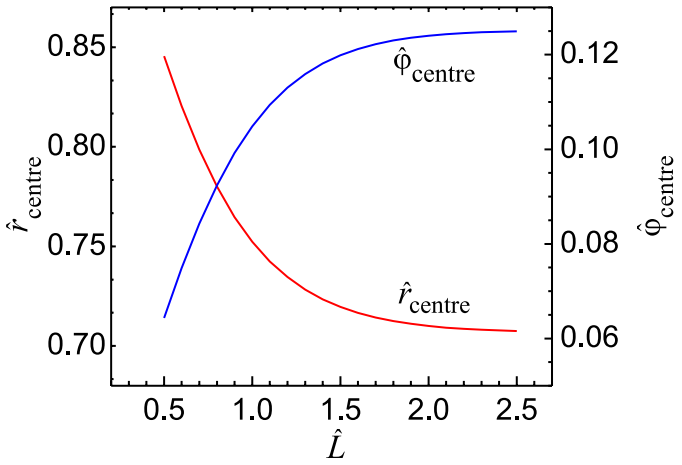

Figure 3.4: Radial position of the vortex centre ($\hat{r}_{\text{centre}}$) for different dimensionless plug lengths ($\hat{L}$) and the corresponding stream functions ($\hat{\phi}_{\text{centre}}$).

the direction towards streamline **S-S**. The magnitude of $\hat{\varphi}_{\text{centre}}$ increases as the vortices expand. For relatively large dimensionless plug length ($\hat{L} > \hat{L}_{\text{long}}$), the vortex centres $\hat{r}_{\text{centre}}$ becomes almost fixed in their locations. Here, $\hat{L}_{\text{long}}$ refers to the dimensionless plug length where the velocity profile $\hat{u}_z$ along **X-X** approaches the fully developed velocity profile as shown in Figure 3.6, which will be explained in Section 3.3.3. The unchanged velocity profiles make the locations of the vortex centres nearly constant.

If the length of the plug approaches infinity ($\hat{L} \rightarrow \infty$), the flow can be simplified to the one-dimensional (1D) flow. For a single phase flow, the fully developed velocity profile in a straight tube is parabolic, and the axial pressure gradient $\Delta p/L$ is independent of r.

$$u_{z,1D}{}' = \frac{\Delta p}{4L\mu}\left(R^2 - r^2\right) \tag{3.24}$$

The mean velocity can be obtained through integration

$$V = \frac{\Delta P R^2}{8L\mu} \tag{3.25}$$

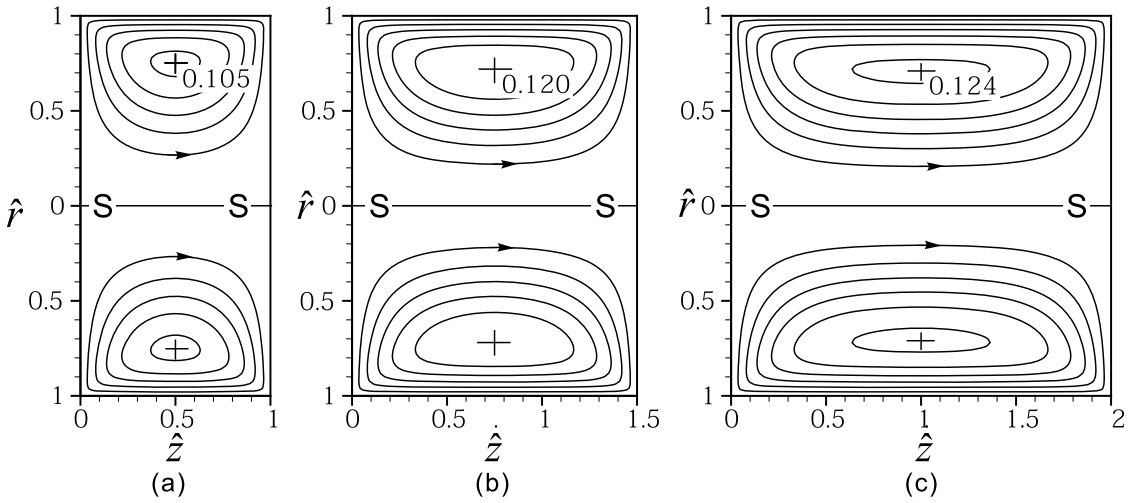

Figure 3.5: Contours of stream function within liquid plugs of different plug lengths. (a) $\hat{L} = 1$, (b) $\hat{L} = 1.5$, and (c) $\hat{L} = 2$. The increment between two consecutive contours is $\Delta\hat{\varphi} = 0.02$. The crosses and the corresponding values in (a–c) indicate the locations and the stream functions of the vortex centres, respectively.

As a result, the dimensionless velocity profile in the translating coordinate system is

$$\hat{u}_{z,1D} = \frac{u_{z,1D}{}' - V}{V} = 1 - 2\hat{r}^2 \tag{3.26}$$

According to the dimensionless group, the dimensionless stream function follows

$$\hat{u}_z = \frac{1}{\hat{r}} \frac{\partial \hat{\varphi}}{\partial \hat{r}} \tag{3.27}$$

Being similar to the stream function boundary condition of plug in Eq. (3.14), the boundary condition for the stream function of the 1D single phase flow in a microcapillary is

$$\hat{\varphi}\,(0) = 0, \quad \hat{\varphi}\,(1) = 0 \tag{3.28}$$

With the velocity profile in Eq. (3.26), the dimension stream function can be

obtained by integration with the boundary condition in Eq. (3.28), and it reads

$$\hat{\varphi}_{1D}(\hat{r}) = \frac{1}{2}\left(\hat{r}^2 - \hat{r}^4\right) \tag{3.29}$$

The vortex centre appears at the minimum/maximum point of the dimensionless stream function. In the case of $\hat{\varphi}_{1D}(\hat{r})$, the maximum value of the dimensionless stream function is $\hat{\varphi}_{centre} = 0.125$ which appears at $\hat{r}_{centre} = \sqrt{2}/2$. This is exactly the asymptotic limit of the stream function and the asymptotic location of the vortex centre as shown in Figure 3.4. This can be regarded as a validation of the proposed model.

3.3.3 Velocity profiles and validation by 1D model

The middle cross section **X-X** is selected as a typical cross section for analysis of the velocity profile in the liquid plug. Figure 3.6**a** compares the 1D solution in Eq. (3.26) with the analytical result in Eq. (3.22) at cross section **X-X** from the proposed analytical model. When the length of the liquid plug approaches infinity, the analytical solution reduces to the 1D solution (such as $\hat{L} = 100$ in Figure 3.6**a**). For a plug with $\hat{L} = 2$ (the length of the plug L is twice of the radius), the predicted velocity profile from the proposed model shows a 4% discrepancy with the 1D solution at point $\hat{r} = 0$. The 4% discrepancy does not mean that the flow in the plug is similar to the 1D flow even $\hat{L} > 2$. In plug flow, as predicted by the analytical model, due to the presence of the front interface, liquid moves from the centre of the plug towards the wall, while due to the presence of the rear interface, liquid moves from the wall to the centre of the plug. Therefore, the effect of the front/rear interface on the flow field near the ends of the plug is expected to be more significant than that in the middle cross section of the plug (section **X-X**).

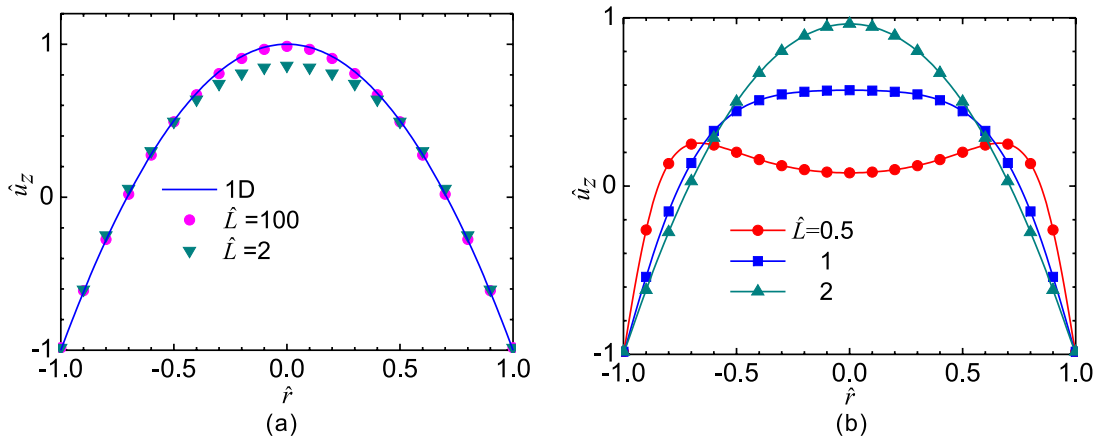

Figure 3.6: Velocity profiles at the cross section **X**-**X** of plugs of different lengths. (a) Comparison with the 1D model. (b) Effect of the dimensionless plug length $\hat{L}$.

Figure 3.6**b** shows the axial component of velocity profiles $\hat{u}_z$ for different plug lengths $\hat{L}$ along cross section **X**-**X**. For long plugs ($\hat{L} = 2$ in Figure 3.6**b**), the velocity profile is approximately fully developed. For short plugs ($\hat{L} = 0.5$ in Figure 3.6**b**), there are two local maximum points of the velocity field, as vortices move towards the wall of the microcapillary.

3.4 Flow resistance of liquid plugs

The analytical model can be used to study flow resistance of liquid plugs. The force balance diagram for the liquid plug is illustrated in Figure 3.7. These forces are in balance, as inertial effect can be neglected due to the low Reynolds number. The frictional force can be derived by integrating the shear stress along the walls

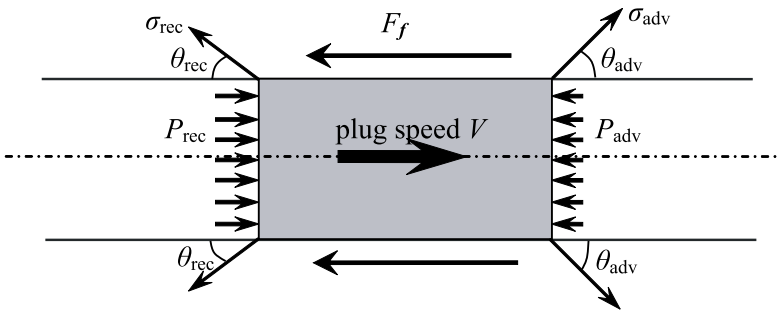

Figure 3.7: Force balance diagram of a liquid plug moving towards right at a speed of V in a microcapillary.

of the microcapillary.

$$\begin{aligned} F_f &= -2\pi R \int_0^L \tau_{rz} dz = -2\pi R\mu \int_0^L \left[\frac{\partial}{\partial r} \left(\frac{1}{r} \frac{\partial}{\partial r} \varphi \right) \right] dz \\ &= -2\mu V R \hat{L} \sum_{n=1}^{\infty} \frac{1-(-1)^n}{n} A_n Q(1) \end{aligned} \tag{3.30}$$

where

$$Q(1) = -\frac{2n\pi I_1\left(n\pi/\hat{L}\right)^2}{\hat{L} I_2\left(n\pi/\hat{L}\right)^2} \tag{3.31}$$

Although flat interfaces are assumed (assumption (3) in Section 3.2.1) in obtaining the flow field, the effects of surface tension and contact angle hysteresis on the flow resistance can be included in the force balance. The surface tension and the contact angle influence the plug speed, while the plug speed affects the flow field in the plug. In this way, the effects of the surface tension and contact angle on the flow field can be considered indirectly through the plug speed. The forces due to surface tension at the front (advancing) and rear (receding) ends are, respectively:

$$F_{adv} = 2\pi R \sigma_{adv} \cos(\theta_{adv}) \tag{3.32}$$

$$F_{rec} = 2\pi R \sigma_{rec} \cos(\theta_{rec}) \tag{3.33}$$

where θ_{adv} and θ_{rec} are the advancing and receding contact angles, respectively. σ_{adv} and σ_{rec} denote the surface tension at the advancing and receding ends, respectively. For different materials of fluids and of the capillaries, the contact angles and surface tensions can be different case by case. They can be obtained through experimental measurements or from handbooks (De Gennes, 1985; Lide and Haynes, 2010).

The force balance equation of the liquid plug is

$$\Delta p \pi R^2 = F_f + F_{\text{rec}} - F_{\text{adv}} \tag{3.34}$$

where $\Delta p = p_{\text{rec}} - p_{\text{adv}}$ is the pressure drop from the receding end to the advancing end of the plug. This leads to the driving pressure

$$\Delta p = -\frac{2\mu V \hat{L}}{\pi R} \sum_{n=1}^{\infty} \frac{1-(-1)^n}{n} A_n Q(1) + \frac{2}{R} \left[\sigma_{\text{rec}} \cos(\theta_{\text{rec}}) - \sigma_{\text{adv}} \cos(\theta_{\text{adv}})\right] \tag{3.35}$$

In Eq. (3.35), the first term is due to shear resistance, and the second term is due to surface tension.

The pressure difference in Eq. (3.35) can be nondimensionalised to plug resistance coefficient C_f, which is defined as the product of the Moody friction factor f and the Reynolds number Re. The characteristic velocity is the speed of the plug V, and the characteristic length is the radius of the mirocapillary R.

$$f = \frac{2R\Delta p}{L\rho V^2} \tag{3.36}$$

$$Re = \frac{\rho V R}{\mu} \tag{3.37}$$

Hence, the plug resistance coefficient C_f can be obtained from Eq. (3.35)

$$C_f \equiv fRe = \underbrace{-\frac{4}{\pi} \sum_{n=1}^{\infty} \frac{1-(-1)^n}{n} A_n Q(1)}_{\text{shear force}} + \underbrace{\frac{4\left[\sigma_{\text{rec}} \cos(\theta_{\text{rec}}) - \sigma_{\text{adv}} \cos(\theta_{\text{adv}})\right]}{\hat{L}\mu V}}_{\text{surface tension}} \tag{3.38}$$

According to Eq. (3.38), the plug resistance coefficient C_f is influenced by the shear force and the surface tension. The contribution of the shear force (the first term

on the right hand side of Eq. (3.38)) depends on the infinite series solution. The surface tension contribution (the second term on the right hand side of Eq. (3.38)) depends on the fluid viscosity μ, plug speed V, contact angles θ and θ_{rec}, and surface tension σ.

Figure 3.8 shows the variation of the plug resistance coefficient C_f with increasing the dimensionless plug length $\hat{L}$. The experimental results for different air/liquid plug systems by Kreutzer et al. (2005) are also shown. However, to compare the analytical results with the experiments, some parameters (θ_{adv}, θ_{rec} and V) remain unknown for the surface tension contribution in Eq. (3.38). To consider the contribution of the surface tension force in the model, here, a coefficient C is introduced in Eq. (3.38).

$$C \equiv \frac{4\left[\sigma_{\text{rec}} \cos\left(\theta_{\text{rec}}\right) - \sigma_{\text{adv}} \cos\left(\theta_{\text{adv}}\right)\right]}{\mu V} \tag{3.39}$$

Therefore, we can simplify Eq. (3.38) into

$$C_f = -\frac{4}{\pi} \sum_{n=1}^{\infty} \frac{1-(-1)^n}{n} A_n Q\left(1\right) + \frac{C}{\hat{L}} = \left(C_f\right)_{\text{friction}} + \left(C_f\right)_{\sigma} \tag{3.40}$$

Equation (3.40) singles out the effect of plug length on the contribution of the surface tension by $\left(C_f\right)_{\sigma} = C/\hat{L}$, which is inversely proportional to the dimensionless plug length $\hat{L}$. This is because the surface tension occurs at the ends of the plug, while the plug resistance coefficient considers the resistance per unit length through average.

The value of the coefficient C in Eq. (3.39) for three experimental fluids can be fitted by the method of least squares from the experimental results in Eq. (3.40), and then the coefficient C is substituted into Eq. (3.40) to calculate the total plug resistance coefficient C_f. The results from the model for three

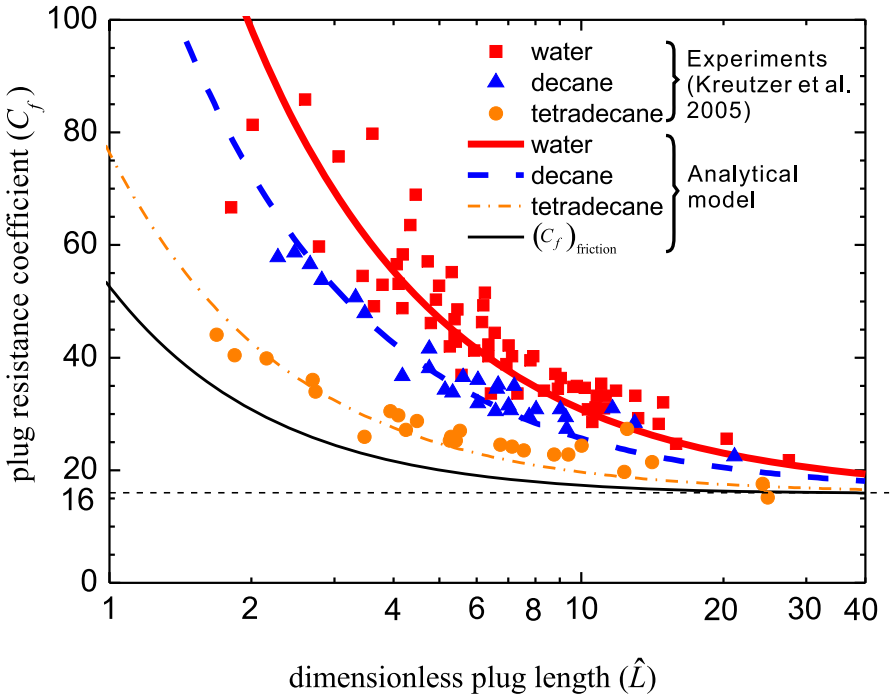

Figure 3.8: Plug resistance coefficient in microcapillaries C_f decreases with increasing dimensionless plug length $\hat{L}$. The symbols are experimental results for air/liquid plug systems by Kreutzer et al. (2005). The solid curves are the results from the proposed analytical model. The thin solid curve is the plug resistance coefficient only considering the contribution of the shear stress. The thick solid curve, the thick dashed curve, and the dot-doshed curve are the analytical results with fitted constant coefficient C as shown in Eq. (3.40) with $C_{\text{water}} = 135.0$, $C_{\text{decane}} = 83.8$, and $C_{\text{tetradecane}} = 23.8$, respectively. The horizontal dashed line with $C_f = 16$ is plotted to show that the plug resistance coefficient approaches 16 as the dimensionless plug length $\hat{L}$ approaches infinity.

experimental fluids are shown in Figure 3.8. From the comparison, we can see that the analytical model agrees well with the experimental data for different air/liquid plug systems. According to Eq. (3.39), when there is no external effect to change the surface tension such as by thermocapillarity (Burns et al., 1996), electrowetting (Mugele and Baret, 2005) and gradients of surfactant concentration, the surface tensions at the advancing end and at the receding end are identical, i.e., $\sigma_{\text{adv}} = \sigma_{\text{rec}}$. Therefore, the constant coefficient C in Eq. (3.39) is proportional to surface tension and inversely proportional to the viscosity, $C \propto (\sigma/\mu\,)$. The surface tensions and the viscosities of the three experimental fluids are $\sigma_{\text{water}} = 73$ mN/m, $\sigma_{\text{decane}} = 24$ mN/m, $\sigma_{\text{tetradecane}} = 26$ mN/m, and $\mu_{\text{water}} = 1.01\,\text{mPa}\cdot\text{s}$, $\mu_{\text{decane}} = 0.924\,\text{mPa}\cdot\text{s}$, $\mu_{\text{tetradecane}} = 2.32\,\text{mPa}\cdot\text{s}$, respectively. Therefore, the ratios σ/μ for the three fluids are

$$(\sigma/\mu\,)_{\text{water}} : (\sigma/\mu\,)_{\text{decane}} : (\sigma/\mu\,)_{\text{tetradecane}} = 72 : 26 : 11 = 6.4 : 2.3 : 1 \qquad (3.41)$$

Meanwhile, the coefficients fitted by the method of least squares for the three experimental fluids are

$$C_{\text{water}} : C_{\text{decane}} : C_{\text{tetradecane}} = 135 : 83.8 : 23.8 = 5.7 : 3.5 : 1 \qquad (3.42)$$

This agreement to $C \propto (\sigma/\mu\,)$ is satisfactory.

Figure 3.8 shows the effect of the dimensionless plug length on the plug resistance coefficient. As the dimensionless plug length $\hat{L}$ increases, the plug resistance coefficient C_f decreases dramatically. This can be explained by the fact that the high velocity gradient at the end of the plug dominate the flow in short plugs, which causes large flow resistance. Hence, short plugs experience a larger resistance coefficient. As the dimensionless plug length $\hat{L}$ increases, plug

resistance coefficient C_f decreases gradually. Even for a long plug such as $\hat{L} = 20$, the region near the front/rear interface is still significantly affected by the end effect (the surface tension and the friction), while the effect on the region near the centre is insignificant. The high velocity gradient at the end of the plug significantly increases the local shear stress on the wall of the microcapillary. Therefore, it requires an extremely long plug to "dilute" the effect of the end on the plug resistance coefficient.

As the dimensionless plug length further increases, the value of C_f gradually approaches an asymptotic limit and it remains above this limit. The dashed horizontal line with $C_f = 16$ is plotted to show that the plug resistance coefficient approaches 16 as the dimensionless plug length $\hat{L}$ approaches infinity, which is exactly the resistance coefficient for single phase fully developed laminar flow in a capillary (White, 2002). From the analytical model, the plug resistance coefficients are always larger than 16, and this value is the asymptotic limit when $\hat{L} \to \infty$, as shown in Figure 3.8. For example, for $C_f = 16.16$ (that is 1% deviation from $C_f = 16$), the corresponding dimensionless plug length is $\hat{L} = 24.6$. In this condition, the plug behaves as if it is the fully developed continuous flow. Therefore, for $\hat{L} < 24.6$, the idealization of a liquid plug as fully developed continuous flow cannot provide an accurate prediction of the pressure loss.

3.5 Summary

An analytical model is presented in this chapter to investigate the plug flow in microcapillaries with circular cross section. The Stokes flow field in the liquid plug is modelled with a fourth-order partial differential equation with its boundary

conditions. Series solution of the governing equation is obtained and the boundary conditions are satisfied. The flow pattern within the liquid plug is characterized by the vortex centre. The results from the analytical model show that the vortex centre shift towards the wall of the microcapillary as the plug length decreases.

The analytical model is utilized to find the flow resistance of liquid plugs. The results show the dependency of the plug resistance on the plug length. For short plugs, the plug resistance coefficient increase dramatically as the dimensionless length decreases. For long plugs and as the dimensionless plug length approaches infinity, the plug resistance coefficient approaches 16, which is the resistance coefficient of continuous laminar flow in a cylindrical tube.

Chapter 4

Plug Flow in Two-Dimensional Microchannels [†].

4.1 Introduction

In this chapter, an analytical model is proposed for plug flow in 2D microchannels. Then this model is used to analyze the heat transfer in a plug moving in microchannels. To understand the heat transfer process, the energy equation for the plug flow are solved based on the analytical flow field. Without numerically solving the flow field, it is a simple and efficient way to analyze the influence of the recirculating vortices on the heat transfer process in plugs.

This chapter is organized as follows. The mathematical formulas are provided in Section 4.2, including the flow field in the liquid plug, the numerical method for the heat transfer process in the constant-surface-temperature condition and the constant-surface-heat-flux condition. In Section 4.3, the stages of heat transfer are identified, and compared with single phase flow. The effects of different boundary

[†]This work has been published in *International Journal of Heat and Mass Transfer (2011) 55 (7-8) 1947-1956.*

conditions, different Peclet numbers, and different plug lengths are analyzed and explained.

4.2 Mathematical modelling

4.2.1 Modelling of flow field in liquid plugs

To model the flow field in a liquid plug in a 2D microchannel, the following dimensionless quantities are introduced,

$$\hat{x} \equiv x/w, \quad \hat{y} \equiv y/w, \quad \hat{u}_x \equiv u_x/V, \quad \hat{u}_y \equiv u_y/V, \quad \hat{L} \equiv L/w \tag{4.1}$$

where w is the width of the microchannel, V is the speed of the liquid plug, and L is the length of the liquid plug. The details of obtaining the flow field and the comparison with experimental results are provided in Appendix B, and the 2D assumption is examined in Appendix C. The dimensionless form of the velocity field in the liquid plug is

$$\begin{aligned}\hat{u}_x = \sum_{n=1,3,5\cdots}^{\infty} & \sin(\beta_n \hat{x}) \left[C_{2n}\beta_n \cosh(\beta_n \hat{y}) + C_{3n}\beta_n \hat{y} \sinh(\beta_n \hat{y})\right. \\ & \left. + C_{3n}\cosh(\beta_n \hat{y}) + C_{4n}\beta_n \hat{y}\cosh(\beta_n \hat{y}) + C_{4n}\sinh(\beta_n \hat{y})\right]\end{aligned} \tag{4.2}$$

$$\begin{aligned}\hat{u}_y = -\sum_{n=1,3,5\cdots}^{\infty} & \beta_n \cos(\beta_n \hat{x}) \\ & \times \left[C_{2n}\sinh(\beta_n \hat{y}) + C_{3n}\hat{y}\cosh(\beta_n \hat{y}) + C_{4n}\hat{y}\sinh(\beta_n \hat{y})\right]\end{aligned} \tag{4.3}$$

where

$$C_{2n} = -\frac{4}{D_n \hat{L}\beta_n}\sinh(\beta_n) - \frac{4}{D_n \hat{L}} \tag{4.4}$$

$$C_{3n} = \frac{4}{D_n \hat{L}}\sinh(\beta_n) + \frac{4\sinh^2(\beta_n)}{\hat{L}\beta_n D_n} \tag{4.5}$$

$$C_{4n} = \frac{4}{D_n \hat{L}\beta_n}\left[-\beta_n \cosh(\beta_n) + \sinh(\beta_n) - \sinh(\beta_n)\cosh(\beta_n) + \beta_n\right] \tag{4.6}$$

$$D_n = {\beta_n}^2 - \sinh^2(\beta_n) \tag{4.7}$$

$$\beta_n = n\pi/\hat{L} \tag{4.8}$$

4.2.2 Analysis of heat transfer

To analyze the heat transfer in a liquid plug, the energy conservation of the plug is considered with a translating frame of reference following the plug. For an incompressible Newtonian fluid with constant properties and no source term, the energy conservation equation is

$$\frac{\partial(T)}{\partial t} + \frac{\partial(u_x T)}{\partial x} + \frac{\partial(u_y T)}{\partial y} = \frac{k}{\rho c_p}\left(\frac{\partial^2 T}{\partial x^2} + \frac{\partial^2 T}{\partial y^2}\right) \tag{4.9}$$

where T is the temperature, ρ is the density of the fluid, k is the thermal conductivity, and c_p is the specific heat capacity. The following dimensionless variables are introduced,

$$\hat{t} \equiv \frac{t}{\tau},\ Pe \equiv \frac{wV}{\alpha},\ \hat{T} \equiv \frac{T - T_0}{T_c} \tag{4.10}$$

where $\tau \equiv w/V$, $\alpha \equiv \frac{k}{\rho c_p}$, T_0 is the inlet temperature, and T_c is the characteristic temperature. The dimensionless form of the energy equation is obtained as follows,

$$\frac{\partial\left(\hat{T}\right)}{\partial \hat{t}} + \frac{\partial\left(\hat{u}_x \hat{T}\right)}{\partial \hat{x}} + \frac{\partial\left(\hat{u}_y \hat{T}\right)}{\partial \hat{y}} = \frac{1}{Pe}\left(\frac{\partial^2 \hat{T}}{\partial \hat{x}^2} + \frac{\partial^2 \hat{T}}{\partial \hat{y}^2}\right) \tag{4.11}$$

where $Pe \equiv wV/\alpha$ is the Peclet number which characterizes the ratio of the rate of heat advection caused by the flow to the rate of heat diffusion driven by the temperature gradient. With this normalization, the dimensionless time $\hat{t}$ and the dimensionless axial location of the plug in the microchannel $\hat{X}$ is related as

$$\hat{t} = \hat{X} \tag{4.12}$$

The flow field, as it is directly known from the analytical solution in Eqs. (4.2) and (4.3), is substituted into Eq. (4.11) for the heat transfer analysis. Equation (4.11) was discretized using the finite volume method (FVM) on staggered grids (Patankar, 1980).

Before entering the microchannel, the liquid plug has an initial uniform temperature field with $\hat{T} = 0$. At the interface between the liquid and gas, the heat transfer at the interface is assumed adiabatic. This is reasonable due to the large conductivity ratio between liquids and gases (such as $k_{\text{water}}/k_{\text{air}} \approx 60$). Therefore,

$$k\frac{\partial T}{\partial x} = 0, \quad \text{at} \quad x = 0 \quad \text{or} \quad x = L \tag{4.13}$$

and in dimensionless form,

$$\frac{\partial \hat{T}}{\partial \hat{x}} = 0, \quad \text{at} \quad \hat{x} = 0 \quad \text{or} \quad \hat{x} = \hat{L} \tag{4.14}$$

On the wall of the microchannel, two types of boundary conditions are considered, the constant-surface-temperature condition and the constant-surface-heat-flux condition, as shown in Figure 4.1.

4.2.2.1 Constant-surface-temperature condition

In the constant-surface-temperature condition, the temperature distribution in the plug can be normalized as

$$\hat{T} \equiv \frac{T - T_0}{T_{\text{w}} - T_0} \tag{4.15}$$

where T_{w} is the wall temperature. The boundary condition is

$$T = T_{\text{w}} \quad \text{at} \quad y = 0 \quad \text{or} \quad y = w \tag{4.16}$$

and in dimensionless form,

$$\hat{T} = 1 \quad \text{at} \quad \hat{y} = 0 \quad \text{or} \quad \hat{y} = 1 \tag{4.17}$$

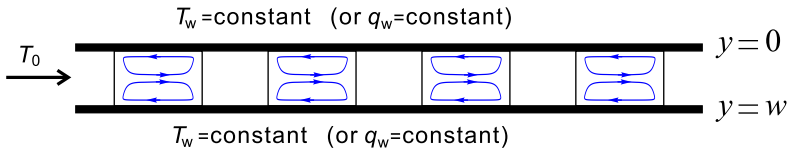

Figure 4.1: Schematic diagram of two types of boundary conditions for heat transfer in liquid plugs in 2D microchannels: the constant-surface-temperature condition and the constant-surface-heat-flux condition.

4.2.2.2 Constant-surface-heat-flux condition

In the constant-surface-heat-flux condition, the temperature distribution in the plug can be normalized as

$$\hat{T} \equiv \frac{T - T_0}{q_w w/k} \tag{4.18}$$

where q_w is the heat flux on the wall of the microchannel. The boundary condition for the plug is

$$\begin{cases} -k\dfrac{\partial T}{\partial y} = q_w, & \text{at} \quad y = 0 \\ -k\dfrac{\partial T}{\partial y} = -q_w, & \text{at} \quad y = w \end{cases} \tag{4.19}$$

and in dimensionless form,

$$\begin{cases} \dfrac{\partial \hat{T}}{\partial \hat{y}} = -1, & \text{at} \quad \hat{y} = 0 \\ \dfrac{\partial \hat{T}}{\partial \hat{y}} = 1, & \text{at} \quad \hat{y} = 1 \end{cases} \tag{4.20}$$

4.2.3 Evaluation of heat transfer

To characterize the heat transfer capabilities of plug flow along the microchannel, and to compare with the single phase flow, three quantities are used, namely Nusselt number Nu (Section 4.2.3.1), heat transfer index η (Section 4.2.3.2), and maximum fluid temperature $\hat{T}_{max}$ (Section 4.2.3.3). To compare between the single phase flow

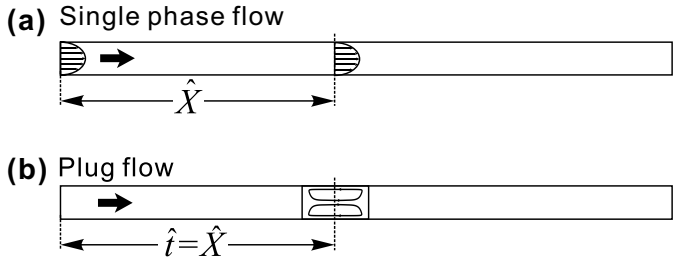

Figure 4.2: Heat transfer is evaluated at the axial location $\hat{X}$ for the single phase flow, and at the same location $\hat{t} = \hat{X}$ as the plug passes for the plug flow.

and the plug flow, these three quantities are calculated (i) at a specific axial location $\hat{X}$ for the single phase flow, as illustrated in Figure 4.2**a**; and (ii) for the plug flow at the instant when the plug passes the same axial location, i.e., $\hat{t} = \hat{X}$, as illustrated in Figure 4.2**b**.

4.2.3.1 Nusselt number

To evaluate the convective heat transfer, the Nusselt number is defined as the ratio of convective to conductive heat transfer normal to the wall,

$$Nu \equiv \frac{hD_H}{k} \tag{4.21}$$

where the hydraulic diameter of the channel is $D_H = 2w$. To analyze the convective heat transfer coefficient of the plug flow h, the mean fluid temperature of a plug unit $\bar{T}_{\text{plug}}$ is used as the reference temperature (Incropera and DeWitt, 2002), which refers to the mean fluid temperature of the plug at the axial location X, and is defined as

$$\bar{T}_{\text{plug}}(X) \equiv \frac{\int_{A_{\text{plug}}} \rho c_p u_x T dA_{\text{plug}}}{\int_{A_{\text{plug}}} \rho c_p u_x dA_{\text{plug}}} \tag{4.22}$$

Therefore, in the dimensionless form, the mean fluid temperature of the plug is

$$\hat{\bar{T}}_{\text{plug}}\left(\hat{X}\right) \equiv \frac{\int_0^1 d\hat{y} \int_0^{\hat{L}} \hat{u}_x \hat{T} d\hat{x}}{\int_0^1 d\hat{y} \int_0^{\hat{L}} \hat{u}_x d\hat{x}} \tag{4.23}$$

Similarly, for the single phase flow, the mean fluid temperature $\hat{\bar{T}}_{\text{sp}}\left(\hat{X}\right)$ refers to the mean temperature of the fluid over the cross section $\hat{X}$ of the channel, and in the dimensionless form, it is (Incropera and DeWitt, 2002)

$$\hat{\bar{T}}_{\text{sp}}\left(\hat{X}\right) \equiv \frac{\int_0^1 \hat{u}_x \hat{T} d\hat{y}}{\int_0^1 \hat{u}_x d\hat{y}} \tag{4.24}$$

4.2.3.1.1 Nusselt number for single phase flow For the single phase flow in microchannels, the convective heat transfer coefficient in the constant-surface-heat-flux condition is

$$h_{q,\text{sp}} \equiv \frac{q_{\text{w}}}{T_{\text{w}} - \bar{T}} \tag{4.25}$$

where q_{w} is the heat flux on the wall, and T_{w} is the local wall temperature of the microchannel. By substituting Eqs. (4.23)–(4.25) into Eq. (4.21), the Nusselt number can be expressed by dimensionless variables as follows,

$$Nu_{q,\text{sp}} = \frac{2}{\left(\hat{T}_{\text{w}} - \hat{\bar{T}}\right)} \tag{4.26}$$

where the subscript 'sp' refers to the single phase flow. Similarly, in the constant-surface-temperature condition, the convective heat transfer coefficient is

$$h_{T,\text{sp}} \equiv \frac{-k(\partial T/\partial y)_{y=0}}{T_{\text{w}} - \bar{T}} \tag{4.27}$$

and the Nusselt number, expressed by dimensionless variables, is

$$Nu_{T,\text{sp}} = \frac{-2\left(\partial \hat{T}/\partial \hat{y}\right)_{\hat{y}=0}}{1 - \hat{\bar{T}}} \tag{4.28}$$

4.2.3.1.2 Nusselt number for plug flow For plug flow in microchannels, the convective heat transfer coefficient h for a plug unit can be calculated as a function of the axial location ($\hat{X}$) as the temperature inside the plug develops. It is calculated based on the average heat flux, the average temperature difference, and the mean fluid temperature of the plug unit. In the constant-surface-temperature condition, we have

$$h_{T,\text{plug}} \equiv \frac{\int_0^L \left(-k\partial T/\partial y\right)_{y=0} dx}{\int_0^L \left(T_\text{w} - \bar{T}\right) dx} \tag{4.29}$$

and the Nusselt number, expressed by dimensionless variables, is

$$Nu_{T,\text{plug}} = \frac{2\int_0^{\hat{L}} \left(-\partial\hat{T}/\partial\hat{y}\right)_{\hat{y}=0} d\hat{x}}{\int_0^{\hat{L}} \left(1 - \hat{\bar{T}}\right) d\hat{x}} \tag{4.30}$$

Similarly, in the constant-surface-heat-flux condition, we have

$$h_{q,\text{plug}} \equiv \frac{q_\text{w} L}{\int_0^L \left(T_\text{w} - \bar{T}\right) dx} \tag{4.31}$$

and the Nusselt number, expressed by dimensionless variables, is

$$Nu_{q,\text{plug}} = \frac{2\hat{L}}{\int_0^{\hat{L}} \left(\hat{T}_\text{w} - \hat{\bar{T}}\right) d\hat{x}} \tag{4.32}$$

4.2.3.2 Heat transfer index in constant-surface-temperature condition

In the constant-surface-temperature condition, a heat transfer index, $\eta(\hat{X}) \equiv Q\left(\hat{t}\right)/Q_\text{max}$, is defined as a function of the axial location $\hat{X}$ to characterize the progress of the heat transfer in the microchannel, where Q_max is the maximum amount of energy transfer that could occur if the process continues to $\hat{t} \to \infty$, while $Q\left(\hat{t}\right)$ is the total energy transferred from the wall to the plug over the time interval 0 to $\hat{t}$. With a uniform temperature maintained on the wall, the maximum possible energy Q_max corresponds to the condition when the whole plug unit has achieved

the uniform wall temperature. Therefore, assuming constant fluid properties, the heat transfer index is

$$\eta_{\text{plug}}\left(\hat{X}\right) \equiv \frac{Q\left(\hat{t}\right)}{Q_{\max}} = \frac{\int_0^w dy \int_0^L \rho c_p \left(T - T_0\right) dx}{\int_0^w dy \int_0^L \rho c_p \left(T_w - T_0\right) dx} = \frac{1}{\hat{L}} \int_0^1 d\hat{y} \int_0^{\hat{L}} \hat{T} d\hat{x} \tag{4.33}$$

The heat transfer index varies from 0 to unity as heat transfer progresses. $\eta = 0$ implies that heat transfer has not begun yet, while $\eta = 1$ implies that the plug unit has achieved the wall temperature. The variation of the heat transfer index against the axial location $\hat{X}$ indicates the progress of heat transfer in the microchannel.

For single phase flow, a corresponding heat transfer index is defined to evaluate the progress of the heat transfer at the cross section $\hat{X}$ of the microchannel as follows,

$$\eta_{\text{sp}}\left(\hat{X}\right) \equiv \frac{Q\left(\hat{X}\right)}{Q_{\max}} = \frac{\int_0^w \rho c_p \left(T - T_0\right) dy}{\int_0^w \rho c_p \left(T_{\text{w}} - T_0\right) dy} = \int_0^1 \hat{T} d\hat{y} \tag{4.34}$$

4.2.3.3 Maximum fluid temperature in constant-surface-heat-flux condition

In the constant-surface-heat-flux condition, a favourable situation is that the fluid remains at a reasonable low temperature. A too high temperature may damage the devices. The highest tolerable fluid temperature is usually a requirement when designing heat exchangers. With this concept, a maximum fluid temperature can be defined in a dimensionless form as

$$\hat{T}_{\max} \equiv \max\left(\hat{T}\right) \tag{4.35}$$

For single phase flow, $\hat{T}_{\max}$ is searched across the cross section $\hat{X}$ of the microchannel, while for plug flow, $\hat{T}_{\max}$ is searched throughout the plug at the instant when the plug passes the cross section, i.e., $\hat{t} = \hat{X}$.

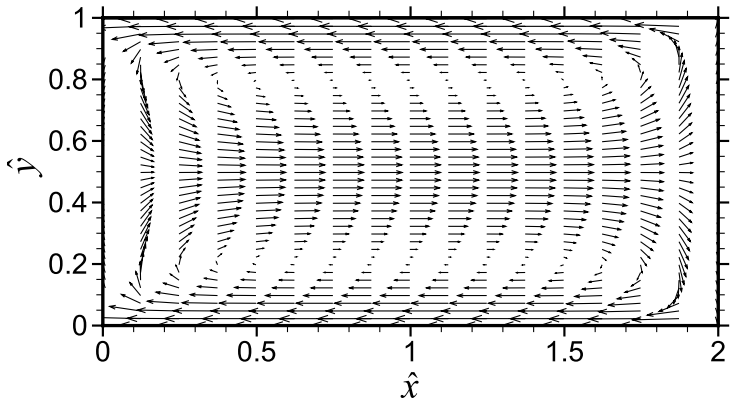

Figure 4.3: Flow field in a typical liquid plug in a 2D microchannel. The dimensionless plug length is $\hat{L} = 2$.

4.3 Results and discussion

4.3.1 Flow field in a typical liquid plug

The flow field in a typical liquid plug, as shown in Figure 4.3, is dominated by two symmetrical vortices as the plug moves forward (from left to right). When the liquid in the plug moves towards the front of the plug, it is blocked by the front interface, changing the flow direction towards the wall of the microchannel. At the wall of the microchannel, due to the friction of the wall, the liquid moves backwards with respect to the translating frame of reference. At the rear of the liquid plug, due to the presence of the rear interface, liquid moves from the wall of the microchannel towards the centre of the plug. Consequently, the presence of the front/rear interfaces produces a recirculating flow pattern within the liquid plug. The transverse flow of the recirculating vortices in the plug is crucial to enhance heat transfer between the wall and the liquid, and it will be explained in Sections 4.3.2 and 4.3.3.

4.3.2 Heat transfer in the constant-surface-temperature condition

4.3.2.1 Heat transfer process and comparison with single phase flow

The time evolution of the isotherms for a liquid plug moving through a 2D microchannel is shown in Figure 4.4**a** (Instants A–H), and their corresponding points are marked in Figure 4.4**b**. The channel wall is subjected to a constant temperature $\hat{T}_{\mathrm{w}} = 1$, the dimensionless plug length is $\hat{L} = 2$, and the Peclet number is $Pe = 100$. The variation of the Nusselt number Nu, the wall temperature $\hat{T}_{\mathrm{w}} = 1$, and the mean fluid temperature of the plug $\hat{\bar{T}}_{\mathrm{plug}}$ [Eq. (4.23)] are plotted against time in Figure 4.4**b**. To compare between the plug flow and the single phase flow, the Nusselt number Nu and the heat transfer index η are plotted in Figures 4.4**c** and **d**, respectively.

For the single phase flow, the flow is assumed fully developed hydrodynamically but thermally developing. The Nusselt number is large near the entrance and decays along the channel to an asymptotic limit ($Nu_{\mathrm{asymp,sp}} = 7.5$) due to the development of the thermal boundary layer along the wall, while the heat transfer can be divided into the thermal entrance region and the fully developed region according to the thickness of the thermal boundary layer, as shown in Figure 4.4**c**.

In contrast, for the plug flow, heat transfer is initiated when the plug enters the microchannel, followed by three subsequent stages of convective heat transfer between the plug and the heated wall: (i) development of thermal boundary layer; (ii) advection of heated/fresh fluid in the plug; and (iii) thermally fully developed flow.

Stage I: *Development of thermal boundary layer (TBL)*, [Figures 4.4**a** and **b** (Instants B–C)]: At the instant that the plug contacts the heated wall, a large temperature difference is formed between the plug and the wall since the plug temperature is uniformly distributed ($\hat{T} = 0$) while the wall temperature is maintained at $\hat{T}_{\mathrm{w}} = 1$. The thin liquid layer in the immediate vicinity of the wall rapidly achieves thermal equilibrium with the wall and forms a thermal boundary layer, [Figure 4.4**a** (Instant B)]. The effect of the wall temperature on the fluid outside the TBL is negligible. In the translating frame of reference following the plug, the fluid velocity in the region near the channel wall is negative as shown in Figure 4.3, and the fluid particles in the TBL moves from the front interface to the rear interface. Hence, the TBL is thinner near the front interface, while it is thicker near the rear interface. As time passes, the effects of heat transfer penetrate further into the plug and the thickness of the TBL grows, until the TBL reaches the centreline of the channel [Figure 4.4**a** (Instant C)], which marks the end of Stage I and the beginning of Stage II.

The TBL is extremely thin when it is initially formed, resulting in a large *Nu*. With the development of the TBL with time, *Nu* decreases dramatically.

TBLs in plug flow have two distinctive features as compared with single phase flow. (i) The thickness of the TBL for plug flow is not only a function of space, but also a function of time. (ii) In single phase flow, fluids usually approaches the wall along the wall direction, while in plug flow, fluids in the plug approaches the wall in the perpendicular direction due to the presence of the front interface. Similarly, at the rear interface, fluids leave the wall in the perpendicular direction due to the presence of the rear interface. Therefore, TBLs in plug flow are more complex than

those in single phase flow.

Stage II: *Advection of heated/fresh fluid in the plug*, [Figures 4.4**a** and **b** (Instant D–F)]: At the rear of the plug, due to the presence of the rear interface, the heated fluid moves towards the central region of the plug. And in the central region, the fluid temperature decreases as the fluid travels in the plug moving direction [Figure 4.4**a** (Instant E)] due to: (i) less influence from the heated channel wall and (ii) thermal mixing with the fresh fluid originally in the central region. At the same time, due to the presence of the front interface, the fresh fluid from the central region of the plug moves transversely to the heated channel wall. In this manner, the heated and the fresh fluids are advected within the plug by the recirculating vortices. As time progresses, the temperature difference between the heated fluid and the fresh fluid decreases, until there is no distinct interface between the heated fluid and the fresh fluid, which marks the end of Stage II and the beginning of Stage III.

At Stage II, the advection of the heated/fresh fluid results in the variation of the heat flux on the wall and the oscillation of the Nusselt number, as shown in Figure 4.4**b**. The details will be discussed in Section 4.3.2.2.

Stage III: *Thermally fully developed flow*, [Figures 4.4**a** and **b** (Instants G to H)]: This stage is characterized by the shapes of the temperature contours within the liquid plug. Although the absolute value of the fluid temperature gradually approaches T_w, the shapes of the temperature contours remain unchanged over time [Figure 4.4**a** (Instant G to H)]. With the unchanged temperature pattern, the Nusselt number approaches an asymptotic limit, $Nu_{asymp,plug} = 31.3$, which is much higher as compared with single phase flow ($Nu_{asymp,sp} = 7.5$), as shown in

Figure 4.4**c**. If the channel is sufficiently long, heat transfer continues until the fluid temperature reaches a uniform temperature being the same as the wall.

In fully developed single phase flow, the streamlines are straight along the channel path. Heat transfer in the transverse direction is via conduction. Only the fluid flowing near to the channel wall is being heated while the fluid near the central region of the channel remains slightly higher than the inlet temperature.

Plug flow, however, creates internal recirculating flow due to high shearing interactions with the channel wall and the presence of the front/rear interfaces. The recirculating flow induces a substantial amount of transverse thermal mixing in the fluid. This transverse convection brings heated liquid from the channel wall to the central region at the rear interface, allows thermal mixing of fluids within the plug, and subsequently transports it back to the wall. In addition, the liquid filament in the plug is stretched by the recirculating flow, which causes an effect of Taylor dispersion (Taylor, 1953) among liquid filaments. Although Taylor dispersion exists in single phase flow, the Taylor dispersion of heat in plugs between liquid filaments is confined within spaces of nanolitre scale. Therefore, the Taylor dispersion within the liquid plug is stronger and more effective to enhance heat transfer.

Figure 4.4**d** compares the heat transfer index η between plug flow and single phase flow. It can be seen that to achieve a given heat transfer index, the required channel length will be significantly shorter to use plug flow than to use single phase flow. These results indicate the heat transfer enhancement by the plug flow.

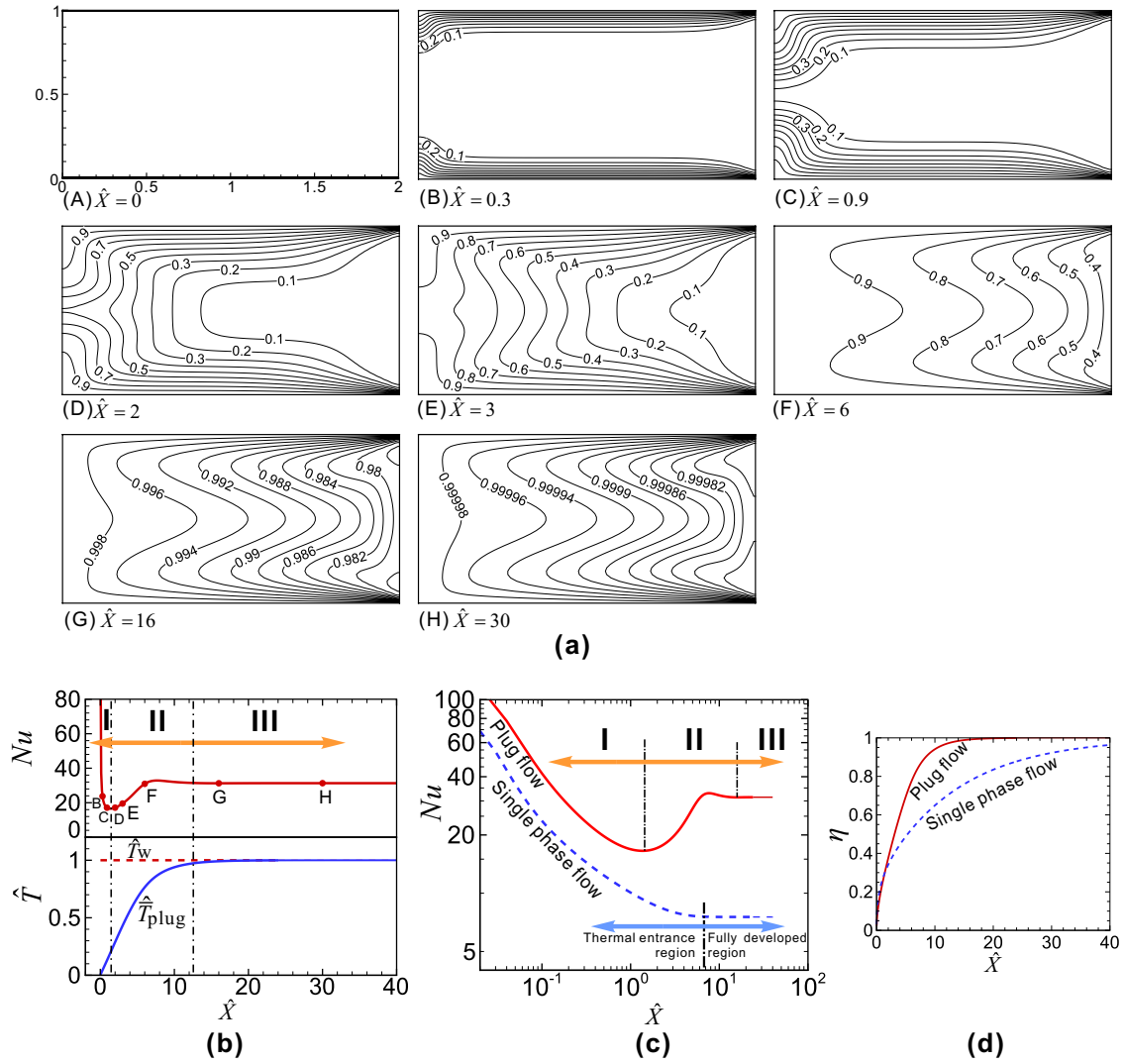

Figure 4.4: Heat transfer process in a typical liquid plug in the constant-surface-temperature boundary condition and its comparison with single phase flow. The dimensionless plug length is $\hat{L} = 2$, and the Peclet number is $Pe = 100$. (a) Sequence of temperature distribution in the plug. (b) Variation of the Nusselt number Nu, the wall temperature $\hat{T}_w$, and the mean fluid temperature in the plug $\hat{\bar{T}}_{plug}$ [Eq. (4.23)]. The marked points correspond to the instants in (a). (c) Log-log plot of Nusselt numbers for the plug flow and for the single phase flow. (d) Heat transfer indices for the plug flow and for the single phase flow.

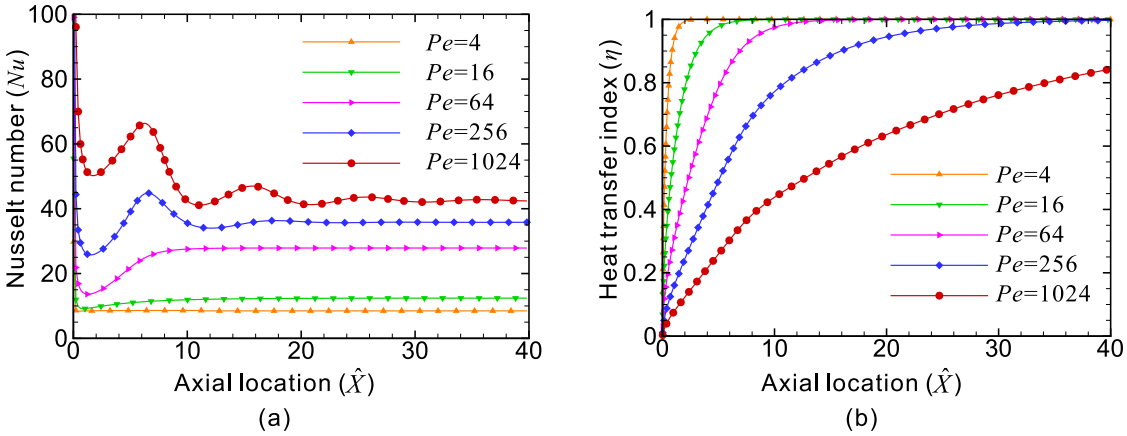

Figure 4.5: (a) Nusselt number Nu and (b) heat transfer index η for plug flow at different Peclet numbers in the constant-surface-temperature condition. The dimensionless plug length is $\hat{L} = 2$.

4.3.2.2 Effect of Peclet number

The effect of the Peclet number on the Nusselt number and the heat transfer index is shown in Figures 4.5**a** and **b**, respectively. In the simulation, the dimensionless plug length is fixed at $\hat{L} = 2$ and Pe is varied from 4 to 1024. Figure 4.5**a** shows that the Nusselt number increases with increasing the Peclet number. At a low Peclet number ($Pe = 4$), the Nusselt number achieves a lower asymptotic limit ($Nu_{\text{asymp},Pe=4} = 8.5$) at Stage III, while at a high Peclet number ($Pe = 1024$), the transport process is dominated by advection, and the asymptotic limit of the Nusselt number at Stage III is higher ($Nu_{\text{asymp},Pe=1024} = 42.4$). The influence of the Peclet number on the heat transfer index shows that the heat transfer index decreases with increasing Pe. This is because a fast flow (a high Peclet number) results in a short residence time in the heated channel.

The Nusselt number for a plug unit, especially at large Peclet numbers,

exhibits an oscillatory behaviour, as shown in Figure 4.5**a**. To analyze the oscillation of *Nu*, *Nu* at a high Peclet number ($Pe = 1024$) is plotted in Figure 4.6**a**, as well as the two important factors that influence *Nu*, namely the mean value of temperature gradient at the wall over the plug length [$\overline{-\partial\hat{T}/\partial\hat{y}} \equiv \frac{1}{\hat{L}}\int_0^{\hat{L}}\left(-\partial\hat{T}/\partial\hat{y}\right)_{\hat{y}=0} d\hat{x}$], and the mean fluid temperature of the plug unit [$\hat{\bar{T}}_{\text{plug}}$ in Eq. (4.23)]. The temperature distribution in the plug at some typical instants are shown in Figure 4.6**b**. From the variation of $\overline{-\partial\hat{T}/\partial\hat{y}}$ and the temperature field, we can see that the oscillation of *Nu* is caused by the recirculating flow in the plug. When the fresh fluid in the central region of the plug is being transported to the heated wall by the recirculating flow [Figure 4.6 Instants A–D], $\overline{-\partial\hat{T}/\partial\hat{y}}$ is large due to the high temperature difference between the wall and the liquid. In addition, $\overline{-\partial\hat{T}/\partial\hat{y}}$ remains constant during this period because fresh fluid is continuously transported to the heated wall by the recirculating flow. In the meantime, the mean fluid temperature of the plug unit $\hat{\bar{T}}_{\text{plug}}$ increases smoothly as shown in Figure 4.6**a**. Hence, according to Eq. (4.30), *Nu* increases in this period. As the heated fluid in the plug is transported back to the heated wall [Figure 4.6**b** (Instants D–F)], $\overline{-\partial\hat{T}/\partial\hat{y}}$ immediately decreases, which results in a decrease in the heat flux and a decrease in *Nu* [Figure 4.6**a** (Instants D–F)]. This oscillation of *Nu* is damped as the temperature difference between the fresh fluid and the heated fluid reduces until there is no distinct interface between the fresh fluid and the heated fluid.

To quantitatively compare the heat transfer between single phase flow and plug flow at different Peclet numbers, the heat transfer indices at the axial location of the channel $\hat{X} = 10$ are calculated and plotted against Peclet number in Figure 4.7. The temperature distributions in the plug at different Peclet numbers

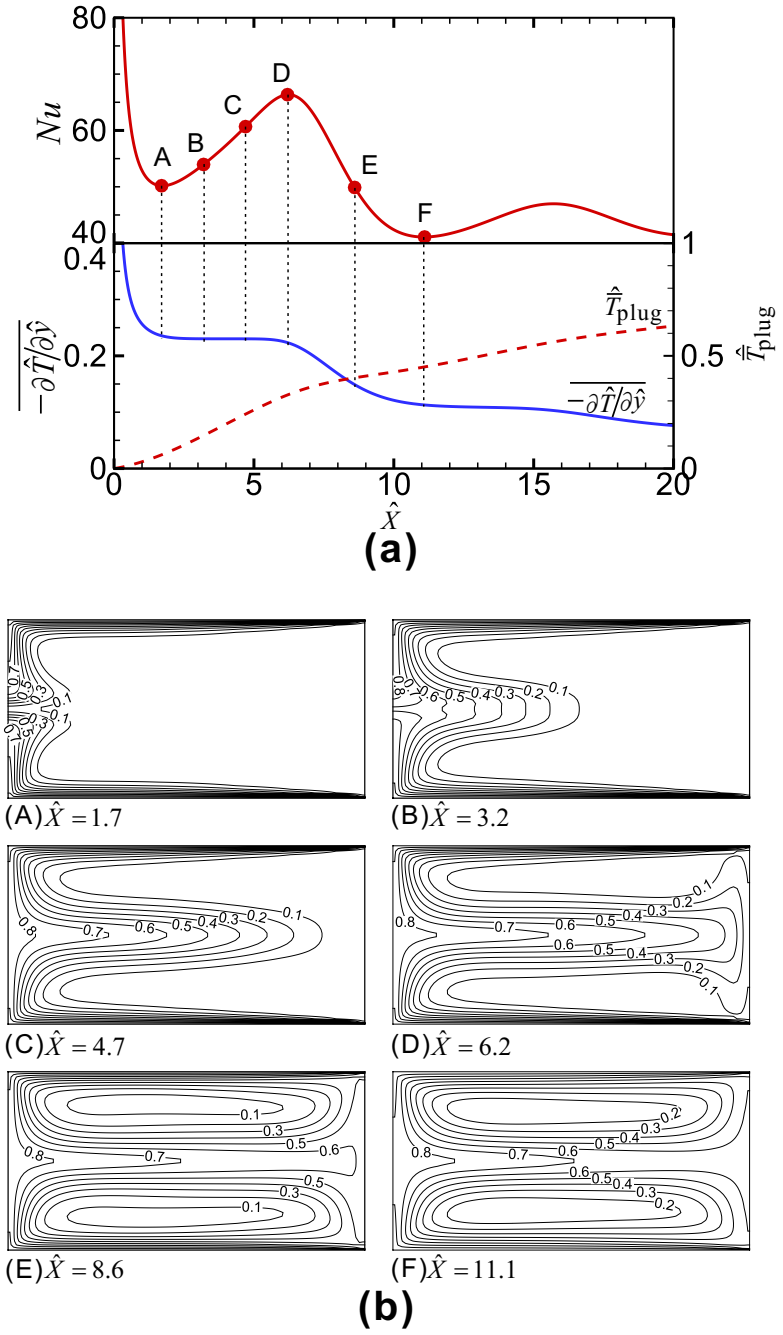

Figure 4.6: Oscillation of the Nusselt number for a liquid plug ($\hat{L} = 2$) at a high Peclet number ($Pe = 1024$) in the constant-surface-temperature condition. The oscillation of Nu is due to the variation of $\overline{-\partial\hat{T}/\partial\hat{y}}$ over time, where $\overline{-\partial\hat{T}/\partial\hat{y}} \equiv \frac{1}{\hat{L}}\int_0^{\hat{L}} \left(-\partial\hat{T}/\partial\hat{y}\right)_{\hat{y}=0} d\hat{x}$ is the mean value of the temperature gradient at the wall over the plug length. (a)Variation of Nu, $\overline{-\partial\hat{T}/\partial\hat{y}}$, and $\hat{\bar{T}}_{plug}$; (b) Evolution of the temperature distribution in the plug. The corresponding points at Instants A–F are marked in (a).

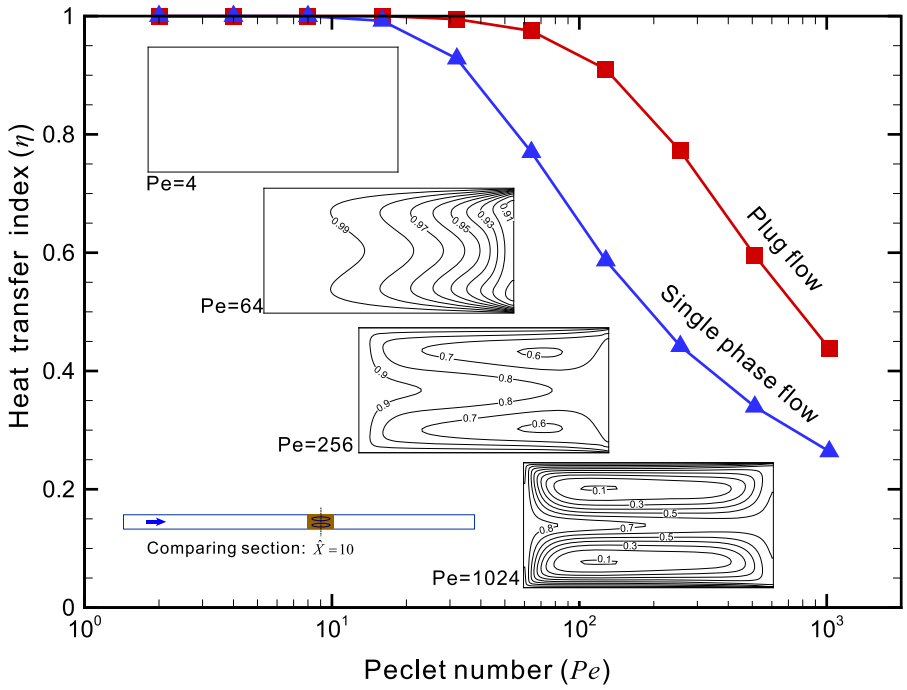

Figure 4.7: Comparison of heat transfer indices between the plug flow and the single phase flow at different Peclet numbers in the constant-surface-temperature condition. The section for comparison is at $\hat{X} = 10$, and the dimensionless plug length is $\hat{L} = 2$. The temperature distributions within the plugs are shown.

are also shown. At a small Peclet number ($Pe = 4$), the heat transfer index is 1 for both single phase flow and plug flow. This means that the fluid has achieved the uniform temperature being the same as the wall. At a large Peclet number (such as $Pe = 1024$), the heat transfer indices are quite different between plug flow and single phase flow. From single phase flow to plug flow, the heat transfer index increases from 0.26 to 0.44. If considering the fact that the growth rate of the heat transfer index ($d\eta/d\hat{X}$) decreases almost exponentially as the fluid flows to the downstream [Figure 4.5**b**], we can conclude that the plug flow can significantly reduce the requirement of the channel length and enhance the heat transfer.

4.3.2.3 Effect of plug length

Flow fields in plugs are important to the heat transfer process. In order to study the influence of plug length on heat transfer, its effects on the flow field are analyzed first in this section.

4.3.2.3.1 Effect of plug length on transverse velocity and recirculating period The heat transfer in plugs is enhanced by the recirculating flow, or more specifically, by the transverse flow near the front and the rear interfaces. Therefore, the magnitude of the transverse velocity is an important factor influencing the heat transfer. The transverse velocity at a typical cross section inside the plug ($\hat{y} = 3/4$) is plotted in Figure 4.8 for different plug lengths. The velocity fields of the respective plug length are also shown in Figure 4.8. For long plugs ($\hat{L} = 4$), the transverse component is almost zero at most axial distance of the plug ($0.2 \leq \hat{x}/\hat{L} \leq 0.8$) except in regions close to the front/rear interfaces. In contrast, for short plugs ($\hat{L} = 1$), the transverse component is significant. Therefore, the recirculating flow in short plugs is more effective in transporting fresh fluid from the central region of the plug to the wall and the heated fluid from the wall back to the plug centre.

Another significant factor influencing the heat transfer is the *recirculating period* $\hat{t}_{\text{recirc}}$, which refers to the time interval for a fluid particle in the plug travelling for one cycle and getting back to its starting point. The fluid particles follow their streamlines when they are advected by the flow. Therefore, $\hat{t}_{\text{recirc}}$ represents the recirculating period not only for one particle, but for all the fluid particles along the streamline. In Figure 4.9, a column of passive tracer particles

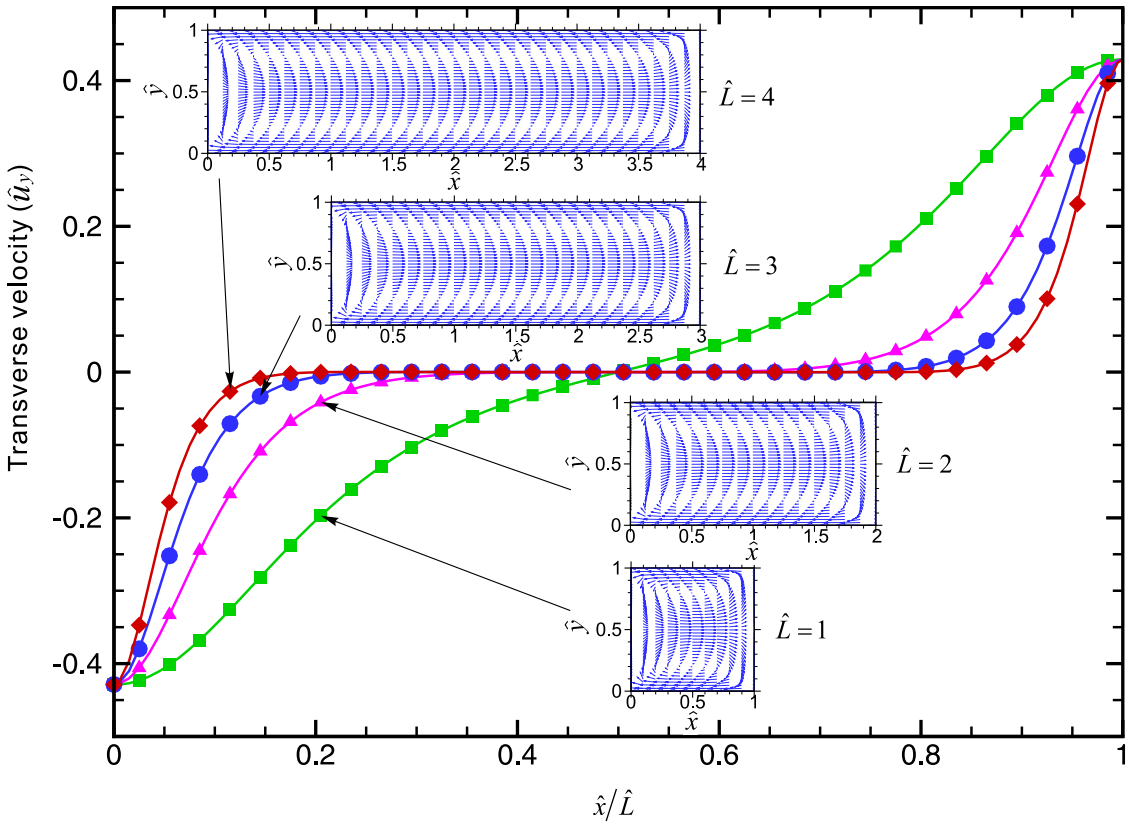

Figure 4.8: Profiles of transverse velocity in plugs of different lengths at cross section $\hat{y} = 3/4$. The velocity fields for the corresponding plug lengths are shown as well.

(along the middle cross section $\hat{x} = \hat{L}/2$ as shown in the inset in Figure 4.9) are tracked using the fourth-order Runge-Kutta (RK) method, and the recirculating periods are calculated for different plug lengths. As the plug length increases, the recirculating period increases significantly. This is because in long plugs, the fluid particles need to travel a long distance along the streamlines. For long plugs ($\hat{L} = 4$), the curve of $\hat{t}_{\text{recirc}}$ versus transverse position $\hat{y}$ has two peaks which correspond to the two vortex centres (or stagnant points) within the plug.

4.3.2.3.2 Effect of plug length on heat transfer The effect of plug length on the Nusselt number is shown in Figure 4.10**a**. In the simulation, the Peclet

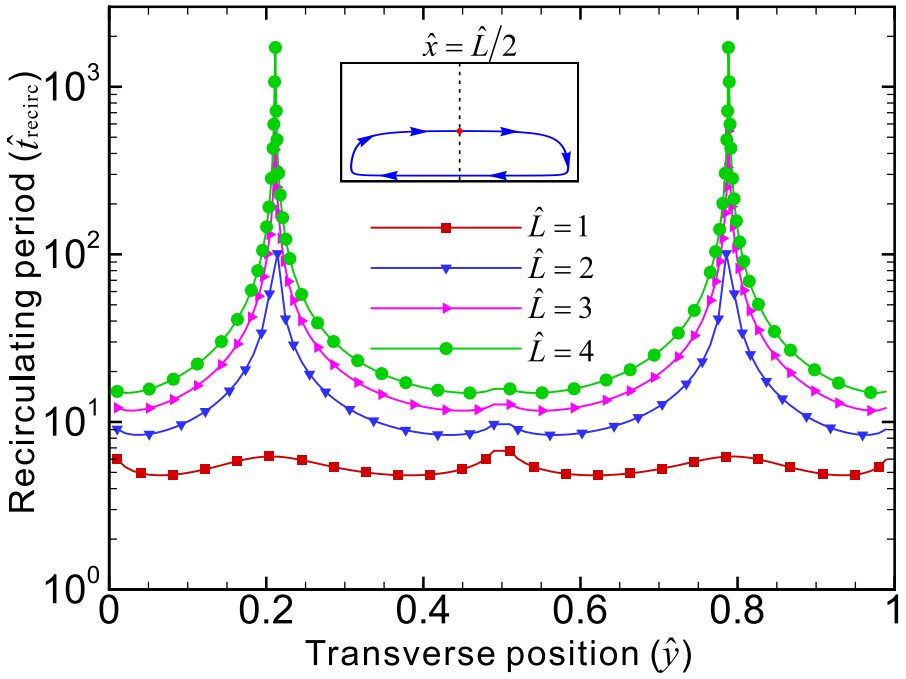

Figure 4.9: Recirculating periods for fluid particles in plugs of different lengths. Passive tracer particles along the middle cross section $\hat{x} = \hat{L}/2$ are tracked to find out their recirculating periods for plugs of different lengths.

number is fixed at 100 and the dimensionless plug length is varied from 1 to 4. For short liquid plugs ($\hat{L} = 1$), due to the development of the thermal boundary layer (Stage I), Nu decreases and achieves a minimum value of 21.3 at $\hat{X} = 0.8$. As the plug moves forward, Nu increases and reaches a maximum value of 39 at $\hat{X} = 4.2$ (Stage II). After that, Nu decreases slowly and approaches an asymptotic limit $Nu_{\text{asymp},\hat{L}=1} = 34.6$ (Stage III). The oscillation of the Nusselt number is due to the recirculating flow as discussed in Section 4.3.2.2. For long plugs ($\hat{L} = 4$), Nu reaches its minimum value of 13.2 at $\hat{X} = 2.3$. The increase in $\hat{X}$ at which point Nu reaches its minimum value is because the recirculating period $\hat{t}_{\text{recirc}}$ increases with increasing $\hat{L}$ [Figure 4.9]. The Nusselt number for $\hat{L} = 4$ finally attains an asymptotic limit of $Nu_{\text{asymp},\hat{L}=4} = 29.8$, which is lower than that of short plugs

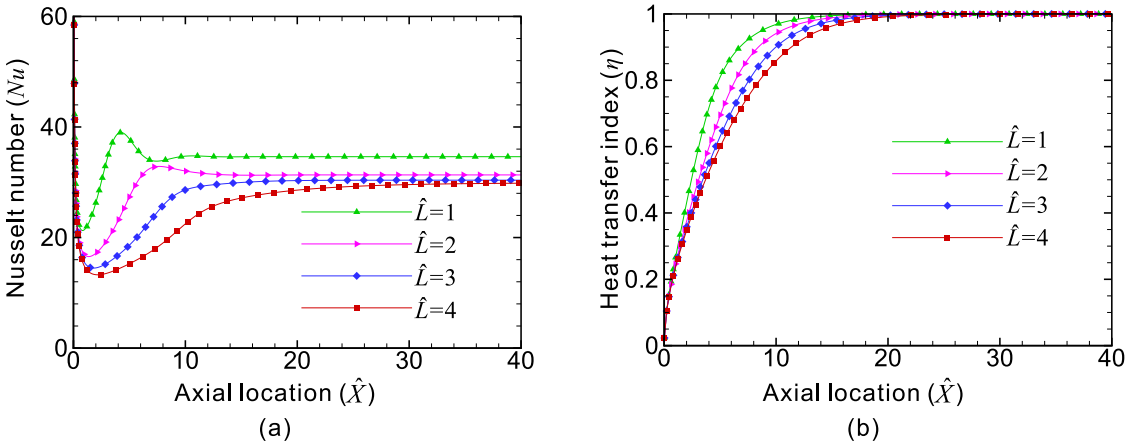

Figure 4.10: (a) Nusselt number Nu and (b) heat transfer index η in liquid plugs of different lengths in the constant-surface-temperature condition. The Peclet number is $Pe = 100$.

($\hat{L} = 1$). As the plug length increases, the asymptotic limit of Nu reduces. This is because of the decrease in the transverse flow, as explained in Figure 4.8. The effect of the plug length on the heat transfer index is shown in Figure 4.10**b**. Due to the higher Nusselt numbers in short plugs, the heat transfer process in short plugs is much faster than that in long plugs.

Figure 4.11 shows the heat transfer index against plug length at a fixed axial location of the microchannel $\hat{X} = 10$. The Peclet number is fixed at 100. The temperature distributions of the respective plug length are also shown. The results indicate that as the plug length increases, the heat transfer index decreases. This is because the transverse velocity decreases as $\hat{L}$ increases, which results in a lower Nu as shown in Figure 4.8 and Figure 4.10**a**. Consequently, long plugs require a longer time and a longer channel length to achieve a uniform temperature T_w.

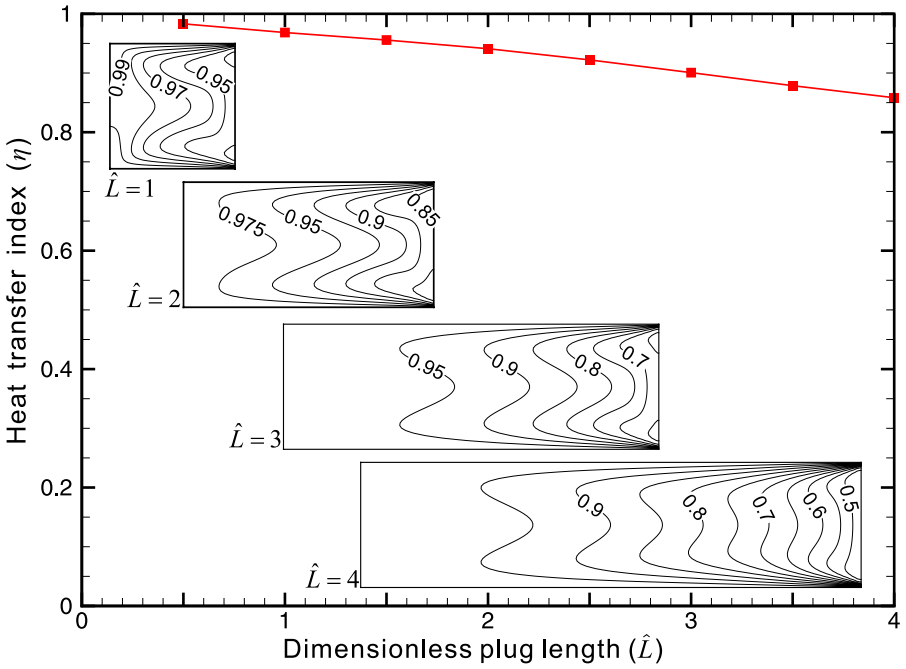

Figure 4.11: Effect of the dimensionless plug length $\hat{L}$ on the heat transfer index η. The axial location of the plug is $\hat{X} = 10$, and the Peclet number is $Pe = 100$. The temperature distributions within the plugs are shown.

4.3.3 Heat transfer in the constant-surface-heat-flux condition

4.3.3.1 Heat transfer process and comparison with single phase flow

The time evolution of the isotherms for a liquid plug moving through a 2D microchannel is shown in Figure 4.12**a** (Instants A–H), and their corresponding points are marked in Figure 4.12**b**. The channel wall is subjected to a constant heat flux, the dimensionless plug length is $\hat{L} = 2$, and the Peclet number is $Pe = 100$. The variation of Nu, $\hat{\bar{T}}_{\rm w}$ (i.e, the mean temperature of the wall over the plug length, $\hat{\bar{T}}_{\rm w} \equiv \frac{1}{\hat{L}} \int_0^{\hat{L}} \hat{T}\Big|_{\hat{y}=0} d\hat{x}$), and $\hat{\bar{T}}_{\rm plug}$ [Eq. (4.23)] are plotted against the axial location $\hat{X}$ in Figure 4.12**b**. To compare between the plug flow and the single phase flow,

Nu and the maximum fluid temperature $\hat{T}_{\max}$ are plotted in Figures 4.12**c** and **d**.

For single phase flow, the Nusselt number is large near the entrance of the channel and decays along the microchannel to the asymptotic limit ($Nu_{\text{asymp,sp}} = 8.2$) due to the development of the thermal boundary layer along the wall, as shown in Figure 4.12**c**. In contrast, the heat transfer in plug flow can be divided into three subsequent stages: (i) development of thermal boundary layer; (ii) advection of heated/fresh fluid in the plug; and (iii) thermally fully developed flow.

Stage I: *Development of thermal boundary layer (TBL)*, [Figures 4.12**a** and **b**, (Instants B–C)]. When the plug contacts the heated wall, a thin liquid layer in the immediate vicinity of the wall rapidly increases its temperature and forms a TBL, while the fluid outside the TBL is unaffected [Figure 4.12**a** (Instant B)]. Due to the negative flow direction in the TBL along the wall, the TBL is thinner at the front of the plug, while it is thicker near the rear. The thickness of the TBL grows with time until the TBL reaches the centreline of the channel [Figure 4.12**a** (Instant C)], which marks the end of Stage I and the beginning of Stage II.

The Nusselt number decreases as the TBL develops. In the constant-surface-heat-flux condition, a constant temperature gradient is maintained at the wall. The TBL is thin initially [Figure 4.12**a** (Instant B)], which results in a small temperature difference between the wall and the plug ($\hat{\bar{T}}_{\text{w}} - \hat{\bar{T}}_{\text{plug}}$) and a large *Nu* [Figure 4.12**b**]. However, as the TBL develops, *Nu* decays rapidly, and ($\hat{\bar{T}}_{\text{w}} - \hat{\bar{T}}_{\text{plug}}$) increases correspondingly with increasing $\hat{X}$, [Figure 4.12**b**].

Stage II: *Advection of heated/fresh fluid in the plug*, [Figures 4.12**a** and **b**, (Instants D–F)]: Due to the presence of the front interface, the fresh fluid is being transported from the central region of the plug to the heated wall; while

due to the presence of the rear interface, the heated fluid is being transported from the wall towards the central region. Instead of forming high temperature gradient and high heat flux between the wall and the fluid (in the constant-surface-temperature condition discussed in Section 4.3.2.1), the advection of heated/fresh fluid reduces the temperature difference $(\hat{\bar{T}}_{\mathrm{w}} - \hat{\bar{T}}_{\mathrm{plug}})$. At Stage II, the advection of the heated/fresh fluid results in the oscillation of the Nusselt number, as shown in Figure 4.12**b**. The details will be discussed in Section 4.3.3.2.

Stage III: *Thermally fully developed flow*, [Figures 4.12**a** and **b**, (Instants G–H)]: Heat transfer continues as a constant heat flux is imposed at the wall, $\hat{\bar{T}}_{\mathrm{plug}}$ increases as the plugs move in the microchannel. At this fully developed stage, the temperature difference between the plug and the wall $(\hat{\bar{T}}_{\mathrm{w}} - \hat{\bar{T}}_{\mathrm{plug}})$ remains constant with increasing $\hat{X}$. As shown in Figure 4.12**a** (Instants G–H), the shapes of the temperature contours remain unchanged. The Nusselt number approaches an asymptotic limit, $Nu_{\mathrm{asymp,plug}} = 40.6$, which is much higher as compared with single phase flow ($Nu_{\mathrm{asymp,sp}} = 8.2$).

The recirculating flow in the plug transports the heated fluid from the wall towards the central region of the plug, and transports the fresh fluid from the central region of the plug towards the wall. Therefore, the recirculating flow effectively reduces $(\hat{\bar{T}}_{\mathrm{w}} - \hat{\bar{T}}_{\mathrm{plug}})$. According to Eqs. (4.25) and (4.26), with a constant surface heat flux, as compared to single phase flow, the decrease in $(\hat{\bar{T}}_{\mathrm{w}} - \hat{\bar{T}}_{\mathrm{plug}})$ results in the increase in h and Nu, as shown in Figure 4.12**b**.

For single phase flow, the maximum fluid temperature $\hat{T}_{\mathrm{max}}$ of an axial location $\hat{X}$ is located at the wall of the microchannel. For plug flow, $\hat{T}_{\mathrm{max}}$ of an axial location $\hat{X}$ is located at the top/bottom corners of the rear interface of the

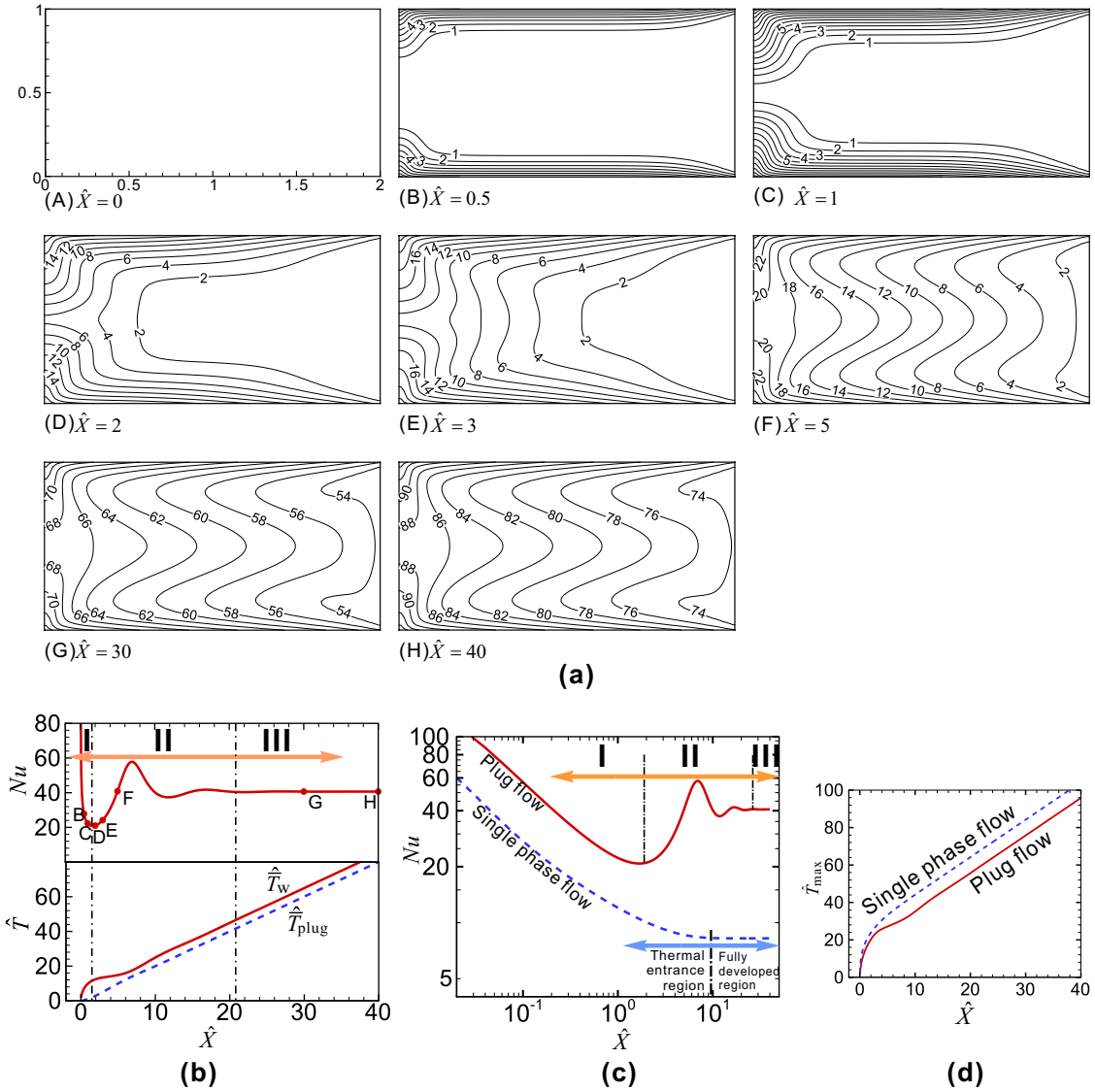

Figure 4.12: Heat transfer process in a typical liquid plug in the constant-surface-heat-flux condition and its comparison with single phase flow. The dimensionless plug length is $\hat{L}=2$, and the Peclet number is $Pe=100$. (a) Sequence of temperature distribution in the liquid plug. (b) Variation of the Nusselt number Nu, the mean fluid temperature of the plug unit $\hat{\bar{T}}_{\text{plug}}$ [Eq. (4.23)] and the mean temperature of the wall over the plug length $[\hat{\bar{T}}_w \equiv \frac{1}{\hat{L}}\int_0^{\hat{L}} \hat{T}\big|_{\hat{y}=0} d\hat{x}]$. The marked points correspond to the instants in (a). (c) Log-log plot of Nusselt numbers for the plug flow and for the single phase flow. (c) Maximum fluid temperature $\hat{T}_{\max}$ for the plug flow and for the single phase flow.

plug (the coordinates are (0, 1) and symmetrically (0, 0) as shown in Figure 4.12**a**). The maximum fluid temperature $\hat{T}_{\max}$ for plug flow, as shown in Figure 4.12**d**, is much lower than that for single phase flow. For single phase flow, the fluid near the wall is continuously heated by the wall as it moves along. For the plug flow, the fluid, after being heated by the wall, moves towards the central region of the plug. The temperature difference within the plug is effectively reduced by spreading the heat throughout the plug. Therefore, $\hat{T}_{\max}$ is considerably lower than that of single phase flow.

4.3.3.2 Effect of Peclet number

With a constant surface heat flux on a wall, Nu and $\hat{T}_{\max}$ versus $\hat{X}$ for different Peclet numbers are plotted in Figure 4.13. The plug length is fixed at 2 while Pe is varied from 4 to 1024. At a low Peclet number ($Pe = 4$), the Nusselt number is relatively low, with an asymptotic limit of $Nu_{\text{asymp},Pe=4} = 10.7$ at Stage III. The Nusselt number increases with increasing Pe. At a high Peclet number ($Pe = 1024$), the asymptotic limit of Nu at Stage III increases to $Nu_{\text{asymp},Pe=1024} = 53.1$. The increase in Nu with increasing Pe is mainly due to the increase in the advection effect, which effectively transports the heated fluid from the wall to the central region of the plug and transports the fresh fluid from the central region to the heated wall.

Similar to the oscillation of Nu in the constant-surface-temperature condition as discussed in Section 4.3.2.2, oscillation of Nu appears in the constant-surface-heat-flux condition as shown in Figure 4.13**a**. Although they share similar features and are both caused by the internal recirculating flow, their mechanisms are

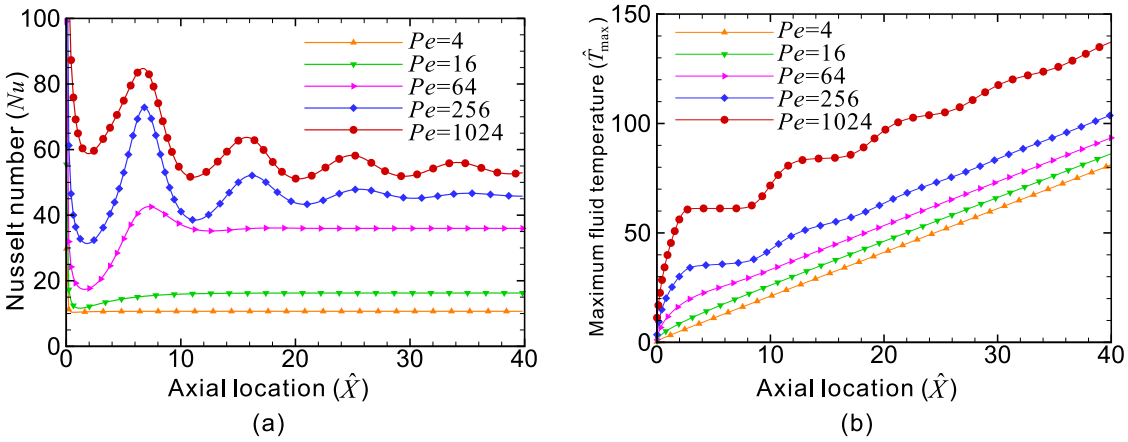

Figure 4.13: (a) Nusselt number Nu and (b) maximum fluid temperature $\hat{T}_{\max}$ in a plug at different Peclet numbers in the constant-surface-heat-flux condition. The dimensionless plug length is $\hat{L} = 2$.

different. The Nusselt number at a high Peclet number ($Pe = 1024$) is plotted in Figure 4.14**a**, as well as the two important factors influencing Nu, namely the mean temperature of the wall over the plug length ($\hat{\bar{T}}_{\rm w}$), and the mean fluid temperature of the plug unit [$\hat{\bar{T}}_{\rm plug}$ in Eq. (4.23)]. The time evolution plots of the temperature distribution in the plug is shown in Figure 4.14**b** (Instants A–F), and the corresponding points are marked in Figure 4.14**a**.

When the fresh fluid in the central region of the plug is being transported to the heated wall by the recirculating flow [Figure 4.14**a** (Instants A–D)], $\hat{\bar{T}}_{\rm w}$ remains almost constant, while $\hat{\bar{T}}_{\rm plug}$ increases linearly. In this period, $(\hat{\bar{T}}_{\rm w} - \hat{\bar{T}}_{\rm plug})$ decreases with increasing $\hat{X}$, hence, the Nusselt number [according to Eq. (4.32)] increases. As the heated fluid in the plug is transported back to the heated wall [Figure 4.14**b** (Instant E)], $\hat{\bar{T}}_{\rm w}$ and $(\hat{\bar{T}}_{\rm w} - \hat{\bar{T}}_{\rm plug})$ increase dramatically, which results in a decrease in Nu. The periodic oscillation of Nu is damped as the temperature difference $(\hat{\bar{T}}_{\rm w} - \hat{\bar{T}}_{\rm plug})$ remains constant during the thermally fully developed stage.

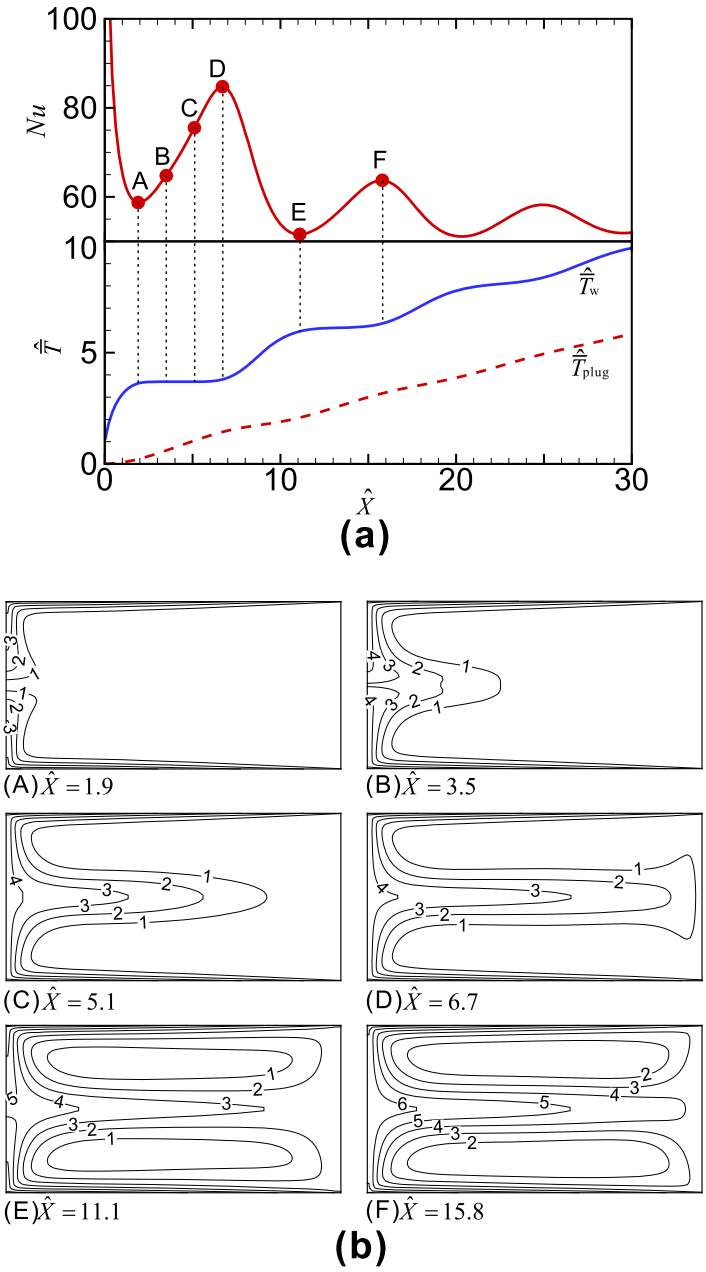

Figure 4.14: Oscillation of the Nusselt number for a plug ($\hat{L} = 2$) at a high Peclet number ($Pe = 1024$) in the constant-surface-heat-flux condition. The oscillation of Nu is due to the stair-shaped increased mean temperature of the wall over the plug length ($\hat{\bar{T}}_w$). (a) Variation of Nu, $\hat{\bar{T}}_w$, and $\hat{\bar{T}}_{plug}$ over time; (b) Evolution of the temperature distribution in the plug. The corresponding points at Instants A–F are marked in (a).

The influence of Pe on $\hat{T}_{\max}$ versus the axial distance $\hat{X}$ [Figure 4.13**b**] shows that $\hat{T}_{\max}$ decreases with increasing Pe. This is because a fast flow (high Pe) has a short residence time in the heated channel. To further quantitatively compare the effect of Pe between the single phase flow and the plug flow, $\hat{T}_{\max}$ is plotted against Pe in Figure 4.15. At a low Peclet number ($Pe = 4$), the difference in $\hat{T}_{\max}$ between the single phase flow and the plug flow is insignificant. $\hat{T}_{\max}$ decreases as Pe increases for both single phase flow and plug flow. At a high Peclet number, $\hat{T}_{\max}$ for single phase flow is higher than that for plug flow. When $Pe = 1024$, $\hat{T}_{\max}$ for single phase flow is 2.67 times for plug flow. These results indicate that at a high Pe, plug flow can significantly reduce $\hat{T}_{\max}$ by the recirculating flow within the liquid plugs.

4.3.3.3 Effect of plug length

In the constant-surface-heat-flux condition, the effect of plug length on Nu is shown in Figure 4.16**a**. The Peclet number is fixed at 100 and the dimensionless plug length is varied from 1 to 4. For longer plugs, the periods of Stage I and Stage II are longer than those of short plugs. This is because the recirculating periods are longer for longer plugs as shown in Figure 4.9. In addition, the oscillation of Nu is weaker for longer plugs than that for short plugs. This is because for long plugs, heat may have dissipated before the heated fluid is transported back to the wall. At Stage III, the asymptotic limit of Nu for long plugs ($\hat{L} = 4$) is smaller than that for short plugs ($\hat{L} = 1$). This is due to the less effect of transverse flow in long plugs, as shown in Figure 4.8.

The effect of the plug length on the maximum fluid temperature in the

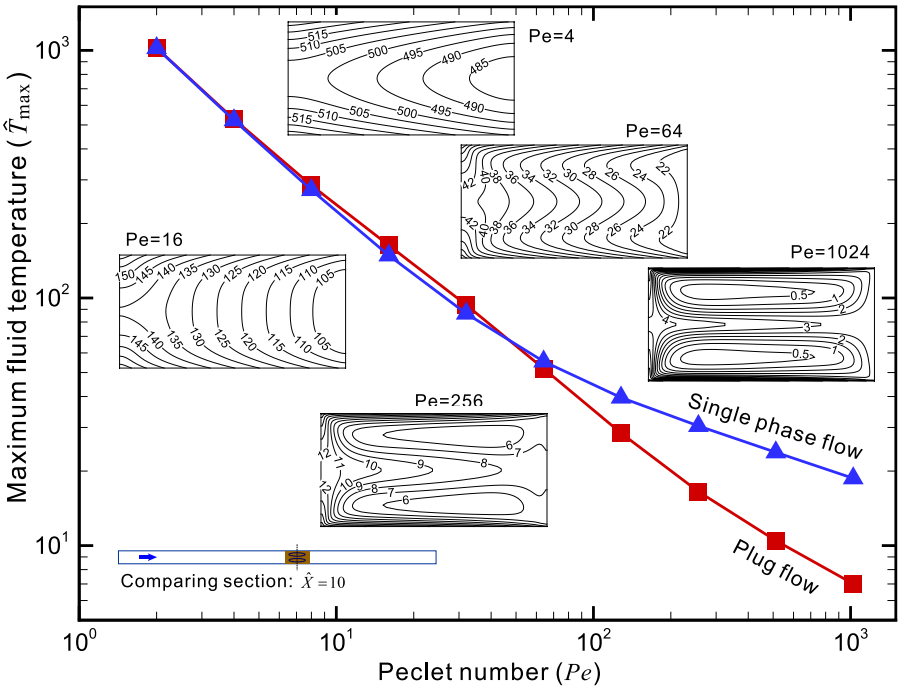

Figure 4.15: Comparison of the maximum fluid temperature $\hat{T}_{\max}$ between the plug flow and the single phase flow for different Peclet numbers in the constant-surface-heat-flux condition. The axial location in the channel is $\hat{X} = 10$, and the dimensionless plug length is $\hat{L} = 2$. The temperature distributions within the plugs are shown.

constant-surface-heat-flux condition is shown in Figure 4.16**b**. Due to the initial oscillation of Nu, the increasing rate of the maximum fluid temperature $d\hat{T}_{\max}/d\hat{X}$ varies with time. As Nu approaches its asymptotic limit, $d\hat{T}_{\max}/d\hat{X}$ remains constant, which reflects that the heat transfer gradually becomes fully developed (Stage III). From the maximum fluid temperature in Figure 4.16**b**, we can also find that $\hat{T}_{\max}$ in short plugs is lower than that in long plugs. This is due to the recirculating period $\hat{t}_{\text{recirc}}$ for fluid particles in plugs of different lengths [Figure 4.9]. The circulation time of fluid particles in plugs can be divided into the heating period $\hat{t}_{\text{heating}}$ and the cooling period $\hat{t}_{\text{cooling}}$. The heating period $\hat{t}_{\text{heating}}$ refers to the period during which the fluid particles are located in the vicinity of the wall and

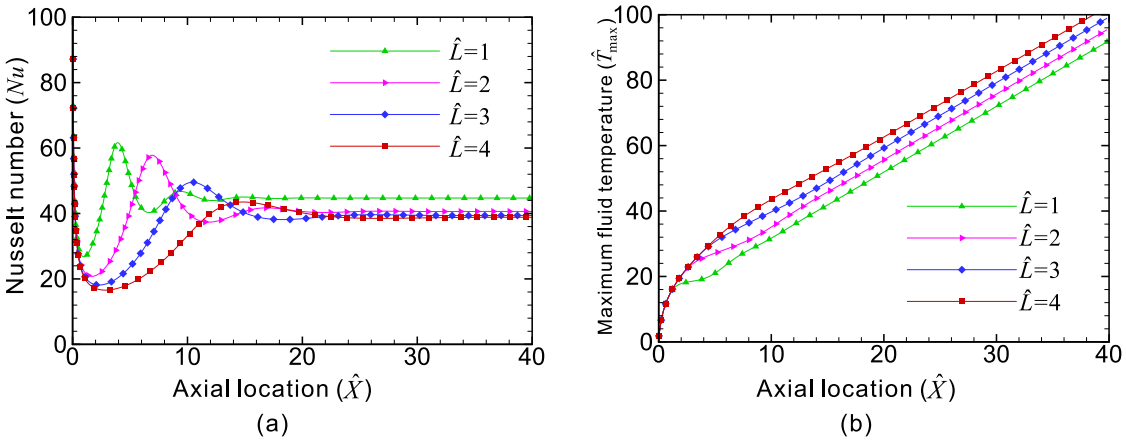

Figure 4.16: (a) The Nusselt number Nu and (b) the maximum fluid temperature $\hat{T}_{\max}$ in liquid plugs of different lengths in the constant-surface-heat-flux condition. The Peclet number is $Pe = 100$.

are receiving heat from the wall, while the cooling period $\hat{t}_{\text{cooling}}$ refers to the period during which the fluid particles are far away from the wall and are rejecting heat to the surrounding fluid. The fluid increases its temperature during the heating period and reduces its temperature during the cooling period. Therefore, a longer plug results in a longer recirculating time $\hat{t}_{\text{recirc}}$, a longer heating period $\hat{t}_{\text{heating}}$, and a longer cooling period $\hat{t}_{\text{cooling}}$, and vice versa. A longer $\hat{t}_{\text{heating}}$ results in a higher $\hat{T}_{\max}$, since $\hat{T}_{\max}$ is the maximum fluid temperature that fluid particles can achieve during the heating period near the heated wall. This can be also seen in the temperature distribution shown in Figure 4.17.

4.4 Summary

In this chapter, the heat transfer of plugs moving in microchannels is investigated systematically. By incorporating the analytical flow field, the heat transfer process in plugs moving in 2D microchannels are simulated. Different boundary

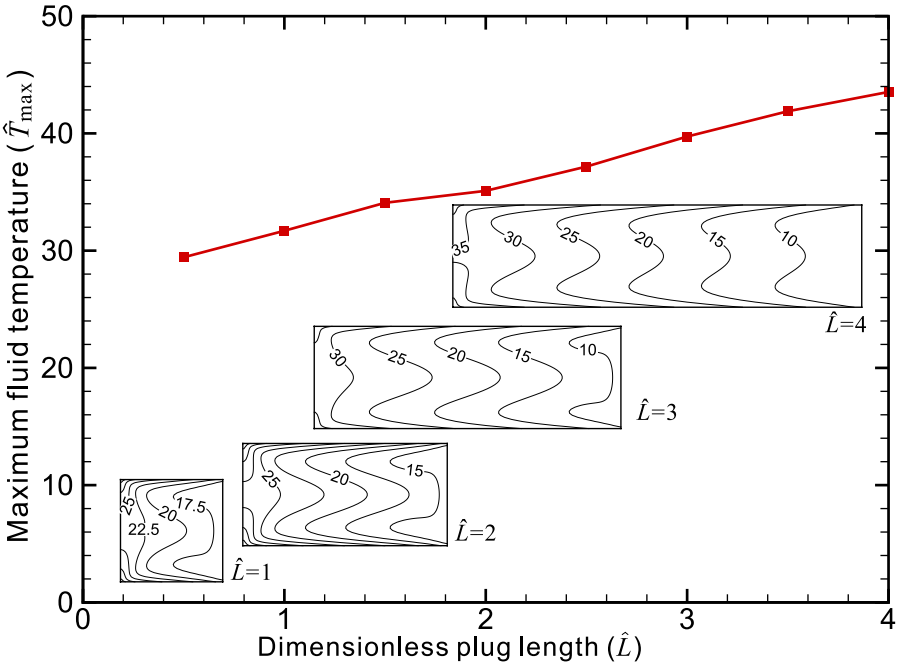

Figure 4.17: Effect of the dimensionless plug length on the maximum fluid temperature $\hat{T}_{max}$ in the constant-surface-heat-flux condition. The axial location of the plug is $\hat{X} = 10$, and the Peclet number is $Pe = 100$. The temperature distributions within the plugs are shown.

conditions, the constant-surface-temperature condition and the constant-surface-heat-flux condition, are investigated. The effects of the Peclet number and the plug length are studied. The heat transfer process is evaluated through the Nusselt number, the heat transfer index, and the maximum fluid temperature.

From this study, we can conclude that

- Heat transfer in plugs can be divided into three stages: (i) development of thermal boundary layer; (ii) advection of heated/fresh fluid in the plug; and (iii) thermally fully developed flow.

- At a high Peclet number, the Nusselt number experience oscillation when the heated/fresh fluid in the central region of the plug is being transported to

the heated wall by the recirculating flow. As the Peclet number decreases, the oscillation of Nusselt number becomes insignificant.

- In the constant-surface-temperature condition, a high Peclet number results in a higher Nusselt number and a lower heat transfer index. In the constant-surface-heat-flux condition, a high Peclet number results in a higher Nusselt number and a lower maximum temperature.

- Short plugs are favourable for heat transfer in microchannels as compared to long plugs. In the constant-surface-temperature condition, shorter plugs can achieve higher heat transfer indices due to the higher transverse velocity. In the constant-surface-heat-flux condition, shorter plugs result in lower values of the maximum fluid temperature due to the shorter recirculating period.

Without numerically solving the flow field and predicting the interface, the method used in this chapter to predict and evaluate the heat transfer in liquid plug is simple and efficient. It can be used to guide the design of plug-based microchannel heat exchangers, to predict and evaluate heat transfer process within liquid plugs in microchannels, and to deepen the understanding of the effects of the recirculating flow in plugs on the heat and mass transfer process in microchannels.

Chapter 5

Plug Flow in Two-Dimensional Curved Microchannels †

5.1 Introduction

In the previous chapter, a model for plug flow in 2D *straight* microchannels is proposed. In microfluidic devices, *curved* channels are often introduced to reduce the chip size without decreasing the channel length. A typical example is incubation channels for chemical or biological reactions, in which extremely long channels are required (Koster et al., 2008). In addition, curvature can be used to induce chaotic mixing in droplets (Song et al., 2003b). In this chapter, an analytical model is proposed for plug flow in 2D curved microchannels.

In a 3D curved channel, Dean vortices may be generated due to the imbalance between the centrifugal force and the radial pressure difference (Dean, 1928a). The vortices get stronger when the Dean number increases, which characterizes the relative effect of the centrifugal force with the viscous force, $De \equiv \frac{\rho V D_H}{\mu}\sqrt{\frac{D_H}{2R}} =$

†This work has been published in *International Journal of Heat and Mass Transfer 53 (9-10) 1977-1985.*

$Re\sqrt{\frac{D_H}{2R}}$, where ρ and μ are, respectively, the density and the dynamic viscosity of the fluid, V is the axial velocity, D_H is the hydraulic diameter of the channel, R is the radius of the curved channel path, and $Re \equiv \rho V D_H/\mu$ is the Reynolds number. However, due to the small dimension and the low flow speed in microchannels, the Reynolds number Re and the Dean number De are usually much less than one. The Dean vortices are much weaker than those in channels of large scale. To examine the centrifugal effect in liquid plugs moving in curved microchannels, numerical simulation was performed and the details are provided in Appendix D. The simulation results show that the centrifugal effect is negligible in most microfluidic devices. Therefore, in the model proposed in this chapter, the centrifugal effect will not be considered.

This chapter is organized as follows, In section 5.2, the mathematical formulae are provided. In Section 5.3, the results are validated against experimental results. The effect of curvature on the flow patterns in plugs and on the flow resistance are studied.

5.2 Analytical model

5.2.1 Problem description and assumptions

Figure 5.1 shows schematically a liquid plug moving in a curved microchannel. The shaded area is the liquid plug of interest. The surrounding area is an immiscible phase such as air. The two ends of the liquid plug are assumed to be flat. The radii of the outer and inner walls of the channel are R_1 and R_2, respectively. Therefore, the width of the channel is $w = R_1 - R_2$. The plug length, L, is measured along

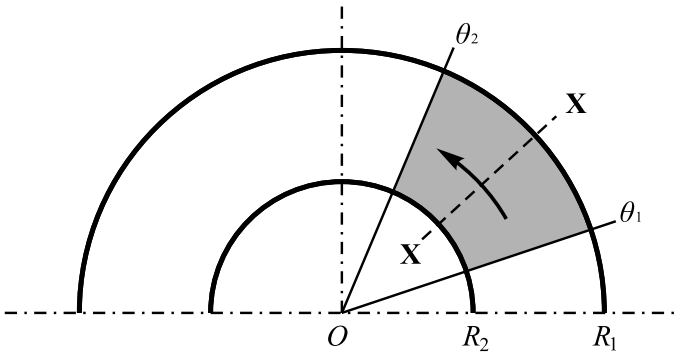

Figure 5.1: Schematic diagram of plug flow in a 2D curved microchannel.

the centreline of the channel. The plug is moving in the anticlockwise direction with an angular speed ω, around the centre point of the curved channel ***O***.

A polar coordinate is built with the origin at the centre ***O*** of the curved channel, as shown in Figure 5.1. The plug takes the region from θ_1 to θ_2. The middle cross section of the plug is indicated by **X**-**X** at $\theta = (\theta_1 + \theta_2)/2$. To simplify the analysis, the coordinate system is rotating at an angular speed ω. Therefore, the liquid plug is stationary with respective to the rotating frame of reference, while the outer and inner walls of the channel are at peripheral speeds of V_{R1} and V_{R2} in the clockwise direction, where $V_{R1} = \omega R_1$ and $V_{R2} = \omega R_2$.

In this analysis, the following assumptions are made: (1) Stokes flow with a low Reynolds number exists inside the plug. The transient term and the convection term are neglected in the momentum equation. (2) No body force is considered. The gravity is neglected and there is no other body force for the liquid plug. (3) The interface is flat and is vertical to the wall of the channel. (4) The microchannel has a high aspect ratio (depth/width), hence the flow can be regarded as 2D. (5) The liquid plug does not slip on the wall of the channel. (6) The viscosity of the adjacent immiscible phase is negligible, and there is no sheer stress on the free surface of the

plug. (7) The liquid is an incompressible Newtonian fluid. More discussion and explanation of these assumptions are provided in Section 3.2 in Chapter 3.

5.2.2 Governing equation and boundary conditions

For the Stokes flow in the plug, the governing equation is

$$\left(\frac{\partial^2}{\partial r^2}+\frac{1}{r}\frac{\partial}{\partial r}+\frac{1}{r^2}\frac{\partial^2}{\partial \theta^2}\right)\left(\frac{\partial^2}{\partial r^2}+\frac{1}{r}\frac{\partial}{\partial r}+\frac{1}{r^2}\frac{\partial^2}{\partial \theta^2}\right)\varphi=0 \tag{5.1}$$

where φ is the stream function, which is defined as

$$u_r \equiv \frac{1}{r}\frac{\partial \varphi}{\partial \theta} \tag{5.2}$$

$$u_\theta \equiv -\frac{\partial \varphi}{\partial r} \tag{5.3}$$

This definition of φ satisfies the continuity equation automatically. Equation 5.1 is often used to describe Stokes flow (Meleshko, 1996; Shankar, 2007) and elastic mechanical problems (Timoshenko, 1951). The stream function is constant on the boundaries. Here, it is set to be zero.

$$\varphi\left(R_1,\theta\right)=\varphi\left(R_2,\theta\right)=\varphi\left(r,\theta_1\right)=\varphi\left(r,\theta_2\right)=0 \tag{5.4}$$

The two ends of the plug are considered as free surfaces, because the viscosity of the adjacent gas is negligible. The boundary conditions at these two ends are, respectively:

$$\frac{1}{r}\frac{\partial}{\partial \theta}u_\theta\left(r,\theta_1\right)=\frac{1}{r^2}\frac{\partial^2}{\partial \theta^2}\varphi\left(r,\theta_1\right)=0, \qquad \frac{1}{r}\frac{\partial}{\partial \theta}u_\theta\left(r,\theta_2\right)=\frac{1}{r^2}\frac{\partial^2}{\partial \theta^2}\varphi\left(r,\theta_2\right)=0 \tag{5.5}$$

The speeds at the outer and the inner walls are V_{R1} and V_{R2} in the clockwise direction relative to the rotating frame of reference.

$$-\frac{\partial}{\partial r}\varphi\left(R_1,\theta\right)=-V_{R1} \tag{5.6}$$

$$-\frac{\partial}{\partial r}\varphi\left(R_2,\theta\right)=-V_{R2} \tag{5.7}$$

5.2.3 Nondimensionalisation

Introducing the following dimensionless parameters,

$$\hat{r} \equiv \frac{r}{R_1}, \quad \hat{\theta} \equiv \frac{\theta - \theta_1}{\Delta\theta}, \quad \hat{u}_\theta \equiv \frac{u_\theta}{V_{R1}}, \quad \hat{u}_r \equiv \frac{u_r \Delta\theta}{V_{R1}}, \quad \hat{\varphi} \equiv \frac{\varphi}{V_{R1} R_1} \tag{5.8}$$

where $\Delta\theta \equiv \theta_2 - \theta_1$. The dimensionless governing equation is

$$\left(\frac{\partial^2}{\partial \hat{r}^2} + \frac{1}{\hat{r}} \frac{\partial}{\partial \hat{r}} + \frac{1}{\hat{r}^2} \frac{1}{\Delta\theta^2} \frac{\partial^2}{\partial \hat{\theta}^2} \right)^2 \hat{\varphi} = 0 \tag{5.9}$$

The radius ratio between the inner wall of the channel to the outer wall represents the curvature of the channel, and it is defined as

$$\hat{R}_2 \equiv R_2 / R_1 \tag{5.10}$$

The dimensionless plug length is defined as

$$\hat{L} \equiv L / (R_1 - R_2) \tag{5.11}$$

The dimensionless boundary conditions are

$$\hat{\varphi}\left(1, \hat{\theta}\right) = \hat{\varphi}\left(\hat{R}_2, \hat{\theta}\right) = 0 \tag{5.12}$$

$$\hat{\varphi}\left(\hat{r}, 0\right) = \hat{\varphi}\left(\hat{r}, 1\right) = 0 \tag{5.13}$$

$$\frac{\partial^2}{\partial \hat{\theta}^2} \hat{\varphi}\left(\hat{r}, 0\right) = \frac{\partial^2}{\partial \hat{\theta}^2} \hat{\varphi}\left(\hat{r}, 1\right) = 0 \tag{5.14}$$

$$\frac{\partial}{\partial \hat{r}} \hat{\varphi}\left(1, \hat{\theta}\right) = 1 \tag{5.15}$$

$$\frac{\partial}{\partial \hat{r}} \hat{\varphi}\left(\hat{R}_2, \hat{\theta}\right) = \hat{R}_2 \tag{5.16}$$

5.2.4 Analytical solution

The governing equation (5.9) and its boundary conditions can be solved using the finite Fourier transform (FFT) (Deen, 1998) method. Its solution can be written

as

$$\hat{\varphi}\left(\hat{r},\hat{\theta}\right)=\sum_{n=0}^{\infty}\left[\phi_n\left(\hat{r}\right)\sin\left(n\pi\hat{\theta}\right)+\psi_n\left(\hat{r}\right)\cos\left(n\pi\hat{\theta}\right)\right] \tag{5.17}$$

which is the Fourier expansion of $\hat{\varphi}\left(\hat{r},\hat{\theta}\right)$. According to the homogeneous boundary conditions Eqs. (5.13) and (5.14), the solution can be written in a simpler form

$$\hat{\varphi}\left(\hat{r},\hat{\theta}\right)=\sum_{n=1}^{\infty}\left[\phi_n\left(\hat{r}\right)\sin\left(n\pi\hat{\theta}\right)\right] \tag{5.18}$$

This format of solution Eq. (5.18) satisfies the boundary conditions Eqs. (5.13) and (5.14) automatically. Function $\phi_n\left(\hat{r}\right)$ can be solved according to the other four boundary conditions Eqs. (5.12), (5.15) and (5.16). Using the FFT method, the stream function can be determined as

$$\begin{aligned}\hat{\varphi}\left(\hat{r},\hat{\theta}\right)=&\sum_{\substack{n=1\\ \&\ \alpha_n\neq 1}}^{\infty}\sin\left(n\pi\hat{\theta}\right)\left(\frac{C_{1n}}{\hat{r}^{\alpha_n}}+C_{2n}\hat{r}^{\alpha_n}+C_{3n}\hat{r}^{\alpha_n+2}+\frac{C_{4n}}{\hat{r}^{\alpha_n-2}}\right)\\&+\sum_{\substack{n=1\\ \&\ \alpha_n=1}}^{\infty}\sin\left(n\pi\hat{\theta}\right)\left[\frac{C'_{1n}}{\hat{r}}+C'_{2n}\hat{r}+C'_{3n}\hat{r}^3+C'_{4n}\hat{r}\ln\left(\hat{r}\right)\right]\end{aligned} \tag{5.19}$$

where $\alpha_n\equiv n\pi/\Delta\theta$. The dimensionless velocity components in the r and θ directions are, respectively:

$$\begin{aligned}\hat{u}_r\left(\hat{r},\hat{\theta}\right)=&\sum_{\substack{n=1\\ \&\ \alpha_n\neq 1}}^{\infty}n\pi\cos\left(n\pi\hat{\theta}\right)\left[\frac{C_{1n}}{\hat{r}^{\alpha_n+1}}+C_{2n}\hat{r}^{\alpha_n-1}+C_{3n}\hat{r}^{\alpha_n+1}+\frac{C_{4n}}{\hat{r}^{\alpha_n-1}}\right]\\&+\sum_{\substack{n=1\\ \&\ \alpha_n=1}}^{\infty}n\pi\cos\left(n\pi\hat{\theta}\right)\left[\frac{C'_{1n}}{\hat{r}^2}+C'_{2n}+C'_{3n}\hat{r}^2+C'_{4n}\ln\left(\hat{r}\right)\right]\end{aligned} \tag{5.20}$$

$$\begin{aligned}\hat{u}_\theta\left(\hat{r},\hat{\theta}\right)=&-\sum_{\substack{n=1\\ \&\ \alpha_n\neq 1}}^{\infty}\sin\left(n\pi\hat{\theta}\right)\\&\times\left[\frac{-\alpha_nC_{1n}}{\hat{r}^{\alpha_n+1}}+\alpha_nC_{2n}\hat{r}^{\alpha_n-1}+C_{3n}\left(\alpha_n+2\right)\hat{r}^{\alpha_n+1}+C_{4n}\left(2-\alpha_n\right)\hat{r}^{1-\alpha_n}\right]\\&-\sum_{\substack{n=1\\ \&\ \alpha_n=1}}^{\infty}\sin\left(n\pi\hat{\theta}\right)\left[-\frac{C'_{1n}}{\hat{r}^2}+C'_{2n}+3C'_{3n}\hat{r}^2+C'_{4n}\left(\ln\left(\hat{r}\right)+1\right)\right]\end{aligned} \tag{5.21}$$

The constant coefficients in these equations can be obtained from the boundary conditions. For $\alpha_n \neq 1$

$$D_n = \frac{1-(-1)^n}{n\pi}\left[\hat{R}_2^2 - \alpha_n^2\hat{R}_2^{2\alpha_n} + \left(2\alpha_n^2-2\right)\hat{R}_2^{2+2\alpha_n} - {\alpha_n}^2\hat{R}_2^{4+2\alpha_n} + \hat{R}_2^{2+4\alpha_n}\right] \tag{5.22}$$

$$\begin{aligned} C_{1n} = D_n\Big[&-\hat{R}_2^{4+\alpha_n} + (1-\alpha_n)\hat{R}_2^{2+2\alpha_n} + \alpha_n\hat{R}_2^{4+2\alpha_n} \\ &+ \alpha_n\hat{R}_2^{2+3\alpha_n} + (1-\alpha_n)\hat{R}_2^{4+3\alpha_n} - \hat{R}_2^{2+4\alpha_n}\Big] \end{aligned} \tag{5.23}$$

$$\begin{aligned} C_{2n} = D_n\Big[&-\hat{R}_2^{2} - \alpha_n\hat{R}_2^{2+\alpha_n} + (1+\alpha_n)\hat{R}_2^{4+\alpha_n} \\ &+ (1+\alpha_n)\hat{R}_2^{2+2\alpha_n} - \alpha_n\hat{R}_2^{4+2\alpha_n} - \hat{R}_2^{4+3\alpha_n}\Big] \end{aligned} \tag{5.24}$$

$$\begin{aligned} C_{3n} = D_n\Big[&\hat{R}_2^{2} - \alpha_n\hat{R}_2^{2\alpha_n} + (-1+\alpha_n)\hat{R}_2^{2+\alpha_n} \\ &- \alpha_n\hat{R}_2^{4+\alpha_n} + (-1+\alpha_n)\hat{R}_2^{2+2\alpha_n} + \hat{R}_2^{2+3\alpha_n}\Big] \end{aligned} \tag{5.25}$$

$$\begin{aligned} C_{4n} = D_n\Big[&\alpha_n\hat{R}_2^{2\alpha_n} + \hat{R}_2^{2+\alpha_n} + (-1-\alpha_n)\hat{R}_2^{2+2\alpha_n} \\ &+ (-1-\alpha_n)\hat{R}_2^{2+3\alpha_n} + \alpha_n\hat{R}_2^{4+3\alpha_n} + \hat{R}_2^{2+4\alpha_n}\Big] \end{aligned} \tag{5.26}$$

and for $\alpha_n = 1$

$$D'_n = \frac{1-(-1)^n}{2n\pi\left(1+\hat{R}_2\right)\left[1-\hat{R}_2^2+\ln\left(\hat{R}_2\right)+\hat{R}_2^2\ln\left(\hat{R}_2\right)\right]} \tag{5.27}$$

$$C'_{1n} = D'_n\hat{R}_2^2\left[1-\hat{R}_2^2-2\hat{R}_2\ln\left(\hat{R}_2\right)\right] \tag{5.28}$$

$$C'_{2n} = D'_n\left[-1+\hat{R}_2^4+\left(-1-\hat{R}_2-\hat{R}_2^2+\hat{R}_2^3\right)2\ln\left(\hat{R}_2\right)\right] \tag{5.29}$$

$$C'_{3n} = D'_n\left[1-\hat{R}_2^2+\left(1+\hat{R}_2+\hat{R}_2^2\right)2\ln\left(\hat{R}_2\right)\right] \tag{5.30}$$

$$C'_{4n} = D'_n\left[-2\left(-1+\hat{R}_2\right)\left(1+\hat{R}_2\right)^3\right] \tag{5.31}$$

The absolute dimensional velocity field of the liquid plug can be obtained as

$$u'_\theta = V_{R1}\hat{u}_\theta + \omega r = V_{R1}\hat{u}_\theta + \frac{r}{R_1}V_{R1} \tag{5.32}$$

$$u'_r = \frac{V_{R1}\hat{u}_r}{\Delta\theta} \tag{5.33}$$

5.2.5 Flow resistance of liquid plugs

The force balance diagram for the liquid plug is shown in Figure 5.2. These forces are in moment balance due to the low Reynolds number. The moment can be derived by integrating the shear stress along the wall of the channel. For unit depth of the channel, the moment of shear force that the inner wall applies to the liquid is

$$\begin{aligned} M_{f2} &= -\int_{\theta_1}^{\theta_2} \left(\tau_{r\theta} r^2\right)_{r=R_2} d\theta \\ &= -\mu \Delta\theta R_1 V_{R1} \left[\sum_{\substack{n=1 \\ \alpha_n \neq 1}}^{\infty} \frac{(-1)^n - 1}{n\pi} P\left(\hat{R}_2\right) + \sum_{\substack{n=1 \\ \& \ \alpha_n = 1}}^{\infty} \frac{(-1)^n - 1}{n\pi} Q\left(\hat{R}_2\right) \right] \end{aligned} \tag{5.34}$$

where

$$\begin{aligned} P(\hat{r}) = {} & \alpha_n (\alpha_n + 2) \hat{r}^{-\alpha_n} C_{1n} + \alpha_n (\alpha_n - 2) \hat{r}^{\alpha_n} C_{2n} \\ & + (\alpha_n + 2) \alpha_n \hat{r}^{\alpha_n + 2} C_{3n} + (\alpha_n - 2) \alpha_n \hat{r}^{-\alpha_n + 2} C_{4n} \end{aligned} \tag{5.35}$$

$$Q(\hat{r}) = 3\hat{r}^{-1} C'_{1n} - \hat{r} C'_{2n} + 3\hat{r}^3 C'_{3n} - \hat{r} \ln(\hat{r}) C'_{4n} \tag{5.36}$$

The moment of shear force caused by the outer wall is

$$M_{f1} = \mu \Delta\theta R_1 V_{R1} \left[\sum_{\substack{n=1 \\ \& \ \alpha_n \neq 1}}^{\infty} \frac{(-1)^n - 1}{n\pi} P(1) + \sum_{\substack{n=1 \\ \& \ \alpha_n = 1}}^{\infty} \frac{(-1)^n - 1}{n\pi} Q(1) \right] \tag{5.37}$$

Although flat interfaces are assumed (Assumption 3 in Section 5.2.1) in the model, the effect of surface tension and contact angle hysteresis on the dynamics of the plug can be included in the moment balance. The surface tension and the contact angle influence the plug speed, while the plug speed influences the flow field in the plug. In this way, the effect of the surface tension and contact angle on the flow field of the plug can be considered indirectly through the plug speed. The moments of surface tension force at the front (advancing) and rear (receding) ends

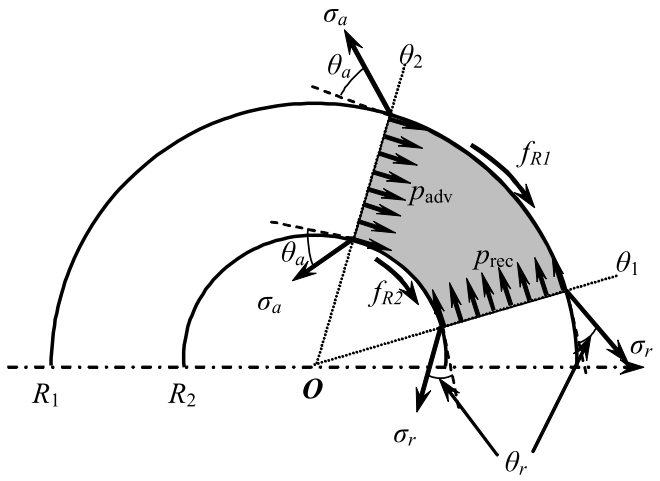

Figure 5.2: Force balance diagram of a liquid plug.

are, respectively:

$$M_{\text{adv}} = \sigma_{\text{adv}} \left(R_1 + R_2\right) \cos\left(\theta_{\text{adv}}\right) \tag{5.38}$$

$$M_{\text{rec}} = \sigma_{\text{rec}} \left(R_1 + R_2\right) \cos\left(\theta_{\text{rec}}\right) \tag{5.39}$$

where θ_{adv} and θ_{rec} are the advancing and receding contact angles, and σ_{adv} and σ_{rec} denote the surface tension at the advancing and receding ends, respectively. The moment balance equation is

$$\int_{R_i}^{R_o} \Delta p r dr = M_{f1} + M_{f2} + M_r - M_{\text{adv}} \tag{5.40}$$

where $\Delta p = p_{\text{rec}} - p_{\text{adv}}$ is the pressure drop from the receding end to the advancing end of the plug. This leads to the driving pressure

$$\Delta p = \left\{ \sum_{\substack{n=1 \\ \& \ \alpha_n \neq 1}}^{\infty} \frac{(-1)^n - 1}{n\pi} \left[P\left(1\right) - P\left(\hat{R}_2\right)\right] + \sum_{\substack{n=1 \\ \& \ \alpha_n = 1}}^{\infty} \frac{(-1)^n - 1}{n\pi} \left[Q\left(1\right) - Q\left(\hat{R}_2\right)\right] \right\} \times \frac{2\mu \Delta\theta R_1 V_{R1}}{\left(R_1^2 - R_2^2\right)} + \frac{2\left[\sigma_{\text{rec}} \cos\left(\theta_{\text{rec}}\right) - \sigma_{\text{adv}} \cos\left(\theta_{\text{adv}}\right)\right]}{R_1 - R_2} \tag{5.41}$$

In Eq. (5.41), the first term is caused by the friction, and the second term is caused by the surface tension and the contact angles.

A dimensionless parameter, the plug resistance coefficient C_f, is used to characterize the flow resistance caused by a single plug. The plug resistance coefficient C_f is the product of the Moody friction factor f and the Reynolds number Re. The characteristic velocity is the average speed of the plug along the centre line of the channel $V = \omega(R_1 + R_2)/2$, and the characteristic length is the width of the channel, $(R_1 - R_2)$. Therefore, the Reynolds number and the Moody friction factor are, respectively:

$$f = \frac{4\Delta p \left(R_1 - R_2\right)}{\Delta\theta \left(R_1 + R_2\right) \rho V^2} \tag{5.42}$$

$$Re = \frac{\rho V \left(R_1 - R_2\right)}{\mu} \tag{5.43}$$

Hence, the plug resistance coefficient is given by

$$C_f \equiv fRe = \left\{ \sum_{\substack{n=1 \\ \& \ \alpha_n \neq 1}}^{\infty} \left[P\left(1\right) - P\left(\hat{R}_2\right)\right] + \sum_{\substack{n=1 \\ \& \ \alpha_n = 1}}^{\infty} \left[Q\left(1\right) - Q\left(\hat{R}_2\right)\right] \right\} \frac{(-1)^n - 1}{n\pi} \times \frac{8R_1 \left(R_1 - R_2\right)}{\left(R_1 + R_2\right)^2} + \frac{8\left(R_1 - R_2\right)\left[\sigma_{\mathrm{rec}} \cos\left(\theta_{\mathrm{rec}}\right) - \sigma_{\mathrm{adv}} \cos\left(\theta_{\mathrm{adv}}\right)\right]}{\mu\Delta\theta \left(R_1 + R_2\right) V} \tag{5.44}$$

5.2.6 Validation by 1D model

Assuming that the liquid plug is infinitely long ($\hat{L} \to \infty$), we can neglect the velocity component in the r and z directions.

$$u_r = u_z = 0 \tag{5.45}$$

Then the momentum equation for the Stokes flow in the curved channel is

$$\frac{\mathrm{d}^2 u_{\theta,1\mathrm{D}}}{\mathrm{d}r^2} + \frac{1}{r}\frac{\mathrm{d}u_{\theta,1\mathrm{D}}}{\mathrm{d}r} - \frac{1}{r^2}u_{\theta,1\mathrm{D}} = \frac{1}{\mu r}\frac{\mathrm{d}p}{\mathrm{d}\theta} \tag{5.46}$$

The boundary condition is

$$u_{\theta,1\mathrm{D}}\left(R_1\right) = u_{\theta,1\mathrm{D}}\left(R_2\right) = 0 \tag{5.47}$$

The solution of this 1D model is

$$u_{\theta,1\mathrm{D}}(r) = \frac{1}{2\mu}\frac{\mathrm{d}p}{\mathrm{d}\theta} \times \left[-\frac{R_1^2 \ln R_1 - R_2^2 \ln R_2}{R_1^2 - R_2^2} r + \frac{(\ln R_1 - \ln R_2) R_1^2 R_2^2}{R_1^2 - R_2^2} \frac{1}{r} + r \ln r \right] \tag{5.48}$$

The average velocity is

$$\begin{aligned} V_{1\mathrm{D}} &= \frac{1}{R_1 - R_2} \int_{R_2}^{R_1} u_{\theta,1\mathrm{D}}(r)\, \mathrm{d}r \\ &= -\frac{1}{2\mu}\frac{\mathrm{d}p}{\mathrm{d}\theta} \frac{\left[R_1^2 - R_2^2 + 2R_1R_2(\ln R_1 - \ln R_2)\right]\left[R_1^2 - R_2^2 - 2R_1R_2(\ln R_1 - \ln R_2)\right]}{4(R_1 - R_2)^2 (R_1 + R_2)} \end{aligned} \tag{5.49}$$

According to Eq. (5.32), the dimensionless relative velocity can be obtained after rearrangement,

$$\begin{aligned} \hat{u}_{\theta,1\mathrm{D}} &= \frac{u_{\theta,1\mathrm{D}}}{V_{R1}} - \frac{r}{R_1} = \frac{u_{\theta,1\mathrm{D}}}{V_{1\mathrm{D}}} \frac{(R_1 + R_2)}{2R_1} - \frac{r}{R_1} \\ &= -\hat{r} + \frac{2\left(1 - \hat{R}_2^2\right)}{\left(1 - \hat{R}_2^2\right)^2 - 4\hat{R}_2^2 \ln^2\left(\hat{R}_2\right)} \left[\hat{R}_2^2 \ln\left(\hat{R}_2\right) \frac{1}{\hat{r}} + \left(\hat{R}_2^2 - 1\right) \hat{r} \ln(\hat{r}) - \hat{R}_2^2 \ln \hat{R}_2 \hat{r} \right] \end{aligned} \tag{5.50}$$

where the dimensionless variables $\hat{r}$ and $\hat{R}_2$ are used.

If the length of the liquid plug tends to infinity ($\hat{L} \to \infty$), the flow can be simplified to 1D. For the dimensionless plug lengths $\hat{L} = 100$, the 2D solution for different radius ratios at cross section **X-X** of the plug reduces to the 1D solution, as shown in Figure 5.3. The radial position is defined as $x \equiv (\hat{r} - \hat{R}_2)/(1 - \hat{R}_2)$. The velocity profile along this cross section is like the Couette flow with pressure gradient.

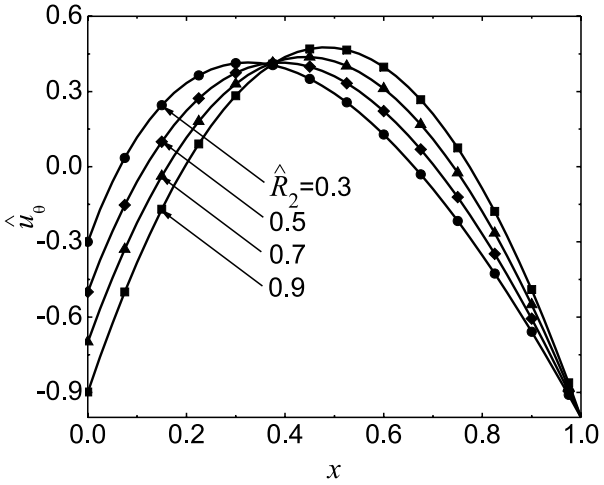

Figure 5.3: Validation of the 2D model by the 1D solution (lines: 1D solution; symbols: 2D solution).

5.3 Results and discussion

5.3.1 Comparison with experimental results

According to Eqs. (5.19)–(5.21), the streamlines and the velocity field in a typical plug is depicted in Figure 5.4, which give a clear picture of the overall flow pattern. The streamlines in Figure 5.4**a** shows the two vortices near the inner and outer walls. Figure 5.4**b** presents the dimensionless velocity field. The inner wall vortex **A** is recirculating in the anticlockwise direction (positive $\hat{\varphi}_A$), while the outer wall vortex **B** (negative $\hat{\varphi}_B$) is recirculating in the clockwise direction. Vortex **B** is larger than vortex **A** due to the curvature effect. One streamline **S-S** separates these two vortices such that $\hat{\varphi}_{\text{S-S}} = 0$ and no particle can cross this streamline by advection. Figure 5.4**c** is the μPIV velocity field measured by Fries et al. (2008). The dimensionless plug length $\hat{L} = 1.6$ in Figure 5.4**c** is calculated in pixels from

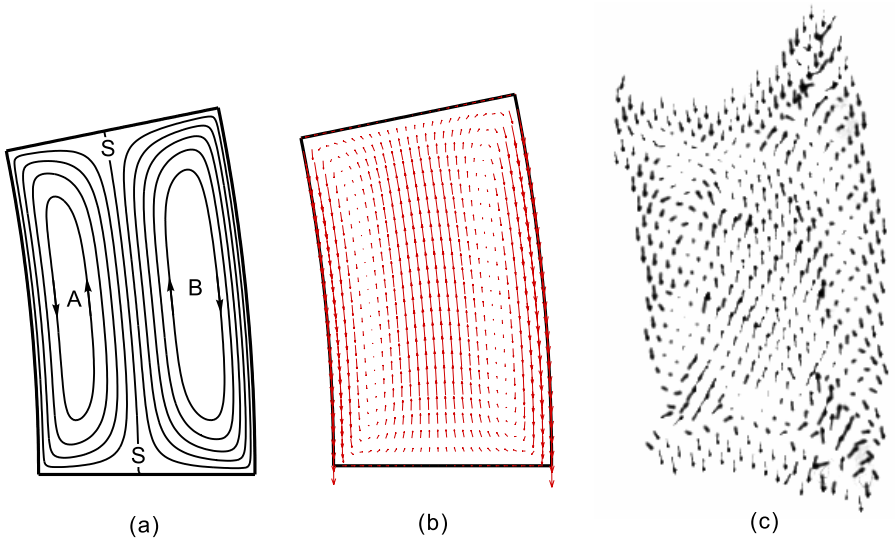

Figure 5.4: Velocity field in a plug with dimensionless plug length $\hat{L} = 1.6$ and radius ratio $\hat{R}_2$=0.8824, (a) Streamlines with the increment of dimensionless stream function $\Delta\hat{\varphi} = 0.002$, (b) Dimensionless velocity field, (c) Velocity field obtained from μPIV by Fries et al. (2008).

the image by a MATLAB program as

$$\hat{L} \equiv \frac{L_{\text{pixel}}}{w_{\text{pixel}}} = \frac{A_{\text{pixel}}}{w_{\text{pixel}}^2} \tag{5.51}$$

where L_{pixel}, w_{pixel} and A_{pixel} are the length, the width, and the area of the liquid plug in pixels, respectively. The two counter-rotating vortices in Figure 5.4**c** can be clearly observed. The comparison with the experimental results shows that the 2D model for microchannels with high aspect ratios captures the large part of the flow field, even though the μPIV measurement was carried out in a 3D microchannel with an aspect ratio of unity.

As plugs move through a straight microchannel, recirculating flow is generated due to the presence of the interfaces (as discussed in Chapter 4). The two vortices in the liquid plug are of equal size due to the symmetrical effect of the channel

walls. As the plug travels through a curved channel, the two halves of the plug experience unequal recirculating flows. One half of the plug is exposed to the inner arc of the curved channel, a shorter channel path, and thus a small recirculating flow is generated as compared to the outer half of the plug which is exposed to the outer arc with a longer channel path. Hence, the two vortices become asymmetrical.

5.3.2 Velocity profiles

5.3.2.1 Effect of curvature

In order to analyze the effect of the channel curvature on the flow profile along the cross section **X**-**X**, the dimensionless plug length is fixed at $\hat{L} = 1$ and the curvature of the channel is varied by changing $\hat{R}_2$. Figure 5.5**a** shows the velocity profile $\hat{u}_\theta$ along **X**-**X** for different curvatures. The maximum velocity increases with increasing $\hat{R}_2$. The velocity component $\hat{u}_\theta$ is nearly symmetric for $\hat{R}_2 = 0.9$ due to the low curvature of the microchannel, as shown in Figure 5.5**a**.

5.3.2.2 Effect of dimensionless plug length

To analyze the effect of the dimensionless plug length on the velocity profile, the radius ratio is kept at $\hat{R}_2 = 0.5$. Figure 5.5**b** presents $\hat{u}_\theta$ along the cross section **X**-**X** for different dimensionless plug lengths. The results clearly show that the dimensionless plug length influences the flow field. For long plugs ($\hat{L} = 2$ in Figure 5.5**b**), the velocity profile is consistence with results reported in Figure 5.3. For short plugs ($\hat{L} = 1/4$ in Figure 5.5**b**), there are two local maximum points of velocity, as vortices **A** and **B** move towards the inner wall and outer wall respectively, which will be explained in the following subsection.

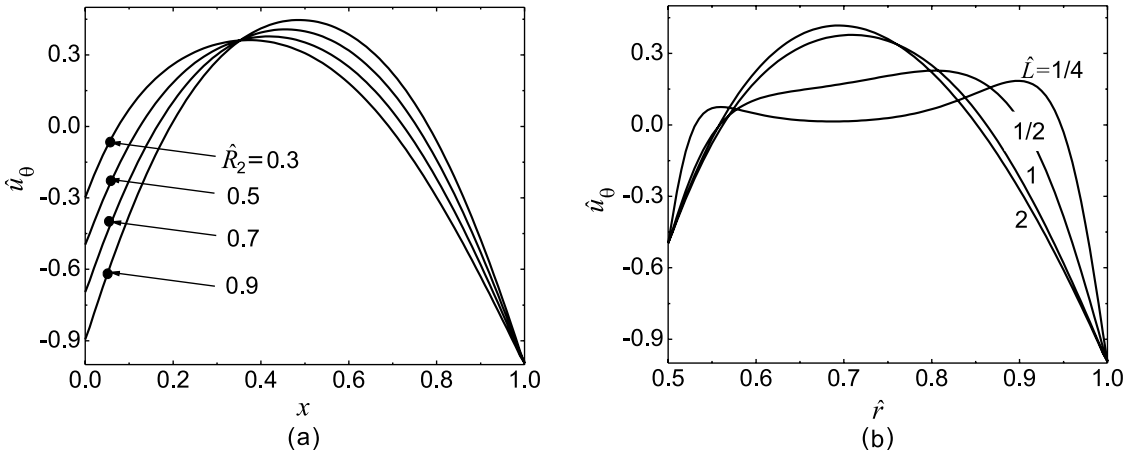

Figure 5.5: Dimensionless velocity component $\hat{u}_\theta$ at the cross section **X**-**X**, (a) for different radius ratios $\hat{R}_2$ (the dimensionless plug length is fixed at $\hat{L} = 1$), (b) for different dimensionless plug lengths $\hat{L}$ (the radius ratio is fixed at $\hat{R}_2 = 0.5$).

5.3.3 Vortex centres

As the stream function is symmetric with respect to the cross section **X**-**X**, the vortex centres are located along **X**-**X**. To quantify the effects of the plug lengths and the curvature, the radial position of the vortex centre in the r direction (x_A and x_B) versus $\hat{L}$ and $\hat{R}_2$ are shown in Figures 5.6**a** and **b**, while the corresponding dimensionless stream functions at the vortex centres ($\hat{\varphi}_{A,\max}$ and $\hat{\varphi}_{B,\min}$) are shown in Figures 5.6**a** and **b**, respectively.

5.3.3.1 Effect of curvature

The movement of the vortex centre location (x_A and x_B) versus the channel curvature (Figures 5.6**a** and **b**) shows that for a given plug length, the vortex centres x_A and x_B move towards the inner wall as the channel curvature increases (i.e., $\hat{R}_2$ decreases). When the channel curvature increases, $\hat{\varphi}_{B,\min}$ increases (Figure 5.6**d**),

and the outer vortex **B** increases in size and strength and compress the inner vortex **A**. Figure 5.6**c** shows that the magnitude of the dimensionless stream function $\hat{\varphi}_{A,\max}$ is small and the inner vortex **A** is relatively weak. This effect of increasing the curvature on the flow patterns can also be clearly observed in Figure 5.7. Figures 5.7 **a**–**f** illustrate the effect of channel curvature at different fixed dimensionless plug lengths $\hat{L} = 1/4$, $1/2$ and 1, respectively.

5.3.3.2 Effect of dimensionless plug length

Figures 5.6a and b show the movement of the vortex centre and the corresponding dimensionless stream functions with channel curvatures and dimensionless plug lengths. It is demonstrated that for a relative low channel curvature (large $\hat{R}_2$), the flow patterns depend on the dimensionless plug length as shown in Figures 5.7**a**, **c**, and **e**. Since the effect of the channel curvature is small, the vortices are nearly symmetrical about the streamline **S**-**S**. Initially, with increasing the plug length, both vortices **A** and **B** increase in size and strength. The vortex centres x_A and x_B move rapidly towards the streamline **S**-**S**, the magnitude of $\hat{\varphi}_{A,\max}$ and $\hat{\varphi}_{B,\min}$ both increase as vortices **A** and **B** expand. For relatively large dimensionless plug length ($\hat{L} > \hat{L}_{\text{long}}$) the vortex centres x_A and x_B becomes almost fixed in their locations. Here $\hat{L}_{\text{long}}$ refers to the dimensionless plug length where $\hat{u}_\theta$ along **X**-**X** approaches the fully developed velocity profile as shown in Figure 5.3. The unchanged velocity profiles make the locations of the vortex centres nearly constant.

For a relatively high channel curvature (small $\hat{R}_2$), the movement of the vortex centres strongly depends on the dimensionless plug length $\hat{L}$, as shown in Figures 5.7**b**, **d**, and **f**. Initially, with increasing $\hat{L}$, vortices **A** and **B** increase

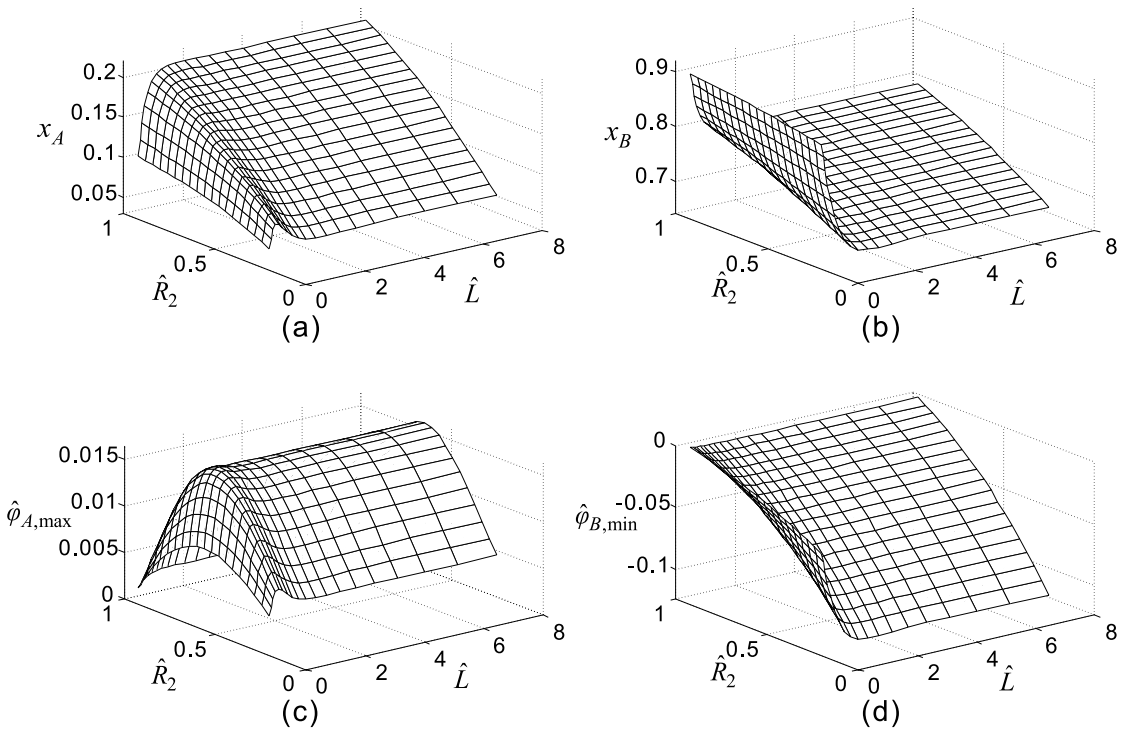

Figure 5.6: Vortex centres and stream functions versus the dimensionless plug length ($\hat{L}$) and the radius ratio ($\hat{R}_2$). (a) Location of vortex centre of vortex **A**; (b) Location of vortex centre of vortex **B**; (c) Stream function at the vortex centre of vortex **A**; (d) Stream function at the vortex centre of vortex **B**.

in size and strength, just like the plugs with low curvatures. The vortex centres x_A and x_B move rapidly towards the streamline **S-S**, and the magnitudes of $\hat{\varphi}_{A,\max}$ and $\hat{\varphi}_{B,\min}$ increase as vortices **A** and **B** expand. However, due to the channel curvature, vortex **B** expands faster than vortex **A**. If the plug length increase to a value beyond $\hat{L}_{\mathrm{m}}$, the vortices will develop to such an extent that the inner vortex **A** is compressed by the outer vortex **B**. Vortex centres x_A moves towards the inner wall while x_B move towards the streamline **S-S** as vortex **B** expands. For example, $\hat{L}_{\mathrm{m}}$ is 0.54 when $\hat{R}_2$ is fixed at 0.25. Similarly to the case of low channel curvatures, at relatively large dimensionless plug lengths ($\hat{L} > \hat{L}_{\mathrm{long}}$), the vortex centres x_A

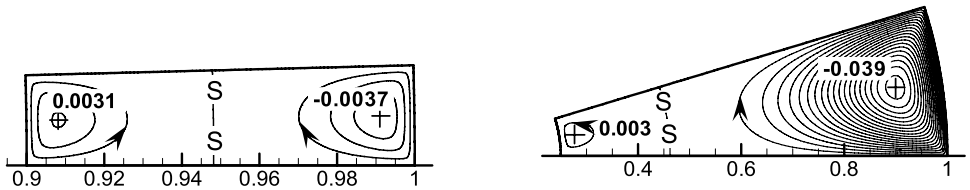

(a) $\hat{L}$= 1/4 , $\hat{R}_2$ = 0.9 , $\Delta\hat{\varphi}$ =0.001

(b) $\hat{L}$= 1/4 , $\hat{R}_2$ = 0.25 , $\Delta\hat{\varphi}$ = 0.002

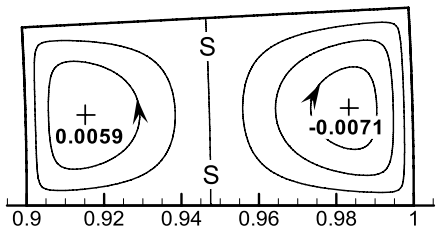

(c) $\hat{L}$= 1/2 , $\hat{R}_2$ = 0.9 , $\Delta\hat{\varphi}$ =0.002

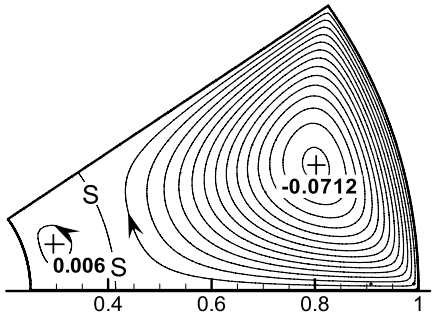

(d) $\hat{L}$ =1/2 , $\hat{R}_2$ = 0.25 , $\Delta\hat{\varphi}$ = 0.005

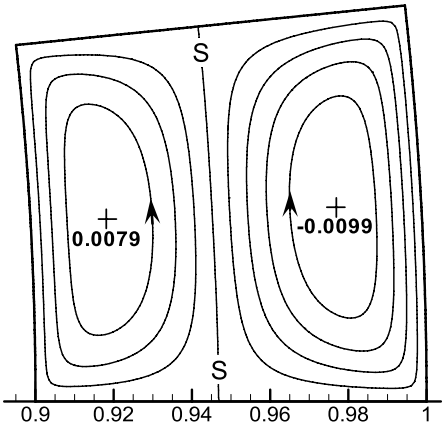

(e) $\hat{L}$ =1 , $\hat{R}_2$ = 0.9 , $\Delta\hat{\varphi}$ =0.002

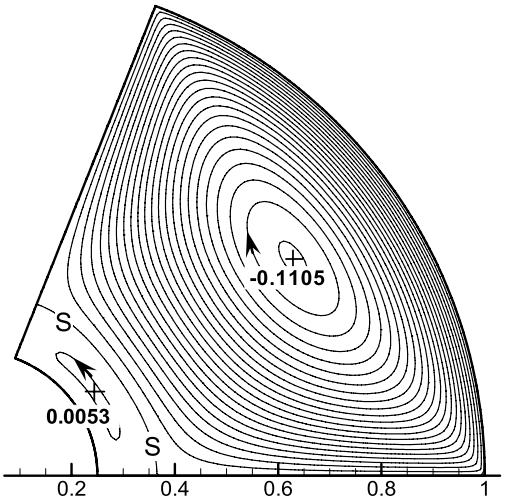

(f) $\hat{L}$ =1 , $\hat{R}_2$ = 0.25 , $\Delta\hat{\varphi}$ =0.005

Figure 5.7: Streamlines in plugs of different dimensionless plug lengths and different curvatures. The crosses and the corresponding values indicate the locations and the stream functions of the vortex centres, respectively. The arrows indicate the direction of recirculation.

and x_B becomes almost fixed in their locations.

5.3.4 Plug resistance coefficient

According to Eq. (5.44), the plug resistance coefficient C_f is influenced by the shear force and the surface tension. For the surface tension contribution, although there are many factors influencing the plug flow resistance C_f, the relationships between plug resistance coefficient C_f and the parameters, such as viscosity μ, plug speed V, contact angles θ_{adv} and θ_{rec}, surface tension σ, are explicitly expressed in the second term on the right hand side of Eq. (5.44). These parameters are different case by case for various fluids and various flow conditions, and they can be obtained through experimental measurements or from handbooks (De Gennes, 1985; Lide and Haynes, 2010). Hence, only the contribution of shear force to the plug resistant coefficient (the first term on the right hand side of Eq. (5.44) is discussed in the following analysis.

Figure 5.8 shows the variation of C_f as the dimensionless plug length $\hat{L}$ increases for different radius ratios. As $\hat{L}$ increases, C_f decreases dramatically, and approaches an asymptotic limit. This can be explained by the high velocity gradient at the end of the plug, which causes large flow resistance. Hence, short plugs experience large resistance coefficient. It is also shown that for small radius ratio $\hat{R}_2$, the large curvature causes high resistance of the plug flow.

For continuous laminar flow between two parallel plates, in the fully developed region, the resistance coefficient can be obtained using its parabolic velocity profile. The resistance coefficient is 24 by using the average velocity as the characteristic velocity (White, 2002). The plug resistance coefficients are always larger than 24. And this value is the asymptotic limit when $\hat{L} \to \infty$ and $\hat{R}_2 \to 1$, as shown in

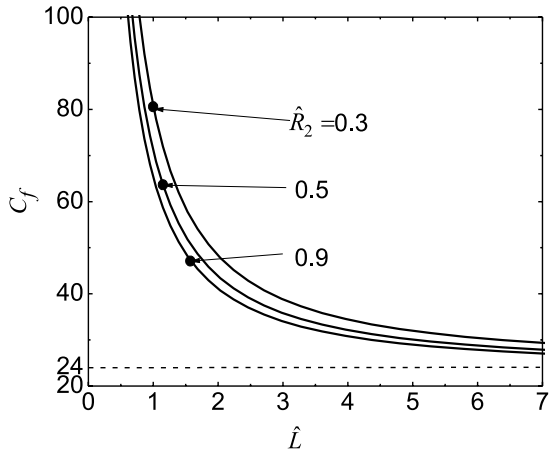

Figure 5.8: Plug resistance coefficient C_f decreases with increasing the dimensionless plug length $\hat{L}$ for different radius ratios $\hat{R}_2$.

Figure 5.8. For example, for $\hat{R}_2 = 0.9$ and $C_f = 24.24$ (that is 1% deviation from 24), the corresponding dimensionless plug length is $\hat{L} = 84.4$. In this condition, the plug behaves as if it is fully developed continuous flow between parallel plates. Therefore, when $\hat{R}_2 = 0.9$ and $\hat{L} < 84.4$, the idealization of a long plug in a curved channel as fully developed continuous flow between parallel plates cannot provide an accurate prediction of the pressure loss.

5.4 Summary

This chapter analytically investigates plug flow in curved microchannels. The finite Fourier transform method is used to solve the governing equation and get the series solution of the stream function. The plug resistance coefficient is derived from the moment balance of the plug. The results show that for plugs moving in curved microchannels, the vortex centres move towards the inner wall as the channel

curvature increases. The plug flow resistance is analyzed and the results show that the plug flow resistance coefficient decreases with increasing the dimensionless plug length and with decreasing the microchannel curvature. The flow resistance coefficient tends to the asymptotic value of 24 as the dimensionless plug length tends to infinity and the radius ratio approaches unity.

Chapter 6

Plug Train Flow in Two-Dimensional Microchannels [†]

6.1 Introduction

In Chapters 3–5, models are built for plug units separated by an immiscible phase with a negligible viscosity, such as a gas. A general case is that the immiscible phase separating the plugs is another liquid whose viscosity is not negligible. The two immiscible plug units with different liquids form *plug trains* which appears periodically in the microchannel, as shown in Figure 6.1**a**. A more general case is a series of consecutive plugs with N different properties, such as different in length, viscosity, density, or chemical content. Any two consecutive plugs are immiscible to each other. Here, *plug train* refers to a series of N consecutive different plugs which repeat periodically in microchannels, as shown in Figure 6.1**b**.

In this chapter, a simplified 2D theoretical model for plug trains in microchannels is presented. This model is then used to analyse chaotic mixing in

[†]This work has been published in *Physical Review E 84, 066309.*

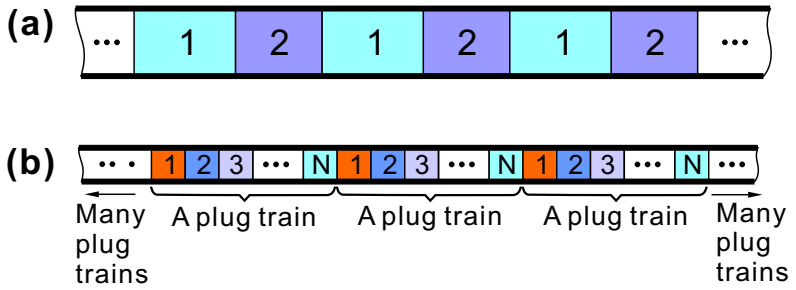

Figure 6.1: Schematic diagrams of plug trains in microchannels. (a) Plugs of two immiscible liquids formed in microchannels. (b) A *plug train* refers to a series of N consecutive different plugs which repeat periodically.

plugs in meandering microchannels. The chaotic mixing process is investigated using the particle tracking method. The proposed model shows two advantages over the numerical methods for particle tracking analysis. First, the computation time for obtaining the flow field is significantly reduced. Therefore, the particle tracking simulation, which requires a large amount of tracer particles and a long computation time, can be performed more easily with the flow field from the model. Second, the model can provide velocities in the whole flow domain, while numerical methods can only provide information at a set of discrete points. Hence, particle tracking simulation can be performed directly on the flow field from the model, and interpolation error is avoided. This model complements the numerical work reported in the literature by providing a simple and efficient way to analyze chaotic mixing in plugs with a broad survey of the parameter space.

This chapter is organized as follows. In Section 6.2, the theoretical model is presented and then validated against experimental results. The particle tracking method for analyzing and evaluating the mixing process is presented in Section 6.3. In Section 6.4, the mechanisms to enhance mixing are elaborated, and the

parameters, such as the curvature of the microchannel, the Peclet number, the length of the plug, and the viscosities of the fluids, are investigated.

6.2 Mathematical modelling of the flow field

6.2.1 Mathematical modelling of the flow in plug trains

To model the flow field mathematically, a Cartesian coordinate system (CS) is built on each of the N plugs, as shown in Figure 6.2. For Plug-i ($1 \leq i \leq N$), the coordinate system CS-i (x_i, y_i) is built with the origin O_i at the centre of Plug-i. Therefore, Plug-i takes the region of $-L_i \leq x_i \leq L_i$, $-h \leq y_i \leq h$, and $2h$ denotes the width of the microchannel, and $2L_i$ denotes the length of Plug-i. All coordinate systems CS-i ($i = 1 \cdots N$) are translating towards the right side at the speed of the plug V. Consequently, the N plug units are stationary with respect to their own translating coordinate systems. The transformation between any two coordinate systems CS-i and CS-j is

$$x_j = x_i + L_i + L_j + 2\sum_{k=i+1}^{j-1} L_k \tag{6.1}$$

$$y_i = y_j \tag{6.2}$$

where $0 \leq i < j \leq N$.

Due to the small dimension of the microchannel, the gravitational force is negligible. The fluid is assumed to be incompressible Newtonian fluid. Due to the low Reynolds number, the flow can be simplified to the Stokes flow. The governing equation for Plug-i is biharmonic (Happel and Brenner, 1983; Meleshko, 2003;

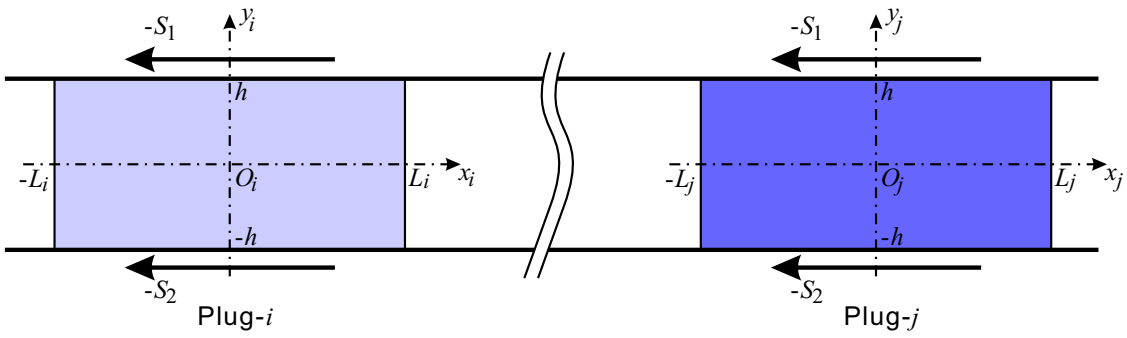

Figure 6.2: Cartesian coordinate systems for a plug train moving in a microchannel.

Shankar, 2007):

$$\left(\frac{\partial^4}{\partial {x_i}^4} + 2\frac{\partial^4}{\partial {x_i}^2 \partial {y_i}^2} + \frac{\partial^4}{\partial {y_i}^4}\right)\varphi_i = 0 \tag{6.3}$$

where φ_i is the stream function in Plug-i $(1 \leq i \leq N)$ which satisfies

$$u_{x,i} \equiv \frac{\partial \varphi_i}{\partial y_i}, \quad u_{y,i} \equiv= -\frac{\partial \varphi_i}{\partial x_i} \tag{6.4}$$

By incorporating the boundary conditions, Eq. (6.3) can be solved and the series solution of the velocity field can be obtained in a dimensionless form as follows:

$$\begin{aligned}\hat{u}_{x,i} = &\sum_{m=1}^{\infty}\left[{p_m^o}'\left(\hat{y}_i\right) + {p_m^e}'\left(\hat{y}_i\right)\right]\frac{(-1)^m}{\alpha_m}X_m\cos\left(\alpha_m\hat{x}_i\right) \\ &+\hat{L}_i\sum_{l=1}^{\infty}(-1)^l\left[q_l^e\left(\hat{x}_i\right)Y_l^e + q_l^o\left(\hat{x}_i\right)Y_l^o\right]\cos\left(\beta_l\hat{y}_i\right)\end{aligned} \tag{6.5}$$

$$\begin{aligned}\hat{u}_{y,i} = &\sum_{m=1}^{\infty}\left[p_m^o\left(\hat{y}_i\right)X_m^o + p_m^e\left(\hat{y}_i\right)X_m^e\right](-1)^m\sin\left(\alpha_m\hat{x}_i\right) \\ &-\hat{L}_i\sum_{l=1}^{\infty}\frac{(-1)^l}{\beta_l}\left[q_l^{e\prime}\left(\hat{x}_i\right)Y_l^e + q_l^{o\prime}\left(\hat{x}_i\right)Y_l^o\right]\sin\left(\beta_l\hat{y}_i\right)\end{aligned} \tag{6.6}$$

where $\hat{L}_i \equiv L_i/h_i$ is the dimensionless plug length. The details for obtaining the solution are provided in Appendix E.

6.2.2 Comparison with experimental results

To validate the 2D model, comparison has been made with the experimental velocity field reported by Günther et al. (2005), as shown in Figure 6.3. The fluids used in the experiment are air and ethanol. The viscosities are, respectively, $\mu_{\text{air}} = 1.827 \times 10^{-5}$ Pa·s and $\mu_{\text{ethanol}} = 1.07 \times 10^{-3}$ Pa·s. The velocity field in the ethanol plug was measured using μPIV. The dimensionless plug length $\hat{L} = 1.57$ is estimated in pixels from Figure 6.3**b** using a MATLAB program as

$$\hat{L} \equiv \frac{L_{\text{pixel}}}{w_{\text{pixel}}} = \frac{A_{\text{pixel}}}{w_{\text{pixel}}^2} \tag{6.7}$$

where L_{pixel}, w_{pixel}, and A_{pixel} are the length, the width, and the area of the ethanol plug in pixels, respectively. The agreement with the experimental results indicates that the 2D model is capable of capturing the main flow features in the plug. The streamline in the plug is shown in Figure 6.3**g**. The pair of vortices can be clearly observed. The upper vortex **A** is circulating in the anticlockwise direction with positive stream function $\hat{\varphi}_A$, while the lower vortex **B** in the clockwise direction with negative stream function $\hat{\varphi}_B$. A streamline **S-S** separates these two vortices with $\hat{\varphi}_{\text{S-S}} = 0$.

6.2.3 Plug trains moving in meandering microchannels

Figure 6.4**a** shows plug flow in a 2D meandering microchannel with two immiscible phases. A *period* of the meandering microchannel refers to a section of channel with two semicircles. The curvature of the microchannel is represented by the radius ratio of the inner wall and outer wall $\hat{R} \equiv R_i/R_o$, where R_i and R_o are, respectively, the radii of the inner wall and outer wall towards the centre of the

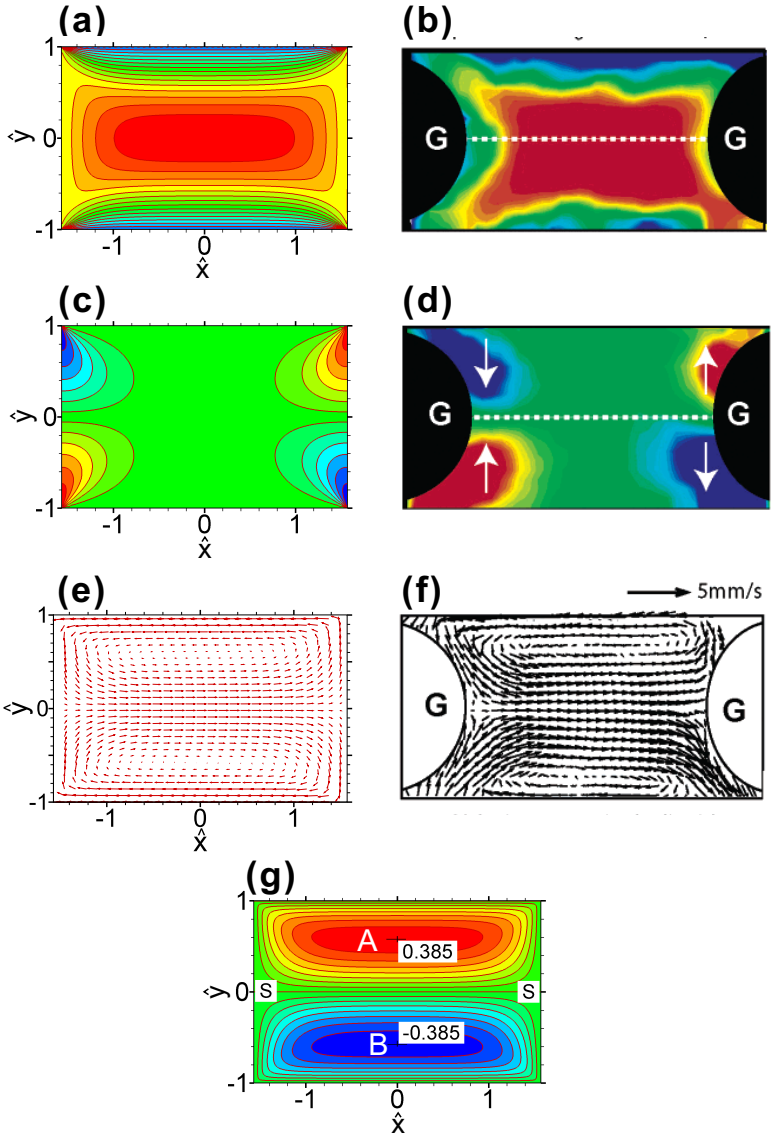

Figure 6.3: Flow field in an ethanol plug of an ethanol/air plug train moving in a microchannel with $\hat{L}$ =1.57: (a) $\hat{u}_x$ from the 2D model; (b) u_x from μPIV (Günther et al., 2005); (c) $\hat{u}_y$ from the 2D model; (d) u_y from μPIV (Günther et al., 2005); (e) Dimensionless velocity vectors from the 2D model; (f) Velocity vectors from μPIV (Günther et al., 2005); (g) Contours of dimensionless stream function $\hat{\varphi}$ from the 2D model with the increment between two successive streamlines $\Delta\hat{\varphi} = 0.05$. The crosses and the corresponding values are the locations and the magnitudes of the maximum/minimum of the dimensionless stream function.

channel path. A smaller value of $\hat{R}$ indicates a larger curvature, and vice versa, as shown in Figure 6.4**b**. When a plug is moving in a microchannel, a pair of vortices is formed in the plug due to the presence of the interfaces (Handique and Burns, 2001). In a frame of reference moving together with the plug, the plug experiences different sliding velocities on each wall, which are proportional to the radius towards the centre of the channel path (see Chapter 5 for details). The inner wall has a lower sliding velocity ωR_i, while the outer wall has a higher sliding velocity ωR_o, where ω is the angular speed of the plug with the centre point of the channel path. Therefore, the vortex near the inner wall is smaller, while the one near the outer wall is larger.

As the plug moves at different stages of the meandering microchannel, the vortex pattern varies with the change of the channel curvature. When the plug is moving in the first semicircle (Stage I), the vortex near the top wall is larger, while the vortex near the bottom wall is smaller. As the plug moves into the second semicircle (Stage II), the two vortices exchange in size, as shown in Figure 6.4**b**. The plugs at different stages of the meandering microchannel can be simplified to rectangular shapes, and the sliding velocities due to the channel curvature are applied on the top and bottom walls of the rectangular plugs, as shown in Figure 6.4**c**. This method to simplify the flow was used by Blanchette (2009). The sliding velocities of the top and bottom walls are denoted $-S_1(t)$ and $-S_2(t)$, respectively. At Stage I, $S_1 = \omega R_o$ and $S_2 = \omega R_i$, while at Stage II, $S_1 = \omega R_i$ and $S_2 = \omega R_o$. The speed of the plugs is $V = [S_1(t) + S_2(t)]/2$, which remains constant over time.

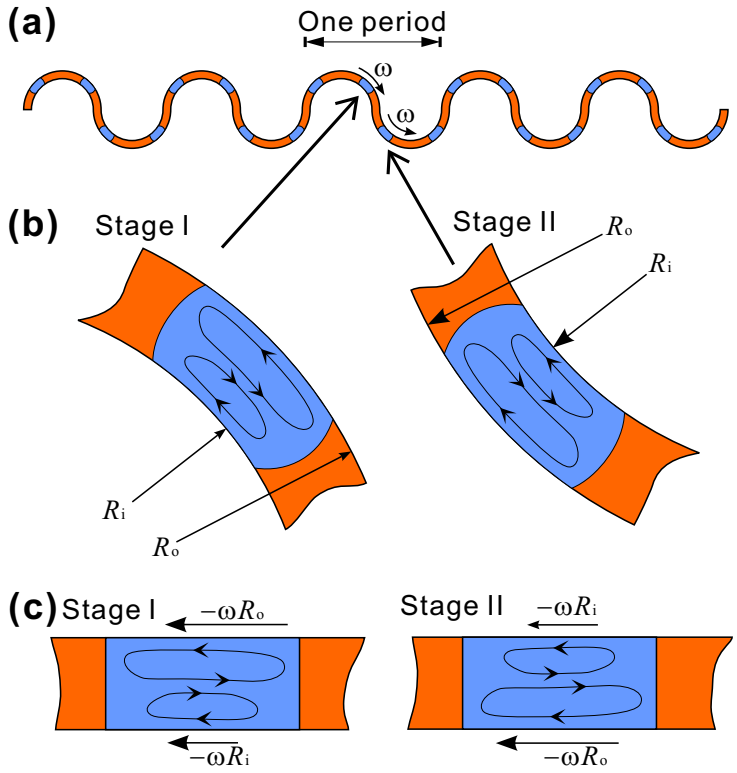

Figure 6.4: Schematic diagram of plugs moving in a meandering microchannel. (a) Plugs moving in a meandering microchannel. (b) Flow patterns in plugs at different stages of the meandering microchannel. Vortices of different sizes are formed near the wall of the microchannel. The vortex near the inner wall (with radius R_i) is smaller, while the vortex near the outer wall (with radius R_o) is larger. (c) Simplified rectangular shaped plugs with sliding walls in a frame of reference moving with the plugs. At Stage I, as shown on the left, the sliding velocities on the top and bottom walls are, respectively, $-\omega R_i$ and $-\omega R_o$. When the plug arrives at a location with a different curvature (Stage II), the sliding velocities on the top and bottom walls exchange.

6.3 Simulation of mixing by the particle tracking method

6.3.1 Convection-diffusion equation

The convection-diffusion equation that governs the transfer of species in the plug is

$$\frac{\partial C}{\partial t} + u_x \frac{\partial C}{\partial x} + u_y \frac{\partial C}{\partial y} = D\left(\frac{\partial^2 C}{\partial x^2} + \frac{\partial^2 C}{\partial y^2}\right) \tag{6.8}$$

where D is the diffusivity of the species in the liquid plug. The above equation can be nondimensionalised by introducing the following dimensionless group,

$$\hat{x} \equiv x/h, \quad \hat{y} \equiv y/h, \quad \hat{t} \equiv \frac{tV}{h}, \quad \hat{u}_x \equiv \frac{u_x}{V}, \quad \hat{u}_y \equiv \frac{u_y}{V}, \quad Pe_D \equiv \frac{hV}{D} \tag{6.9}$$

where Pe_D is the Peclet number. We can obtain that

$$\frac{\partial C}{\partial \hat{t}} + \hat{u}_x \frac{\partial C}{\partial \hat{x}} + \hat{u}_y \frac{\partial C}{\partial \hat{y}} = \frac{1}{Pe_D}\left(\frac{\partial^2 C}{\partial \hat{x}^2} + \frac{\partial^2 C}{\partial \hat{y}^2}\right) \tag{6.10}$$

Therefore, particle tracking simulation is performed in a dimensionless scale and the Peclet number is used to consider the relative effect between convection and diffusion. At the boundaries of the plug, no chemical reaction is assumed, and the adjacent plug and the wall are impermeable to the species. Therefore, we can obtain the boundary conditions of the mixing process in the plug,

$$\frac{\partial C}{\partial \hat{x}} = 0 \quad \text{at} \quad \hat{x} = \pm\hat{L} \tag{6.11}$$

$$\frac{\partial C}{\partial \hat{y}} = 0 \quad \text{at} \quad \hat{y} = \pm 1 \tag{6.12}$$

6.3.2 Advection by the flow

Evaluation of the performance of the mixing process uses the particle tracking method, which places passive and non-interacting particles in the flow fields to observe the advection and diffusion of these particles and to visualize the mixing effect. The tracer particles are advected by the flow in a dimensionless form as follows:

$$\frac{d\hat{x}\left(\hat{t}\right)}{d\hat{t}} = \hat{u}_x\left(\hat{t}\right), \quad \frac{d\hat{y}\left(\hat{t}\right)}{d\hat{t}} = \hat{u}_y\left(\hat{t}\right) \tag{6.13}$$

The above equations were integrated using the fourth-order Runge-Kutte (RK) method. Different time steps were repeatedly refined until passive particles faithfully followed the streamline in the plug. The dimensionless time step used in the simulation was $\Delta\hat{t} = 10^{-3}$.

Integrating Eq. (6.13) requires information on velocity at any spatial location ($-\hat{L} \leq \hat{x} \leq \hat{L}$, $-1 \leq \hat{y} \leq 1$). The series expression of the flow field in Eqs. (6.5) and (6.6) shows an advantage of the model because it offers the solution at any point in the domain, rather than the solution at a set of discrete grid points.

6.3.3 Diffusion by random walk

The diffusion of the passive particles is simulated using the random walk method (Muradoglu et al., 2007).

$$x_k = x_k^* + \zeta_{x,k}\sqrt{2D\Delta t}, \quad y_k = y_k^* + \zeta_{y,k}\sqrt{2D\Delta t} \tag{6.14}$$

where (x_k^*, y_k^*) is the location of the Particle-k after the advection time step, and $\zeta_{x,k}$ and $\zeta_{y,k}$ are two independent random numbers with normal distribution for Particle-

k at the current time step. After nondimensionalisation, Eq. (6.14) becomes

$$\hat{x}_k = \hat{x}_k^* + \zeta_{x,k}\sqrt{\frac{2\Delta\hat{t}}{Pe_D}}, \quad \hat{y}_k = \hat{y}_k^* + \zeta_{y,k}\sqrt{\frac{2\Delta\hat{t}}{Pe_D}} \tag{6.15}$$

The tracer particle may go out of the plug domain due to the random walk by diffusion or integration error by advection. The particles crossing the boundary are mirror-reflected back to the plug (Muradoglu et al., 2007). This corresponds to the impermeable boundary condition in Eqs. (6.11)–(6.12).

6.3.4 Evaluation of mixing

The mixing process is characterized and evaluated by the mixing index, η (Funakoshi, 2008). To calculate the mixing index at an instant t, the plug domain is divided into M equal-size bins. The standard deviation of particle numbers in the bins is then calculated as follows,

$$\sigma(t) = \sqrt{\frac{1}{M}\sum_{j=1}^{M}\left[c_j(t) - \bar{c}\right]^2} \tag{6.16}$$

where M is the number of bins $M = 40 \times 20$ in the simulation), and $c_j(t)$ is the number of particles in Bin-j at time t, and $\bar{c}$ is the average number of particles per bin in the ideal-mixed case,

$$\bar{c} = \frac{NP}{M} \tag{6.17}$$

where NP is the total number of particles used for particle tracking ($NP = 20000$ in the simulation). During the mixing process, the standard deviation σ_0 is initially large, then decreases gradually. Ideally, $\sigma(t)$ finally approaches 0 when the fluid particles are homogeneously dispersed in the whole domain. In the simulation, when the particles achieves complete spatial randomness, $\sigma(t)$ approaches an asymptotic limit depending on NP and M (Phelps and Tucker III, 2006). The

mixing index η is the standard deviation normalized by the initial standard deviation σ_0, which is the most segregated case:

$$\eta = \frac{\sigma\left(t\right)}{\sigma_0} \tag{6.18}$$

In addition, when the tracer particles achieve the complete spatial randomness, the asymptotic limit of the mixing index is $\eta_{\text{asymp}} = 1/\sqrt{NP}$ (Phelps and Tucker III, 2006). In this investigation, $NP = 20000$, therefore, $\eta = 0.00707$ indicates the homogeneous state with randomly distributed particles. As the mixing progresses, η varies from unity to 0.00707.

6.3.5 Particle tracking algorithm

The algorithm for the particle tracking method with the random walk method is summarized as follows:

(1) Initialize the locations of the particles, i.e. ($\hat{x}_k$, $\hat{y}_k$).

(2) Determine the velocity of each particle from Eqs. (6.5) and (6.6), i.e. ($\hat{u}_{x,k}$, $\hat{u}_{y,k}$).

(3) Integrate Eq. (6.13) to get the location of the particle after advection, i.e. ($\hat{x}_k^*$, $\hat{y}_k^*$).

(4) Determine the location of the particle after random walk using Eq. (6.15) , i.e. ($\hat{x}_k$, $\hat{y}_k$).

(5) Check whether any particle goes out of the plug. For a particle out of the plug, reflect it back to the plug with mirror reflection.

(6) Calculate the mixing index η using Eq. (6.18).

Steps 2-6 are repeated until the plug goes out of the microchannel.

6.4 Results and discussion

6.4.1 The mechanisms of plug mixing in a meandering microchannel

In the following analysis, the results are limited to mixing within the first plug of a plug train with two plugs, i.e., $N = 2$. For plug trains with more plugs ($N > 2$), simulation can be carried out similarly by replacing the flow field with that in the corresponding plug.

When a liquid plug moves in a meandering microchannel, three effects on the mixing–stretching, folding, and diffusion–interplay as the mixing progresses. They are illustrated in Figure 6.5 and explained as follows.

6.4.1.1 Stretching of fluid filaments by the vortices

The effect of stretching of liquid filaments by the vortices is shown in Figure 6.5**a**. Initially, all the tracer particles ($NP = 20000$) are evenly placed in a statistical bin ($0.3 < x < 0.4$, $0.3 < y < 0.4$). As the liquid plug is moving forwards, the particle blob is stretched by the recirculating flow, as shown in Figure 6.5**a** from $\hat{t} = 0$ to $\hat{t} = 8$. The stretching increases the contact area of the tracer particles with the surrounding fluid. A velocity gradient is necessary to stretch the liquid filaments. During advection, a larger velocity gradient is preferred because it results in two adjacent tracer particles departing rapidly from each other.

6.4.1.2 Folding of fluid filaments by changing channel curvature

The flow within the plug is dominated by a pair of counter-rotating vortices. In a straight channel, the tracer particles faithfully follow the streamlines of their own vortex, and diffusion is the only mechanism that can transfer the tracer particle across different vortices. In contrast, for a meandering microchannel, once the direction of the channel curvature changes, the sizes of the two vortices exchange. Consequently, some tracer particles that originally follow one vortex may follow the other vortex. Therefore, the exchange of the vortex pattern can greatly enhance the transfer of particles across vortices by flow advection and, thereafter, facilitate the mixing process in the liquid plug. The folding effect, together with the stretching effect, produces entangled long liquid filaments in the plug, as shown in Figure 6.5**b**.

Poincaré section is a tool to reveal the chaotic nature of mixers (Aref, 1984; Ottino, 1989). To study the combination of stretching and folding of liquid filaments, a Poincaré section for plug flow in a meandering microchannel with $\hat{R} = 0.7$ was constructed as shown in Figure 6.5**c**. This Poincaré section was generated by releasing 20 tracer particles into the flow and recording their positions after each period of the meandering microchannel. The flow can advect the fluid particles throughout the plug. Therefore, the meandering microchannel can result in chaotic behaviour of the fluid particles upon exchange of the sizes of the two vortices in plugs.

6.4.1.3 Diffusion

The effect of diffusion on mixing is shown in Figure 6.5**d**. Diffusion has the effect of reducing the concentration gradient. The combining effect of stretching and

folding can effectively create entangled liquid filaments, as shown in Figure 6.5**b**. Diffusion, at the same time, blurs the interface of the liquid filaments with the surrounding fluid.

6.4.1.4 A typical result

With the effects of stretching, folding, and diffusion, the mixing process in a typical liquid plug is shown in Figure 6.6. Initially, all the tracer particles ($NP = 20000$) are evenly placed in a bin ($0.3 < x < 0.4$, $0.3 < y < 0.4$). The particles are advected by the vortices, and stretched into a long thin filament. When the plug enters the next stage, the fluid filament of tracer particles follows the new streamlines. Therefore, exchange of the vortex pattern entangles the fluid filament of tracer particles. At the same time, diffusion can effectively blur the interface between the tracer particles and the surrounding fluid. In this way, as the time passes as shown in Figure 6.6, a group of tracer particles initially located in a bin ($\hat{t} = 0$), first expands to take the top half of the plug ($\hat{t} = 50$), gradually transfers to the bottom half of the plug ($\hat{t} = 100$), then disperses throughout the plug ($\hat{t} = 200$), and, finally, achieves a homogeneous state with randomly distributed particles.

6.4.2 Effect of curvature

In a straight microchannel, the two counter-rotating vortices in a plug are of equal size. If the microchannel is curved, the two vortices become asymmetric. The size difference between the two vortices increases with an increase in the curvature, as shown in Figure 6.7**b**. Therefore, with a larger curvature (such as $\hat{R} = 0.5$) the folding effect is applied to more liquid filaments at the location where the curvature

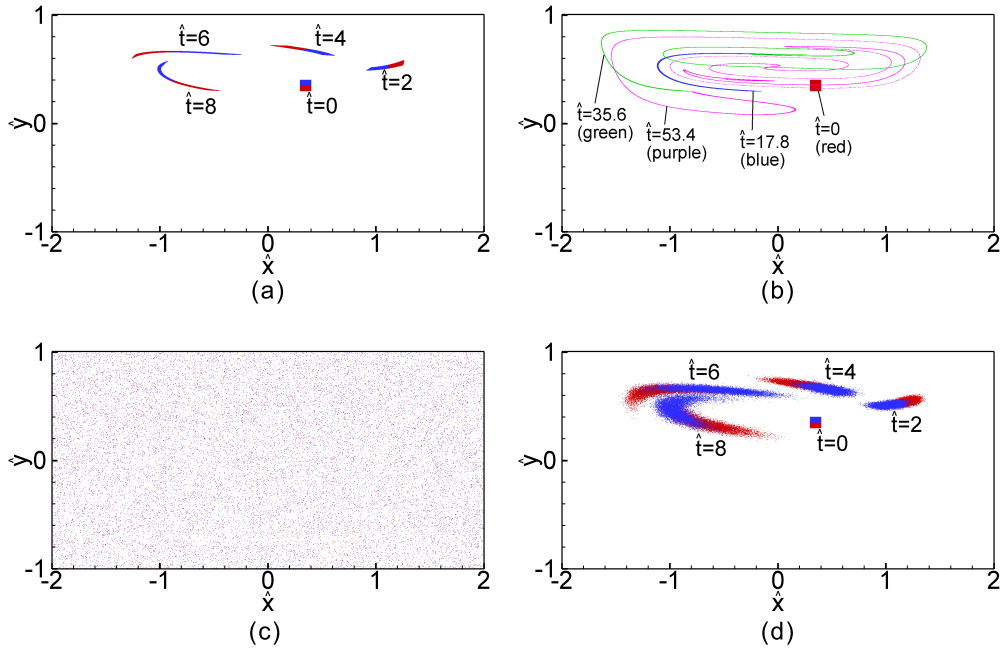

Figure 6.5: Mechanisms to enhance mixing in a plug moving in meandering microchannels: stretching of liquid filaments by vortices, folding of liquid filaments by changing channel curvature, and diffusion. The dimensionless plug length is $\hat{L} = 2$, the radius ratio of the microchannel is $\hat{R} = 0.7$, and the viscosity ratio is $\mu_1/\mu_2 = 1$. (a) Stretching of liquid filaments in a liquid plug as it is moving in a microchannel. (b) Folding of liquid filaments by alternation of the direction of the channel curvature. The scattering of tracing particles at different time illustrates the folding effect. The dimensionless time are, respectively: Red: $\hat{t} = 0$; Blue: $\hat{t} = 17.8$; Green: $\hat{t} = 35.6$; Purple: $\hat{t} = 53.4$. The corresponding locations of the plug in the meandering microchannel are 0, 0.5, 1, 1.5, and 2 periods, respectively. (c) Poincaré section for a plug flowing in a meandering microchannel (for 1000 periods with 20 particles). This Poincaré section was generated by releasing the tracer particles into the flow and recording their positions after each period of the meandering microchannel. (d) Scattering of tracer particles by the diffusion effect, which accelerates the mixing process. The Peclet number is $Pe_D = 10^4$.

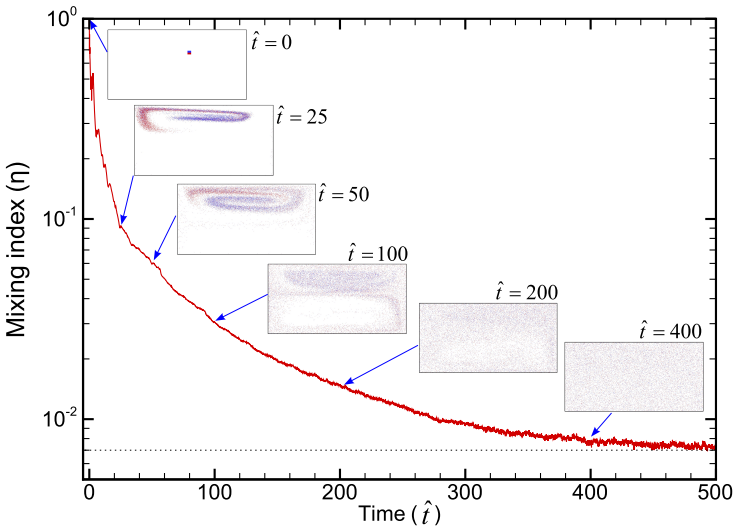

Figure 6.6: Mixing process in a typical liquid plug under the effects of stretching, folding, and diffusion. The dashed horizontal line $\eta_{\text{asymp}} = 0.00707$ indicates the homogeneous state with randomly distributed particles. The radius ratio of the microchannel is $\hat{R} = 0.7$, the Peclet number is $Pe_D = 10^4$, the viscosity ratio is $\mu_1/\mu_2 = 1$, and the dimensionless plug length is $\hat{L} = 2$.

direction changes. Consequently, a larger curvature produces rapid mixing in the plug, while a smaller curvature (such as $\hat{R} = 0.9$) results in slow mixing, as shown in Figure 6.7**a**. The corresponding mixing patterns at the instant $\hat{t} = 100$ are shown in Figure 6.7**c**. With a large curvature ($\hat{R} = 0.5$), a homogeneous state of randomly distributed particles is almost achieved at $\hat{t} = 100$. In contrast, the tracer particles only occupy the top-half of the plug at a small curvature ($\hat{R} = 0.9$). These results show that a larger curvature is preferred for rapid plug mixing in meandering microchannels.

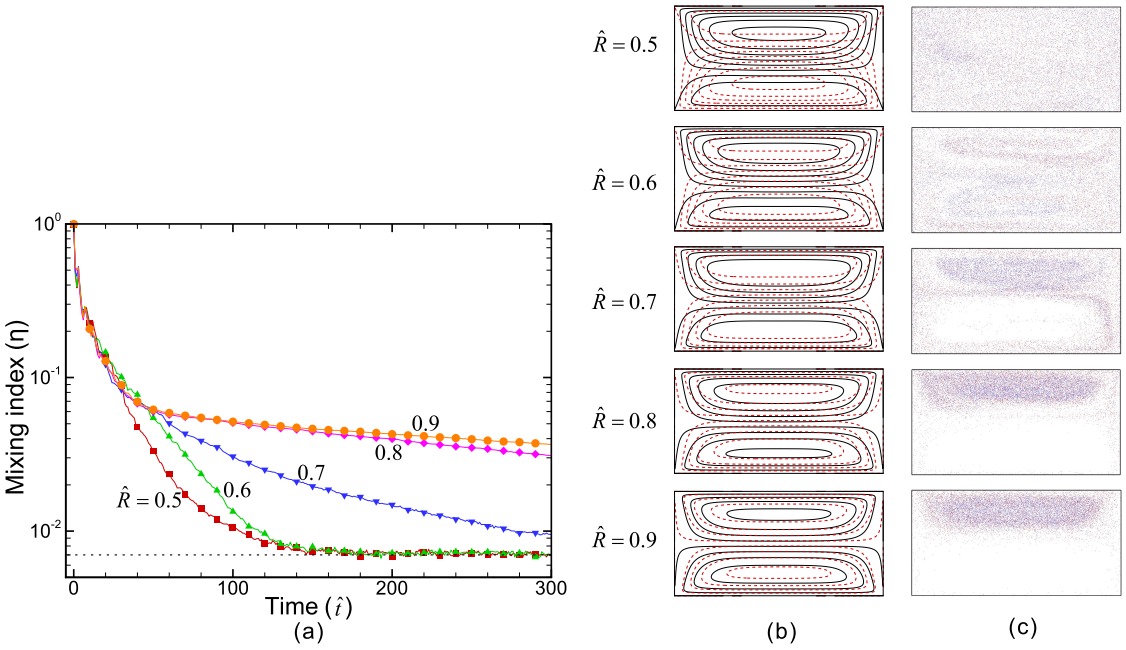

Figure 6.7: Effect of the curvature on the mixing process in plugs. The Peclet number is $Pe_D = 10^4$, the viscosity ratio is $\mu_1/\mu_2 = 1$, and the dimensionless plug length is $\hat{L} = 2$. (a) Variation of mixing indices with time for microchannels of different curvatures. The dashed horizontal line $\eta_{\text{asymp}} = 0.00707$ indicates the homogeneous state with randomly distributed particles. (b) Flow pattern in plugs moving in meandering microchannels with different curvatures. The solid contours indicate the streamlines at Stage I (Figure 6.4**b**), while the dashed contours indicate the streamlines at Stage II (Figure 6.4**b**). (c) Visualization of mixing patterns at $\hat{t} = 100$ for microchannels with different curvatures.

6.4.3 Effect of Peclet number

The effect of the Peclet number on the mixing process is shown in Figure 6.8. At a high Peclet number, the mixing process is dominated by advection. As the Peclet number decreases, the relative effect of diffusion increases. The diffusion can effectively smear the interface between liquid filaments of different species.

The diffusion effect increases with increasing Pe_D. Therefore, at a high Peclet number, such as $Pe_D = \infty$ in Figure 6.8, the mixing is slow. In addition, the mixing index fluctuates when a large amount of tracer particles moves together from one statistical bin to another. At a low Peclet number, such as $Pe_D = 10^2$, mixing is rapid due to the strong effect of diffusion. Because diffusion can smear the interface between the region of tracer particles and the surrounding area, the fluctuation of mixing index is insignificant, as shown in Figure 6.8**a**. To show the variation of the mixing indices with the change of the Peclet number, the particle distributions at $\hat{t} = 100$ are plotted and compared them in Figure 6.8**b**. At a low Peclet number ($Pe_D = 10^2$), a homogeneous state of randomly distributed particles is achieved at $\hat{t} = 100$. In contrast, at a high Peclet number ($Pe_D = \infty$), the tracer particles are stretched into thin filaments, and are mainly distributed in the top-half of the plug. Therefore, a low Peclet number is preferred for rapid plug mixing in meandering microchannels.

6.4.4 Effect of viscosity

The mixing indices are plotted against time for different viscosity ratios in Figure 6.9**a**. To show the variation of the mixing indices as the viscosity ratio changes, the mixing indices were probed and compared at $\hat{t} = 100$ in the inset in Figure 6.9**a**. The flow streamlines in plugs are plotted in Figure 6.9**b**, and the distribution of tracer particles at $\hat{t} = 100$ is shown in Figure 6.9**c**. At a high viscosity ratio ($\mu_1/\mu_2 = 100$), the mixing index at $\hat{t} = 100$ is $\eta_{\hat{t}=100} = 0.0355$. If the viscosity ratio decreases, the mixing index also decreases, such as $\mu_1/\mu_2 = 1$, which indicates rapid mixing in the plug. If the viscosity ratio decreases further,

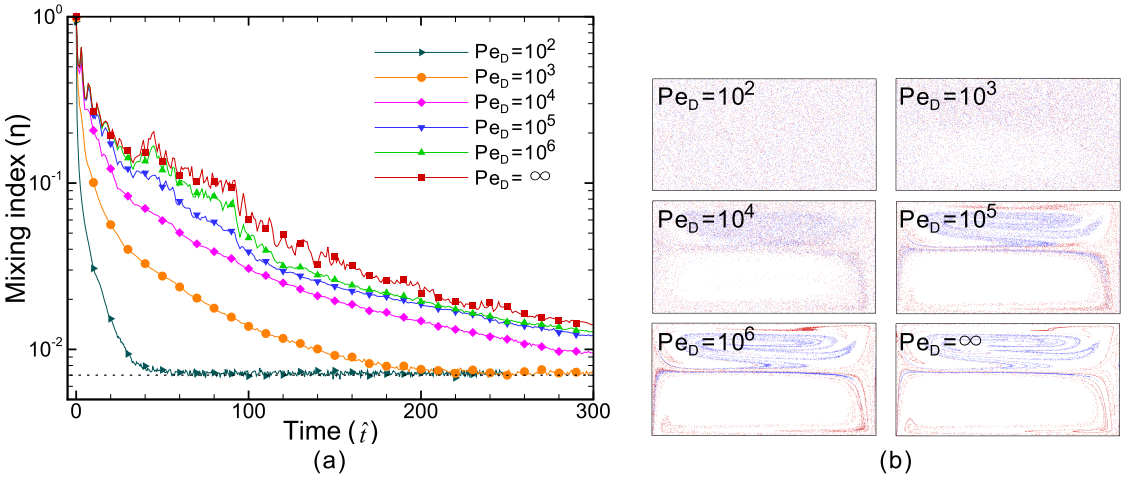

Figure 6.8: Effect of the Peclet number on mixing process in plugs. The radius ratio of the meandering microchannel is $\hat{R} = 0.7$, the viscosity ratio is $\mu_1/\mu_2 = 1$, and the dimensionless plug length is $\hat{L} = 2$. (a) Variation of mixing indices with time for different Peclet numbers. The dashed horizontal line $\eta_{\text{asymp}} = 0.00707$ indicates the homogeneous state with randomly distributed particles. (b) Visualization of mixing patterns at $\hat{t} = 100$ for different Peclet numbers.

such as $\mu_1/\mu_2 = 0.01$, the mixing index increases, which indicates relatively slow mixing in the plug.

The variation of mixing performance with the viscosity ratio can be explained from the vortex pattern in the plug. At the interface between the two plugs, the tangential stress acting on the left side of the interface is $\tau_{xy,1}$, while the tangential stress acting on the right side of the interface is $\tau_{xy,2}$. The two shear stresses should be balanced, as shown in Figure 6.10. At a high viscosity ratio (such as $\mu_1/\mu_2 = 100$), the vortex pattern is shown in Figure 6.9**b**. The effect of shear stress on the flow in Plug-1 is insignificant because Plug-1 is extremely viscous and the flow inside is difficult to be deformed. If the viscosity ratio decreases, the viscosity in Plug-1 decreases, and the effect of shear stress on the flow in

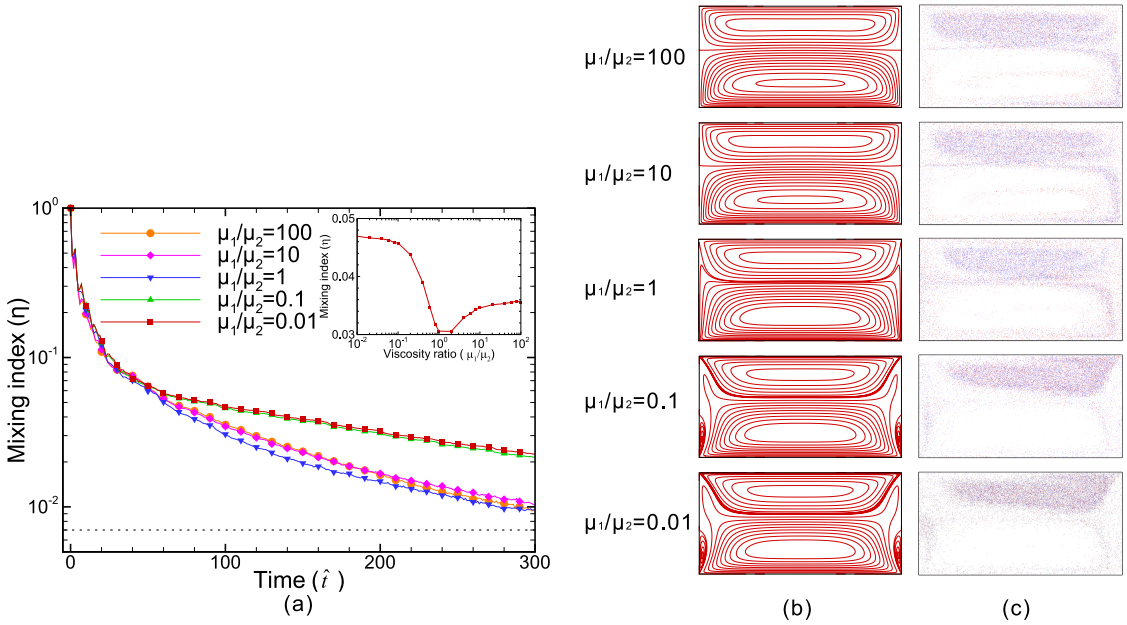

Figure 6.9: Effect of the viscosity ratio on mixing process in plugs. The radius ratio of the meandering microchannel is $\hat{R} = 0.7$, the Peclet number is $Pe_D = 10^4$, and the dimensionless plug length is $\hat{L} = 2$. (a) Variation of mixing indices with time in plugs with different viscosities. The dashed horizontal line $\eta_{\text{asymp}} = 0.00707$ indicates the homogeneous state with randomly distributed particles. Inset: The variation of mixing indices with viscosity ratio at $\hat{t} = 100$. (b) Flow pattern in plugs for fluids with different viscosities, secondary vortices are formed when the viscosity ratio μ_1/μ_2 is small. (c) Visualization of mixing patterns at $\hat{t} = 100$ for fluids with different viscosities.

Plug-1 increases. Because the vortex near the inner wall (Vortex **A**) is relatively smaller and weaker than the vortex near the outer wall (Vortex **B**), Vortex **A** is first affected when the viscosity ratio is decreasing. The fluid in Plug-1 near the interface is dragged downwards by the shear stress $\tau_{xy,2}$, which is in the opposite direction with Vortex **A** and in the same direction as Vortex **B**. Therefore, Vortex **A** shrinks while vortex **B** expands and occupies the region near the interface, as illustrated in Figure 6.10**a**. The distorted vortex pattern increases the difference

of the vortex pair, and consequently enhances mixing in the plug by increasing the folding effect.

If the viscosity ratio decreases further, the viscosity of Plug-1 is much smaller than that of Plug-2. The shear stress by Plug-2 at the interface $\tau_{xy,2}$ is more significant, which not only affects the region near Vortex **A**, but also affects the region near Vortex **B**. If the shear stress $\tau_{xy,2}$, which is in the opposite direction from Vortex **B**, is sufficiently strong, a secondary vortex is formed between the interface and Vortex **B**, as illustrated in Figure 6.10**b**. The secondary vortices hinder the mixing in the plug because the transfer of species between vortices is limited by diffusion. The strength of the secondary vortices increases with the decrease of the viscosity ratio μ_1/μ_2. This phenomenon was observed numerically and experimentally by Sarrazin et al. (2006; 2008) and by Blanchette (2009). They found that mixing is slow at the front and the rear of the droplets.

6.4.5 Effect of plug length

The effect of the plug length on the mixing process is shown in Figure 6.11. The Peclet number and the viscosity ratio are fixed at $Pe_D = 10^4$ and $\mu_1/\mu_2 = 1$, respectively, while the dimensionless plug length $\hat{L}$ is varied from 1 to 5. The mixing indices are plotted against time for different $\hat{L}$ in Figure 6.11**a**. For long plugs, such as $\hat{L} = 5$, mixing is slow with a relatively high mixing index η. The mixing index decreases with decreasing $\hat{L}$, which indicates better mixing. If $\hat{L}$ decreases further, the mixing index η increases, which indicates that mixing becomes slow again. This effect can also be seen from the mixing patterns at $\hat{t} = 100$ for different $\hat{L}$, as shown in Figure 6.11**b**.

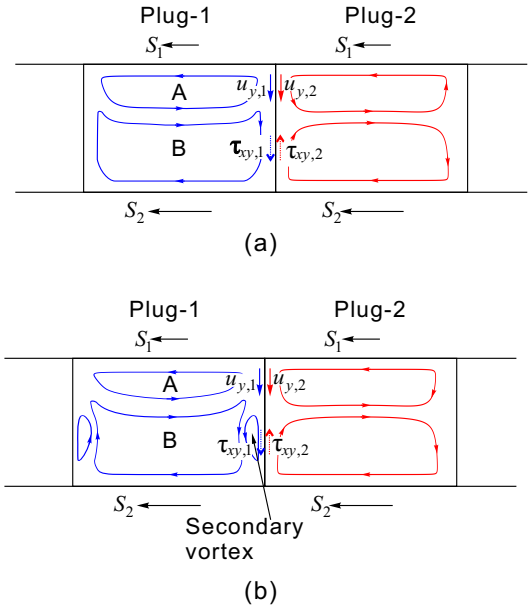

Figure 6.10: Flow diagrams of the plug train with different viscosity ratios: (a) Distortion of vortex pattern by the shear stress at the interface $\tau_{xy,2}$; (b) Formation of secondary vortices when the shear stress is sufficiently large due to the small μ_1/μ_2.

The effect of L on the mixing process in mainly due to its effect on flow patterns in plugs, as shown in Figure 6.11**c**. The flow in a plug can be divided into three regions (the front region, the middle region, and the rear region), as shown in the inset in Figure 6.11**d**. The front region and the rear region are dominated by transverse flow due to the presence of the front/rear interfaces, whereas the middle region is characterized by parallel flow without a significant interface effect. The length of the middle region increases with increasing $\hat{L}$. For long plugs ($\hat{L} = 5$), the middle region is long, therefore, a longer time is required for the particles to be advected during one cycle, and the parallel flow leads to slow mixing in the plug.

For short plugs, the middle region is short and almost the whole plug is affected by the transverse flow due to the front/rear interfaces. The velocity profiles at the three typical cross sections are plotted in Figure 6.11**d**. In the middle region,

the velocity profile is almost parabolic, while in the front/rear regions, the velocity profile is mostly flat ($-0.5 < \hat{y} < 0.5$ as shown in Figure 6.11**d**). When flowing through the middle regions, the fluid elements are stretched due to the velocity gradient. In contrast, when flowing in the front/rear region, the fluid elements is only deformed slightly due to the flat velocity profile. Therefore, in short plugs, a blob of tracer particles may simply rotate under the recirculating flow. However, it cannot be stretched into a long thin filament. Consequently, the mixing is relatively slow in short plugs, and plugs with a moderate $\hat{L}$ value are preferred for rapid mixing in the meandering microchannels.

6.5 Summary

In this chapter, a simplified two-dimensional model is proposed to investigate plug trains in microchannels. The model is used to study the mixing process in plugs moving in meandering microchannels using the particle tracking method. The mixing process in plugs is the combined effects of the stretching of fluid filaments by the vortices, folding of fluid filaments by changing the direction of the channel curvature, and the diffusion of species between liquid filaments. The effects of the channel curvature, the Peclet number, the viscosity ratio, and the plug length are investigated. The results show that a large curvature, a low Peclet number, a moderate viscosity ratio, and a moderate plug length are preferred for rapid mixing in liquid plugs. The current study can help to optimize the micromixing in liquid plugs travelling in meandering microchannels, and to guide the design of lab-on-a-chip devices for applications such as chemical reactions, particle syntheses, and protein crystallization.

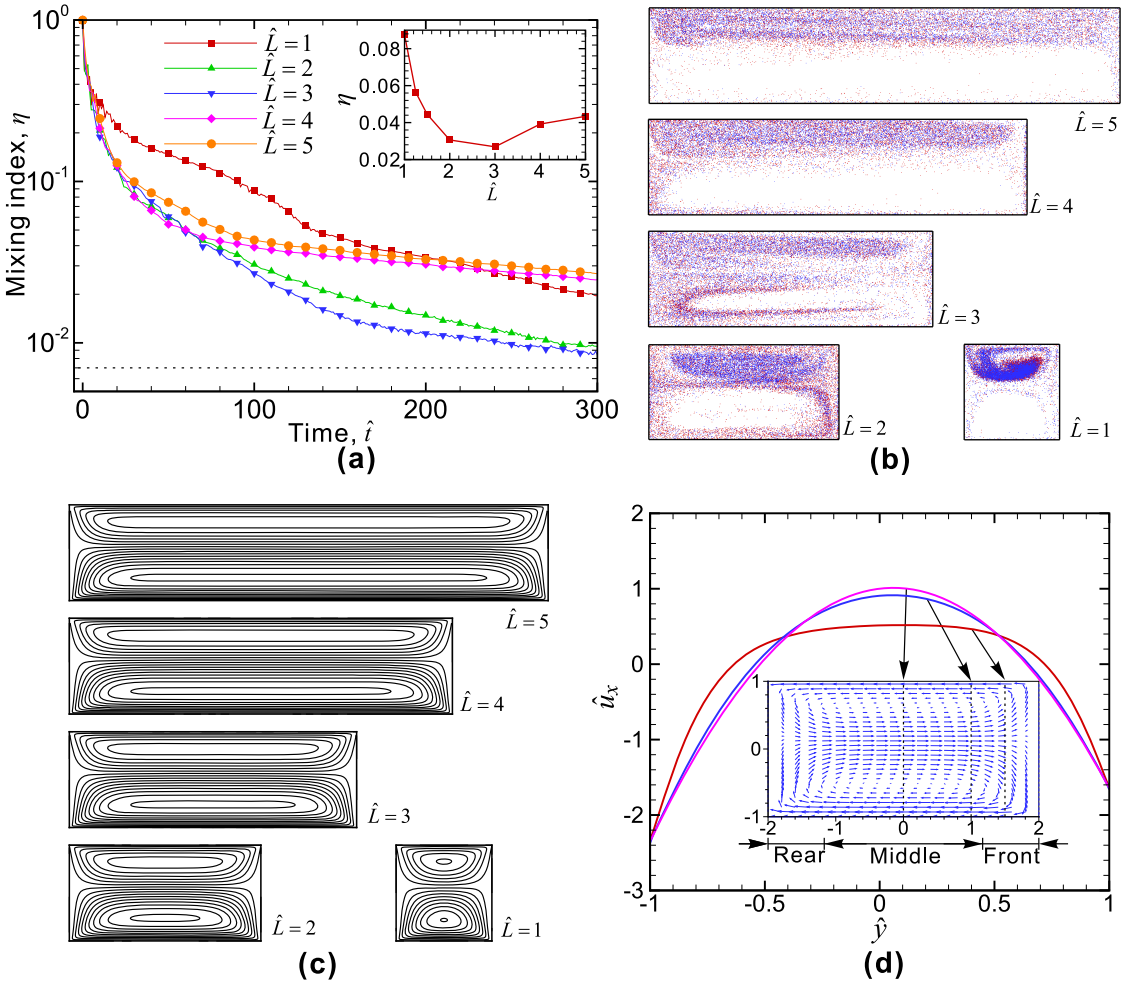

Figure 6.11: Effect of dimensionless plug length on mixing process in plugs. The radius ratio of the meandering microchannel is $\hat{R} = 0.7$, the Peclet number is $Pe_D = 10^4$, and the viscosity ratio is $\mu_1/\mu_2 = 1$. (a) Variation of mixing indices with time in plugs with different $\hat{L}$. The dashed horizontal line $\eta_{\text{asymp}} = 0.00707$ indicates the homogeneous state with randomly distributed particles. Inset: The variation of mixing indices with $\hat{L}$ at $\hat{t} = 100$. (b) Visualization of mixing patterns at $\hat{t} = 100$ for plugs with different $\hat{L}$. (c) Flow pattern in plugs of different $\hat{L}$. (d) The flow in a plug can be divided into three regions, the front region, the middle region, and the rear region. The velocity profiles at three typical cross sections, $\hat{x} = 0$, $\hat{x} = 1$, and $\hat{x} = 1.5$, are plotted. In the middle region (such as $\hat{x} = 0$), the velocity profile is almost parabolic, while in the front/rear regions (such as $\hat{x} = 1.5$), the velocity profile is mostly flat ($-0.5 < \hat{y} < 0.5$).

Chapter 7

Hydrodynamically Mediated Breakup of Droplets in Microchannels [†]

7.1 Introduction

The capacity of a droplet-based analysis can be scaled up by splitting a droplet into two or more daughter droplets. After splitting, the concentrations of the reagent in all daughter droplets are identical and suitable for subsequent parallel processes. To split droplets in a microchannel, a bifurcation junction can be used to assist the breakup of droplets (Link et al., 2004), as shown Figure 7.1**a** and reviewed in Chapter 2. In this chapter, a method is proposed to split droplets based on hydrodynamic focusing. This method provides a way to further adjust the size of a droplet after its formation. At a bifurcation channel, a droplet is split along its transverse direction, as shown in Figure 7.1**a**. In contrast, the droplet at a flow focusing junction is divided along its length in the flow direction. As discussed in Chapter 6, mixing in each half of the droplet in a microchannel is easy, while mixing

[†]This work has been published in *Applied Physics Letters 98, 5, 054102.*

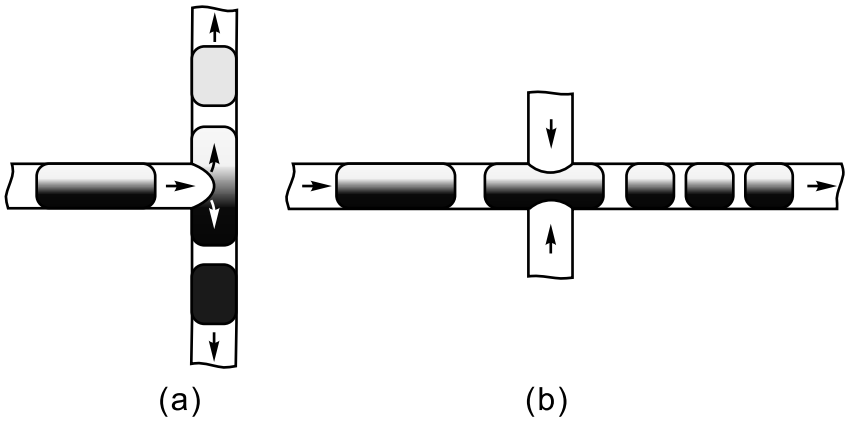

Figure 7.1: Schematic diagram of breakup of droplets at (a) a bifurcation and (b) a flow focusing junction in microchannels. At a flow focusing junction, identical contents in daughter droplets are easy to be ensured, and the number and the size of the daughter droplets can be obtained by tuning the splitting flow rate.

across the two halves are relatively difficult. Therefore, the splitting method at a flow focusing junction is favourable if identical contents in daughter droplets are required to be ensured. Moreover, with a flow focusing junction, the number and the size of the daughter droplets can be tuned by changing the splitting flow rate of the continuous phase without alternating the geometry of the microchannel. In contrast, a bifurcation can only result in two daughter droplets.

In this chapter, droplet splitting behaviours at a flow focusing junction are investigated experimentally. The experimental details are provided in Section 7.2, and the results are presented and discussed in Section 7.3.

7.2 Experimental

To investigate the breakup process of droplets based on hydrodynamic focusing, water droplets in oil were formed at a flow focusing junction, as shown in Figure 7.2.

Droplets are formed at the first junction (droplet formation junction) and then split at the second junction (droplet splitting junction).

The PDMS microchannel was fabricated using the soft-lithography method (Xia and Whitesides, 1998; Duffy et al., 1998). A plastic mask was designed in AutoCAD (Autodesk, USA) and printed on a 5 inch plastic transparent film (Infinite Graphics Pte Ltd, Singapore). Negative photoresist SU8 (MicroChem, USA) was spin coated on a silicon wafer [Figure 7.3**a**]. After a soft bake to harden the SU8 layer, the SU8 layer was exposed to UV light with the transparent mask [Figure 7.3**b**]. Then the SU8 layer was developed in SU8 developer (MicroChem, USA), and briefly rinsed in isopropanol. The unexposed portion of the photoresist is dissolved by the photoresist developer, while the exposed portion is insoluble to the photoresist developer and forms the SU8 master for the microchannel [Figure 7.3**c**]. PDMS and its curing agent (Sylgard 184, Dow Corning, USA), after well mixed (10:1 by weight) and de-gassed, was poured over the SU8 master [Figure 7.3**d**]. After curing in an oven at 80°C for 2 hours, the PDMS was slowly peeled from the SU8 master [Figure 7.3**e**]. Holes were punched on the PDMS for fluid inlets/outlets [Figure 7.3**f**]. The PDMS was bonded with another piece of flat PDMS immediately after treatment of oxygen plasma [Figure 7.3**g**]. The chip is ready to use after heat treatment, which assists the channel surface return to a hydrophobic state. A image of the microchannel is shown in Figure 7.4.

Deionized (DI) water and mineral oil (Sigma M5904, St. Louis, USA) were used as the dispersed phase and the continuous phase, respectively. Nonionic surfactant Span 80 (Sigma S6760) 2% by weight was added into the mineral oil to assist the formation of droplets and to stabilize them against coalescence. Fluids

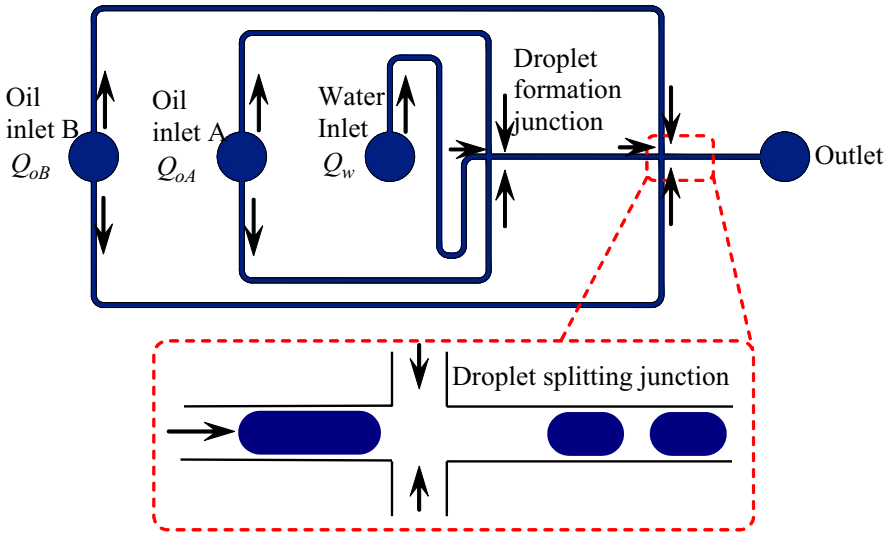

Figure 7.2: Schematic diagram of the microfluidic device. Droplets are formed at the first junction (droplet formation junction) and then split at the second junction (droplet splitting junction). The width and the depth of the channel are, respectively 100 and 70 μm. The oil inlet B is used for droplet splitting.

were introduced at each inlet by syringe pumps (KD scientific, Hollistan, MA, USA) to control the flow rates. A high speed camera (Photron FASTCAM APX RS, San Diego, CA, USA) was attached to an inverted microscope (Nikon ECLIPSE TE2000-E, Tokyo, Japan) to capture the images of the droplets. The high speed images were captured at a frame rate of 250 or 500 fps and a resolution of 1024×128 pixels. The dimensionless length of the droplets $\hat{L}$ were used to quantify the size of the drops, and it was measured with a MATLAB program from the high speed images of the droplets in pixels as follows,

$$\hat{L} \equiv \frac{L_{\text{pixel}}}{w_{\text{pixel}}} = \frac{A_{\text{pixel}}}{w_{\text{pixel}}^2} \tag{7.1}$$

where L_{pixel}, w_{pixel} and A_{pixel} are the length of the droplet, the width of the microchannel, and the area of the droplet in pixels, respectively.

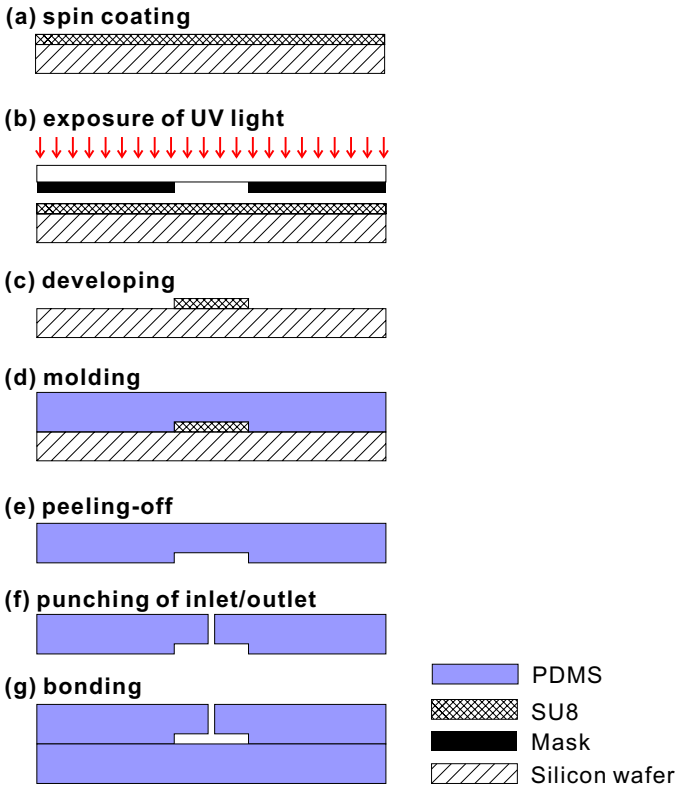

Figure 7.3: Schematic diagram of the soft-lithographic method to fabricate the microchannel.

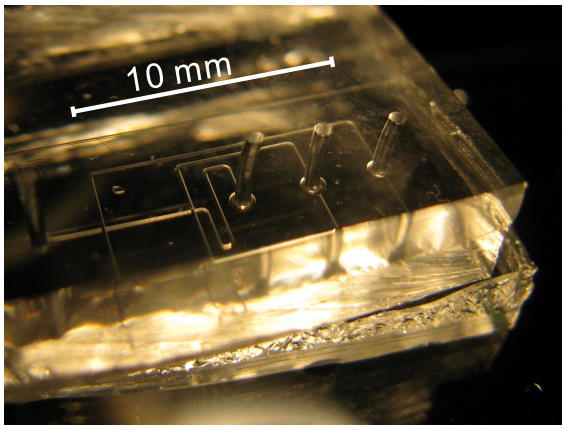

Figure 7.4: Image of the microfluidic device.

7.3 Results and discussion

The typical process of splitting a droplet is shown in Figure 7.5. A droplet in the form of a plug arriving at the flow focusing junction undergoes five stages to produce the first daughter droplet: Bulging [Figure 7.5**b**], blocking [Figure 7.5**c**], squeezing/stretching [Figure 7.5**d**], breaking [Figure 7.5**e**], and recovering [Figure 7.5**f**]. After the breakup of the first daughter droplet, if the remaining droplet is sufficiently large, it can be further split by the focusing flow. Due to the lack of time for shape recovery, the remaining droplet has a slender head, facilitating the instability for the subsequent breakup. The second daughter droplet is therefore smaller than the first daughter droplet [Figure 7.5**i**]. The breakup process repeats itself until the remaining droplet is not large enough for further breakup. The final droplet passes the junction without breakup [Figure 7.5**j**].

7.3.1 Splitting performance

7.3.1.1 Effect of splitting flow rate

The splitting performance was studied by varying the flow rate of the oil Q_{oB} and by varying the mother droplet size. The splitting flow rate of Q_{oB} was varied while the flow rates at other inlets Q_{w} and Q_{oA} were fixed. Therefore, different splitting flow rates were applied on identical droplets. For small splitting flow rates such as $Q_{\mathrm{oB}} = 50\ \mu\mathrm{L/h}$ [Figure 7.6], the droplet passes through the flow focusing junction without producing daughter droplets. As the splitting flow rates Q_{oB} increase, the squeezing and stretching force of the splitting oil also increases. When the splitting flow rate Q_{oB} is larger than the first critical value $Q_{\mathrm{oB,c1}} = 60\,\mu\mathrm{L/h}$, the

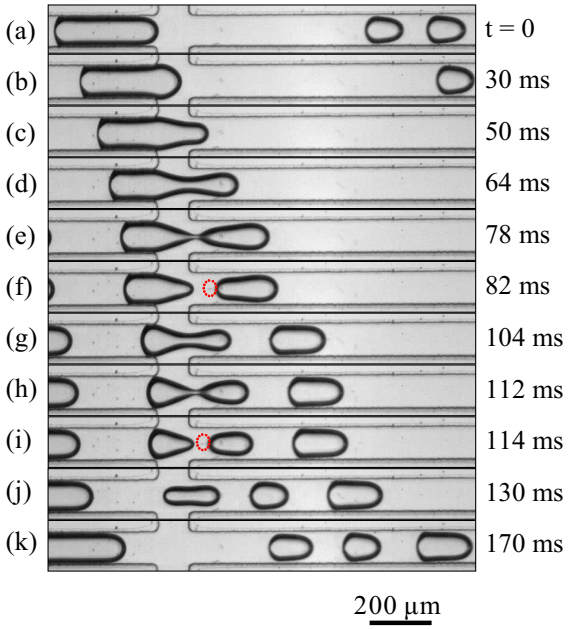

Figure 7.5: Sequences of a typical breakup process at the flow focusing junction. The flow rates are, respectively, $Q_{\mathrm{w}} : Q_{\mathrm{oA}} : Q_{\mathrm{oB}} = 40 : 40 : 140$ μL/h. Satellite droplets are highlighted with dashed circles in (f) and (i). (a) The mother droplet arrives at the junction. (b) Bulging of the head of the mother droplet. (c) The head partially blocks the downstream channel. (d) The mother droplet is squeezed and stretched. (e) The waist of the mother droplet shrinks. (f) The detached daughter droplet recovers its plug shape. (g) The remaining droplet is squeezed and stretched. (h) The waist shrinks to form the second daughter droplet. (i) The second daughter droplet recovers its plug shape. (j) The remaining droplet passes the junction without breakup. (k) The three daughter droplets of plug shapes flow downstream.

squeezing force is sufficiently large and is able to squeeze and stretch the waist of the droplet. The droplet subsequently breaks up into two parts. When the splitting flow rate Q_{oB} further increases, the squeezing and stretching effects need less time to develop the instability. The location of the surface instability shifts toward the front of the mother droplet, resulting in a smaller daughter droplet. The remaining droplet after the first breakup is large enough to form a second daughter droplet at a second critical splitting flow rate of $Q_{oB,c1} = 100\,\mu L/h$. Increasing the splitting flow rate further, more daughter droplets can be produced [Figure 7.6]. The size of the last droplet is determined mainly by the amount of the remaining fluid after the previous breakup. The splitting process shares some common features with the continuous droplet formation at a flow focusing geometry. For the cases of obtaining two or more daughter droplets, the relationship between the sizes of the first daughter droplet and the splitting flow rates Q_{oB} is fitted by the least square method as

$$\hat{L} = \alpha {Q_{oB}}^{-\beta}. \tag{7.2}$$

It obtained $\hat{L}_1 = 70{Q_{oB}}^{-0.76}$ [Figure 7.6]. The size of the second daughter droplet was also fitted to $\hat{L}_2 = 41{Q_{oB}}^{-0.73}$.

At a higher flow rate Q_{oB}, the breakup of the droplet will shift to a jetting regime where the breakup process happens at the end of a long column of liquid downstream of the flow focusing junction [Figure 7.7]. In this regime, the size of the daughter droplet is smaller than the width of the microchannel. The droplet breakup is dominated by Rayleigh capillary instability, and it appears to be less controlled (Anna and Mayer, 2006).

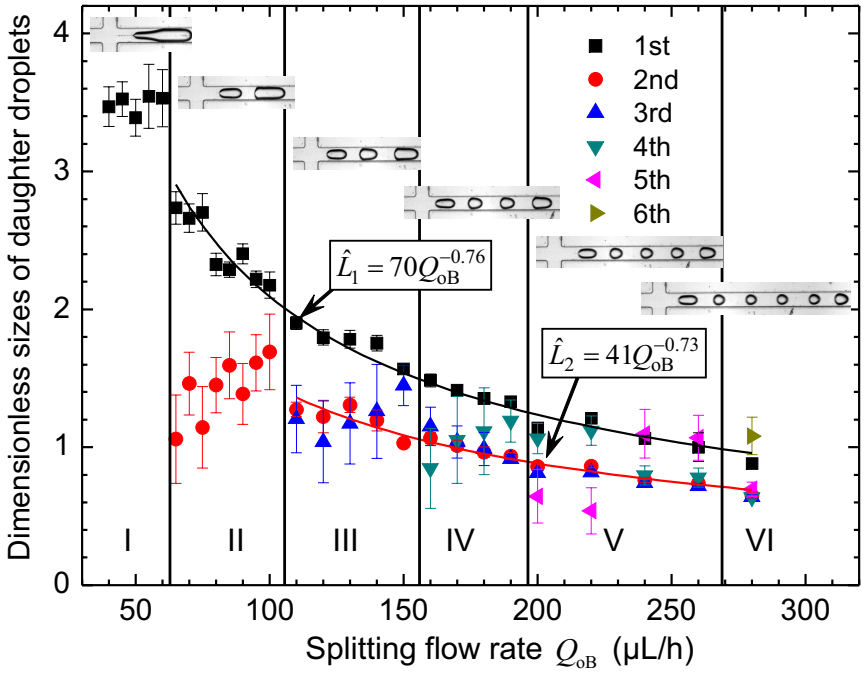

Figure 7.6: Regimes of droplet splitting performance at different flow rates.

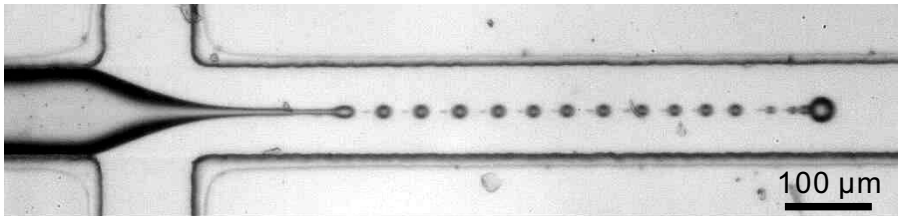

Figure 7.7: Breakup of droplet in the jetting regime Q_w : Q_{oA} : Q_{oB} = 40 : 40 : 1000 μL/h.

7.3.1.2 Effect of mother droplet size

To investigate the effect of the size of the mother droplet on the splitting process, the flow rates to produce mother droplets Q_w and Q_{oA} were varied while maintaining a constant total flow rate $Q_w + Q_{oA}$. The flow rate of droplet splitting Q_{oB} was also fixed to apply a constant focusing flow to droplets of different sizes.

The regimes of droplet splitting performance for mother droplets of different sizes are shown in Figure 7.8. After passing the formation junction, the mother droplet can break into daughter droplets of different numbers and different sizes. When passing the splitting junction, small droplets do not break up because they are stiff against squeezing and are hard to deform. When the mother droplet exceeds a critical size ($\hat{L}_{c1} = 2.35$ in the experiment), the splitting oil has sufficient time to squeeze and stretch the droplet, leading to instability. Consequently, two daughter droplets are formed, with the second daughter droplet being smaller than the first. As the size of the mother droplet further increases, the second daughter droplet gradually increases in size while the size variation of the first daughter droplet is insignificant. If the remaining droplet is sufficiently large, the focusing flow is able to form further daughter droplets. Although this scenario is similar to the breakup of the first daughter droplet when the droplet size increases, it has some unique features. As shown in Figure 7.8, after the breakup of the first daughter droplet, the remaining droplet does not need to reach $\hat{L}_{c1}$ for further splitting. From Figure 7.8, we can observe that the critical size for the second breakup is $\hat{L}_{c2} = 1.80$. This phenomenon can also be observed for the third breakup [Figure 7.8]. The critical size for the third breakup is $\hat{L}_{c3} = 1.75$.

Figure 7.8 shows that the critical size of the first breakup is much larger than the second breakup and the third breakup, i.e., $\hat{L}_{c1} > \hat{L}_{c2} \approx \hat{L}_{c3}$. This can be explained from the sequence of droplet breakup at the flow focusing junction. After the mother droplet arrives at the flow focusing junction, the front of the mother droplet bulges without the confinement of the wall at the junction, and this results in a large head of the mother droplet, as shown in Figure 7.5**b**. After the breakup of

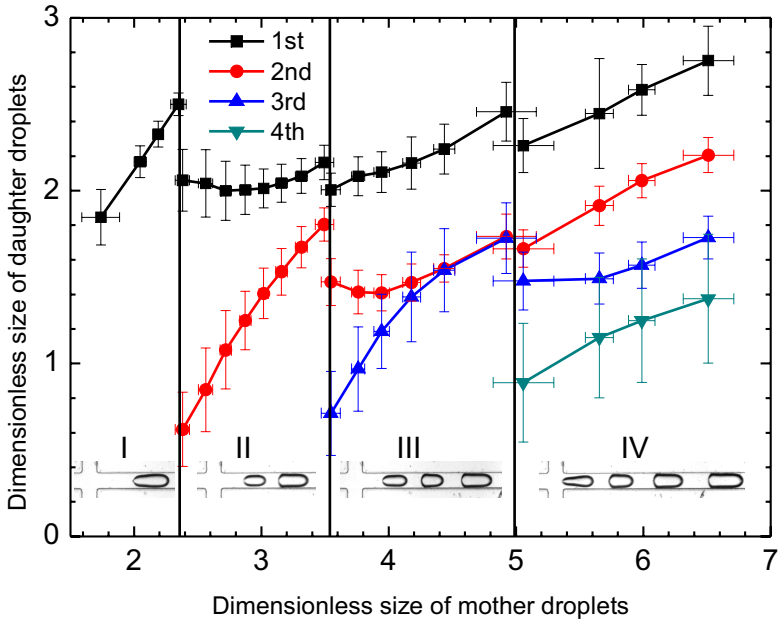

Figure 7.8: Regimes of droplet splitting performance for different sizes of the mother droplet.

the first daughter droplet, the front of the remaining droplet is squeezed to a slender head, and there is no sufficient time for its recovery to a bulged shape, as shown in Figure 7.5**f**. The slender head facilitates the subsequent breakup in compared to the bugled droplet head before the first breakup. Therefore, the critical size of the second breakup is much smaller than the critical size of the first breakup, i.e., $\hat{L}_{c1} > \hat{L}_{c2}$. In addition, because the second breakup also results a slender droplet head, as shown in Figure 7.5**i**, the critical size of the third breakup is similar with that of the second breakup, i.e., $\hat{L}_{c2} \approx \hat{L}_{c3}$.

7.4 Summary

In this chapter, the breakup of droplets mediated by hydrodynamic focusing is investigated. When passing a flow focusing junction, a mother droplet can be split

into two or more daughter droplets. The number and the size of the daughter droplets depend on the splitting flow rate and the size of the mother droplet. The splitting process was recorded and analyzed by high speed photography. The splitting performance was investigated by the number and the size of the daughter droplets. More droplets of smaller sizes were obtained by applying a high splitting flow rate. Alternatively, large mother droplets could also produce more daughter droplets without changing the splitting flow rates. With the flow focusing junction to split droplets in microchannels, the robustness, reliability, and flexibility to control the number and size of the daughter droplets will make it a useful tool for various droplet-based microfluidic applications.

Chapter 8

Formation and Breakup of Pendant Drops at the Tip of a Capillary †

8.1 Introduction

The growth and the subsequent breakup of pendant drops from the tip of a capillary are common phenomena in nature (Eggers, 1997). They are of great importance in many applications, such as ink-jet printing (Le, 1998), spraying, and food engineering (Eggers, 1997). Moreover, they are of great scientific interests due to the richness of the underlying physics. When the flow rate of the liquid in the capillary is sufficiently large, the breakup of drops at the capillary tip is in the jetting regime, where drops detach from the ends of long columns of the liquid far downstream of the capillary tip (Ambravaneswaran et al., 2004; Eggers and Villermaux, 2008). For a small flow rate of the liquid in the capillary, the growth and breakup of pendant drops is in the dripping regime. In this regime, the process of growth and breakup includes two main stages (Wilson, 1988; Zhang,

†This work has been published in *Chemical Engineering Science 66 (21) 5293-5300.*

1999). During the first stage, i.e.,the growing stage, the size of the pendant drop slowly grows, and the pendant drop is quasistatic at every instant. The shape of the pendant drop and the flow within it are determined by surface tension force, gravitational force, and viscous force. As the pendant drop grows in size, it gradually reaches a critical size, at which the surface tension force cannot support the weight of the pendant drop. Consequently, the process goes into the second stage, i.e., the pinch-off stage, during which the neck of the pendant drop in the vicinity of the tip suddenly shrinks and less weight can be supported by the surface tension force. As a result, Plateau-Rayleigh instability (Michael, 1981) suddenly accelerates the pinch-off process and the drop finally detaches from the tip of the capillary.

During the growing stage, the pendant drop is determined by the interplay of the surface tension force, gravitational force, and viscous force. The inertial force comes into play when the process goes into the pinch-off stage (Zhang and Stone, 1997). The dimensionless groups involved include the Bond number Bo, the capillary number Ca, and the Weber number We. The Bond number, which characterizes the relative effect between gravitational force and the surface tension force, is defined as $Bo = \rho g L^2/\sigma$, where ρ is the density of the fluid, g is the gravitational acceleration, L is the characteristic length, and σ is the surface tension. The capillary number, which characterizes the relative effect between the viscous force and the surface tension force, is defined as $Ca = \mu V/\sigma$, where μ is the viscosity of the liquid, and V is the characteristic velocity. The Weber number, which characterizes the relative effect between the inertial force and the surface tension force, is defined as $We = \rho V^2 L/\sigma$.

From the above dimensionless groups, it is clear that the pinch-off process can be controlled by changing the surface tension of the liquid. The pinch-off process can also be manipulated by heat which induces surface tension gradient and Marangoni stress along the surface of the pendant drop (Suryo and Basaran, 2006), or alternatively by electric fields, which can deform the pendant drop and facilitate the pinch-off (Zhang and Basaran, 1996), or even create a tip-streaming phenomenon under a strong electric field (Collins et al., 2008).

The growth and pinch-off process for different types of fluids besides Newtonian fluids, such as viscoelastic fluids (Tirtaatmadja et al., 2006; Wagner et al., 2005), shear thinning fluids (Yildirim and Basaran, 2001; Davidson and Cooper-White, 2006), and viscoplastic fluids (German and Bertola, 2010) have been reported. The pinch-off of superfluid (^{4}He), which is a distinctly different class of fluid, has been investigated to realize an ideal inviscid fluid as a consequence of vanishing viscosity in the superfluid state (Burton et al., 2007). Suspending particles in the liquid can affect the pinch-off process by resisting the shrinking of the liquid thread before the detachment (Furbank and Morris, 2004).

Pendant drops exhibit many interesting behaviours during the growth and breakup process, and many underlying physics can be uncovered by studying these behaviours. Before the detachment of a drop from the capillary, a liquid thread is formed connecting the to-be-formed drop and the remnant fluid at the tip. Experimental observations revealed that the breakup of the liquid thread showed a self-similar behaviour during the final period of the pinch-off process (Burton and Taborek, 2007; Eggers, 1997). By examining the pinch-off of several hundred drops, Ambravaneswaran et al. (2000) studied the nonlinear response of drops.

Their results showed that the time interval of dripping exhibited bifurcation and hysteresis from the time return map and the bifurcation diagram.

To investigate the process of growth and pinch-off of pendant drops, high speed imaging systems were often employed to record the surface evolution during the growth and pinch-off process. Due to the fast nature of the interface evolution at the instant of pinch-off, the acquisition speed of high speed imaging systems may be up to 10^8 frames per second (Chen et al., 2002).

To analyze the process of growth and pinch-off of pendant drops, simplification can be made based on the axisymmetric nature of the process. Egger and Dupont (1994) presented a one-dimensional model based on a slender-jet approximation with conservation of mass and momentum in the axial direction. This model has successfully captured flow behaviours such as nonlinear response (Ambravaneswaran et al., 2000), dripping-jetting transitions (Ambravaneswaran et al., 2004), and the effects of surfactants (Xu et al., 2007).

Numerical simulation is a powerful tool as it is able to provide valuable insights into the growth and breakup of pendant drops, especially when experimental devices are not capable of resolving the flow at a time scale which may range from microseconds to seconds and a length scale from micrometres to millimetres. According to the methods to treat the interface explicitly or implicitly, the numerical methods to predict the interface can be categorized into two main groups. The first group tracks the interface position explicitly, and it includes the front tracking method (Tryggvason et al., 2001; Chung et al., 2009), the boundary integration method (Hou et al., 2001), and the moving mesh method (Perot and Nallapati, 2003; Xue et al., 2008). The second group treats the interface implicitly,

and it includes the phase field method (Anderson et al., 1998), the volume of fluid method (Scardovelli and Zaleski, 1999; Dietsche and Neubauer, 2009), the lattice Boltzmann method (Chen and Doolen, 1998; Amaya-Bower and Lee, 2011) and the level set method (Osher and Fedkiw, 2003). Among these methods for interface tracking or capturing, the level set method is comparatively easy to implement. Topological changes, such as breakup and coalescence, are handled automatically. Besides, it offers the ease of calculating geometrical properties, e.g. volume, surface area, and curvature.

Although the growth and pinch-off of pendant drops has been widely studied in the literature, the upstream pressure effect, to the best of the author's knowledge, has not been studied before. In this chapter, numerical simulation were carried out to investigate the upstream pressure fluctuation during the growth and pinch-off of pendant drops. To account for the surface tension effect, which is important on the upstream pressure fluctuation, an accurate evaluation of the curvature is required. The level set method, which offers easy and accurate evaluation of curvature (Osher and Fedkiw, 2003), is used to predict the evolution of the pendant drops. This chapter is organized as follows. In Section 8.2, the problem and the numerical method are described . The numerical results are presented and discussed in Section 8.3. The sequences of drop growth and pinch-off and the corresponding upstream pressure fluctuation are analyzed. The effects of the surface tension and the outer diameter of the capillary are investigated. In Section 8.4, a method to measure surface tension is proposed based on the pressure fluctuation during the growth and breakup process of pendant drops.

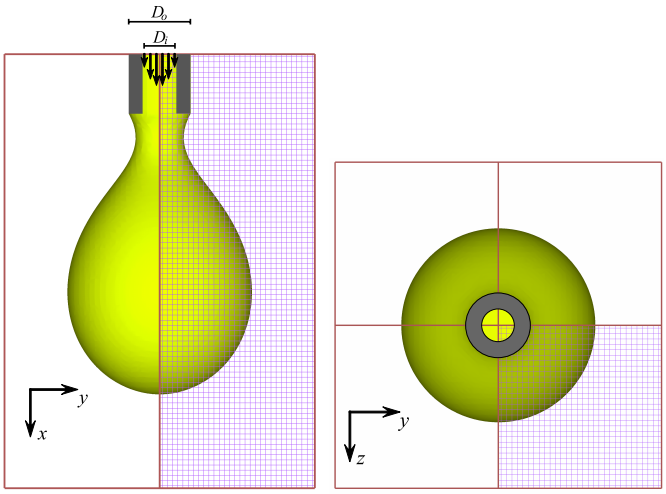

(a) Side view (b) Top view

Figure 8.1: Schematic diagram of the computational domain of the pendant drop at the tip of a capillary. One quarter of the region indicated by the mesh is used for simulation. (a) Side view of the pendant drop at the instant of pinch-off. (b) Top view of the computational domain with the pendant drop.

8.2 Numerical method

The physical problem of the growth and pinch-off of pendant drops from the tip of a capillary is shown schematically in Figure 8.1. The inner diameter of the capillary tip is D_i, while the outer diameter is D_o. Due to the symmetry, only a quarter of the region ($y \geq 0$, $z \geq 0$) is simulated to reduce the computation time, as shown in Figure 8.1. The density ρ and viscosity μ of the Newtonian isothermal fluid is assumed to be constant in this study. Unless otherwise specified, the properties of the working fluids are as listed in Table 8.1. The gravitational force is included in the simulation with a gravitational acceleration $g = 9.81$ m/s^2. A parabolic velocity profile is imposed at the inlet of the capillary with a volumetric flow rate of Q. A 3D Cartesian coordinate system is built with the gravitational force in the

positive x direction.

The computational domain ($L_x \times L_y \times L_z$) should be selected sufficiently large that the side boundary and the outlet boundary are far from the pendant drop that the flow around the pendant drop is not affected by the selection of the boundary. Finally $L_x = 7D_o$ and $L_y = L_z = 2.5D_o$ are selected after many tests by a compromise with the computational time. At the two symmetrical boundary $x0y$ plane ($z = 0$ plane) and $x0z$ plane ($y = 0$ plane), the symmetrical boundary condition is specified, while on the side boundary of the computational domain ($y = L_y$ plane and $z = L_z$ plane), the free slip boundary condition is specified. Both the symmetrical boundary condition and the free slip boundary condition state that the velocity components perpendicular to the boundary $\mathbf{u} \cdot \mathbf{n}$ vanish.

$$\mathbf{u} \cdot \mathbf{n} = 0 \tag{8.1}$$

while the gradient of the velocity components tangential to the boundary $\mathbf{u} \cdot (\mathbf{I} - \mathbf{nn})$ is zero,

$$\frac{\partial}{\partial n} \left[\mathbf{u} \cdot (\mathbf{I} - \mathbf{nn}) \right] = 0 \tag{8.2}$$

where $\mathbf{I}$ is the identity matrix of size three, and $\mathbf{n}$ is the unit direction vector normal to the boundary.

Table 8.1: Properties of the fluids and the sizes of the capillary.

Properties	Values
Viscosity of water μ_l	10^{-3} Pa·s
Viscosity of air μ_g	1.78×10^{-5} Pa·s
Density of water ρ_l	1000 kg/m^3
Density of air ρ_g	1.25 kg/m^3
Surface tension of water σ	72.8 mN/m
Inner diameter D_i	0.5 mm
Outer diameter D_o	1 mm

8.2.1 Governing equations

The Navier-Stokes equation is discretized using the finite volume method (FVM) (Patankar, 1980). For both fluids, water and air, the governing equations for the flow are

$$\frac{\partial \rho}{\partial t} + \nabla \cdot (\rho \mathbf{u}) = 0 \tag{8.3}$$

$$\frac{\partial (\rho \mathbf{u})}{\partial t} + \nabla \cdot (\rho \mathbf{u}\mathbf{u}) = -\nabla p + \nabla \cdot \left[\mu \left(\nabla \mathbf{u} + \nabla \mathbf{u}^T\right)\right] + \rho \mathbf{g} \tag{8.4}$$

where ρ is the density, μ is the viscosity, $\mathbf{u}$ is velocity vector, p is the pressure, t is the time, and $\mathbf{g}$ is the gravitational acceleration. For multiphase flow, the density ρ and the viscosity μ at each control volume are calculated as:

$$\rho = H\rho_l + (1 - H)\,\rho_g \tag{8.5}$$

$$\frac{1}{\mu} = \frac{H}{\mu_l} + \frac{1 - H}{\mu_g} \tag{8.6}$$

where H is the smoothed Heaviside function, which varies smoothly across the interface from 0 in the gas phase to 1 in the liquid phase. The exact form of H will be presented in Section 8.2.2. The ghost fluid method (Kang et al., 2000; Liu et al., 2000) is used to account for the surface tension through the pressure term.

$$[p] = -\kappa\sigma \tag{8.7}$$

where $[p]$ indicates the pressure jump across the interface and $\kappa \equiv \nabla \cdot \mathbf{n}$ is the curvature of the interface. The symbol $\mathbf{n}$ denotes the unit direction vector normal to the interface, which will be presented in Eq. (8.11).

8.2.2 Interface prediction method

The evolution of the interface is predicted using the level set method. The level set function ϕ is the signed distance from the interface. It is positive in one phase and negative in the other phase. The interface is implicitly represented by the zero level set $\phi = 0$. The level set equation and the re-initialization equation for the distance function ϕ are, respectively:

$$\frac{\partial \phi}{\partial t} + \mathbf{u} \cdot \nabla \phi = 0 \tag{8.8}$$

$$\frac{\partial \phi}{\partial \tau} = \text{sign}(\phi)(1 - |\nabla \phi|) \tag{8.9}$$

where τ is the pseudo-time for the re-initialization. To obtain an accurate numerical solution, the spatial terms in Eqs. (8.8) and (8.9) are discretized using the fifth-order weighted essentially non-oscillatory (WENO) scheme (Osher and Fedkiw, 2003), and the temporal terms are approximated using the third-order Runge-Kutta (RK) scheme with the total variation diminishing (TVD) property (Osher and Fedkiw, 2003).

The smooth Heaviside function H in Eqs. (8.5) and (8.6) is defined using the distance function as follows,

$$H \equiv \begin{cases} 0, & \phi < -\varepsilon \\ \frac{\phi+\varepsilon}{2\varepsilon} + \frac{1}{2\pi} \sin\left(\frac{\pi\phi}{\varepsilon}\right), & -\varepsilon < \phi < \varepsilon \\ 1, & \phi > \varepsilon \end{cases} \tag{8.10}$$

where ε is set to 1.5 times of the mesh size. From the distance function ϕ, the curvature in Eq. (8.7) can be obtained as follows

$$\kappa \equiv \nabla \cdot \mathbf{n} = \nabla \cdot \frac{\nabla \phi}{|\nabla \phi|} \tag{8.11}$$

During the evolution of the pendant drop, the contact line of the pendant drop, as shown in Figure 8.3, is pinned at the outer circumference of the capillary tip, which is due to the wettability of the fluid to the capillary. Therefore, the contact line is specified at the outer circumference during the simulation. In addition, the initial shape of the pendant drop at the capillary tip is specified as a hemispherical shape with a diameter of D_o. The simulation was carried out for a time longer than the pinch-off of the first drop until the interface shape exactly coincide with the shape before the pinch-off. Hence, the flow has achieved a self-sustained state, and the initial assumption of the hemispherical interface shape does not affect the simulation results.

8.2.3 Mesh independence study

Mesh independence study was carried out using three computational meshes, namely $42 \times 15 \times 15$, $84 \times 30 \times 30$, and $126 \times 45 \times 45$ control volumes, while the time step sizes were also changed proportionally with the spatial grid sizes, and they were, respectively, 2×10^{-5} s, 1×10^{-5} s, and 0.67×10^{-5} s for the three different meshes. As shown in Figure 8.2, the comparison of the solutions at different time steps shows that the $84 \times 30 \times 30$ mesh is sufficiently fine to capture most of the flow features of the problem and offers mesh independent solution. Therefore, simulations in this study were carried out using the $84 \times 30 \times 30$ mesh.

8.2.4 Validation against experimental results

In order to validate the numerical results, comparison has been made with experimental images, as shown in Figure 8.3. A glass capillary (Sigma-Aldrich

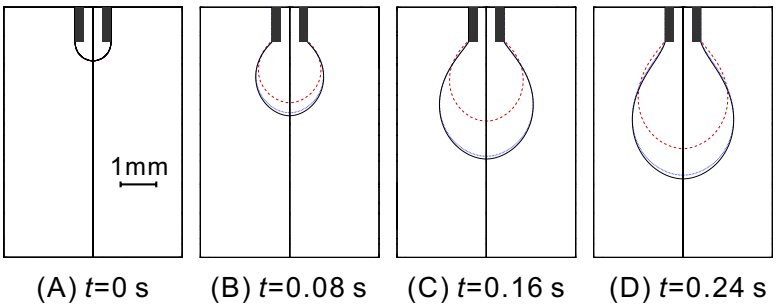

(a)

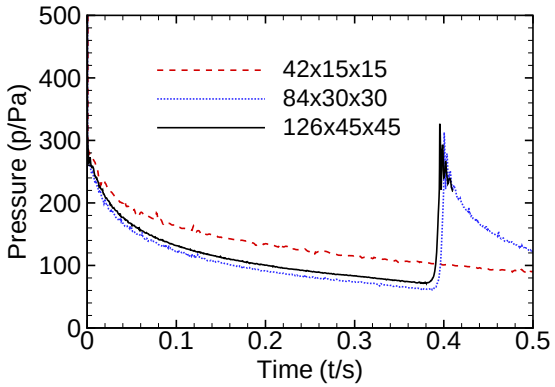

(b)

Figure 8.2: Mesh independence study for pendant drops. (a) Sequences of results for pendant drops simulated with different mesh densities. (b) Upstream pressures in the capillary with different mesh densities. The red dashed line, the blue dotted line, and the black solid line show the numerical results based on mesh densities of $42 \times 15 \times 15$, $84 \times 30 \times 30$, and $126 \times 45 \times 45$ control volumes, respectively. The time step sizes for the three different meshes are 2×10^{-5} s, 1×10^{-5} s, and 0.667×10^{-5} s, respectively. The mesh with $84 \times 30 \times 30$ control volumes, which offers a mesh independent solution by capturing most of the flow features of the interface evolution and the pressure variation, was selected for the following simulations.

P0674) was used and the inner and outer diameters of the capillary are 0.5 mm and 1 mm, respectively. DI water was introduced to the capillary by a syringe pump (KD scientific). The evolution of the pendant drop was recorded by a high speed camera (HiSpec 1, Fastec Imaging) at a frequency of 100 frames per second (fps) together with a lens with magnification ranging from 0.3× to 1× (Computar, Japan).

Initially, the radius of the pendant drop is small, as shown in Figure 8.3**a**. The weight of the pendant drop is supported by the surface tension. As more fluid is introduced into the pendant drop, the size of the pendant drop increases gradually (Figure 8.3**b**). As time passes, the gravitational force increases as the volume of the pendant drop increases. The size of the pendant drop will increase until the surface tension force cannot support the pendent drop. Then the neck of the pendant drop shrinks and finally breaks due to the Plateau-Rayleigh instability (Figure 8.3**c**). The liquid breaks into two parts, the lower part and the upper part. The lower part forms a drop and leaves the simulation domain due to gravity, while the upper part recoils to the tip of the capillary and forms a new pendent drop of a small size. In this way, the pendant drop grows and breaks up periodically. The comparison in Figure 8.3 shows that the numerical results agree well with the experimental results.

(a) (b) (c) (d) (e)

Figure 8.3: Sequence of the growth and pinch-off of a pendant drop from a capillary tip to validate the numerical results. The red lines indicate the numerical prediction of the pendant drop. They are overlaid on the experimental images obtained from a high speed camera. The time for experiments is $t_1 = 0$ s, $t_2 = 0.2$ s, $t_3 = 0.4$ s, $t_4 = 0.6$ s, and $t_5 = 0.8$ s respectively, while the time for the numerical simulation is $t_1 = 0$ s, $t_2 = 0.22$ s, $t_3 = 0.48$ s, and $t_4 = 0.65$ s, $t_5 = 0.84$ s, respectively.

8.3 Results and discussion

8.3.1 Pressure fluctuation for a typical pendant drop

The pressure within the capillary is probed at Point **S**, a typical point on the axis with a distance of 0.5 mm towards the tip, as indicated in Figure 8.4. The pressure at several other locations in the capillary is also probed, and the results at different locations show the same trend. Therefore, the pressure at Point **S** is used as a representative pressure in the capillary, and it is plotted against time in Figure 8.4 during the growth and breakup of a typical pendant drop.

Initially, the pressure in the capillary is relatively large due to the small size of the pendant drop, as shown in Figure 8.4 ($t = 0.05$ s). The pressure in the capillary gradually reduces as the size of the pendent drop increases. The neck of the pendant drop shrinks when the size of the pendant drop reaches such an extent

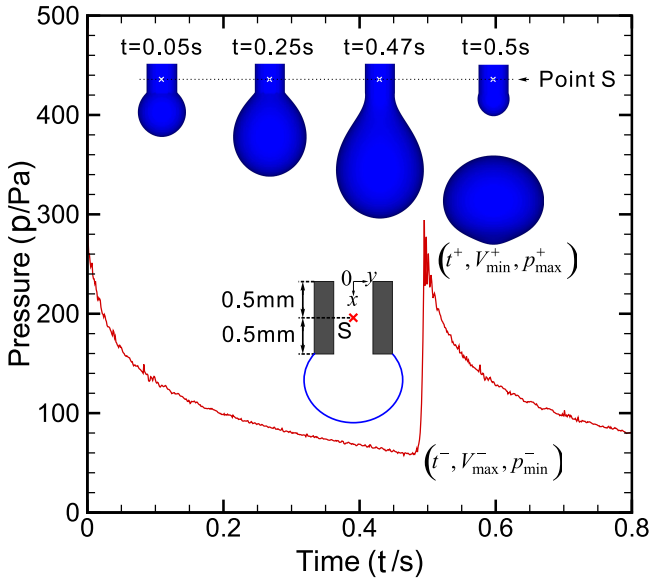

Figure 8.4: Pressure fluctuation within the capillary during the growth and breakup of a typical pendant drop. The dimension of the capillary and the properties of the fluid are as shown in Table 8.1. The pressure is probed at Point **S**, which is located on the axis of the capillary. The coordinate of Point **S** is (0.5 mm, 0, 0), and its distance towards the capillary tip is 0.5 mm.

that the gravitational force is sufficiently large to overcome the surface tension force. Therefore, the critical size of the pendant drop corresponds to the minimum pressure in the capillary ($t = 0.47$ s in Figure 8.4). Then the pendant drop breaks up in such a short period of time that the sudden evolution of the interface causes the pressure in the capillary to increase dramatically. After the breakup of the pendant drop, a new small pendant drop is formed by recoiling of the remnant fluid to the capillary tip, and the corresponding pressure in the capillary is relatively large ($t = 0.5$ s in Figure 8.4). The pendant drop at the tip grows and breaks up periodically and the pressure in the capillary fluctuates correspondingly.

To quantitatively analyze the pressure fluctuation, the magnitude Δp and the

period T of the pressure fluctuation are used. The magnitude Δp is determined by the pressure before and after the pinch-off of the pendant drop, $p^-_{\min}$ and $p^+_{\max}$, i.e.,

$$\Delta p = p^+_{\max} - p^-_{\min} \tag{8.12}$$

The two instants are denoted as t^- (for the instant before the pinch-off) and t^+ (for the instant after the pinch-off), respectively. The volume of the pendant drops at these two instants are $V^-_{\max}$ and $V^+_{\min}$, respectively. Variation of the surface tension σ or variation of $V^-_{\max}$ or $V^+_{\min}$ will affect Δp, since the pressure fluctuation is produced by the Laplace pressure, which is proportional to the surface tension and the curvature, as shown in Eq. (8.7).

The period of the pressure fluctuation T, which is the time interval between two successive pinch-off events at the capillary tip, is another parameter to quantitatively describe the pressure fluctuation. At a fixed volumetric flow rate of liquid Q, the period T is determined by the volume of the pendant drop before and after the pinch-off $V^-_{\max}$ and $V^+_{\min}$,

$$T = \frac{V^-_{\max} - V^+_{\min}}{Q} \tag{8.13}$$

Therefore, factors influencing $V^-_{\max}$ or $V^+_{\min}$ will affect the period of the pressure fluctuation T .

In the next two subsections, two essential factors that affect the magnitude and the period of the pressure fluctuation are investigated, namely the surface tension of the fluid σ and the outer diameter of the capillary tip D_o. The outer diameter, rather than the inner diameter, is used because the contact line of the pendant drop is pinned at the outer circumference during the numerical simulation and experimental observation for DI water and glass capillaries (a wetting condition), as shown in Figure 8.3.

8.3.2 Effect of surface tension on pressure fluctuation

The pressure fluctuation in the capillary for fluids with different surface tensions is shown in Figure 8.5. The magnitude of the pressure fluctuation Δp increases as the surface tension increases. With a larger surface tension, according to Eq. (8.7), a higher Laplace pressure is produced in the pendant drop. Therefore, a larger surface tension results in a larger Δp during the shape evolution of the pendant drop, as shown in Figure 8.5**a**.

The period of the pressure fluctuation T increases as the surface tension increases. This can be explained from the sizes of the pendant drop before and after the pinch-off, which are represented by $V_{\max}^{-}$ and $V_{\min}^{+}$. For fluids with a larger surface tension (σ = 72.8 mN/m), $V_{\max}^{-}$ is larger because a larger surface tension can support more liquid at the capillary tip, as shown in Figure 8.5**b**.D. Therefore, according to Eq. (8.13), a larger surface tension results in a larger period of pressure fluctuation T, and vice versa.

8.3.3 Effect of capillary diameter on pressure fluctuation

The pressure fluctuation in capillaries with different outer diameters D_o is shown in Figure 8.6. The magnitude of the pressure fluctuation Δp increases as the outer diameter decreases. With a large outer diameter (D_o = 1.5 mm), the amplitude of the pressure fluctuation is Δp = 161 Pa. If the outer diameter decreases to D_o = 0.6 mm, the amplitude increases to Δp = 414 Pa. With a fixed surface tension, the effect of D_o on Δp is mainly due to its influence on $V_{\min}^{+}$ at the instant after the pinch-off (t^{+}). The surface tension force at this instant t^{+} is much larger

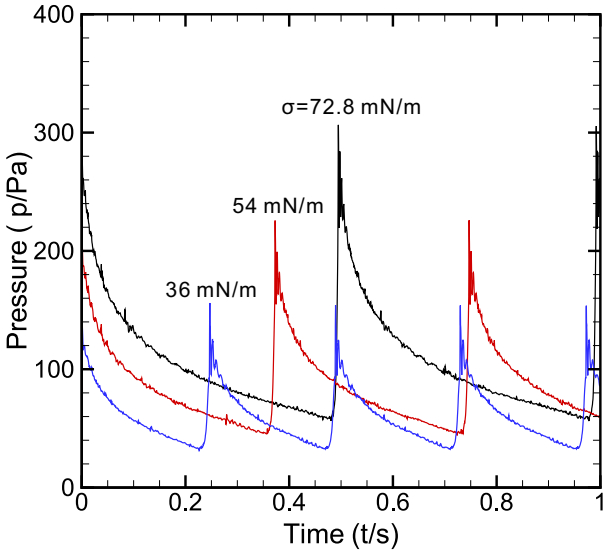

(a)

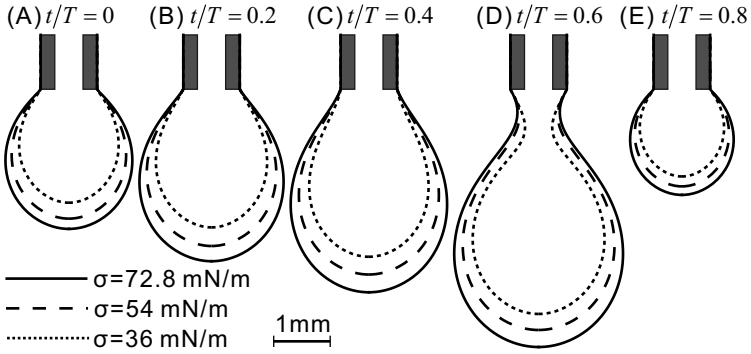

(b)

Figure 8.5: Effect of the surface tension σ on the upstream pressure fluctuation during the growth and breakup of pendant drops. (a) Fluctuation of pressure against time; (b) Image sequences showing the growth and breakup of pendant drops. Using $4Q/(\pi D_o^2)$ as the characteristic velocity, the dimensionless groups are, respectively: (i) for $\sigma = 72.8$ mN/m: $We = 0.034$, $Ca = 6.8 \times 10^{-4}$, $Bo = 0.13$; (ii) for $\sigma = 54$ mN/m: $We = 0.046$, $Ca = 9.2 \times 10^{-4}$, $Bo = 0.18$; (iii) for $\sigma = 36$ mN/m: $We = 0.069$, $Ca = 0.0014$, $Bo = 0.27$. The time intervals between two successive images in (b) are $0.2T$, where T is the period of pressure fluctuation, $T_{\sigma=72.8\text{mN/m}} = 0.50\,\text{s}$, $T_{\sigma=54\text{mN/m}} = 0.37\,\text{s}$, and $T_{\sigma=36\text{mN/m}} = 0.25\,\text{s}$. The dimension of the capillary and the properties of the fluid (except the surface tension σ) are the same as those shown in Table 8.1.

than the gravitational force ($Bo = 0.14$ for $D_o = 1$ mm). The large surface tension force results in a pendant drop with an equilibrium shape of hemisphere, whose size is proportional to D_o, as shown in Figure 8.6**b**.E. Therefore, a larger D_o leads to a larger $V_{\min}^{+}$. Consequently, according to Eq. (8.12), a larger D_o results in a smaller Laplace pressure, and a smaller amplitude of the pressure fluctuation Δp, and vice versa.

The period of the pressure fluctuation T increases as the outer diameter D_o increases. This can be explained from the sizes of the pendant drop before and after the pinch-off, which are represented by $V_{\max}^{-}$ and $V_{\min}^{+}$, respectively. For a capillary with a larger outer diameter (such as $D_o = 1.5$ mm in Figure 8.6), the size of the pendant drop at the instant before the pinch-off $V_{\max}^{-}$ is larger, as shown in Figure 8.6**b**.D. This is because for a larger D_o, the neck connecting the pendant drop and the capillary tip is larger. Since the surface tension force is proportional to the circumference of the neck, a larger neck results in a larger surface tension force, which can support more fluid at the capillary tip until the pinch-off. Consequently, at a fixed flow rate Q, according to Eq. (8.13), a larger outer diameter results in a larger period of the breakup and a larger period of the pressure fluctuation T. When the outer diameter D_o increases from 0.6 mm to 1.5 mm, the period of the pressure fluctuation increases from 0.29 s to 0.77 s, as shown in Figure 8.6.

8.3.4 Shape oscillation after detachment and its effect on upstream pressure fluctuation

At the instant before the detachment of the pendant drop, the pendant drop is stretched with a thin neck connecting the bottom of the pendant drop and the

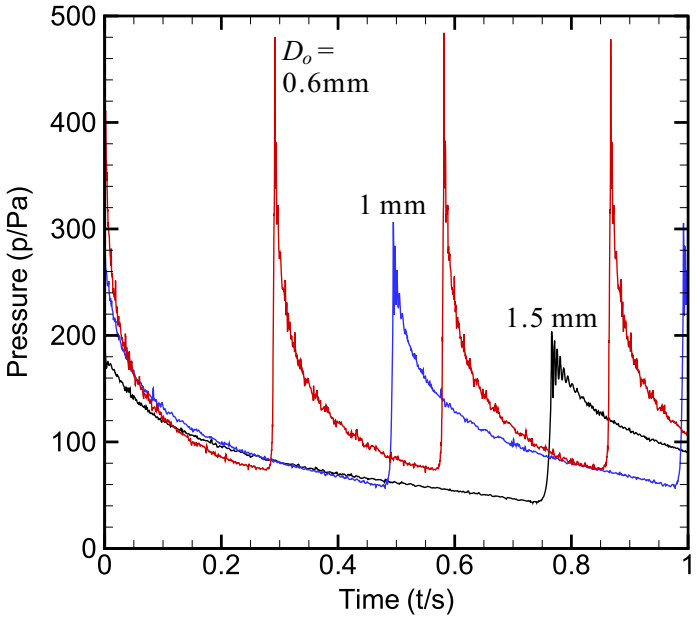

(a)

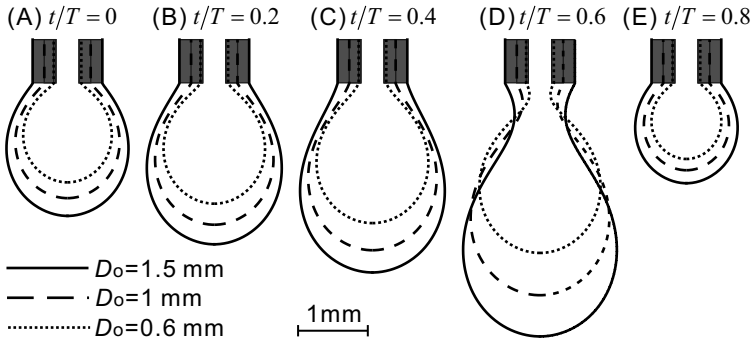

(b)

Figure 8.6: Effect of the outer diameter of the capillary tip D_o on the upstream pressure fluctuation during the growth and breakup of pendant drops. (a) Fluctuation of pressure against time; (b) Image sequences showing the growth and breakup of pendant drops. Using $4Q/(\pi D_o^2)$ as the characteristic velocity, the dimensionless groups are, respectively: (i) for $D_o = 1.5$mm: $We = 0.01$, $Ca = 3\times10^{-4}$, $Bo = 0.3$; (ii) for $D_o = 1$mm: $We = 0.034$, $Ca = 6.8 \times 10^{-4}$, $Bo = 0.13$; (iii) for $D_o = 0.6$ mm: $We = 0.16$, $Ca = 0.0019$, $Bo = 0.049$. The time intervals between two successive images in (b) are $0.2T$, where T is the period of pressure fluctuation, $T_{D_o=1.5\text{mm}} = 0.77$ s, $T_{D_o=1\text{mm}} = 0.5$ s, and $T_{D_o=0.6\text{mm}} = 0.29$ s. The dimension of the capillary (except the outer diameter of the capillary D_o) and the properties of the fluid are the same as those shown in Table 8.1.

fluid at the tip of the capillary, as shown in Figure 8.3**c**. After the breakup of the thin neck, the surface tension will minimize the surface area. The extra surface energy will cause the surface of the pendant drop to deform and oscillate.

The shape oscillation of the pendant drop is investigated by monitoring the bottom region of the pendant drop (indicated by the dashed rectangle in Figure 8.7**a**). The oscillation is quantified by the movement of the lowest point at the bottom region (highlighted by Point **P** in Figure 8.7**a**). The displacement of Point **P** with time is plotted in Figure 8.7**b** together with the pressure variation in the capillary. The deformation of the pendant drop at some representative instants (Points **A** to **F** in Figure 8.7**b**) is shown in Figure 8.7**c**. By comparing the curves of the displacement and the pressure in Figure 8.7**b**, it can be found that the pressure oscillation in the capillary is due to the shape oscillation of the pendant drop.

The forces involved during the oscillation include the surface tension force, the gravitational force, the inertial force, and the viscous force. The relative effects of these forces can be estimated from the dimensionless groups. By setting the outer diameter of the capillary D_o as the characteristic length, the average interface speed (from **A** to **B** in Figure 8.7**b**) as the characteristic velocity, the dimensionless groups are $We = 2.3$, $Ca = 0.0057$, and $Bo = 0.13$, respectively. Therefore, the inertial force and the surface tension force dominate the flow during the oscillation, while the gravitational force and the viscous force are relatively small as compared to the other forces.

At the instant after the breakup of the neck, the bottom of the remnant fluid has a conical shape with a large surface area and a high total surface energy (Figure 8.7**c**.A). The surface tension, which has an effect of minimizing the surface

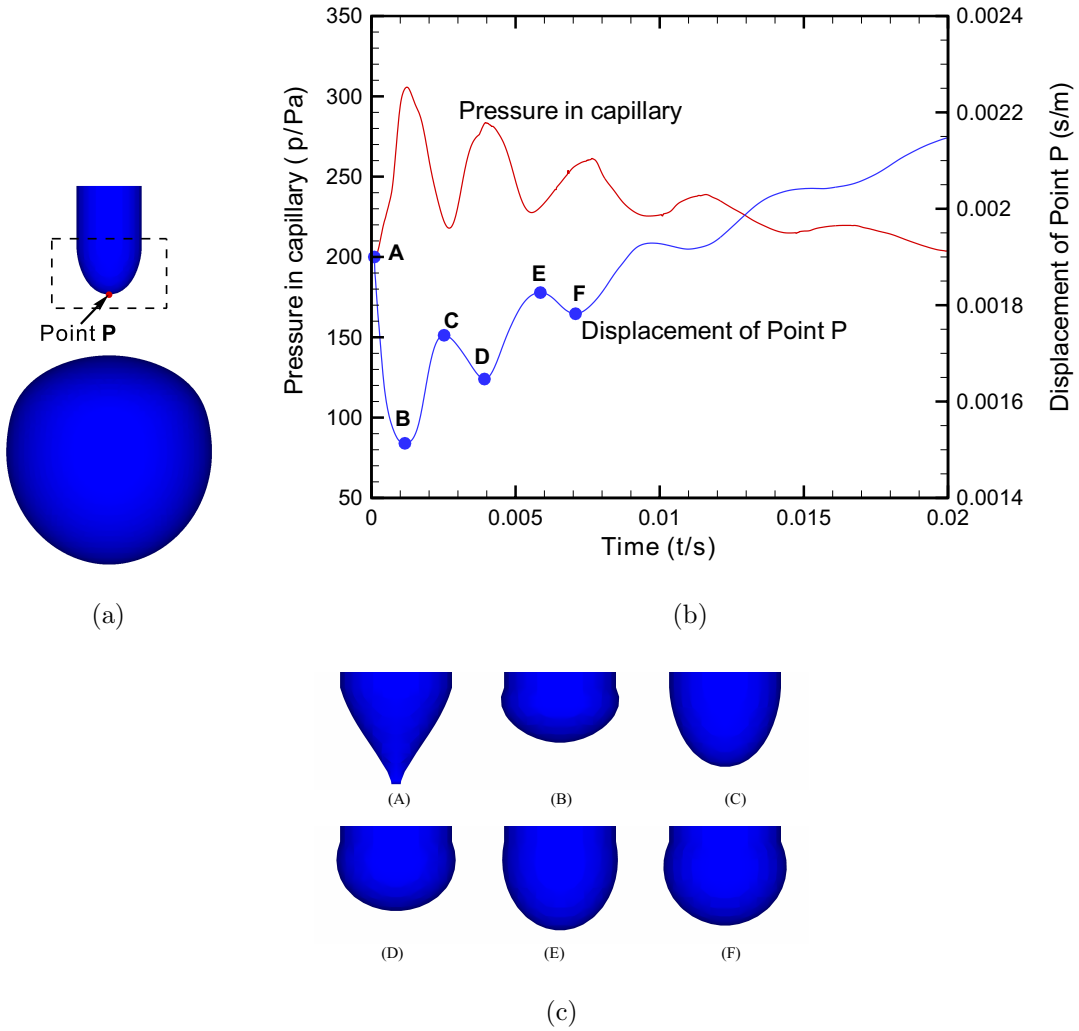

Figure 8.7: Shape oscillation of the pendant drop after the breakup of the liquid neck. (a) The shape of the pendant drop at a typical instant after the breakup of the liquid neck. The dashed rectangular region is monitored to study the shape oscillation. The lowest point (Point **P**) at the bottom of the pendant drop is highlighted. (b) The displacement of Point **P** with time and the corresponding pressure variation in the capillary. (c) Image sequence of the pendant drop in the rectangular region as indicated in (a) at some representative instants (Points **A**–**F** in (b)).

area, pulls the bottom upwards to decrease the surface energy. Hence, the surface energy is partially converted to the kinetic energy of the liquid. A spherical shape, which has a minimum surface area, would be the equilibrium shape if neglecting the gravity. However, the momentum of the liquid will cause an overshoot of the equilibrium shape (Figure 8.7**c**.B) due to the large inertial force. Therefore, the interchange of the surface energy and the kinetic energy produces the shape oscillation of the pendant drop (Figure 8.7**c**.A–F), and correspondingly the pressure fluctuation in the capillary. Although the viscous force is small, it always exists and plays the role of resisting the shape oscillation. Therefore, as time passes, the effect of the viscous force gradually appears, and eventually damps out the shape oscillation of the pendant drop, as shown in Figure 8.7**b**. In addition, after the oscillations are dampen out, the size of the pendant drop increases gradually because the fluid continuously flows into the pendant drop from the capillary. As a results, the displacement of Point **P** continues to grow, and the pressure continues to decrease as time passes.

8.4 A method for surface tension measurement

From the results of the pressure fluctuation for different surface tensions, here a method to measure surface tension is proposed, as schematically shown in Figure 8.8**a**. The sample fluid is pumped into a capillary by a syringe pump at a constant flow rate, and then leaves the capillary by periodical breakup of pendant drops. A pressure sensor can be installed in the capillary to monitor the variation of the pressure. During the growth and pinch-off of pendant drops, the pressure in the capillary fluctuates with a period being the same with that of the pinch-off.

The surface tension of the fluid σ can be determined through the period of pressure fluctuation T.

Comparing with other methods for surface tension measurement, this method has some potential advantages: good accuracy, simplicity, and low cost of the equipment.

(1) **Accuracy**: Based on the simulation results, the period of the pressure fluctuation T is plotted as a function of surface tension σ in Figure 8.8**b**. The good linearity between T and σ facilitate obtaining accurate measurement results. The accuracy can also be easily increased by recording many pinch-off events to find out the average period.

(2) **Simplicity**: The surface tension measurement method through the pressure fluctuation is a simple method since it does not require any instrument for optical acquisition and image analysis. A pump, a capillary, and a pressure sensor constitute the essential parts of the measurement system, as schematically shown in Figure 8.8**a**.

(3) **Low cost**: Due to the simplicity, the cost of this measurement system is much lower than that of traditional optical methods for surface tension measurements.

8.5 Summary

In this chapter, the growth and breakup of pendant drops were investigated numerically and their effects on the upstream pressure fluctuation were analyzed. To study the growth and breakup process of pendant drops, three-dimensional

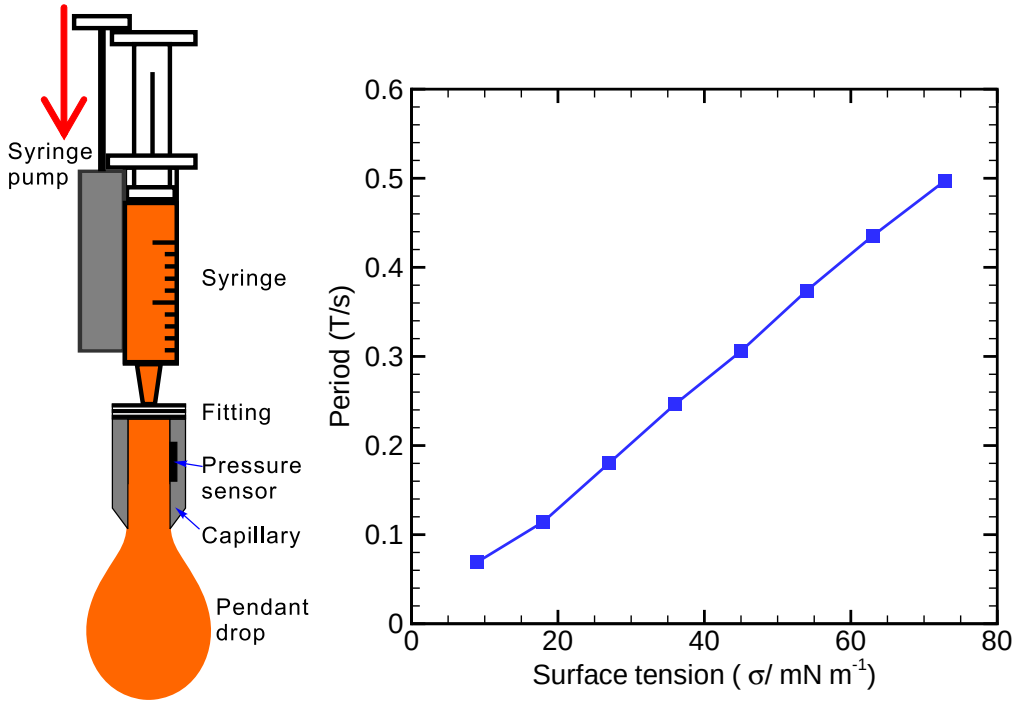

(a) (b)

Figure 8.8: (a) Schematic diagram of a surface tension measurement method through pressure fluctuation during the growth and breakup of pendant drops. (b) Numerical results of pinch-off periods of pendant drops for liquids with different surface tensions. The fluid properties (except the surface tension) and the capillary geometry are the same as those listed in Table 8.1.

numerical simulation was carried out with the level set method to predict the interface shape. The program was validated against experimental images showing the growth and breakup of pendant drops. By varying the surface tension of the fluids and the outer diameter of the capillary, the effects of the surface tension and the outer diameter on the pressure fluctuation were analyzed. For fluids with a larger surface tension, the magnitude of the pressure fluctuation is larger, and the period is longer. For a larger capillary outer diameter, the magnitude of the pressure fluctuation is smaller, and the period is longer. The simulation results also

show high frequency pressure fluctuation after the instant of breakup. The high frequency pressure fluctuation is caused by the surface oscillation due to the excess surface energy after the breakup, and is gradually damped out by the viscosity of the fluids.

Based on the results in this study, a method for surface tension measurement is proposed. Due to the good linear relationship between the surface tension and the pinch-off period, the surface tension can be measured by detecting the period of the pressure fluctuation in the capillary. The method of surface tension measurement is believed to be accurate, simple, and low-cost.

Chapter 9

Formation and Breakup of Compound Pendant Drops at the Tip of a Capillary †

9.1 Introduction

In the previous chapter, the leaving of fluids from a capillary in the form of pendant drops were studied, which results in upstream pressure fluctuation. When the fluid in microchannels/microcapillaries containing dispersed bubbles/droplets, the leaving of fluids at the outlet of microchannels/microcapillaries will be in the form of compound pendant drops (CPD), i.e., pendant drops containing smaller bubbles or droplets in them (Johnson and Sadhal, 1985). Compound drops have many promising applications in pharmaceutical industry, food industry, and waste water management. The behaviours of compound drops have been studied in various flow conditions, such as moving in quiescent flow (Johnson and Sadhal, 1985), impact

†This work has been published in *International Journal of Heat and Mass Transfer 5 (4) 1022-1029.*

on flat surfaces (Tasoglu et al., 2010), flow under thermocapillarity (Borhan et al., 1992; Rosenfeld et al., 2009), formation in microcapillaries (Utada et al., 2005) and in microchannels (Okushima et al., 2004), synthesis of polymeric microparticles (Dendukuri and Doyle, 2009; Park et al., 2010). The combination of pendant drops with compound drops will result in many distinctive flow phenomena, and may trigger novel applications in chemical engineering, food processing industry, and pharmaceutical industry. For example, the capillary can be used as a tool to transfer or deliver an individual compound drop by hanging the compound pendant drop at the capillary tip with the inner fluid intact. The outer phase of the compound pendant drops can serve as vials for reactions or syntheses in the inner fluid, in which the processes of reactions or syntheses can be controlled individually and accurately. The outer phase can also be used as a protective layer for the inner phase, such as food additives, drugs, or personal care products. If the inner phase is volatile or/and harmful to the environment, the outer phase can also minimize the mass transfer from the inner phase to the surrounding fluid. However, to the best of the author's knowledge, the formation and breakup of compound pendant drops has never been studied before.

In this chapter, the formation and breakup process of CPDs at a vertical tip of a capillary are studied. During the formation and breakup, if a constant velocity is maintained at the upstream of the capillaries or microchannels, the simple or compound pendant drop causes large variation of Laplace pressure, as discussed in Chapter 8. In contract, if a constant pressure is maintained in the upstream, the upstream velocity may fluctuate. The upstream velocity fluctuation can be welcome or unwelcome, depending on the application. A stable flow is required

in applications such as detections in capillaries or microchannels. In order to get accurate results, the time for the samples to pass through the detection zone in capillaries or microchannels, should be controlled in an accurate manner (deMello, 2006; Janasek et al., 2006). For reaction applications, the reaction time is a key factor influencing the products and should be accurately controlled (Song et al., 2003a). Therefore, velocity fluctuation should be avoided in these applications. On the contrary, velocity variation is preferred in some other applications, such as in micromixing (Niu and Lee, 2003; Nguyen and Huang, 2005; Ma et al., 2008). The perturbation of velocity oscillation can enhance the mixing process by twisting the trajectory of the fluid particles and by stretching and folding the fluids layers (Ottino, 1989; Aref, 2002). Steijn et al. (2007) studied the velocity fluctuation of gas/liquid plug flow in a microchannel, and they found that the velocity variation can be up to 30% of the mean velocity. Beer et al. (2009) confirmed this effect for liquid/liquid systems. However, to the best of the author's knowledge, the velocity fluctuation produced by formation and breakup of simple and compound pendant drops has not been studied.

This chapter is organized as follows. First, the experimental details are described in Section 9.2, including the microchannel setup, the properties of the fluids, and the flow visualization method. Then, the experimental results are provided and analyzed in Section 9.3. The stages of formation and breakup of CPDs are identified from sequences of images. The velocity fluctuation caused by the formation and breakup of CPDs is analyzed, and the effect of surfactant is investigated. The size distribution of the produced compound drop is quantified.

9.2 Experimental

9.2.1 Formation of compound pendant drops

The experimental setup is shown schematically in Figure 9.1**a**. To form CPDs at the tip of a capillary, air/water plug flow was generated using a horizontal flow focusing geometry in a polymethylmethacrylate (PMMA) channel. A glass capillary was connected to the outlet of the microchannel perpendicularly to the PMMA channel and positioned downwards. The air bubbles and the water plugs travel in the horizontal PMMA flow channel (Figure 9.1**b**), subsequently flow into the glass capillary, and finally leave the capillary in the form of CPDs at the tip of the capillary (Figure 9.1**c**).

The flow focusing geometry (Figures 9.1**b**) was fabricated on a cast PMMA sheet with thickness of 1 mm (Ying Kwang Acrylic Trading, Singapore). Three layers of PMMA were cut by CO_2 laser cutting platform (Universal M-300, USA). They were subsequently aligned and bounded. At the outlet of the PMMA flow channel, a glass capillary (Sigma-Aldrich P0674, USA) was connected perpendicularly in the downward direction. The inner diameter (D_i) and the outer diameter (D_o) of the capillary are 0.5 mm and 1 mm, respectively. The glass capillary was cut to a length of 91 mm.

To avoid the breakup of bubbles at the connecting point between the PMMA microchannel and the glass capillary, a step structure was fabricated on the PMMA microchannel, as shown in Figure 9.1**d**. The step structure is of a circular shape with the inner/outer diameters being the same as the inner/outer diameters of the

glass capillary, which facilitates the alignment between the microchannel and the glass capillary, and ensures a smooth fluid flow to the glass capillary. Epoxy was applied at the corner to permanently connect the PMMA channel and the glass capillary. An image of the microchannel with the capillary tip connected is shown in Figure 9.1**e**.

To form air/water plug flow in the PMMA microchannel, air was used as the dispersed phase and was introduced by a constant pressure through a water column of 14 cm. DI water with/without surfactant sodium dodecyl sulfate (SDS) (Sigma-Aldrich L4509, USA) was used as the continuous phase, and was introduced by a syringe pump (KD scientific, USA). The properties of air, DI water, and the SDS solution (2% by weight in DI water) are listed in Table 9.1. The surface tension of the SDS solution was measured using the pendant drop method by an FTA 200 system (First Ten Ångstroms, USA).

9.2.2 Image acquisition and processing

The flow in the glass capillary was recorded by a CCD camera (PULNiX TM-6701AN, USA). The frame rate of the CCD camera was 30 frames per second (fps) during the experiment. A lens with a focal length of 16 mm (TAMRON, Japan) was mounted on the CCD. A white plate was used to provide a clear background for the CCD image. A halogen lamp was used to shine light on the background to

Table 9.1: Properties of the fluids.

	Air	Water	SDS solution
Density (kg/m^3)	1.204	997	997
Viscosity (Pa·s)	1.84×10^{-5}	1×10^{-3}	1×10^{-3}
Surface tension (mN/m)		72.8	36.16

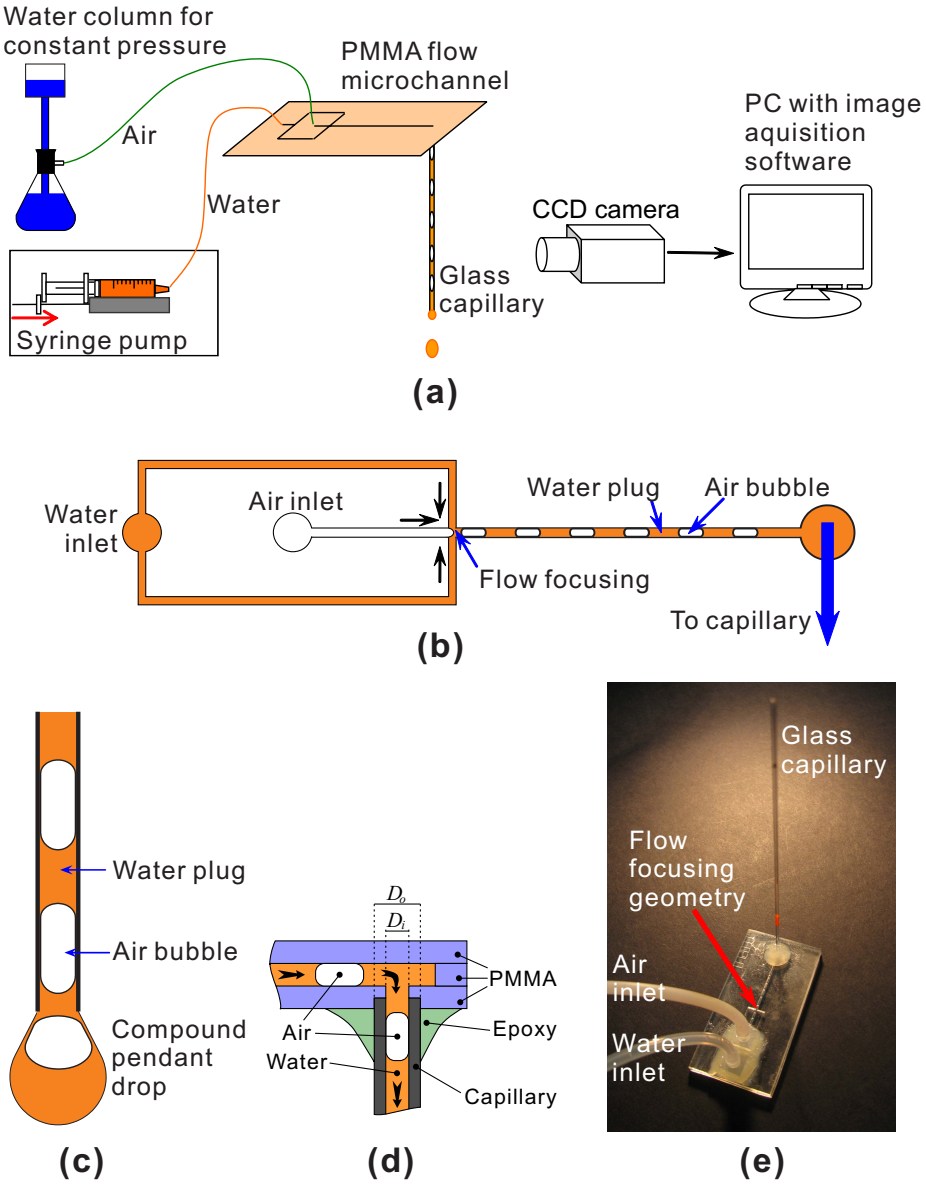

Figure 9.1: Experimental setup: (a) Schematic diagram of the experimental setup; (b) Schematic diagram of the air bubble formation in the microchannel; (c) Schematic diagram of the air/water plug flow in the capillary and the compound pendant drop at the tip of the capillary; (d) Schematic diagram of the connection between the PMMA channel and the glass capillary. (e) Image of the microchannel with a glass capillary connected to the outlet of the microchannel.

provide the illumination for the image acquisition.

The image sequences of the air/water plug flow in the glass capillary was exported and processed by a customized MATLAB program. The velocity of the fluids was obtained by comparing the positions of the front and the rear of the bubble in every two successive frames of the video. The image processing procedure are illustrated in Figure 9.2 and listed as follows: (a) Read the video file. (b) Crop the region of the capillary. (c) Average many frames to get the background image. (d) Subtract the background image in each frame to obtain the bubbles in the images, and increase the contrast. (e) Convert the grayscale images to black-and-white binary image. (f) Take the average of the brightness. (g) Take the gradient of the black-and-white binary images to find out the location of the front and rear of the bubbles. (h) Calculate the velocities of the fronts/rears of the air bubbles by comparing two successive frames. Average the velocities of the fronts/rears of the bubbles and take the average as the velocity of the fluids at that time. They are calculated as follows,

$$u(t_k) = \frac{1}{N} \sum_{i=1}^{N} \frac{\Delta x_i}{t_{k+1} - t_k} \tag{9.1}$$

where t_k and t_{k+1} are the time for the two successive frames, Δx_i is the displacement of the fronts/rears of the air bubbles between the two successive frames, N is the number of fronts and rears of the air bubbles in the observing window.

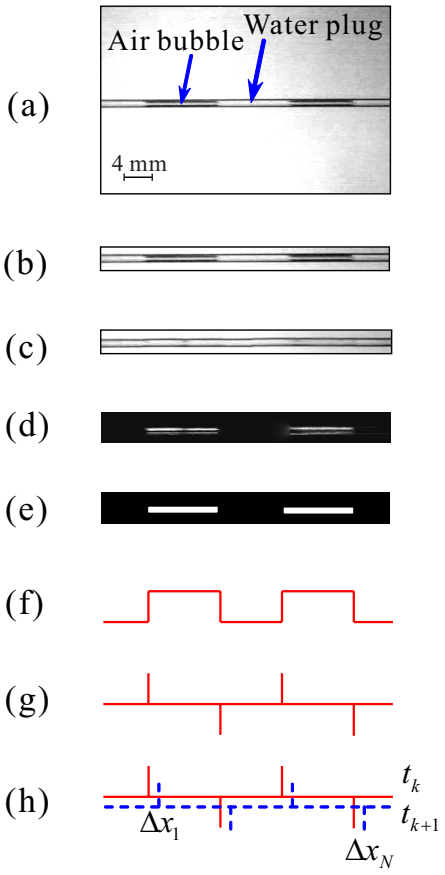

Figure 9.2: Procedure of image processing to obtain the velocity from the experimental video: (a) A typical frame of the video; (b) Cropping the region of the capillary for further analysis; (c) The background image obtained by averaging many frames; (d) Subtracting the background image in each frame to obtain the bubbles in the images; (e) Converting the grayscale images to black-and-white binary image to get a clear bubble; (f) Averaging the image pixels by column to get the profile; (g) Taking the gradient of the profile to find out the location of the front and rear of the bubbles; (h) Calculating the velocities of the front and rear of the bubble by comparing two successive frames. Averaging the velocities of the fronts and the rears of the bubbles and take the average $u(t_k)$ as the velocity of the fluids at that time t_k.

9.3 Results and discussion

9.3.1 Formation and breakup of CPDs for air/water system

The formation and breakup of CPDs at the tip of a vertical capillary shares some common features with simple pendant drops. However, due to the presence of the gas bubbles, the formation and breakup of CPDs is more complex, and it has many distinctive features different from the simple pendant drops. To study the dynamics of CPDs, a high speed camera (Fastec HiSpec 1, Fastec Imaging, USA) and a macro lens with magnification of 0.3× to 1× (Computar, Japan) was used to focus at the tip of the glass capillary.

The typical stages in time sequence of the formation and breakup of a CPD are summarized as follows. After the breakup of the previous CPD, a small amount of liquid is left at the tip of the capillary, which forms a small pendant drop. (I) *Initialization*: Firstly, an air bubble in the capillary flows into the small liquid pendant drop to initialize a small CPD, as shown in Figure 9.3. (II) *Accumulation*: A liquid plug flows into the CPD, and the liquid in the CPD accumulates. The CPD increases in weight and in size, as shown in Figure 9.4. (III) *Coalescence*: An air bubble flows into the CPD, and it coalesces with the existing air bubble in the CPD. The CPD increases in size, as shown in Figure 9.5. (IV) *Breakup*: Stages II and III repeat, until the CPD reaches a critical weight, then the CPD finally breaks up to produce a compound drop, as shown in Figure 9.6. The four stages repeat and CPDs are formed and breaks up periodically. Each stage is analyzed in detail in the following subsections.

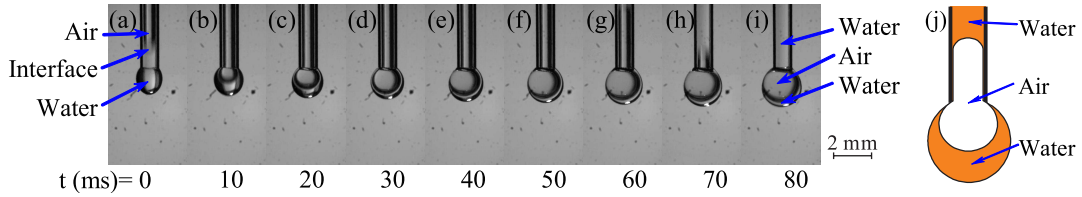

Figure 9.3: Initialization of a small compound pendant drop by entering an air bubble into a small pendant drop: (a–i) Sequence of images; and (j) Schematic illustration.

9.3.1.1 Initialization of a small compound pendant drop

After the breakup of the previous CPD, a small liquid pendant drop is left at the tip of the glass capillary. Due to the small size of the liquid pendant drop, the gravitational force is negligible. Hence, the pendant drop is almost spherical, as shown in Figure 9.3**a**. As the first air bubble flows into the pendant drop, it experiences a scenario that part of the bubble is in the capillary and the rest is in the pendant drop. This is shown in Figure 9.3**b**–**h**, while the schematic illustration is shown in Figure 9.3**j**. The part of the bubble in the pendant drop is almost spherical due to its small size. As the whole air bubble enters into the pendant drop, it relaxes to spherical shape due to the effect of surface tension, as shown in Figure 9.3**i**. This step marks the end of Stage I and the beginning of Stage II.

9.3.1.2 Accumulation of liquid in the compound pendant drop

With an air bubble relaxes to spherical shape from Stage I in the CPD, the flow of water into the CPD is affected by the presence of the air bubble. Due to gravity, water is accumulated at the bottom, while the air bubble remains at the top of the CPD, as shown in Figure 9.4**a**. The air bubble partially blocks the outlet of the capillary. After flowing out of the capillary, water flows to the bottom of the

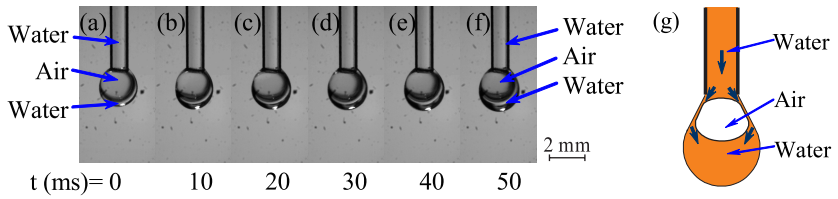

Figure 9.4: Accumulation of liquid in the compound pendant drop: (a–f) Sequence of images and (g) Schematic illustration.

CPD through the thin liquid film on the side of the bubble, as shown in the image sequence Figure 9.4**a**–**f**, while the schematic illustration is shown in Figure 9.4**g**. It was observed that the bubble on the axis of the capillary centreline is unstable, as it experiences the pushing force by the water flowing from the capillary. Consequently, the water pushes the bubble off the axis to reduce the flow resistance, which causes the CPD to vibrate.

9.3.1.3 Coalescence of bubble with the subsequent air bubble

After a liquid plug flows out of the capillary into the CPD, an air bubble begins to flow out of the capillary and coalesce with the existing bubble in the CPD and Stage III begins, as shown in Figure 9.5. When the air bubble leaves the capillary, it coalesces with the existing bubble in the CPD immediately (Aarts et al., 2005; Aarts and Lekkerkerker, 2008; Chan et al., 2011), and forms a larger bubble inside the CPD, as shown in Figure 9.5**b**–**e**, while the schematic illustration is shown in Figure 9.5**j**. During the coalescence process, the surface area of the bubble is minimized, and surface energy is released. The extra energy will cause the CPD to vibrate slightly. The vibration of the CPD dissipates as time passes.

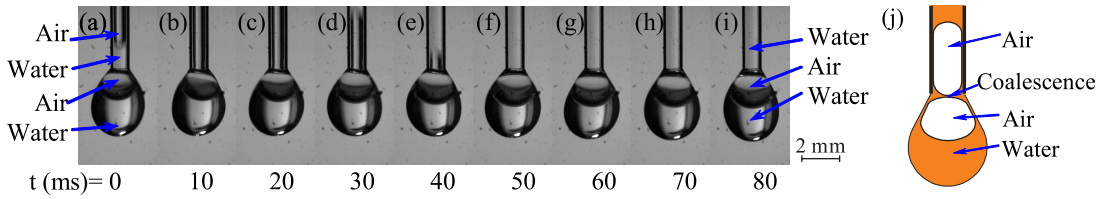

Figure 9.5: Coalescence of the bubble in the CPD with the subsequent air bubble: (a–i) Sequence of images; and (j) Schematic illustration.

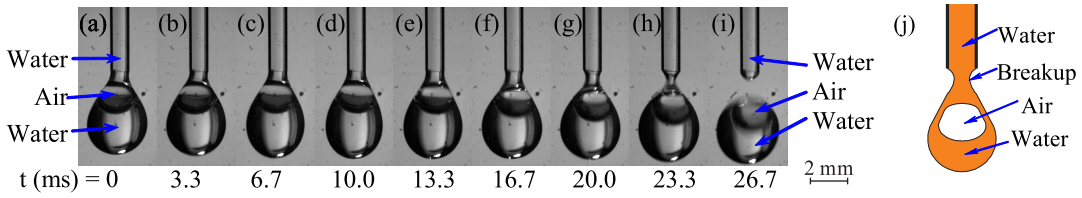

Figure 9.6: Breakup of the CPD: (a–i) Sequence of images; and (j) Schematic illustration.

9.3.1.4 Breakup of the compound pendant drop

As more water plugs and air bubbles enter the CPD alternatively, the accumulation of fluids causes the CPD to grow both in weight and in size. The breakup of the CPD, as shown in Figure 9.6, happens when the gravitational force is sufficiently large that the surface tension force cannot support the weight of the CPD. The neck of the CPD shrinks due to the pulling of the gravitational force, as illustrated in Figure 9.6**j**. Plateau-Rayleigh instability (Michael, 1981) accelerates the breakup of the CPD, and a compound drop is formed, where the air bubble is fully engulfed by the water phase, as shown in Figure 9.6**i**.

After the breakup of the CPD, the remaining liquid at the tip of the capillary recoils to form a new pendant drop of small size. The stages of initialization, accumulation, coalescence, and breakup repeat as more air bubbles and water plugs

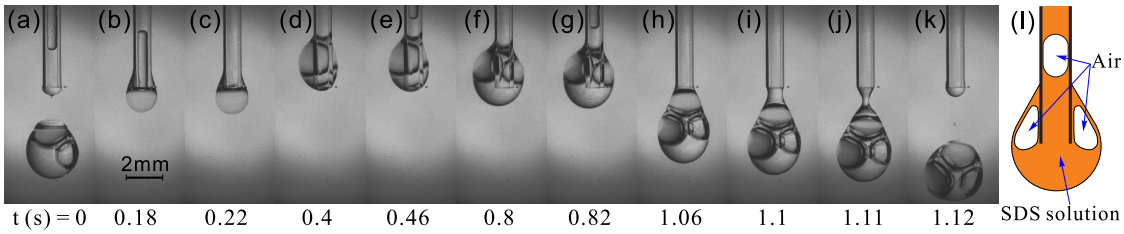

Figure 9.7: Formation and breakup of CPDs for air/SDS-solution system: (a–k) Sequence of images; and (l) Schematic illustration.

are introduced to the tip of the capillary.

9.3.2 Formation and breakup of CPDs for air/SDS-solution system

For the air/SDS-solution system, a significant difference from the air/water system is that the bubbles in CPDs do not coalesce, as show in Figure 9.7. This is because the surfactant SDS reduces the air/water surface tension, and stabilizes the thin liquid film between bubbles by reducing film fluctuations (Tadros, 2005).

Another difference between the air/water system and the air/SDS-solution system is about the contact line of the liquid on the capillary during the formation and breakup of the CPDs. For the CPDs of the air/water system, the contact line is fixed at the outer circumference of the capillary tip, as shown in Figures 9.3–9.6. In contrast, for the CPDs of the air/SDS-solution system, the contact line moves with time. After the breakup of the previous CPD, the contact line of the liquid climbs the capillary. This is because the surfactant increases the wettability of the liquid on the capillary. A simple measurement of contact angles confirmed that by adding SDS into the DI water, the contact angle decreases from 61° to 31°

(see Appendix F for details). With the accumulation of fluids in the CPD, the contact line moves downwards along the capillary until the CPD reaches a critical weight that the surface tension force cannot support, as shown in Figure 9.7**h** and illustrated in Figure 9.7**l**. Then the neck of the CPD immediately shrinks off, and forms a compound drop with several bubbles in it, as shown in Figure 9.7**k**.

Due to the movement of the contact line during the growth of the CPD, the bubble in the CPD may ascend to the vicinity of the contact line due to the buoyancy, as shown in Figures 9.7**d**–**g**. Therefore, the shape of the CPD becomes asymmetric due to presence of the bubbles around the capillary.

9.3.3 Upstream velocity fluctuation caused by the breakup of compound pendant drops

Figure 9.8 illustrates the mechanisms of the breakup at the capillary tip affecting the upstream flow. As a pendant drop is formed at the tip, the Laplace pressure $\Delta p(t)$ depends on the size of the drop. Initially, the radius of the pendant drop is small, which results in a large Laplace pressure. As more fluids accumulate in the pendant drop (Stages II and III), the size of the pendant drop increases, and the Laplace pressure decreases gradually. This process continues until the breakup of the pendant drop, which results in a minimum pendant drop and a maximum Laplace pressure. The sudden increase in the Laplace pressure during the breakup will decelerate the flow in the capillary. The periodic breakup of pendant drops causes velocity fluctuation in the capillary. The fluctuated velocity in the capillary was recorded in the observation window, as shown in Figure 9.8.

The velocity fluctuation in the capillary $u(t)$ was calculated from the

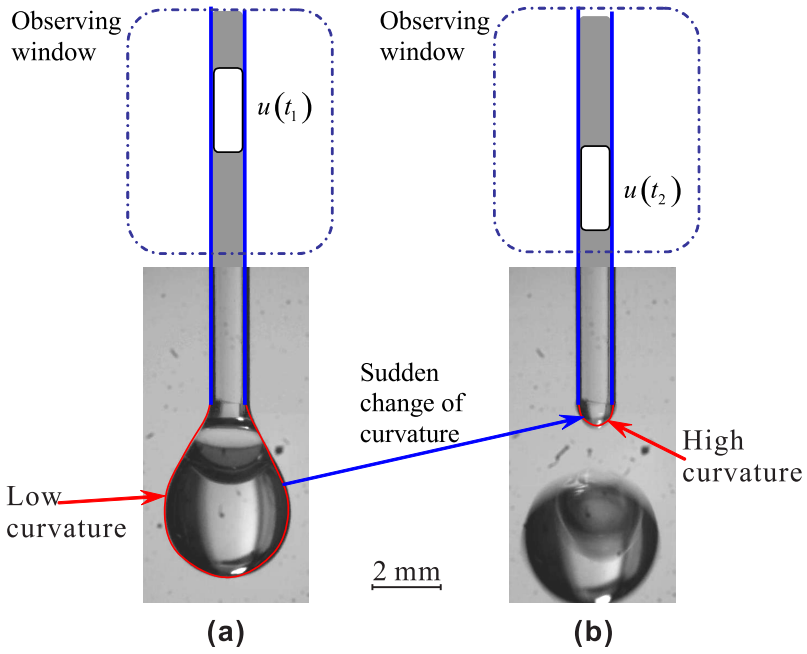

Figure 9.8: Schematic diagram of the upstream velocity fluctuation caused by the breakup of CPDs: (a) The large radius the CPD produces a low curvature, a low Laplace pressure, and a low pressure inside the capillary. (b) The small size of the CPD after the breakup produces a high curvature, a high Laplace pressure, and a high pressure inside the capillary. The sudden increases in the curvature will increase the pressure in the capillary (from $p(t_1)$ to $p(t_2)$) and decelerate the flow in the capillary (from $u(t_1)$ to $u(t_2)$). The velocity fluctuation was recorded at the observation window.

sequences of images using Eq. (9.1). Figure 9.10 shows the variation of the normalized velocity with time in the upstream at different flow rates. The normalized velocity is defined as

$$\hat{u}(t) \equiv \frac{u(t)}{U} \tag{9.2}$$

where U is the time-average velocity, which is defined as

$$U \equiv \frac{1}{T}\int_0^T u(t)\,dt \tag{9.3}$$

where T is the selected time period that U remains unchanged. In the analysis, T

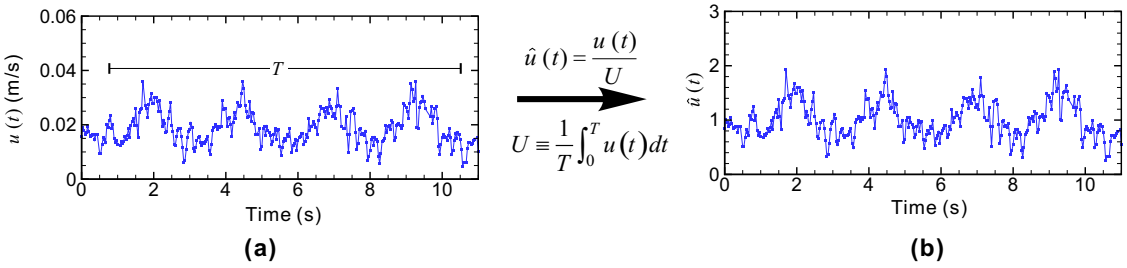

Figure 9.9: The velocity of the fluid $u(t)$ is normalized by U, which is the average velocity of the fluid over interval T. (a) Absolute velocity of the fluid $u(t)$; (b) Normalized velocity of the fluid $\hat{u}(t)$.

is selected about four periods of the fluctuation, as illustrated in Figure 9.9. After the normalization, $\hat{u}(t)$ preserves the feature of the velocity fluctuation, and gives a clear view of the relative magnitude of the velocity fluctuation.

The volume fractions of the air at different flow rates of DI water were measured from the images of the air/water plug flow in the capillary as follows

$$f_{\text{air}} \equiv \frac{L_{\text{air-bubble}}}{L_{\text{air-bubble}} + L_{\text{water-plug}}} \tag{9.4}$$

where $L_{\text{air-bubble}}$ and $L_{\text{water-plug}}$ are the lengths of the air bubbles and the water plugs in the images. For the air/water system, when the flow rate of DI water increases from 0.6 ml/min to 0.9 ml/min, the volume fraction of the air decreases from 0.42 to 0.32.

The velocity fluctuation of air/water system is shown in Figure 9.10. With increasing the flow rate, the magnitude of the fluctuation of the normalized velocity decreases. This is due to the fact that with increasing the flow rate, the time average velocity U increases proportionally. But the size of the pendant drop remains almost unchanged, which causes the Laplace pressure within the pendant drop nearly unchanged. Therefore, the fluctuation of the normalized velocity $\hat{u}$

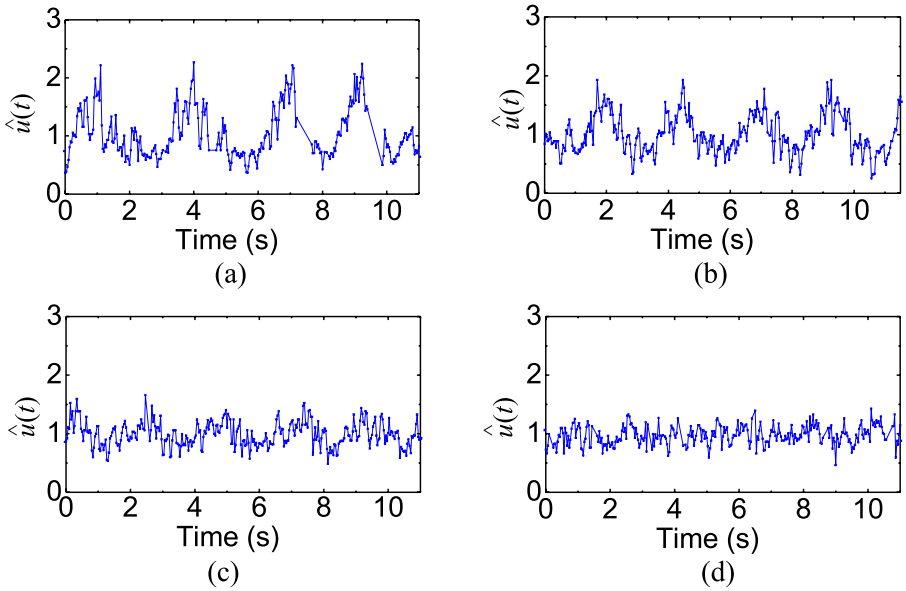

Figure 9.10: Velocity fluctuations in the capillary for CPDs of the air/water system at different flow rates of DI water. The flow rates are (a) 0.6 ml/min, (b) 0.7 ml/min, (c) 0.8 ml/min, and (d) 0.9 ml/min, respectively. The superficial velocities of the water stream are 5.1, 5.9, 6.8, and 7.6 cm/s, respectively, and the volume fractions of air f_{air} are 0.42, 0.40, 0.33, and 0.32, respectively.

decreases.

Figure 9.11 shows the variation of normalized velocity for the air/SDS-solution system. By adding the surfactant into DI water, the surface tension is reduced from 72.8 mN/m to 36.16 mN/m, as shown in Table 9.1. Because the Laplace pressure is proportional to the surface tension, a smaller surface tension results in a smaller Laplace pressure, and a smaller magnitude of velocity fluctuation. Another reason of reducing the velocity fluctuation by the surfactant may be due to the movement of the contact line for the air/SDS-solution system as discussed in Section 9.3.2. For the air/water system, the contact line is fixed at the outer circumference of the capillary tip during the formation and the breakup

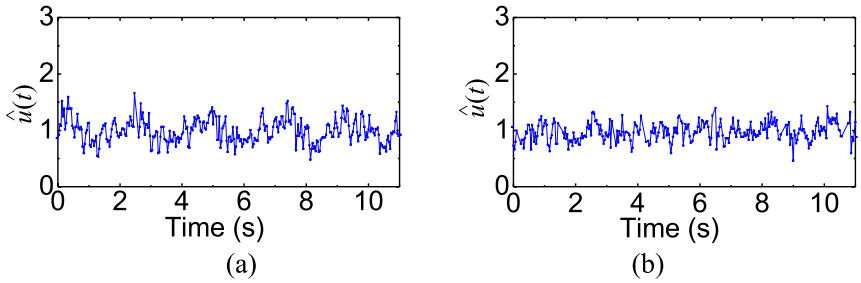

Figure 9.11: Velocity fluctuations in the capillary for CPDs of the air/SDS-solution system at different flow rates of the SDS solution. The flow rates are (a) 0.6 ml/min, and (b) 0.9 ml/min, respectively. The superficial velocities of the SDS solution are 5.1 and 7.6 cm/s, respectively, and the volume fractions of air f_{air} are 0.57 and 0.49, respectively.

of the CPDs. After the pinch-off of the previous CPD, a new small CPD results in a large Laplace pressure and a large magnitude of velocity fluctuation. In contrast, for the air/SDS-solution system, the surfactant reduces the contact angle of the liquid on the glass capillary. The contact line moves upwards along the capillary when the CPD is small. The upward movement of the contact line results that the CPD engulfs the capillary tip, which increases the visual volume of the CPD (i.e., the volume wrapped by the surface of the CPD) and decreases the curvature. Therefore, the movement of the contact line may reduce the variation of the Laplace pressure and reduces the velocity fluctuation in the upstream.

9.3.4 Size distribution of the compound drops

The size of the compound drops produced by the breakup of CPDs depends on two breakup events, (i) the generation of bubbles in the flow focusing geometry in the microchannel, and (ii) the breakup of CPDs at the tip of the glass capillary. In the microchannel, the flow focusing geometry has the capability to produce

monodisperse bubbles when working in the squeezing or dripping regimes (Anna et al., 2003; Christopher and Anna, 2007), during which the capillary number is low. When the capillary number is sufficiently high, breakup of bubbles happens in the jetting regime, during which the bubbles are polydisperse. The second breakup event, i.e., the breakup at the capillary tip, may occur in the dripping or jetting regimes depending on the Weber number We, which characterizes the relative effect between the inertial force and the surface tension force. Dripping of drops at the capillary tip happens when We is small. In the dripping regime, the drops produced at the capillary tip are monodisperse. Therefore, the system used in this study has the potential to produce monodisperse compound drops when (i) the breakup of bubbles at the flow focusing junction is in the squeezing or the dripping regime, and (ii) the breakup of CPDs at the capillary tip is in the dripping regime.

To characterize the size distribution of the compound drops produced by breakup of the CPDs, the sizes of the compound drops were measured from the high speed images using a customized MATLAB program, i.e., A_{pixel}, the area of the compound drops in images by pixel. The histogram of A_{pixel} was plotted in Figure 9.12**a**. The histogram of A_{pixel} shows that the size of the compound drops are monodisperse with a polydispersity of $\zeta_{A_{\text{pixel}}} = 8.5\%$, which is defined as the standard deviation of A_{pixel} divided by the average value of A_{pixel}.

Because there are two immiscible fluids (liquid and gas) in each compound drops, the consistency of the liquid volumes in different compound drops is important to ensure the monodispersity of the compound drops. Since the liquid was introduced into the microchannel at a constant flow rate, the volume of the liquid in a compound drop could be calculated from the time interval between two

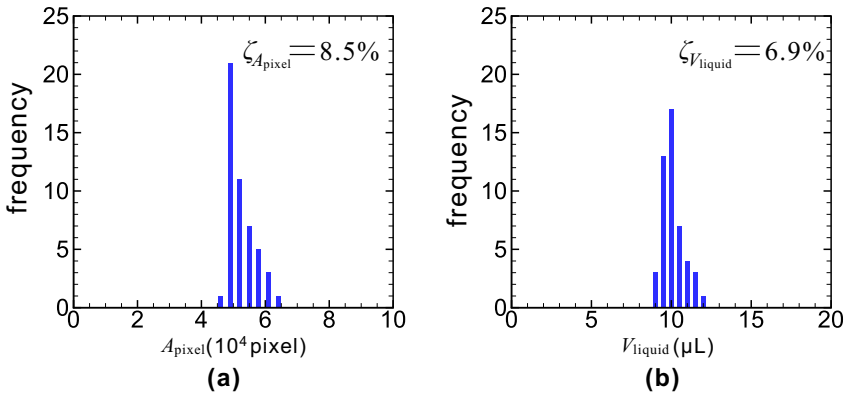

Figure 9.12: Size distribution of the compound drops produced by breakup of CPDs at the capillary tip. The liquid is the SDS solution (2% by weight in water), and its flow rate is 0.6 ml/min. (a) Histogram of the area of the compound drops A_{pixel} measured from high speed images. (b) Histogram of the liquid volume V_{liquid} determined by counting the frames of the high speed images (500 fps) between two consecutive breakup events at the capillary tip.

consecutive breakup events at the capillary tip ΔT.

$$V_{\text{liquid}} = Q\Delta T \tag{9.5}$$

The time interval ΔT was determined by counting the frames of the high speed images (500 fps) between two consecutive breakup events at the capillary tip. The histogram of V_{liquid} was plotted in Figure 9.12**b**, which shows that the liquid volumes in different compound drops are monodisperse. The polydispersity of V_{liquid} is $\zeta_{V_{\text{liquid}}} = 6.9\%$, which is defined as the standard deviation of V_{liquid} divided by the average volume of V_{liquid}.

9.4 Summary

In this chapter, the formation and breakup of compound pendant drops has been experimentally investigated. Four typical stages for the air/water system have been identified: (1) initialization of a small compound pendant drop, (2) accumulation of liquid in the compound pendant drop, (3) coalescence of the bubble with the subsequent air bubble, and finally (4) breakup of the compound pendant drops. These four stages of initialization, accumulation, coalescence, and breakup repeat as more air bubbles and water plugs are introduced to the tip of the capillary. For the air/SDS-solution system, due to the presence of the surfactant, the bubbles in the CPDs do not coalesce, and the contact line of the CPDs initially climbs along the capillary and then moves downwards with the increases of the weight of the CPDs. The breakup of the CPDs results into compound drops with several bubbles within it. At the capillary tip, the formation and breakup of the compound pendant drops cause velocity fluctuation in the upstream. The velocity fluctuation reduces by adding surfactant into the liquid. The size distribution of the compound drops produces by the breakup of CPDs are affected by the breakup event at the flow focusing geometry and the breakup event at the capillary tip. The current system is able to produce monodisperse compound drops. The polydispersity of the compound drops in this experiment was less than 10%.

Chapter 10

Conclusions and Future Work

10.1 Conclusions

Multiphase microfluidics attracted many researchers' attention due to its wide potential applications in different areas, such as analytical chemistry, chemical engineering, pharmaceutical and biomedical sciences, and life science industry. In this thesis, the hydrodynamics of droplets in microfluidics was analyzed and its influences on transport phenomena were investigated.

To understand the flow pattern within liquid plugs in microchannels, four models were built for plugs in different channel geometries, such as microcapillaries/microchannels with circular cross section [Chapter 3], two-dimensional microchannels [Chapter 4], curved microchannels [Chapter 5], and plug trains in two-dimensional microchannels [Chapter 6]. These models offer conveniences for subsequent analyses since the transport phenomena can be analyzed directly with the known flow field. Different applications were demonstrated with the proposed models, such as the flow resistance, the heat transfer in plugs, and the chaotic mixing in plugs moving in meandering microchannels. The results show

- The flow resistance of plugs is plug-length dependent and it is much higher than that of continuous flow. The idealization of a short liquid plug as fully developed continuous flow cannot provide an accurate prediction of the pressure loss.

- The heat transfer in plugs can be significantly enhanced by the recirculating vortices as compared to the continuous flow. The heat transfer process can be divided into three stages: Stage I: development of thermal boundary layer; Stage II: advection of the heated/fresh fluid in the plug; and Stage III: thermally fully developed flow. At a high Peclet number, the Nusselt number experiences oscillation in Stage II when the heated/fresh fluid in the central region of the plug is being transported to the heated wall by the recirculating flow. As the Peclet number decreases, the oscillation of the Nusselt number becomes insignificant. To achieve a higher heat transfer index in the constant-surface-temperature condition, a lower Peclet number and a short plug length are preferred, while to achieve a lower maximum fluid temperature in the constant-surface-heat-flux condition, a higher Peclet number and a short plug length are preferred.

- The vortex pattern in plugs can be manipulated by changing the plug length and the curvature of the microchannel. For plugs moving in microchannels, the vortex centres shift towards the inner wall as the channel curvature increases. The plug resistance coefficient increases with increasing the channel curvature.

- Rapid chaotic mixing can be achieved in plugs moving in meandering

microchannels. The mixing process in plugs is the combined effect of the stretching of fluid filaments by the vortices in the plugs, the folding of fluid filaments by changing the direction of the channel curvature, and the diffusion of species between liquid filaments. A large curvature, a low Peclet number, a moderate viscosity ratio, and a moderate plug length are preferred for rapid mixing in the plugs.

Based on the results provided in Chapters 3–6, some ideas were proved to manipulate/utilize droplets in microfluidics.

- A method to breakup droplets mediated by hydrodynamic focusing was proposed and investigated. The number and the size of the daughter droplets can be controlled by the splitting flow rate and the size of the mother droplet. With the robustness, reliability, and flexibility, splitting droplets by hydrodynamic focusing can serve as a useful tool for various droplet-based microfluidic applications.

- The investigation shows that a continuous liquid leaves a microcapillary in the form of pendant drops. During the growth and the breakup of pendant drops, with a fixed flow rate at the inlet of the capillary, upstream pressure fluctuation is produced by the size variation of the pendant drop. For fluids with a larger surface tension, the magnitude of the pressure fluctuation is larger, and the period is longer. For a larger capillary outer diameter, the magnitude of the pressure fluctuation is smaller, and the period is longer. High frequency pressure fluctuation after the instant of breakup is produced by the surface oscillation of the pendant drop due to the excess surface energy after the breakup, and is gradually damped by the viscosity of the fluids. The

pressure fluctuation can be used to measure the surface tension of the fluid by measuring the period of the pressure fluctuation.

- Gas/liquid plugs leave a microcapillary in the form of compound pendant drops. The formation and breakup of air/water compound pendant drop consists of four typical stages: (i) initialization of a small compound pendant drop; (ii) accumulation of liquid in the compound pendant drop; (iii) coalescence of bubble with the subsequent air plug; and finally (iv) breakup of the compound pendant drops. With a fixed upstream pressure, the formation and breakup of pendant drop causes velocity fluctuation in the upstream. The system is capable of producing monodisperse compound drops.

10.2 Future work

Having performed the above investigations, some recommendations are made as follows for future research in order to achieve better understanding of the multiphase microfluidics.

- **Three-dimension effect of the flow on transport phenomena**. The two-dimensional models developed in this thesis are the extreme condition of microchannels with large aspect ratios. Although it reveals most of the flow features in plugs moving in microchannels, three-dimensional flow fields can provide more information in the third dimension, which may affect the transport phenomena such as mixing and heat transfer.

- **The effects of multiphyical fields on multiphase microfluidics**. Many physical fields may affect the flow in multiphase microfluidics, such as

electric fields, magnetic fields, and acoustic fields. Study of the flow field and transport phenomena in multiphase microfluidics with the presence of different fields can deepen the understanding, and develop novel tools and applications in different areas.

- **Chemical reactions in multiphase microfluidics**. The effects of the recirculating flow on chemical reactions are still unclear. Numerical and experimental investigations of reactions in multiphase microfluidics may help precise control over various chemical applications.

- **Phase-change heat transfer in microchannels**. If phase change (boiling or condensation) in microchannels can be achieved in a stable and controllable manner, the droplet based heat transfer in microchannels can be more efficient than that without phase change because (i) it can make good use of the latent heat of the fluid for heat transfer, and (ii) it can simplify the heat exchanger by removing the droplet-formation unit.

Appendix A

Effects of Contact Angles and Curved Interface Shapes on the Flow Pattern in Plugs

To validate the flat interface assumption in Section 3.2.1, and to examine the effects of the contact angle and the curvature on the flow pattern in liquid plugs, numerical simulations were carried out using Fluent 6.3.26 with the finite volume method (FVM). Different contact angles were specified and interface shapes of spherical caps were assumed, as shown in Figure A.1. The result with a flat interface has a contact angle $\theta = 90°$, as shown in Figure A.1**i**. When the contact angle is slightly changed $\theta = 90° \pm 22.5°$, the flow pattern within the liquid plug is almost identical, as shown in Figure A.1**g** and **k**. If the contact angle changes further $\theta = 90° \pm 45°$, the curvature of the interfaces increases. The flow in the plug is still similar to the case with flat interfaces, as shown in Figure A.1**e** and **m**. If the contact angle changes to an extreme condition $\theta = 0°$, the wall is superhydrophilic, and the interface is highly curved, as shown in Figure A.1**a**. The other extreme condition

of contact angle is $\theta = 180°$, where the wall is superhydrophobic. In this condition, the flow near the spherical cap of the interface is slow (because the corresponding streamlines are sparse), as shown in Figure A.1**q**. However, the flow is dominated by the counter-rotating vortices. This is a significant feature of plug flow and is captured with flat-interface assumption. Therefore, the proposed model can be used for a group of plug flow in microchannels where the contact angle is not far from 90°.

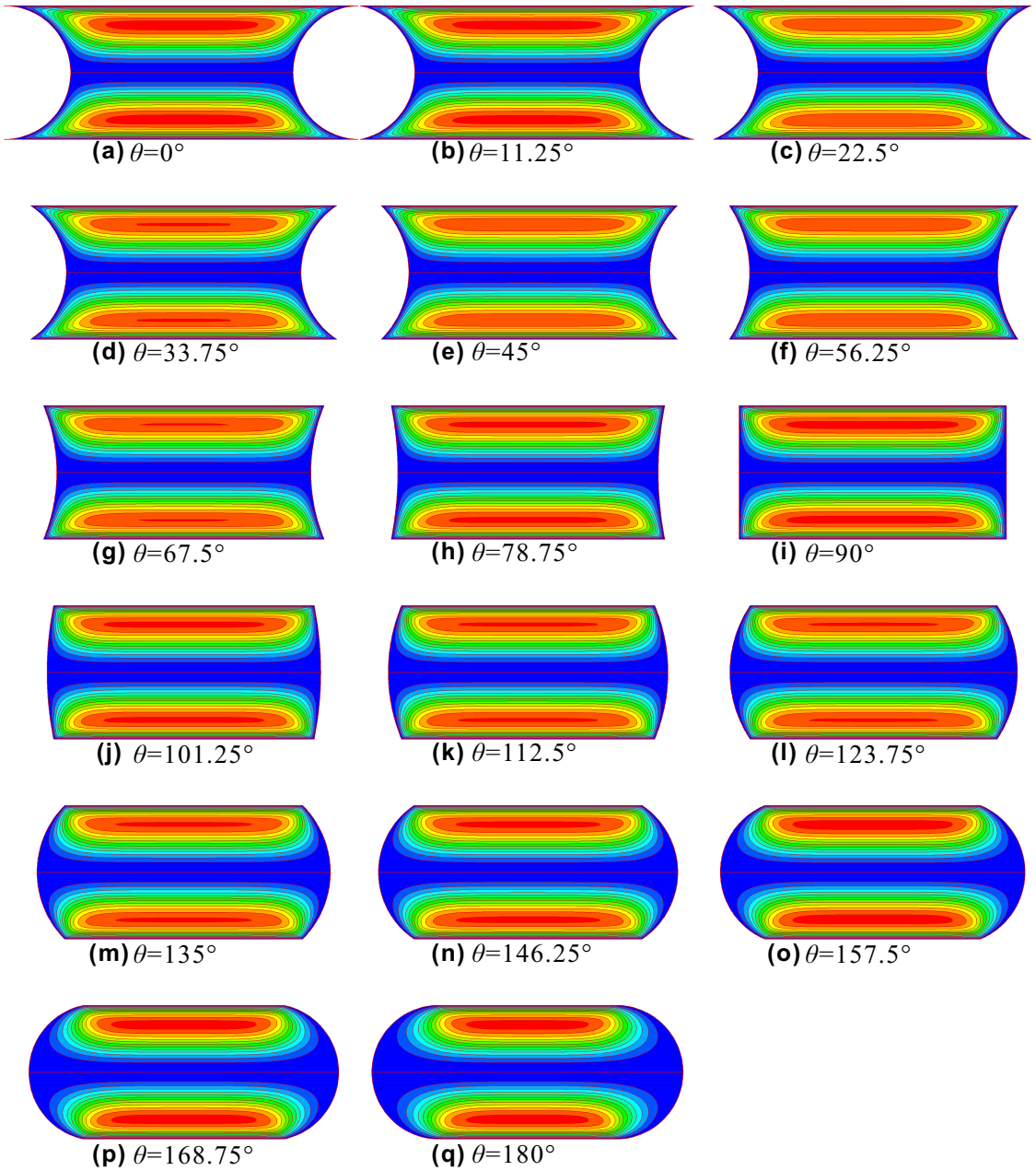

Figure A.1: Flow patterns in liquid plugs with different contact angles. The interfaces at the front and rear ends are assumed to be shapes of spherical caps. Rotational symmetric simulation was carried out via Fluent (version 6.3.26, Ansys Inc.). Grid independence was tested by repeating refinement of the grid until grid independent solutions were obtained. The number of control volumes for each plug was around 10^4.

Appendix B

Solution of Flow Field in Two-Dimensional Plugs

To model the flow field in a liquid plug, a Cartesian coordinate is built on the liquid plug, as shown in Figure B.1. The coordinate is translating together with the plug at a speed V towards right. Therefore, the plug unit is stationary relative to the translating coordinate system, while the wall of the microchannel is sliding towards left at a speed of V. The plug takes the region of $0 \leq x \leq L$, $0 \leq y \leq w$.

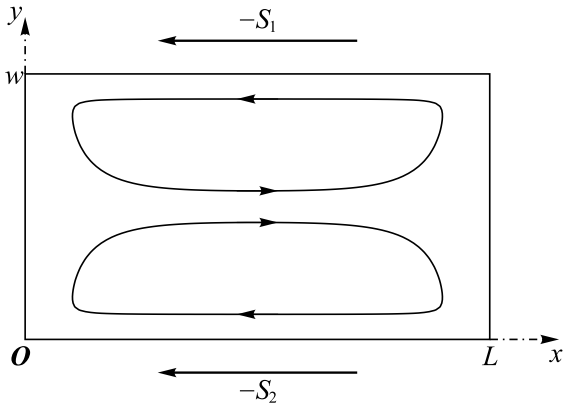

Figure B.1: Schematic diagram of a plug moving in a microchannel.

B.1 Analysis of flow field

For the Stokes flow in the plug, the governing equation is biharmonic

$$\nabla^4 \varphi = 0 \tag{B.1}$$

where φ is the stream function, which is defined as

$$u_x \equiv \frac{\partial \varphi}{\partial y}, \quad u_y \equiv -\frac{\partial \varphi}{\partial x} \tag{B.2}$$

This definition of φ satisfies the continuity equation automatically. This biharmonic equation is usually used to describe the Stokes flow (Meleshko, 2003; Shankar, 2007) and elastic mechanical problems (Timoshenko, 1951). In a Cartesian coordinate system, the biharmonic operator ∇^4 is

$$\nabla^4 \equiv \left(\frac{\partial^4}{\partial x^4} + 2\frac{\partial^4}{\partial x^2 \partial y^2} + \frac{\partial^4}{\partial y^4} \right) \tag{B.3}$$

The stream function is constant on the boundaries. Here, φ is set to be zero

$$\varphi(0, y) = 0, \quad \varphi(L, y) = 0 \tag{B.4}$$

$$\varphi(x, 0) = 0, \quad \varphi(x, w) = 0 \tag{B.5}$$

The front and rear of the plug are considered as free flat surfaces, and the viscosity of the air is neglected. The boundary conditions at these two sides are, respectively:

$$\frac{\partial^2}{\partial x^2}\varphi(0, y) = 0, \quad \frac{\partial^2}{\partial x^2}\varphi(L, y) = 0 \tag{B.6}$$

The velocities at the upper and lower walls are $-S_1$ and $-S_2$, respectively:

$$\frac{\partial}{\partial y}\varphi(x, w) = -S_1 \tag{B.7}$$

$$\frac{\partial}{\partial y}\varphi(x, 0) = -S_2 \tag{B.8}$$

Using the width of the channel as characteristic length, and the speed of the plug unit as the characteristic velocity V to nondimensionalise x, y, u_x, u_y, and φ, we have

$$\hat{x} \equiv x/w, \quad \hat{y} \equiv y/w \tag{B.9}$$

$$\hat{u}_x \equiv u_x/V, \quad \hat{u}_y \equiv u_y/V \tag{B.10}$$

$$\hat{\varphi} \equiv \varphi/(wV) \tag{B.11}$$

Therefore, the governing equation in dimensionless form is

$$\hat{\nabla}^4 \hat{\varphi} = \left(\frac{\partial^4}{\partial \hat{x}^4} + 2\frac{\partial^4}{\partial \hat{x}^2 \hat{y}^2} + \frac{\partial^4}{\partial \hat{y}^4} \right) \hat{\varphi} = 0 \tag{B.12}$$

The boundary conditions in Eqs. (B.4)–(B.8) reduce to

$$\hat{\varphi}\left(0, \hat{y}\right) = 0, \quad \hat{\varphi}\left(\hat{L}, \hat{y}\right) = 0 \tag{B.13}$$

$$\hat{\varphi}\left(\hat{x}, 0\right) = 0, \quad \hat{\varphi}\left(\hat{x}, 1\right) = 0 \tag{B.14}$$

$$\frac{\partial^2}{\partial \hat{x}^2}\hat{\varphi}\left(0, \hat{y}\right) = 0, \quad \frac{\partial^2}{\partial \hat{x}^2}\hat{\varphi}\left(\hat{L}, \hat{y}\right) = 0 \tag{B.15}$$

$$\frac{\partial}{\partial \hat{y}}\hat{\varphi}\left(\hat{x}, 1\right) = -\xi_1 \tag{B.16}$$

$$\frac{\partial}{\partial \hat{y}}\hat{\varphi}\left(\hat{x}, 0\right) = -\xi_2 \tag{B.17}$$

where $\hat{L} \equiv L/w$ is the dimensionless plug length, $\xi_1 \equiv S_1/V$ and $\xi_2 \equiv S_2/V$.

Using the finite Fourier transform (FFT) method (Deen, 1998), the solution of the biharmonic equation can be written as

$$\hat{\varphi}\left(\hat{x}, \hat{y}\right) = \sum_{n=0}^{\infty} \left[\phi_n\left(\hat{y}\right) \sin\left(\alpha_n \hat{x}\right) + \psi_n\left(\hat{y}\right) \cos\left(\alpha_n \hat{x}\right) \right] \tag{B.18}$$

where $\alpha_n \equiv n\pi/\hat{L}$. From the boundary conditions, Eqs. (B.4) and (B.6), we can write the solution in a simpler format

$$\hat{\varphi}\left(\hat{x}, \hat{y}\right) = \sum_{n=1}^{\infty} \phi_n\left(\hat{y}\right) \sin\left(\alpha_n \hat{x}\right) \tag{B.19}$$

Equation (B.19) satisfies the boundary conditions in Eqs. (B.13) and (B.15), automatically. $\phi_n(\hat{y})$ can be solved using to the other four boundary conditions. Using the FFT method, the stream function can be determined as

$$\hat{\varphi}(\hat{x},\hat{y}) = \sum_{n=1,3,5\cdots}^{\infty} \sin(\alpha_n \hat{x}) \times [C_{1n}\cosh(\alpha_n\hat{y}) + C_{2n}\sinh(\alpha_n\hat{y}) + C_{3n}\hat{y}\cosh(\alpha_n\hat{y}) + C_{4n}\hat{y}\sinh(\alpha_n\hat{y})] \tag{B.20}$$

And the dimensionless velocity components in the $\hat{x}$ and $\hat{y}$ directions are, respectively:

$$\begin{aligned}\hat{u}_x \equiv \frac{\partial}{\partial\hat{y}}\hat{\varphi}(\hat{x},\hat{y}) = &\sum_{n=1,3,5\cdots}^{\infty} \sin(\alpha_n\hat{x}) \\ &\times [C_{1n}\alpha_n\sinh(\alpha_n\hat{y}) + C_{2n}\alpha_n\cosh(\alpha_n\hat{y}) + C_{3n}\alpha_n\hat{y}\sinh(\alpha_n\hat{y}) \\ &+C_{3n}\cosh(\alpha_n\hat{y}) + C_{4n}\alpha_n\hat{y}\cosh(\alpha_n\hat{y}) + C_{4n}\sinh(\alpha_n\hat{y})]\end{aligned} \tag{B.21}$$

$$\hat{u}_y \equiv -\frac{\partial}{\partial\hat{x}}\hat{\varphi}(\hat{x},\hat{y}) = -\sum_{n=1,3,5\cdots}^{\infty} \alpha_n\cos(\alpha_n\hat{x}) \times [C_{1n}\cosh(\alpha_n\hat{y}) + C_{2n}\sinh(\alpha_n\hat{y}) + C_{3n}\hat{y}\cosh(\alpha_n\hat{y}) + C_{4n}\hat{y}\sinh(\alpha_n\hat{y})] \tag{B.22}$$

The constant coefficients in these equations can be obtained from the boundary conditions.

$$C_{1n} = 0 \tag{B.23}$$

$$C_{2n} = -\frac{4\xi_1}{D_n\hat{L}\alpha_n}\sinh(\alpha_n) - \frac{4\xi_2}{D_n\hat{L}} \tag{B.24}$$

$$C_{3n} = \frac{4\xi_1}{D_n\hat{L}}\sinh(\alpha_n) + \frac{4\xi_2\sinh^2(\alpha_n)}{\hat{L}\alpha_n D_n} \tag{B.25}$$

$$C_{4n} = \frac{4\xi_1}{D_n\hat{L}\alpha_n}[-\alpha_n\cosh(\alpha_n) + \sinh(\alpha_n)] + \frac{4\xi_2}{D_n\hat{L}\alpha_n}[-\sinh(\alpha_n)\cosh(\alpha_n) - \alpha_n] \tag{B.26}$$

where

$$D_n = {\alpha_n}^2 - \sinh^2(\alpha_n) \tag{B.27}$$

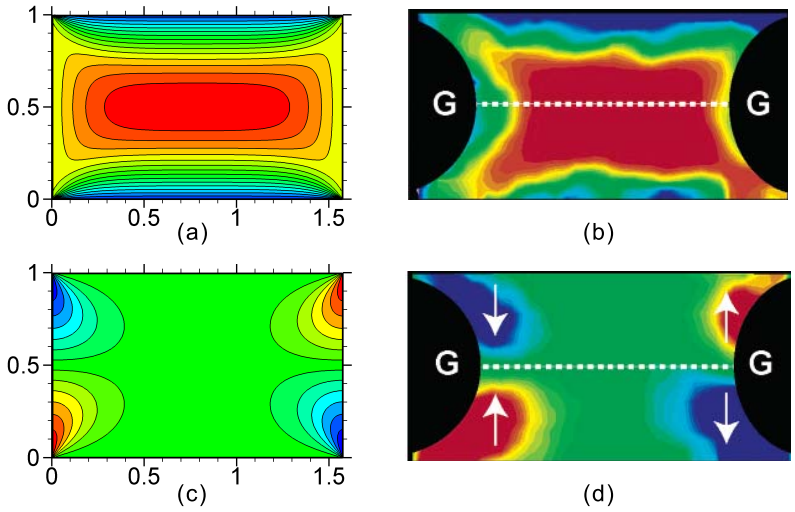

Figure B.2: Comparison between analytical results and experimental results obtained from μPIV (Günther et al., 2005). (a) $\hat{u}_x$ from the 2D model; (b) u_x from μPIV; (c) $\hat{u}_y$ from the 2D model; (d) u_y from μPIV.

B.2 Comparison with experimental results

To validate the 2D model for plug flow in a straight microchannel, comparison has been made with the velocity field measured from μPIV (Günther et al., 2005), as shown in Figure B.2. In the μPIV measurement, a contact angle exists when the liquid plug contact both the wall and the gas. The liquid curvature in the experiment is caused by the properties of the channel (fabricated of PMDS) and the fluid (ethanol). Though the interface curvature is not considered in the 2D model, the reasonable agreement between those results indicates that the 2D analytical model is capable in predicting the flow field in the liquid plug.

Appendix C

Effect of Channel Depth on Flow Pattern within Plug Flow

To examine the 2D assumption in Section 4.2, and to study the 3D effect on the flow pattern within liquid plugs, numerical simulations were carried out using Fluent (version 13.0 Ansys Inc.) with the finite volume method (FVM). The dimension of the microchannel is shown in Figure C.1, where w and d are the width and the depth of the channel, and L is the length of the liquid plug. Grid independence was tested by repeating refinement of the grid until grid independent solutions were obtained. The number of control volumes for each plug was around 10^5.

The numerical results are shown in Figure C.2. For a small d, the flow pattern in the liquid plug is affected by the top and the bottom walls of the microchannel. As the depth of the microchannel increases, the effect of the top and the bottom walls decreases, and the flow profile along **X-X** gradually approaches an unchanged shape. Figure C.2**b** shows that the flow in the middle cross section $z = 0$ can be regarded as 2D when the depth of the channel is $d > 5w$. Therefore, for microchannels with depths of $d > 5w$, the 2D model can accurately predict the

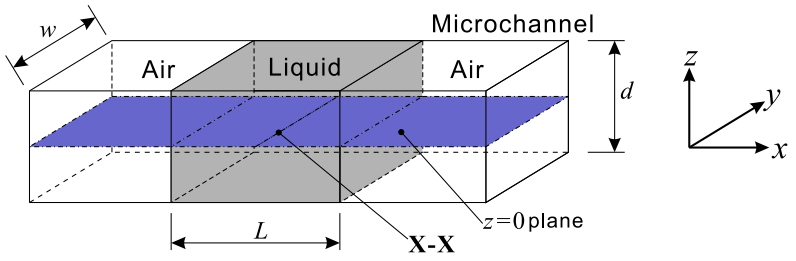

Figure C.1: Schematic diagram of a 3D liquid plug moving in a 3D microchannel. The width of the microchannel is w. The depth of the microchannel is d. The plug length is L. The middle depth plane $z = 0$ is indicated.

flow in the liquid plug. For microchannels with depths of $d < 5w$, the accuracy of the 2D model is reduced, but it can still qualitatively predict the two counter-rotating vortices, which is a significant feature of plug flow.

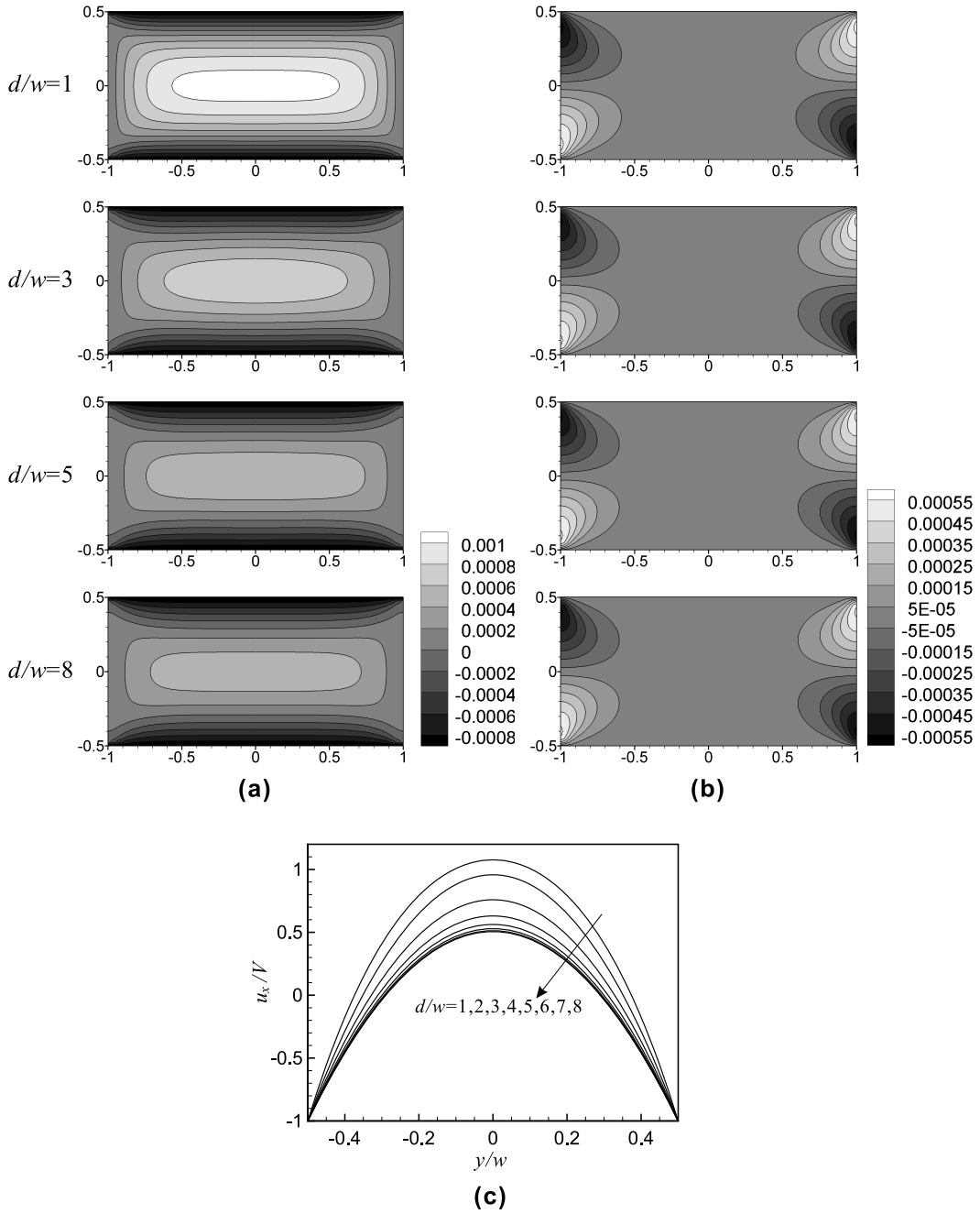

Figure C.2: Effect of the channel depth on the flow pattern in plugs. The width of the microchannel is w, the depth of the channel d is varied from w to $8w$. The length of the plug is $L = 2w$. The Reynolds number $Re \equiv \frac{\rho V w}{\mu} = 10^{-2}$. (a) Contours of velocity component u_x in the middle depth plane $z = 0$ as indicated in Figure C.1. (b) Contours of velocity component u_y in the middle depth plane $z = 0$. (c) Profiles of u_x/V along **X-X** indicated in Figure C.1.

Appendix D

Centrifugal Effect on Flow Pattern within Plug Flow in Curved Microchannels

To consider the centrifugal effect on the flow in liquid plugs, numerical simulations were carried out using Fluent (version 13.0, Ansys Inc.) with the finite volume method (FVM). The dimension of the microchannel is shown in Figure D.1, where w is the width of the microchannel ($w = 50\,\mu$m), d is the depth of the channel ($d = w$), R_1 and R_2 are the outer and inner radii of the walls of the curved microchannel ($R_1 = 2w$, $R_2 = w$), and L is the length of the liquid plug ($L = 1.125w$).

The Dean number, which characterizes the relative effect between the centrifugal force and the viscous force, was varied in the simulation, $De \equiv \frac{\rho V D_H}{\mu}\sqrt{\frac{D_H}{2R}} = Re\sqrt{\frac{D_H}{2R}}$, where ρ and μ are, respectively, the density and the dynamic viscosity of the fluid (The properties of water are used in the simulation $\rho = 10^3$ kg/m^3, $\mu = 10^{-3}$ Pa·s), V is the speed of the plug unit, D_H is the hydraulic diameter of the channel ($D_H = w$), R is the radius of the curved channel path ($R = \frac{3}{2}w$), and $Re \equiv \frac{\rho V D_H}{\mu}$ is the Reynolds number. The Dean number is varied from 0.002887 to 28.87 by changing the velocity of the plug from 10^{-4} to

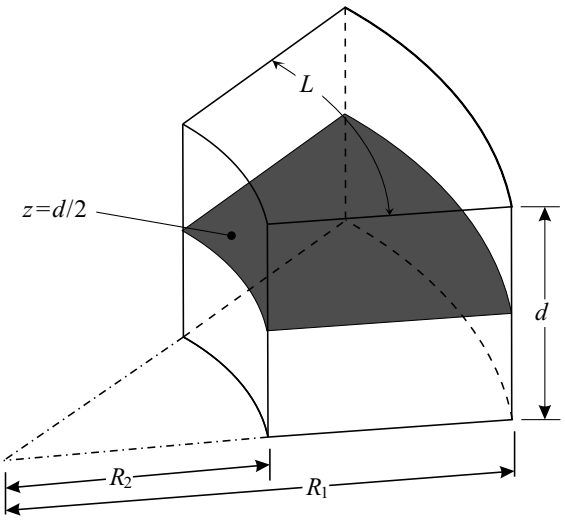

Figure D.1: Schematic diagram of the numerical simulation for a liquid plug in a 3D curved microchannel.

1 m/s.

The streamlines in the middle depth plane ($z = d/2$, Figure D.1) are plotted in Figure D.2. For a small Dean number, the flow is characterized by a pair of asymmetric counter-rotating vortices, and the centrifugal effect is negligible. When the Dean number increases to 2.887, the flow is affected by the centrifugal effect. The centrifugal effect is significant when the Dean number is 28.87. In most microfluidic devices, due to the small dimension and the low flow speed, the Dean number is usually much less than 1. Therefore, the centrifugal effect on plug flow is usually negligible.

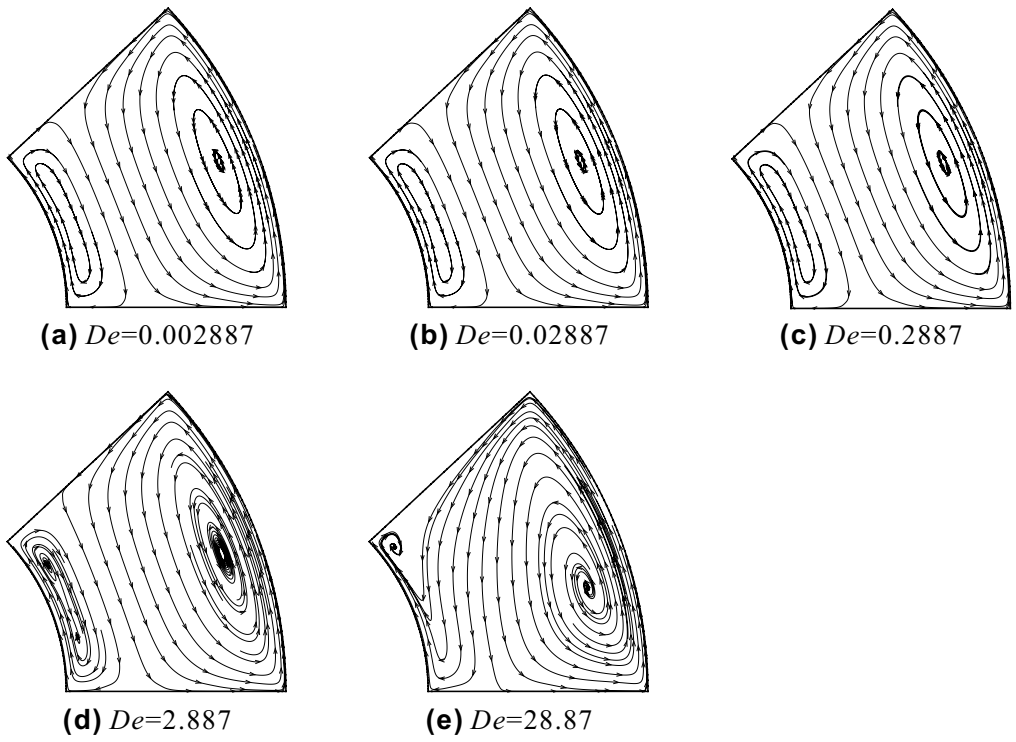

Figure D.2: Streamlines in the middle depth plane ($z = d/2$) in the liquid plug at different Dean numbers. Grid independence was tested by repeating refinement of the grid until grid independent solutions were obtained. The number of control volumes was 2.16×10^5.

Appendix E

Solution of the Flow Field in Plug Trains

E.1 Boundary conditions of the liquid plugs

The stream function φ_i is constant at the boundaries of Plug-i $(1 \leq i \leq N)$, and it is set to be zero.

$$\varphi_i\left(x_i, -h\right) = 0, \quad \varphi_i\left(x_i, h\right) = 0 \tag{E.1}$$

$$\varphi_i\left(-L_i, y_i\right) = 0, \quad \varphi_i\left(L_i, y_i\right) = 0 \tag{E.2}$$

The sliding velocities at the walls are $-S_1$ and $-S_2$, respectively:

$$\frac{\partial}{\partial y_i}\varphi_i\left(x_i, h\right) = -S_1\left(t\right) \tag{E.3}$$

$$\frac{\partial}{\partial y_i}\varphi_i\left(x_i, -h\right) = -S_2\left(t\right) \tag{E.4}$$

At the interface of the two successive plugs, the velocity component u_x is zero.

$$\frac{\partial}{\partial y_i}\varphi_i\left(L_i, y_i\right) = 0, \quad \frac{\partial}{\partial y_i}\varphi_i\left(-L_i, y_i\right) = 0 \tag{E.5}$$

The tangential velocity component u_y and the shear stress τ_{xy} along the interface of the two consecutive plugs should be continuous across the interface, as

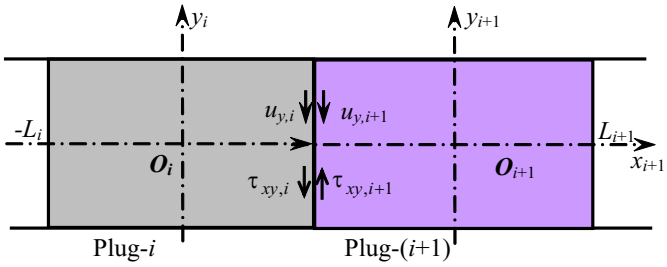

Figure E.1: Matching of the velocity components (u_y) and the shear stresses (τ_{xy}) at the interface of two consecutive plugs (Plug-i and Plug-(i+1), where $1 \leq i < N$).

illustrated in Figure E.1. From the velocities and the shear stresses at the right side of Plug-i and at the left side of Plug-(i+1), we have, respectively

$$-\frac{\partial}{\partial x_i}\varphi_i\left(L_i, y_i\right) = -\frac{\partial}{\partial x_{i+1}}\varphi_{i+1}\left(-L_{i+1}, y_{i+1}\right) \tag{E.6}$$

$$-\mu_i\frac{\partial^2}{\partial x_i^2}\varphi_i\left(L_i, y_i\right) = -\mu_{i+1}\frac{\partial^2}{\partial x_{i+1}^2}\varphi_{i+1}\left(-L_{i+1}, y_{i+1}\right) \tag{E.7}$$

where $1 \leq i < N$. At the interface between Plug-1 and Plug-N, the matching of the velocity components u_y and the shear stresses τ_{xy} applies between the right side of Plug-N and the left side of Plug-1.

$$-\frac{\partial}{\partial x_N}\varphi_N\left(L_N, y_N\right) = -\frac{\partial}{\partial x_1}\varphi_1\left(-L_1, y_1\right) \tag{E.8}$$

$$-\mu_N\frac{\partial^2}{\partial x_N^2}\varphi_N\left(L_N, y_N\right) = -\mu_1\frac{\partial^2}{\partial x_1^2}\varphi_1\left(-L_1, y_1\right) \tag{E.9}$$

E.2 Nondimensionalisation

Using half of the channel width h as the characteristic length and plug velocity V as the characteristic velocity to nondimensionalise the governing equation (Eq. (6.3))

and the boundary conditions (Eqs. (E.1)–(E.9)), we have for Plug-i $(1 \leq i \leq N)$

$$\hat{x}_i \equiv x_i/h, \quad \hat{y}_i \equiv y_i/h, \quad \hat{L}_i \equiv L_i/h, \quad \hat{u}_{x,i} \equiv u_{x,i}/V, \quad \hat{u}_{y,i} \equiv u_{y,i}/V, \quad \hat{\varphi}_i \equiv \varphi_i/(hV) \tag{E.10}$$

where $\hat{L}_i$ is the dimensionless plug length of Plug-i. The dimensionless governing equation is

$$\left(\frac{\partial^4}{\partial \hat{x}_i^4} + 2\frac{\partial^4}{\partial \hat{x}_i^2 \partial \hat{y}_i^2} + \frac{\partial^4}{\partial \hat{y}_i^4}\right)\hat{\varphi}_i = 0 \tag{E.11}$$

The boundary conditions are

$$\hat{\varphi}_i\left(\hat{x}_i, -1\right) = 0, \quad \hat{\varphi}_i\left(\hat{x}_i, 1\right) = 0 \tag{E.12}$$

$$\hat{\varphi}_i\left(-\hat{L}_i, \hat{y}_i\right) = 0, \quad \hat{\varphi}_i\left(\hat{L}_i, \hat{y}_i\right) = 0 \tag{E.13}$$

$$\frac{\partial}{\partial \hat{y}_i}\hat{\varphi}_i\left(\hat{x}_i, 1\right) = -\xi_1\left(\hat{t}\right), \quad \frac{\partial}{\partial \hat{y}_i}\hat{\varphi}_i\left(\hat{x}_i, -1\right) = -\xi_2\left(\hat{t}\right) \tag{E.14}$$

$$\frac{\partial}{\partial \hat{y}_i}\hat{\varphi}_i\left(\hat{L}_i, \hat{y}_i\right) = 0, \quad \frac{\partial}{\partial \hat{y}_i}\hat{\varphi}_i\left(-\hat{L}_i, \hat{y}_i\right) = 0 \tag{E.15}$$

where $1 \leq i < N$, $\xi_1\left(\hat{t}\right) \equiv S_1(t)/V$, and $\xi_2\left(\hat{t}\right) \equiv S_2(t)/V$. The matching of velocity components and shear stresses at the interface of two consecutive plugs yields

$$\frac{\partial}{\partial \hat{x}_i}\hat{\varphi}_i\left(\hat{L}_i, \hat{y}_i\right) = \frac{\partial}{\partial \hat{x}_{i+1}}\hat{\varphi}_{i+1}\left(-\hat{L}_{i+1}, \hat{y}_{i+1}\right) \tag{E.16}$$

$$\hat{\mu}_i \frac{\partial^2}{\partial \hat{x}_i^2}\hat{\varphi}_i\left(\hat{L}_i, \hat{y}_i\right) = \hat{\mu}_{i+1}\frac{\partial^2}{\partial \hat{x}_{i+1}^2}\hat{\varphi}_{i+1}\left(-\hat{L}_{i+1}, \hat{y}_{i+1}\right) \tag{E.17}$$

$$\frac{\partial}{\partial \hat{x}_N}\hat{\varphi}_N\left(\hat{L}_N, \hat{y}_N\right) = \frac{\partial}{\partial \hat{x}_1}\hat{\varphi}_1\left(-\hat{L}_1, \hat{y}_1\right) \tag{E.18}$$

$$\hat{\mu}_N \frac{\partial^2}{\partial \hat{x}_N^2}\hat{\varphi}_N\left(\hat{L}_N, \hat{y}_N\right) = \hat{\mu}_1\frac{\partial^2}{\partial \hat{x}_1^2}\hat{\varphi}_1\left(-\hat{L}_1, \hat{y}_1\right) \tag{E.19}$$

where $\hat{\mu}_i \equiv \mu_i/\mu_0$ is the viscosity ratio with μ_0 as a reference viscosity.

E.3 Series solution

The format of the solution of the biharmonic equation for Plug-i can be constructed as (Meleshko, 1996)

$$\begin{aligned}\hat{\varphi}_i\left(\hat{x}_i,\hat{y}_i\right) = &\sum_{m=1}^{\infty}\frac{\left(-1\right)^m}{\alpha_m}\left[p_m^o\left(\hat{y}_i\right)X_m^o + p_m^e\left(\hat{y}_i\right)X_m^e\right]\cos\left(\alpha_m\hat{x}_i\right)\\ &+\hat{L}_i\sum_{l=1}^{\infty}\frac{\left(-1\right)^l}{\beta_l}\left[q_l^e\left(\hat{x}_i\right)Y_l^e + q_l^o\left(\hat{x}_i\right)Y_l^o\right]\sin\left(\beta_l\hat{y}_i\right)\end{aligned} \tag{E.20}$$

where

$$\alpha_m = \frac{2m-1}{2\hat{L}_i}\pi \tag{E.21}$$

$$\beta_l = l\pi \tag{E.22}$$

$$p_m^o\left(\hat{y}_i\right) = \frac{\sinh\left(\alpha_m\hat{y}_i\right)}{\cosh\left(\alpha_m\right)} - \hat{y}_i\tanh\left(\alpha_m\right)\frac{\cosh\left(\alpha_m\hat{y}_i\right)}{\cosh\left(\alpha_m\right)} \tag{E.23}$$

$$p_m^e\left(\hat{y}_i\right) = \tanh\left(\alpha_m\right)\frac{\cosh\left(\alpha_m\hat{y}_i\right)}{\cosh\left(\alpha_m\right)} - \hat{y}_i\frac{\sinh\left(\alpha_m\hat{y}_i\right)}{\cosh\left(\alpha_m\right)} \tag{E.24}$$

$$q_l^o\left(\hat{x}_i\right) = \hat{L}_i\frac{\sinh\left(\beta_l\hat{x}_i\right)}{\cosh\left(\beta_l\hat{L}_i\right)} - \hat{x}_i\tanh\left(\beta_l\hat{L}_i\right)\frac{\cosh\left(\beta_l\hat{x}_i\right)}{\cosh\left(\beta_l\hat{L}_i\right)} \tag{E.25}$$

$$q_l^e\left(\hat{x}_i\right) = \hat{L}_i\tanh\left(\beta_l\hat{L}_i\right)\frac{\cosh\left(\beta_l\hat{x}_i\right)}{\cosh\left(\beta_l\hat{L}_i\right)} - \hat{x}_i\frac{\sinh\left(\beta_l\hat{x}_i\right)}{\cosh\left(\beta_l\hat{L}_i\right)} \tag{E.26}$$

The values of Eqs. (E.23)–(E.26) are all zero at the end points of the intervals $-\hat{L}_i \le \hat{x}_i \le -\hat{L}_i$ and $-1 \le \hat{y}_i \le 1$. This setting can make Eq. (E.20) satisfy the biharmonic equation and the homogeneous boundary conditions of $\hat{\varphi}_i = 0$ at the boundary. The coefficients X_m^o, X_m^e, Y_l^o, and Y_l^e of $\hat{\varphi}_i\left(\hat{x}_i,\hat{y}_i\right)$ in Eq. (E.20) can be obtained from boundary conditions of velocity (Eq. (E.14), (E.16), and (E.18)) and shear stress (Eqs. (E.17) and (E.19)).

From the dimensionless stream function in Eq. (E.20), the dimensionless

velocity field can be obtained as

$$\hat{u}_{x,i} \equiv \frac{\partial}{\partial \hat{y}_i}\hat{\varphi}_i\left(\hat{x}_i,\hat{y}_i\right) = \sum_{m=1}^{\infty}\left[{p_m^o}'\left(\hat{y}_i\right)X_m^o + {p_m^e}'\left(\hat{y}_i\right)X_m^e\right]\frac{(-1)^m}{\alpha_m}\cos\left(\alpha_m\hat{x}_i\right) + \hat{L}_i\sum_{l=1}^{\infty}(-1)^l\left[q_l^e\left(\hat{x}_i\right)Y_l^e + q_l^o\left(\hat{x}_i\right)Y_l^o\right]\cos\left(\beta_l\hat{y}_i\right) \tag{E.27}$$

$$\hat{u}_{y,i} \equiv -\frac{\partial}{\partial \hat{x}_i}\varphi_i\left(\hat{x}_i,\hat{y}_i\right) = \sum_{m=1}^{\infty}\left[p_m^o\left(\hat{y}_i\right)X_m^o + p_m^e\left(\hat{y}_i\right)X_m^e\right](-1)^m\sin\left(\alpha_m\hat{x}_i\right) - \hat{L}_i\sum_{l=1}^{\infty}\frac{(-1)^l}{\beta_l}\left[q_l^{e\prime}\left(\hat{x}_i\right)Y_l^e + q_l^{o\prime}\left(\hat{x}_i\right)Y_l^o\right]\sin\left(\beta_l\hat{y}_i\right) \tag{E.28}$$

where

$${p_m^o}'\left(\hat{y}_i\right) = \left[\alpha_m - \tanh\left(\alpha_m\right)\right]\frac{\cosh\left(\alpha_m\hat{y}_i\right)}{\cosh\left(\alpha_m\right)} - \hat{y}_i\alpha_m\tanh\left(\alpha_m\right)\frac{\sinh\left(\alpha_m\hat{y}_i\right)}{\cosh\left(\alpha_m\right)} \tag{E.29}$$

$${p_m^e}'\left(\hat{y}_i\right) = \left[\alpha_m\tanh\left(\alpha_m\right) - 1\right]\frac{\sinh\left(\alpha_m\hat{y}_i\right)}{\cosh\left(\alpha_m\right)} - \hat{y}_i\alpha_m\frac{\cosh\left(\alpha_m\hat{y}_i\right)}{\cosh\left(\alpha_m\right)} \tag{E.30}$$

$$q_l^{o\prime}\left(\hat{x}_i\right) = \left[\beta_l\hat{L}_i - \tanh\left(\beta_l\hat{L}_i\right)\right]\frac{\cosh\left(\beta_l\hat{x}_i\right)}{\cosh\left(\beta_l\hat{L}_i\right)} - \hat{x}_i\beta_l\tanh\left(\beta_l\hat{L}_i\right)\frac{\sinh\left(\beta_l\hat{x}_i\right)}{\cosh\left(\beta_l\hat{L}_i\right)} \tag{E.31}$$

$$q_l^{e\prime}\left(\hat{x}_i\right) = \left[\beta_l\hat{L}_i\tanh\left(\beta_l\hat{L}_i\right) - 1\right]\frac{\sinh\left(\beta_l\hat{x}_i\right)}{\cosh\left(\beta_l\hat{L}_i\right)} - \hat{x}_i\beta_l\frac{\cosh\left(\beta_l\hat{x}_i\right)}{\cosh\left(\beta_l\hat{L}_i\right)} \tag{E.32}$$

Introducing a modified Fourier transform FX (Meleshko 1996)

$$\mathrm{FX}[f\left(\hat{x}_i\right)] = \frac{(-1)^{m-1}}{\hat{L}_i}\int_{-\hat{L}_i}^{\hat{L}_i} f\left(\hat{x}_i\right)\cos\left(\alpha_m\hat{x}_i\right)d\hat{x}_i \tag{E.33}$$

Applying the modified Fourier transform FX to Eq. (E.14) yields

$$\frac{4\xi_1\left(\hat{t}\right)\alpha_m}{\pi\left(2m-1\right)} = -\left[\Delta_1^o\left(\alpha_m\right)X_m^o + \Delta_1^e\left(\alpha_m\right)X_m^e\right] + \sum_{l=1}^{\infty}\frac{4\alpha_m^2\beta_l Y_l^e}{\left(\alpha_m^2+\beta_l^2\right)^2} \tag{E.34}$$

$$\frac{4\xi_2\left(\hat{t}\right)\alpha_m}{\pi\left(2m-1\right)} = -\left[\Delta_1^o\left(\alpha_m\right)X_m^o - \Delta_1^e\left(\alpha_m\right)X_m^e\right] + \sum_{l=1}^{\infty}\frac{4\alpha_m^2\beta_l Y_l^e}{\left(\alpha_m^2+\beta_l^2\right)^2} \tag{E.35}$$

where

$$\Delta_1^o\left(\alpha_m\right) \equiv {p_m^o}'\left(\hat{y}_i=1\right) = \frac{\alpha_m}{\cosh^2\left(\alpha_m\right)} - \tanh\left(\alpha_m\right) \tag{E.36}$$

$$\Delta_1^e\left(\alpha_m\right) \equiv {p_m^e}'\left(\hat{y}_i=1\right) = \frac{-\alpha_m}{\cosh^2\left(\alpha_m\right)} - \tanh\left(\alpha_m\right) \tag{E.37}$$

Introducing another modified Fourier transform FY,

$$\mathrm{FY}[f(\hat{y}_i)] = (-1)^{l-1} \int_{-1}^{1} f(\hat{y}_i) \sin(\beta_l \hat{y}_i)\, d\hat{y}_i \tag{E.38}$$

Applying the modified Fourier transform FY to Eqs. (E.16) and (E.17) yields

$$\begin{aligned} &\left[-\sum_{m=1}^{\infty} X_m^o \frac{4\alpha_m \beta_l^2 \tanh^2(\alpha_m)}{\left(\alpha_m^2 + \beta_l^2\right)^2} + \hat{L}\left[\Delta_2^e\left(\beta_l \hat{L}\right) Y_l^e + \Delta_2^o\left(\beta_l \hat{L}\right) Y_l^o \right] \right]_{\text{Plug-}i} \\ &= \left[\sum_{m=1}^{\infty} X_m^o \frac{4\alpha_m \beta_l^2 \tanh^2(\alpha_m)}{\left(\alpha_m^2 + \beta_l^2\right)^2} + \hat{L}\left[-\Delta_2^e\left(\beta_l \hat{L}\right) Y_l^e + \Delta_2^o\left(\beta_l \hat{L}\right) Y_l^o \right] \right]_{\text{Plug-}(i+1)} \end{aligned} \tag{E.39}$$

$$\left[\mu \left[\Delta_3^e\left(\beta_l \hat{L}\right) Y_l^e + \Delta_3^o\left(\beta_l \hat{L}\right) Y_l^o \right] \right]_{\text{Plug-}i} = \left[\mu \left[\Delta_3^e\left(\beta_l \hat{L}\right) Y_l^e - \Delta_3^o\left(\beta_l \hat{L}\right) Y_l^o \right] \right]_{\text{Plug-}(i+1)} \tag{E.40}$$

where

$$\Delta_2^o\left(\beta_l \hat{L}_i\right) \equiv \beta_l \hat{L}_i - \tanh\left(\beta_l \hat{L}_i\right) - \left(\beta_l \hat{L}_i\right) \tanh^2\left(\beta_l \hat{L}_i\right) \tag{E.41}$$

$$\Delta_2^e\left(\beta_l \hat{L}_i\right) \equiv -\beta_l \hat{L}_i - \tanh\left(\beta_l \hat{L}_i\right) + \left(\beta_l \hat{L}_i\right) \tanh^2\left(\beta_l \hat{L}_i\right) \tag{E.42}$$

$$\Delta_3^o\left(\beta_l \hat{L}_i\right) \equiv 2\beta_l \hat{L}_i \tanh^2\left(\beta_l \hat{L}_i\right) \tag{E.43}$$

$$\Delta_3^e\left(\beta_l \hat{L}_i\right) \equiv -2\beta_l \tag{E.44}$$

Similarly, applying the modified Fourier transform FY to Eqs. (E.18) and (E.19) yields respectively

$$\begin{aligned} &\left[-\sum_{m=1}^{\infty} X_m \frac{4\alpha_m \beta_l^2 \tanh^2(\alpha_m)}{\left(\alpha_m^2 + \beta_l^2\right)^2} + \hat{L}\left[\Delta_2^e\left(\beta_l \hat{L}_i\right) Y_l^e + \Delta_2^o\left(\beta_l \hat{L}\right) Y_l^o \right] \right]_{\text{Plug-}N} \\ &= \left[\sum_{m=1}^{\infty} X_m \frac{4\alpha_m \beta_l^2 \tanh^2(\alpha_m)}{\left(\alpha_m^2 + \beta_l^2\right)^2} + \hat{L}\left[-\Delta_2^e\left(\beta_l \hat{L}_i\right) Y_l^e + \Delta_2^o\left(\beta_l \hat{L}\right) Y_l^o \right] \right]_{\text{Plug-1}} \end{aligned} \tag{E.45}$$

$$\begin{aligned} &\left[\mu \left[\Delta_3^e\left(\beta_l \hat{L}\right) Y_l^e + \Delta_3^o\left(\beta_l \hat{L}\right) Y_l^o \right] \right]_{\text{Plug-}N} \\ &= \left[\mu \left[\Delta_3^e\left(\beta_l \hat{L}\right) Y_l^e - \Delta_3^o\left(\beta_l \hat{L}\right) Y_l^o \right] \right]_{\text{Plug-1}} \end{aligned} \tag{E.46}$$

Equations (E.34), (E.35), (E.39), (E.40), (E.45) and (E.46) form a set of infinite algebra linear equations like $AX = b$ with unknowns X_m^e, X_m^o, Y_l^e, and Y_l^o.

The number of unknowns is $4N \times \infty$, and the number of equations is $4N \times \infty$, where ∞ corresponds to the coefficients of the infinite series. These equations can be solved using the method of reduction (Meleshko, 1996; Song et al., 2010) by truncating the infinite series after the first N^* terms. Therefore, the number of unknowns reduces to $4N \times N^*$, and the solution precision can be as high as needed by increasing N^*.

Appendix F

Measurement of Contact Angles on the Glass Capillary

To quantitatively measure the contact angle of DI water or the SDS solution on the glass capillary, we used a glass slide (75 mm×50 mm) and spread the water or the SDS solution on it, as shown in Figure F.1. The liquid was sufficient to result in a flat surface of liquid. Subsequently, the glass capillary was dipped vertically into the liquid, and observed horizontally from the side using a CCD camera. Figures F.2**a**–**b** are the images obtained from the CCD camera for DI water and for the SDS solution, respectively. From the images, we can confirm that adding the surfactant SDS into DI water increases the wettability of the liquid on the glass capillary. The contact angle decreases from 61° to 31° by adding surfactant SDS into DI water.

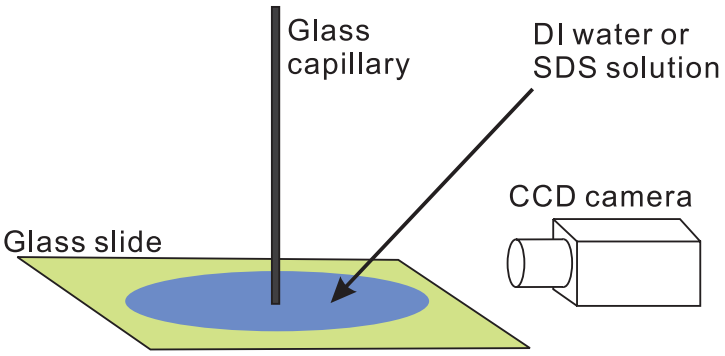

Figure F.1: Schematic diagram of measuring the contact angles of DI water and the SDS solution on the wall of the glass capillary.

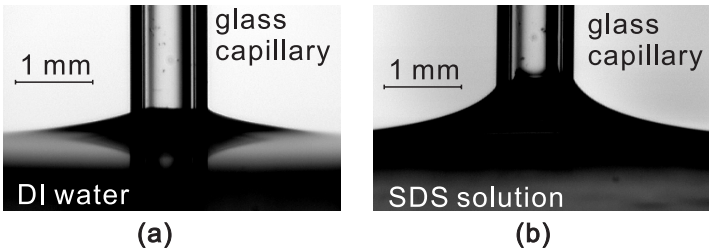

Figure F.2: Images for contact angle measurement on the glass capillary. (a) The image of contact angle for DI water on the glass capillary. The contact angle for DI water is 61°. (b) The image of contact angle for the SDS solution on the glass capillary. The contact angle for the SDS solution is 31°.

Publications Arising from This Thesis

Journal Papers

(1) **Z. Che**, T. N. Wong, N.-T. Nguyen. [2010]. An analytical model for a liquid plug moving in curved microchannels, *International Journal of Heat and Mass Transfer* 53 (9-10) 1977-1985.

(2) J. Sivasamy, **Z. Che**, T. N. Wong, N.-T. Nguyen, L. Yobas. [2010]. A simple method for evaluating and predicting chaotic advection in microfluidic slugs, *Chemical Engineering Science* 65 (19) 5382-5391.

(3) B. Xu, T. N. Wong, N.-T. Nguyen, **Z. Che**, J. C. Chai. [2010]. Thermal mixing of two miscible fluids in a T-shaped microchannel, *Biomicrofluidics* 4 (4) 044102.

(4) **Z. Che**, N.-T. Nguyen, T. N. Wong. [2011]. Hydrodynamically mediated breakup of droplets in microchannels, *Applied Physics Letters* 98 (5) 054102.

(5) **Z. Che**, T. N. Wong, N.-T. Nguyen. [2011]. An analytical model for plug flow in microcapillaries with circular cross section, *International Journal of Heat and Fluid Flow* 32 (5) 935-943.

(6) **Z. Che**, T. N. Wong, N.-T. Nguyen, Y. F. Yap, J. C. Chai. [2011] Numerical

investigation of upstream pressure fluctuation during growth and breakup of pendant drops,*Chemical Engineering Science* 66 (21) 5293-5300.

(7) **Z. Che**, T. N. Wong, N.-T. Nguyen, J. C. Chai, [2011] Formation and breakup of compound pendant drops at the tip of a capillary and its effect on upstream velocity fluctuations *International Journal of Heat and Mass Transfer* 55 (4) 1022-1029.

(8) **Z. Che**, N.-T. Nguyen, T. N. Wong, [2011] Analysis of chaotic mixing in plugs moving in meandering microchannels,*Physical Review E* 84, 066309.

(9) **Z. Che**, T. N. Wong, N.-T. Nguyen, [2011] Heat transfer enhancement by recirculating flow within liquid plugs in microchannels,*International Journal of Heat and Mass Transfer* 55 (7-8) 1947-1956.

Conference Papers

(1) **Z. Che**, T. N. Wong, N.-T. Nguyen. [2010] Analytical modeling of flow fields of liquid plugs moving in microchannels, 2nd European Conference in Microfluidics (μFlu'10). December 8-10, 2010, Toulouse, France.

(2) **Z. Che**, T. N. Wong, N.-T. Nguyen, J. C. Chai, Y. F. Yap. [2011] Numerical simulation of growth and pinch-off of pendant drops from a microcapillary, The Joint Conference on Advances in Microfluidics and Nanofluidics and Asian-Pacific International Symposium on Lab on Chip (AMN - APLOC 2011). January 5-7, 2011, Singapore.

References

Aarts, D. G. A. L. and Lekkerkerker, H. N. W. [2008]. Droplet coalescence: drainage, film rupture and neck growth in ultralow interfacial tension systems. *Journal of Fluid Mechanics*, **606**:275–294.

Aarts, D. G. A. L., Lekkerkerker, H. N. W., Guo, H., Wegdam, G. H., and Bonn, D. [2005]. Hydrodynamics of Droplet Coalescence. *Physcal Review Letters*, **95**(16):164503.

Abate, A., Poitzsch, A., Hwang, Y., Lee, J., Czerwinska, J., and Weitz, D. [2009]. Impact of inlet channel geometry on microfluidic drop formation. *Physical Review E*, **80**(2):026310.

Abate, A. R. and Weitz, D. A. [2009]. High-order multiple emulsions formed in poly(dimethylsiloxane) microfluidics. *Small*, **5**(18):2030–2032.

Abate, A. R., Hung, T., Mary, P., Agresti, J. J., and Weitz, D. A. [2010a]. High-throughput injection with microfluidics using picoinjectors. *Proceedings of the National Academy of Sciences*, **107**(45):19163–19166.

Abate, A. R., Thiele, J., Weinhart, M., and Weitz, D. A. [2010b]. Patterning microfluidic device wettability using flow confinement. *Lab on a Chip*, **10**(14):1774.

Abate, A. R., Thiele, J., and Weitz, D. A. [2011]. One-step formation of multiple emulsions in microfluidics. *Lab on a Chip*, **11**(2):253.

Abbassi, H., Turki, S., and Ben Nasrallah, S. [2001]. Numerical investigation of forced convection in a plane channel with a built-in triangular prism. *International Journal of Thermal Sciences*, **40**(7):649–658.

Adamson, D. N., Mustafi, D., Zhang, J. X. J., Zheng, B., and Ismagilov, R. F. [2006]. Production of arrays of chemically distinct nanolitre plugs via repeated splitting in microfluidic devices. *Lab on a Chip*, **6**(9):1178–1186.

Adrian, R. J. [1991]. Particle-imaging techniques for experimental fluid mechanics. *Annual Review of Fluid Mechanics*, **23**(1):261–304.

Ahmed, D., Mao, X., Juluri, B. K., and Huang, T. J. [2009]. A fast microfluidic mixer based on acoustically driven sidewall-trapped microbubbles. *Microfluidics and Nanofluidics*, **7**(5):727–731.

Ahn, K., Agresti, J., Chong, H., Marquez, M., and Weitz, D. A. [2006a]. Electrocoalescence of drops synchronized by size-dependent flow in microfluidic channels. *Applied Physics Letters*, **88**(26):264105.

Ahn, Y.-C., Jung, W., and Chen, Z. [2006b]. Turbid two-phase slug flow in a microtube: Simultaneous visualization of structure and velocity field. *Applied Physics Letters*, **89**(6):064109.

Amaya-Bower, L. and Lee, T. [2011]. Numerical simulation of single bubble rising in vertical and inclined square channel using lattice Boltzmann method. *Chemical Engineering Science*, **66**(5):935–952.

Ambravaneswaran, B., Phillips, S. D., and Basaran, O. A. [2000]. Theoretical analysis of a dripping faucet. *Physical Review Letters*, **85**(25):5332.

Ambravaneswaran, B., Subramani, H. J., Phillips, S. D., and Basaran, O. A. [2004]. Dripping-jetting transitions in a dripping faucet. *Physical Review Letters*, **93**(3):034501.

Anderson, D. M., McFadden, G. B., and Wheeler, A. A. [1998]. Diffuse-interface methods in fluid mechanics. *Annual Review of Fluid Mechanics*, **30**(1):139–165.

Anna, S. L. and Mayer, H. C. [2006]. Microscale tipstreaming in a microfluidic flow focusing device. *Physics of Fluids*, **18**(12):092105.

Anna, S. L., Bontoux, N., and Stone, H. A. [2003]. Formation of dispersions using "flow focusing" in microchannels. *Applied Physics Letters*, **82**(3):364–366.

Aref, H. [1984]. Stirring by chaotic advection. *Journal of Fluid Mechanics*, **143**:1–21.

Aref, H. [2002]. The development of chaotic advection. *Physics of Fluids*, **14**(4):1315–1325.

Baird, E. and Mohseni, K. [2008]. Digitized heat transfer: A new paradigm for thermal management of compact micro systems. *IEEE Transactions on Components and Packaging Technologies*, **31**(1):143–151.

Baird, E. and Mohseni, K. [2009]. Numerical simulations for digitized heat transfer. In *ASME 2009 InterPACK Conference*, volume 2, pages 923–931.

Barbier, V., Tatoulian, M., Li, H., Arefi-Khonsari, F., Ajdari, A., and Tabeling, P. [2006]. Stable modification of PDMS surface properties by plasma polymerization: application to the formation of double emulsions in microfluidic systems. *Langmuir*, **22**(12):5230–5232.

Beer, N. R., Rose, K. A., and Kennedy, I. M. [2009]. Observed velocity fluctuations in monodisperse droplet generators. *Lab on a Chip*, **9**(6):838–840.

Belder, D. [2005]. Microfluidics with droplets. *Angewandte Chemie - International Edition*, **44**(23):3521–3522.

Berger, S. A., Talbot, L., and Yao, L. S. [1983]. Flow in curved pipes. *Annual Review of Fluid Mechanics*, **15**(1):461–512.

Bessoth, F. G., DeMello, A. J., and Manz, A. [1999]. Microstructure for efficient continuous flow mixing. *Analytical Communications*, **36**(6):213–215.

Blanchette, F. [2009]. Flow lines and mixing within drops in microcapillaries. *Physical Review E*, **80**(6):066316.

Borhan, A., Haj-Hariri, H., and Nadim, A. [1992]. Effect of surfactants on the thermocapillary migration of a concentric compound drop. *Journal of Colloid and Interface Science*, **149**(2):553–560.

Bozzi, L. A., Feng, J. Q., Scott, T. C., and Pearlstein, A. J. [1997]. Steady axisymmetric motion of deformable drops falling or rising through a homoviscous fluid in a tube at intermediate Reynolds number. *Journal of Fluid Mechanics*, **336**:1–32.

Bremond, N., Thiam, A. R., and Bibette, J. [2008]. Decompressing emulsion droplets favors coalescence. *Physical Review Letters*, **100**(2):024501.

Burns, J. R. and Ramshaw, C. [2001]. The intensification of rapid reactions in multiphase systems using slug flow in capillaries. *Lab on a Chip*, **1**(1):10–15.

Burns, M. A., Mastrangelo, C. H., Sammarco, T. S., Man, F. P., Webster, J. R., Johnson, B. N., Foerster, B., Jones, D., Fields, Y., Kaiser, A. R., and Burke, D. T. [1996]. Microfabricated structures for integrated DNA analysis. *Proceedings of the National Academy of Sciences of the United States of America*, **93**(11):5556–5561.

Burton, J. C. and Taborek, P. [2007]. Two-dimensional inviscid pinch-off: An example of self-similarity of the second kind. *Physics of Fluids*, **19**(10):102109.

Burton, J. C., Rutledge, J. E., and Taborek, P. [2007]. Fluid pinch-off in superfluid and normal ^{4}He. *Physical Review E*, **75**(3):036311.

Chabert, M., Dorfman, K. D., and Viovy, J. L. [2005]. Droplet fusion by alternating current (AC) field electrocoalescence in microchannels. *Electrophoresis*, **26**(19):3706–3715.

Chan, D. Y. C., Klaseboer, E., and Manica, R. [2011]. Film drainage and coalescence between deformable drops and bubbles. *Soft Matter*, **7**(6):2235–2264.

Chang, C. C. and Yang, R. J. [2006]. A particle tracking method for analyzing chaotic electroosmotic flow mixing in 3D microchannels with patterned charged surfaces. *Journal of Micromechanics and Microengineering*, **16**(8):1453–1462.

Chen, A. U., Notz, P. K., and Basaran, O. A. [2002]. Computational and experimental analysis of pinch-off and scaling. *Physical Review Letters*, **88**(17):174501.

Chen, S. and Doolen, G. D. [1998]. Lattice Boltzmann method for fluid flows. *Annual Review of Fluid Mechanics*, **30**(1):329–364.

Chen, Y. and Cheng, P. [2005]. Condensation of steam in silicon microchannels. *International Communications in Heat and Mass Transfer*, **32**(1-2):175–183.

Chiu, D. T., Lorenz, R. M., and Jeffries, G. D. M. [2009]. Droplets for ultrasmall-volume analysis. *Analytical Chemistry*, **81**(13):5111–5118.

Choi, J.-H., Lee, S.-K., Lim, J.-M., Yang, S.-M., and Yi, G.-R. [2010a]. Designed pneumatic valve actuators for controlled droplet breakup and generation. *Lab on a Chip*, **10**(4):456.

Choi, S.-W., Zhang, Y., and Xia, Y. [2010b]. A temperature-sensitive drug release system based on phase-change materials. *Angewandte Chemie - International Edition*, **49**(43):7904–7908.

Christopher, G. F. and Anna, S. L. [2007]. Microfluidic methods for generating continuous droplet streams. *Journal of Physics D: Applied Physics*, **40**(19):R319–R336.

Christopher, G. F., Noharuddin, N. N., Taylor, J. A., and Anna, S. L. [2008]. Experimental observations of the squeezing-to-dripping transition in T-shaped microfluidic junctions. *Physical Review E*, **78**(3):036317.

Chung, C., Kim, J. M., Hulsen, M. A., Ahn, K. H., and Lee, S. J. [2009]. Effect of viscoelasticity on drop dynamics in 5:1:5 contraction/expansion microchannel flow. *Chemical Engineering Science*, **64**(22):4515–4524.

Collins, R. T., Jones, J. J., Harris, M. T., and Basaran, O. A. [2008]. Electrohydrodynamic tip streaming and emission of charged drops from liquid cones. *Nature Physics*, **4**(2):149–154.

Davidson, M. R. and Cooper-White, J. J. [2006]. Pendant drop formation of shear-thinning and yield stress fluids. *Applied Mathematical Modelling*, **30**(11):1392–1405.

De Gennes, P. G. [1985]. Wetting: Statics and dynamics. *Reviews of Modern Physics*, **57**(3):827–863.

De Menech, M., Garstecki, P., Jousse, F., and Stone, H. A. [2008]. Transition from squeezing to dripping in a microfluidic T-shaped junction. *Journal of Fluid Mechanics*, **595**:141–161.

Dean, W. R. [1927]. Note on the motion of fluid in a curved pipe. *Philosophical Magazine Series 7*, **4**(20):208 – 223.

Dean, W. R. [1928a]. Fluid motion in a curved channel. *Proceedings of the Royal Society of London Series A*, **121**(787):402–420.

Dean, W. R. [1928b]. The stream-line motion of fluid in a curved pipe. *Philosophical Magazine Series 7*, **5**(30):673 – 695.

Deen, W. M. [1998]. *Analysis of Transport Phenomena*. Oxford University Press, New York.

deMello, A. J. [2006]. Control and detection of chemical reactions in microfluidic systems. *Nature*, **442**(7101):394–402.

Dendukuri, D. and Doyle, P. S. [2009]. The synthesis and assembly of polymeric microparticles using microfluidics. *Advanced Materials*, **21**(41):4071–4086.

Dietsche, L. J. and Neubauer, A. C. [2009]. Computational fluid dynamics model of viscous droplet breakup. *Chemical Engineering Science*, **64**(22):4543–4552.

Dogan, H., Nas, S., and Muradoglu, M. [2009]. Mixing of miscible liquids in gas-segmented serpentine channels. *International Journal of Multiphase Flow*, **35**(12):1149–1158.

Duda, J. L. and Vrentas, J. S. [1971]. Steady flow in the region of closed streamlines in a cylindrical cavity. *Journal of Fluid Mechanics*, **45**(02):247–260.

Duffy, D. C., McDonald, J. C., Schueller, O. J. A., and Whitesides, G. M. [1998]. Rapid prototyping of microfluidic systems in poly(dimethylsiloxane). *Analytical Chemistry*, **70**(23):4974–4984.

Eggers, J. [1997]. Nonlinear dynamics and breakup of free-surface flows. *Reviews of Modern Physics*, **69**(3):865.

Eggers, J. and Dupont, T. F. [1994]. Drop formation in a one-dimensional approximation of the Navier-Stokes equation. *Journal of Fluid Mechanics*, **262**:205–221.

Eggers, J. and Villermaux, E. [2008]. Physics of liquid jets. *Reports on Progress in Physics*, **71**(3):036601.

Fidalgo, L. M., Abell, C., and Huck, W. T. S. [2007]. Surface-induced droplet fusion in microfluidic devices. *Lab on a Chip*, **7**(8):984–986.

Fries, D. M. and Rudolf von Rohr, P. [2008]. Impact of inlet design on mass transfer in gas-liquid rectangular microchannels. *Microfluidics and Nanofluidics*, **6**(1):doi:10.1007/s10404–008–0292–6.

Fries, D. M. and von Rohr, P. R. [2009]. Liquid mixing in gas-liquid two-phase flow by meandering microchannels. *Chemical Engineering Science*, **64**(6):1326–1335.

Fries, D. M., Waelchli, S., and Rudolf von Rohr, P. [2008]. Gas-liquid two-phase flow in meandering microchannels. *Chemical Engineering Journal*, **135**(Supplement 1):S37–S45.

Fujioka, H. and Grotberg, J. B. [2004]. Steady propagation of a liquid plug in a two-dimensional channel. *Journal of Biomechanical Engineering-Transactions of the ASME*, **126**(5):567–577.

Fujioka, H. and Grotberg, J. B. [2005]. The steady propagation of a surfactant-laden liquid plug in a two-dimensional channel. *Physics of Fluids*, **17**(8):1–17.

Fujioka, H., Takayama, S., and Grotberg, J. B. [2008]. Unsteady propagation of a liquid plug in a liquid-lined straight tube. *Physics of Fluids*, **20**(6):062104.

Funakoshi, M. [2008]. Chaotic mixing and mixing efficiency in a short time. *Fluid Dynamics Research*, **40**(1):1–33.

Furbank, R. J. and Morris, J. F. [2004]. An experimental study of particle effects on drop formation. *Physics of Fluids*, **16**(5):1777–1790.

Garstecki, P., Gitlin, I., Diluzio, W., Whitesides, G. M., Kumacheva, E., and Stone, H. A. [2004]. Formation of monodisperse bubbles in a microfluidic flow-focusing device. *Applied Physics Letters*, **85**(13):2649–2651.

Garstecki, P., Stone, H. A., and Whitesides, G. M. [2005]. Mechanism for flow-rate controlled breakup in confined geometries: A route to monodisperse emulsions. *Physical Review Letters*, **94**(16):1–4.

Garstecki, P., Fuerstman, M. J., Stone, H. A., and Whitesides, G. M. [2006]. Formation of droplets and bubbles in a microfluidic T-junction - Scaling and mechanism of break-up. *Lab on a Chip*, **6**(3):437–446.

German, G. and Bertola, V. [2010]. Formation of viscoplastic drops by capillary breakup. *Physics of Fluids*, **22**(3):1–11.

Gu, H., Murade, C. U., Duits, M. H. G., and Mugele, F. [2011]. A microfluidic platform for on-demand formation and merging of microdroplets using electric control. *Biomicrofluidics*, **5**(1):011101.

Günther, A. and Jensen, K. F. [2006]. Multiphase microfluidics: From flow characteristics to chemical and materials synthesis. *Lab on a Chip*, **6**(12):1487–1503.

Günther, A., Khan, S. A., Thalmann, M., Trachsel, F., and Jensen, K. F. [2004]. Transport and reaction in microscale segmented gas-liquid flow. *Lab on a Chip*, **4**(4):278–286.

Günther, A., Jhunjhunwala, M., Thalmann, M., Schmidt, M. A., and Jensen, K. F. [2005]. Micromixing of miscible liquids in segmented gas-liquid flow. *Langmuir*, **21**(4):1547–1555.

Handique, K. and Burns, M. A. [2001]. Mathematical modeling of drop mixing in a slit-type microchannel. *Journal of Micromechanics and Microengineering*, **11**(5):548–554.

Happel, J. and Brenner, H. [1983]. *Low Reynolds Number Hydrodynamics: With Special Applications to Particulate Media*. Martinus Nijhoff Publishers, The Hague, 2nd edition.

Harlow, F. H. and Welch, J. E. [1965]. Numerical calculation of time-dependent viscous incompressible flow of fluid with free surface. *Physics of Fluids*, **8**(12):2182–2189.

Harries, N., Burns, J. R., Barrow, D. A., and Ramshaw, C. [2003]. A numerical model for segmented flow in a microreactor. *International Journal of Heat and Mass Transfer*, **46**(17):3313–3322.

Henkel, T., Bermig, T., Kielpinski, M., Grodrian, A., Metze, J., and Köhler, J. M. [2004]. Chip modules for generation and manipulation of fluid segments for micro serial flow processes. *Chemical Engineering Journal*, **101**(1-3):439–445.

Hennequin, Y., Pannacci, N., de Torres, C. P., Tetradis-Meris, G., Chapuliot, S., Bouchaud, E., and Tabeling, P. [2009]. Synthesizing microcapsules with controlled geometrical and mechanical properties with microfluidic double emulsion technology. *Langmuir*, **25**(14):7857–7861.

Hessel, V., Hardt, S., Löwe, H., and Schönfeld, F. [2003]. Laminar mixing in different interdigital micromixers: I. Experimental characterization. *AIChE Journal*, **49**(3):566–577.

Hou, T. Y., Lowengrub, J. S., and Shelley, M. J. [2001]. Boundary integral methods for multicomponent fluids and multiphase materials. *Journal of Computational Physics*, **169**(2):302–362.

Hung, L. H., Choi, K. M., Tseng, W. Y., Tan, Y. C., Shea, K. J., and Lee, A. P. [2006]. Alternating droplet generation and controlled dynamic droplet fusion in microfluidic device for CdS nanoparticle synthesis. *Lab on a Chip*, **6**(2):174–178.

Icoz, T. and Jaluria, Y. [2006]. Design optimization of size and geometry of vortex promoter in a two-dimensional channel. *Journal of Heat Transfer*, **128**(10):1081–1092.

Incropera, F. P. and DeWitt, D. P. [2002]. *Fundamentals of Heat and Mass Transfer*. John Wiley & Sons, New York, 5th edition.

Jacqmin, D. [1999]. Calculation of two-phase Navier-Stokes flows using phase-field modeling. *Journal of Computational Physics*, **155**(1):96–127.

Janasek, D., Franzke, J., and Manz, A. [2006]. Scaling and the design of miniaturized chemical-analysis systems. *Nature*, **442**(7101):374–380.

Jin, B. J., Kim, Y. W., Lee, Y., and Yoo, J. Y. [2010]. Droplet merging in a straight microchannel using droplet size or viscosity difference. *Journal of Micromechanics and Microengineering*, **20**(3):035003.

Johnson, R. E. and Sadhal, S. S. [1985]. Fluid mechanics of compound multiphase drops and bubbles. *Annual Review of Fluid Mechanics*, **17**(1):289–320.

Kang, M., Fedkiw, R. P., and Liu, X. D. [2000]. A boundary condition capturing method for multiphase incompressible flow. *Journal of Scientific Computing*, **15**(3):323–360.

Kang, T. G. and Kwon, T. H. [2004]. Colored particle tracking method for mixing analysis of chaotic micromixers. *Journal of Micromechanics and Microengineering*, **14**(7):891–899.

Kashid, M. N., Gerlach, I., Goetz, S., Franzke, J., Acker, J. F., Platte, F., Agar, D. W., and Turek, S. [2005]. Internal circulation within the liquid slugs of a liquid-liquid slug-flow capillary microreactor. *Industrial & Engineering Chemistry Research*, **44**(14):5003–5010.

Kashid, M. N., Agar, D. W., and Turek, S. [2007]. CFD modelling of mass transfer with and without chemical reaction in the liquid-liquid slug flow microreactor. *Chemical Engineering Science*, **62**(18-20 SPEC. ISS.):5102–5109.

Kawahara, A., Chung, P. Y., and Kawaji, M. [2002]. Investigation of two-phase flow pattern, void fraction and pressure drop in a microchannel. *International Journal of Multiphase Flow*, **28**(9):1411–1435.

Kim, B. J., Liu, Y. Z., and Sung, H. J. [2004]. Micro PIV measurement of two-fluid flow with different refractive indices. *Measurement Science & Technology*, **15**(6):1097–1103.

Kim, H., Luo, D., Link, D., Weitz, D. A., Marquez, M., and Cheng, Z. [2007]. Controlled production of emulsion drops using an electric field in a flow-focusing microfluidic device. *Applied Physics Letters*, **91**(13):133106.

King, C., Walsh, E., and Grimes, R. [2007]. PIV measurements of flow within plugs in a microchannel. *Microfluidics and Nanofluidics*, **3**(4):463–472.

Kinoshita, H., Kaneda, S., Fujii, T., and Oshima, M. [2007]. Three-dimensional measurement and visualization of internal flow of a moving droplet using confocal micro-PIV. *Lab on a Chip*, **7**(3):338–346.

Knight, J. B., Vishwanath, A., Brody, J. P., and Austin, R. H. [1998]. Hydrodynamic focusing on a silicon chip: Mixing nanoliters in microseconds. *Physical Review Letters*, **80**(17):3863–3866.

Köhler, J. M., Henkel, T., Grodrian, A., Kirner, T., Roth, M., Martin, K., and Metze, J. [2004]. Digital reaction technology by micro segmented flow - components, concepts and applications. *Chemical Engineering Journal*, **101**(1-3):201–216.

Koster, S., Angile, F. E., Duan, H., Agresti, J. J., Wintner, A., Schmitz, C., Rowat, A. C., Merten, C. A., Pisignano, D., Griffiths, A. D., and Weitz, D. A. [2008]. Drop-based microfluidic devices for encapsulation of single cells. *Lab on a Chip*, **8**(7):1110–1115.

Kreutzer, M. T., Kapteijn, F., Moulijn, J. A., Kleijn, C. R., and Heiszwolf, J. J. [2005]. Inertial and interfacial effects on pressure drop of Taylor flow in capillaries. *AIChE Journal*, **51**(9):2428–2440.

Kroujiline, D. and Stone, H. A. [1999]. Chaotic streamlines in steady bounded three-dimensional Stokes flows. *Physica D*, **130**(1-2):105–132.

Lai, A., Bremond, N., and Stone, H. A. [2009]. Separation-driven coalescence of droplets: an analytical criterion for the approach to contact. *Journal of Fluid Mechanics*, **632**:97.

Le, H. P. [1998]. Progress and trends in ink-jet printing technology. *Journal of Imaging Science and Technology*, **42**(1):49–62.

Lee, C. Y., Lin, Y. H., and Lee, G. B. [2008a]. A droplet-based microfluidic system capable of droplet formation and manipulation. *Microfluidics and Nanofluidics*, **6**(5):599–610.

Lee, S. H., van Noort, D., Lee, J. Y., Zhang, B.-T., and Park, T. H. [2009]. Effective mixing in a microfluidic chip using magnetic particles. *Lab on a Chip*, **9**(3):479.

Lee, W., Walker, L. M., and Anna, S. L. [2008b]. Impact of viscosity ratio on the dynamics of droplet breakup in a microfluidic flow focusing device. In *AIP Conference Proceedings*, volume 1027, pages 994–996.

Li, L. and Ismagilov, R. F. [2010]. Protein crystallization using microfluidic technologies based on valves, droplets, and slipChip. *Annual Review of Biophysics*, **39**(1):139–158.

Lide, D. R. and Haynes, W. M. [2010]. *CRC Handbook of Chemistry and Physics, Internet Version 2010*. CRC Press, Cleveland, Ohio, 90th edition.

Link, D. R., Anna, S. I., Weitz, D. A., and Stone, H. A. [2004]. Geometrically mediated breakup of drops in microfluidic devices. *Physical Review Letters*, **92**(5):545031–545034.

Link, D. R., Grasland-Mongrain, E., Duri, A., Sarrazin, F., Cheng, Z., Cristobal, G., Marquez, M., and Weitz, D. A. [2006]. Electric control of droplets in microfluidic devices. *Angewandte Chemie - International Edition*, **45**(16):2556–2560.

Liu, D. and Wang, S. [2008]. Hydrodynamics of Taylor flow in noncircular capillaries. *Chemical Engineering and Processing: Process Intensification*, **47**(12):2098–2106.

Liu, F. and Wang, L. [2009]. Analysis on multiplicity and stability of convective heat transfer in tightly curved rectangular ducts. *International Journal of Heat and Mass Transfer*, **52**(25-26):5849–5866.

Liu, H. and Zhang, Y. [2009]. Droplet formation in a T-shaped microfluidic junction. *Journal of Applied Physics*, **106**(3):034906.

Liu, K., Ding, H., Chen, Y., and Zhao, X. Z. [2007]. Droplet-based synthetic method using microflow focusing and droplet fusion. *Microfluidics and Nanofluidics*, **3**(2):239–243.

Liu, X. D., Fedkiw, R. P., and Kang, M. [2000]. A boundary condition capturing method for Poisson's equation on irregular domains. *Journal of Computational Physics*, **160**(1):151–178.

Lorber, N., Sarrazin, F., Guillot, P., Panizza, P., Colin, A., Pavageau, B., Hany, C., Maestro, P., Marre, S., Delclos, T., Aymonier, C., Subra, P., Prat, L., Gourdon, C., and Mignard, E. [2011]. Some recent advances in the design and the use of miniaturized droplet-based continuous process: Applications in chemistry and high-pressure microflows. *Lab on a Chip*, **11**(5):779.

Lorenceau, E., Utada, A. S., Link, D. R., Cristobal, G., Joanicot, M., and Weitz, D. A. [2005]. Generation of polymerosomes from double-emulsions. *Langmuir*, **21**(20):9183–9186.

Lorenceau, E., Sang, Y. Y. C., Höhler, R., and Cohen-Addad, S. [2006]. A high rate flow-focusing foam generator. *Physics of Fluids*, **18**(9):097103.

Lumma, D., Best, A., Gansen, A., Feuillebois, F., auml, dler, J. O., and Vinogradova, O. I. [2003]. Flow profile near a wall measured by double-focus fluorescence cross-correlation. *Physical Review E*, **67**(5):056313.

Ma, Y., Sun, C. P., Fields, M., Li, Y., Haake, D. A., Churchill, B. M., and Ho, C. M. [2008]. An unsteady microfluidic T-form mixer perturbed by hydrodynamic pressure. *Journal of Micromechanics and Microengineering*, **18**(4):045015.

Meis, M., Varas, F., Velazquez, A., and Vega, J. M. [2010]. Heat transfer enhancement in micro-channels caused by vortex promoters. *International Journal of Heat and Mass Transfer*, **53**(1-3):29–40.

Meleshko, V. V. [1996]. Steady Stokes flow in a rectangular cavity. *Proceedings of the Royal Society A-Mathematical, Physical and Engineering Sciences*, **452**(1952):1999–2022.

Meleshko, V. V. [2003]. Selected topics in the history of the two-dimensional biharmonic problem. *Applied Mechanics Reviews*, **56**(1):33–85.

Ménétrier-Deremble, L. and Tabeling, P. [2006]. Droplet breakup in microfluidic junctions of arbitrary angles. *Physical Review E*, **74**(3):035303.

Michael, D. H. [1981]. Meniscus stability. *Annual Review of Fluid Mechanics*, **13**(1):189–216.

Miessner, U., Lindken, R., and Westerweel, J. [2008]. Velocity measurements in microscopic two-phase flows by means of micro PIV. In *ASME 2008 6th International Conference on Nanochannels, Microchannels, and Minichannels (ICNMM2008)*, PART B, pages 1111–1118.

Miyake, R., Lammerink, T. S. J., Elwenspoek, M., and Fluitman, J. H. J. [1993]. Micro mixer with fast diffusion. In *Proceedings of the 1993 IEEE Micro Electro Mechanical Systems - MEMS*, pages 248–253.

Mugele, F. and Baret, J. C. [2005]. Electrowetting: From basics to applications. *Journal of Physics: Condensed Matter*, **17**(28):R705–R774.

Muradoglu, M. and Stone, H. A. [2005]. Mixing in a drop moving through a serpentine channel: A computational study. *Physics of Fluids*, **17**(7):1–9.

Muradoglu, M., Günther, A., and Stone, H. A. [2007]. A computational study of axial dispersion in segmented gas-liquid flow. *Physics of Fluids*, **19**(7):072109.

Murshed, S., Tan, S., Nguyen, W., N.T., T.N., and Yobas, L. [2009]. Microdroplet formation of water and nanofluids in heat-induced microfluidic T-junction. *Microfluidics and Nanofluidics*, **6**(2):253–259.

Muzychka, Y. S., Walsh, E., and Walsh, P. [2010]. Simple models for laminar thermally developing slug flow in noncircular ducts and channels. *Journal of Heat Transfer*, **132**(11):111702.

Naphon, P. and Wongwises, S. [2006]. A review of flow and heat transfer characteristics in curved tubes. *Renewable and Sustainable Energy Reviews*, **10**(5):463–490.

Ng, W. Y., Goh, S., Lam, Y. C., Yang, C., and Rodríguez, I. [2009]. DC-biased AC-electroosmotic and AC-electrothermal flow mixing in microchannels. *Lab on a Chip*, **9**(6):802.

Nguyen, N.-T. [2008]. *Micromixers: Fundamentals, Design and Fabrication*. Micro & Nano Technologies. William Andrew, Norwich, NY.

Nguyen, N.-T. and Huang, X. [2005]. Mixing in microchannels based on hydrodynamic focusing and time-interleaved segmentation: modelling and experiment. *Lab on a Chip*, **5**(11):1320–1326.

Nguyen, N. T. and Wu, Z. [2005]. Micromixers - A review. *Journal of Micromechanics and Microengineering*, **15**(2):R1–R16.

Nguyen, N. T., Wang, C., Wong, T. N., Low, L. N., and Ho, S. S. [2006]. A silicon/glass-based microfluidic device for invetigation of Lagrangian velocity field in microdroplets. *Journal of Physics: Conference Series*, **34**(1):130–135.

Nguyen, N. T., Ting, T. H., Yap, Y. F., Wong, T. N., Chai, J. C. K., Ong, W. L., Zhou, J., Tan, S. H., and Yobas, L. [2007]. Thermally mediated droplet formation in microchannels. *Applied Physics Letters*, **91**(8):084102.

Nie, Z., Seo, M., Xu, S., Lewis, P. C., Mok, M., Kumacheva, E., Whitesides, G. M., Garstecki, P., and Stone, H. A. [2008]. Emulsification in a microfluidic flow-focusing device: Effect of the viscosities of the liquids. *Microfluidics and Nanofluidics*, **5**(5):585–594.

Nisisako, T. [2008]. Microstructured devices for preparing controlled multiple emulsions. *Chemical Engineering & Technology*, **31**(8):1091–1098.

Nisisako, T., Okushima, S., and Torii, T. [2005]. Controlled formulation of monodisperse double emulsions in a multiple-phase microfluidic system. *Soft Matter*, **1**(1):23–27.

Niu, X. and Lee, Y. K. [2003]. Efficient spatial-temporal chaotic mixing in microchannels. *Journal of Micromechanics and Microengineering*, **13**(3):454–462.

Niu, X., Gulati, S., Edel, J. B., and Demello, A. J. [2008]. Pillar-induced droplet merging in microfluidic circuits. *Lab on a Chip*, **8**(11):1837–1841.

Oh, D. W., Jin, J. S., Choi, J. H., Kim, H. Y., and Lee, J. S. [2007]. A microfluidic chaotic mixer using ferrofluid. *Journal of Micromechanics and Microengineering*, **17**(10):2077–2083.

Oishi, M., Kinoshita, H., Fujii, T., and Oshima, M. [2009]. Confocal micro-PIV measurement of droplet formation in a T-shaped micro-junction. *Journal of Physics: Conference Series*, **147**(1):012061.

Okushima, S., Nisisako, T., Torii, T., and Higuchi, T. [2004]. Controlled production of monodisperse double emulsions by two-step droplet breakup in microfluidic devices. *Langmuir*, **20**(23):9905–9908.

Ong, W. L., Hua, J., Zhang, B., Teo, T. Y., Zhuo, J., Nguyen, N. T., Ranganathan, N., and Yobas, L. [2007]. Experimental and computational analysis of droplet formation in a high-performance flow-focusing geometry. *Sensors and Actuators A-Physical*, **138**(1):203–212.

Osher, S. and Fedkiw, R. P. [2001]. Level set methods: An overview and some recent results. *Journal of Computational Physics*, **169**(2):463–502.

Osher, S. and Fedkiw, R. P. [2003]. *Level Set Methods and Dynamic Implicit Surfaces*. Applied Mathematical Sciences. Springer, New York.

Ottino, J. M. [1989]. *The Kinematics of Mixing: Stretching, Chaos, and Transport*. Cambridge University Press, Cambridge.

Palm, B. [2001]. Heat transfer in microchannels. *Microscale Thermophysical Engineering*, **5**(3):155 – 175.

Park, J. I., Saffari, A., Kumar, S., Günther, A., and Kumacheva, E. [2010]. Microfluidic synthesis of polymer and inorganic particulate materials. *Annual Review of Materials Research*, **40**(1):415–443.

Patankar, S. V. [1980]. *Numerical heat transfer and fluid flow*. Series in computational methods in mechanics and thermal sciences. Hemisphere Pub. Corp., Washington.

Peng, X. F. and Wang, B. X. [1993]. Forced convection and flow boiling heat transfer for liquid flowing through microchannels. *International Journal of Heat and Mass Transfer*, **36**(14):3421–3427.

Perot, B. and Nallapati, R. [2003]. A moving unstructured staggered mesh method for the simulation of incompressible free-surface flows. *Journal of Computational Physics*, **184**(1):192–214.

Phelps, J. H. and Tucker III, C. L. [2006]. Lagrangian particle calculations of distributive mixing: Limitations and applications. *Chemical Engineering Science*, **61**(20):6826–6836.

Priest, C. [2010]. Surface patterning of bonded microfluidic channels. *Biomicrofluidics*, **4**(3):032206.

Priest, C., Herminghaus, S., and Seemann, R. [2006]. Controlled electrocoalescence in microfluidics: Targeting a single lamella. *Applied Physics Letters*, **89**(13):134101.

Priezjev, N. V., Darhuber, A. A., and Troian, S. M. [2005]. Slip behavior in liquid films on surfaces of patterned wettability: Comparison between continuum and molecular dynamics simulations. *Physical Review E*, **71**(4):041608.

Qian, S. and Bau, H. H. [2002]. A chaotic electroosmotic stirrer. *Analytical Chemistry*, **74**(15):3616–3625.

Rahnama, M. and Hadi-Moghaddam, H. [2005]. Numerical investigation of convective heat transfer in unsteady laminar flow over a square cylinder in a channel. *Heat Transfer Engineering*, **26**(10):21 – 29.

Rhee, M. and Burns, M. A. [2007]. Drop mixing in a microchannel for lab-on-a-chip platforms. *Langmuir*, **24**(2):590–601.

Rosenfeld, L., Lavrenteva, O. M., and Nir, A. [2009]. On the thermocapillary motion of partially engulfed compound drops. *Journal of Fluid Mechanics*, **626**:263–289.

Ryskin, G. and Leal, L. G. [1984]. Numerical solution of free-boundary problems in fluid mechanics. Part 2. Buoyancy-driven motion of a gas bubble through a quiescent liquid. *Journal of Fluid Mechanics*, **148**:19–35.

Sang, L., Hong, Y., and Wang, F. [2008]. Investigation of viscosity effect on droplet formation in T-shaped microchannels by numerical and analytical methods. *Microfluidics and Nanofluidics*, **6**(5):621–635.

Santiago, J. G., Wereley, S. T., Meinhart, C. D., Beebe, D. J., and Adrian, R. J. [1998]. A particle image velocimetry system for microfluidics. *Experiments in Fluids*, **25**(4):316–319.

Sarrazin, F., Loubière, K., Prat, L., Gourdon, C., Bonometti, T., and Magnaudet, J. [2006]. Experimental and numerical study of droplets hydrodynamics in microchannel. *AIChE Journal*, **52**(12):4061–4070.

Sarrazin, F., Bonometti, T., Prat, L., Gourdon, C., and Magnaudet, J. [2008]. Hydrodynamic structures of droplets engineered in rectangular micro-channels. *Microfluidics and Nanofluidics*, **5**(1):131–137.

Sato, H., Matsumura, H., Keino, S., and Shoji, S. [2006]. An all SU-8 microfluidic chip with built-in 3D fine microstructures. *Journal of Micromechanics and Microengineering*, **16**(11):2318–2322.

Scardovelli, R. and Zaleski, S. [1999]. Direct numerical simulation of free-surface and interfacial flow. *Annual Review of Fluid Mechanics*, **31**:567–603.

Schneider, T., Burnham, D. R., VanOrden, J., and Chiu, D. T. [2011]. Systematic investigation of droplet generation at T-junctions. *Lab on a Chip*, **11**:2055–2059.

Shankar, P. N. [2007]. *Slow Viscous Flows: Qualitative Features and Quantitative Analysis Using Complex Eigenfunction Expansions*. Imperial College Press, London.

Shestopalov, I., Tice, J. D., and Ismagilov, R. F. [2004]. Multi-step synthesis of nanoparticles performed on millisecond time scale in a microfluidic droplet-based system. *Lab on a Chip*, **4**(4):316–321.

Shui, L., Mugele, F., van den Berg, A., and Eijkel, J. C. T. [2008]. Geometry-controlled droplet generation in head-on microfluidic devices. *Applied Physics Letters*, **93**(15):153113.

Shui, L., van den Berg, A., and Eijkel, J. C. T. [2009]. Capillary instability, squeezing, and shearing in head-on microfluidic devices. *Journal of Applied Physics*, **106**(12):124305.

Singh, P. and Aubry, N. [2007]. Transport and deformation of droplets in a microdevice using dielectrophoresis. *Electrophoresis*, **28**(4):644–657.

Sivasamy, J., Chim, Y. C., Wong, T. N., Nguyen, N. T., and Yobas, L. [2010]. Reliable addition of reagents into microfluidic droplets. *Microfluidics and Nanofluidics*, **8**(3):409–416.

Sivasamy, J., Wong, T. N., Nguyen, N. T., and Kao, L. T. H. [2011]. An investigation on the mechanism of droplet formation in a microfluidic T-junction. *Microfluidics and Nanofluidics*, **11**:1–10.

Song, H., Bringer, M. R., Tice, J. D., Gerdts, C. J., and Ismagilov, R. F. [2003a]. Experimental test of scaling of mixing by chaotic advection in droplets moving through microfluidic channels. *Applied Physics Letters*, **83**(22):4664–4666.

Song, H., Tice, J. D., and Ismagilov, R. F. [2003b]. A microfluidic system for controlling reaction networks in time. *Angewandte Chemie - International Edition*, **42**(7):768–772.

Song, H., Chen, D. L., and Ismagilov, R. F. [2006a]. Reactions in droplets in microfluidic channels. *Angewandte Chemie - International Edition*, **45**(44):7336–7356.

Song, H., Li, H. W., Munson, M. S., Ha, T. G. V., and Ismagilov, R. F. [2006b]. On-chip titration of an anticoagulant argatroban and determination of the clotting time within whole blood or plasma using a plug-based microfluidic system. *Analytical Chemistry*, **78**(14):4839–4849.

Song, Y., Xu, J., and Yang, Y. [2010]. Stokes flow past a compound drop in a circular tube. *Physics of Fluids*, **22**(7):072003.

Squires, T. M. and Quake, S. R. [2005]. Microfluidics: Fluid physics at the nanoliter scale. *Reviews of Modern Physics*, **77**(3):977–1026.

Steegmans, M. L. J., Schroën, K. G. P. H., and Boom, R. M. [2009]. Characterization of emulsification at flat microchannel Y junctions. *Langmuir*, **25**(6):3396–3401.

Stone, Z. B. and Stone, H. A. [2005]. Imaging and quantifying mixing in a model droplet micromixer. *Physics of Fluids*, **17**(6):1–11.

Stroock, A. D. and Whitesides, G. M. [2003]. Controlling flows in microchannels with patterned surface charge and topography. *Accounts of Chemical Research*, **36**(8):597–604.

Stroock, A. D., Dertinger, S. K. W., Ajdari, A., Mezic, I., Stone, H. A., and Whitesides, G. M. [2002]. Chaotic mixer for microchannels. *Science*, **295**(5555):647–651.

Suryo, R. and Basaran, O. A. [2006]. Dripping of a liquid from a tube in the absence of gravity. *Physical Review Letters*, **96**(3):034504.

Tabeling, P. [2009]. A brief introduction to slippage, droplets and mixing in microfluidic systems. *Lab on a Chip*, **9**(17):2428–2436.

Tabeling, P. [2010]. Investigating slippage, droplet breakup, and synthesizing microcapsules in microfluidic systems. *Physics of Fluids*, **22**(2):021302.

Tadros, T. [2005]. *Applied surfactants: principles and applications*. Wiley-VCH, Weinheim.

Taha, T. and Cui, Z. F. [2004]. Hydrodynamics of slug flow inside capillaries. *Chemical Engineering Science*, **59**(6):1181–1190.

Taha, T. and Cui, Z. F. [2006a]. CFD modelling of slug flow in vertical tubes. *Chemical Engineering Science*, **61**(2):676–687.

Taha, T. and Cui, Z. F. [2006b]. CFD modelling of slug flow inside square capillaries. *Chemical Engineering Science*, **61**(2):665–675.

Tan, S. H., Sohel Murshed, S. M., Nguyen, N. T., Wong, T. N., and Yobas, L. [2008]. Thermally controlled droplet formation in flow focusing geometry: Formation regimes and effect of nanoparticle suspension. *Journal of Physics D: Applied Physics*, **41**(16):165501.

Tan, Y. C., Ho, Y. L., and Lee, A. P. [2007]. Droplet coalescence by geometrically mediated flow in microfluidic channels. *Microfluidics and Nanofluidics*, **3**(4):495–499.

Tanthapanichakoon, W., Aoki, N., Matsuyama, K., and Mae, K. [2006]. Design of mixing in microfluidic liquid slugs based on a new dimensionless number for precise reaction and mixing operations. *Chemical Engineering Science*, **61**(13):4220–4232.

Tasoglu, S., Kaynak, G., Szeri, A. J., Demirci, U., and Muradoglu, M. [2010]. Impact of a compound droplet on a flat surface: A model for single cell epitaxy. *Physics of Fluids*, **22**(8):082103.

Taylor, G. [1953]. Dispersion of soluble matter in solvent flowing slowly through a tube. *Proceedings of the Royal Society of London. Series A, Mathematical and Physical Sciences*, **219**(1137):186–203.

Teh, S. Y., Lin, R., Hung, L. H., and Lee, A. P. [2008]. Droplet microfluidics. *Lab on a Chip*, **8**(2):198–220.

Theberge, A. B., Courtois, F., Schaerli, Y., Fischlechner, M., Abell, C., Hollfelder, F., and Huck, W. T. S. [2010]. Microdroplets in microfluidics: An evolving platform for discoveries in chemistry and biology. *Angewandte Chemie - international Edition*, **49**(34):5846–5868.

Thome, J. R. [2004]. Boiling in microchannels: A review of experiment and theory. *International Journal of Heat and Fluid Flow*, **25**(2):128–139.

Thorsen, T., Roberts, R. W., Arnold, F. H., and Quake, S. R. [2001]. Dynamic pattern formation in a vesicle-generating microfluidic device. *Physical Review Letters*, **86**(18):4163–4166.

Tice, J. D., Song, H., Lyon, A. D., and Ismagilov, R. F. [2003]. Formation of droplets and mixing in multiphase microfluidics at low values of the Reynolds and the Capillary numbers. *Langmuir*, **19**(22):9127–9133.

Timoshenko, S. [1951]. *Theory of Elasticity*. Engineering Societies Monographs. McGraw-Hill, New York, 2nd edition.

Ting, T. H., Yap, Y. F., Nguyen, N. T., Wong, T. N., Chai, J. C. K., and Yobas, L. [2006]. Thermally mediated breakup of drops in microchannels. *Applied Physics Letters*, **89**(23):234101.

Tirtaatmadja, V., McKinley, G. H., and Cooper-White, J. J. [2006]. Drop formation and breakup of low viscosity elastic fluids: Effects of molecular weight and concentration. *Physics of Fluids*, **18**(4):043101.

Trachsel, F., Günther, A., Khan, S., and Jensen, K. F. [2005]. Measurement of residence time distribution in microfluidic systems. *Chemical Engineering Science*, **60**(21):5729–5737.

Triplett, K. A., Ghiaasiaan, S. M., Abdel-Khalik, S. I., and Sadowski, D. L. [1999]. Gas-liquid two-phase flow in microchannels part I: Two-phase flow patterns. *International Journal of Multiphase Flow*, **25**(3):377–394.

Tryggvason, G., Bunner, B., Esmaeeli, A., Juric, D., Al-Rawahi, N., Tauber, W., Han, J., Nas, S., and Jan, Y. J. [2001]. A front-tracking method for the computations of multiphase flow. *Journal of Computational Physics*, **169**(2):708–759.

Tung, K.-Y., Li, C.-C., and Yang, J.-T. [2009]. Mixing and hydrodynamic analysis of a droplet in a planar serpentine micromixer. *Microfluidics and Nanofluidics*, **7**(4):545–557.

Turki, S., Abbassi, H., and Ben Nasrallah, S. [2003]. Two-dimensional laminar fluid flow and heat transfer in a channel with a built-in heated square cylinder. *International Journal of Thermal Sciences*, **42**(12):1105–1113.

Unverdi, S. O. [1992]. A front-tracking method for viscous, incompressible, multifluid flows. *Journal of Computational Physics*, **100**(1):25–37.

Utada, A. S., Lorenceau, E., Link, D. R., Kaplan, P. D., Stone, H. A., and Weitz, D. A. [2005]. Monodisperse double emulsions generated from a microcapillary device. *Science*, **308**(5721):537–541.

Vainchtein, D. L., Widloski, J., and Grigoriev, R. O. [2007]. Mixing properties of steady flow in thermocapillary driven droplets. *Physics of Fluids*, **19**(6):067102.

Valencia, A. and Sen, M. [2003]. Unsteady flow and heat transfer in plane channels with spatially periodic vortex generators. *International Journal of Heat and Mass Transfer*, **46**(17):3189–3199.

van Steijn, V., Kreutzer, M. T., and Kleijn, C. R. [2007]. Velocity fluctuations of segmented flow in microchannels. *Chemical Engineering Journal*, **135**(SUPPL. 1):S159–S165.

van Steijn, V., Kleijn, C. R., and Kreutzer, M. T. [2009]. Flows around confined bubbles and their importance in triggering pinch-off. *Physical Review Letters*, **103**(21):214501.

van Steijn, V., Kleijn, C. R., and Kreutzer, M. T. [2010]. Predictive model for the size of bubbles and droplets created in microfluidic T-junctions. *Lab on a Chip*, **10**(19):2513–2518.

Versteeg, H. K. and Malalasekera, W. [2007]. *An Introduction to Computational Fluid Dynamics: The Finite Volume Method*. Pearson Education Ltd., New York, 2nd edition.

Wagner, C., Amarouchene, Y., Bonn, D., and Eggers, J. [2005]. Droplet detachment and satellite bead formation in viscoelastic fluids. *Physical Review Letters*, **95**(16):1–4.

Walker, S. W. and Shapiro, B. [2006]. Modeling the fluid dynamics of electrowetting on dielectric (EWOD). *Journal of Microelectromechanical Systems*, **15**(4):986–1000.

Walsh, P. A., Walsh, E. J., and Muzychka, Y. S. [2010]. Heat transfer model for gas-liquid slug flows under constant flux. *International Journal of Heat and Mass Transfer*, **53**(15-16):3193–3201.

Wan, J., Bick, A., Sullivan, M., and Stone, H. A. [2008]. Controllable microfluidic production of microbubbles in water-in-oil emulsions and the formation of porous microparticles. *Advanced Materials*, **20**(17):3314–3318.

Weber, M. W. and Shandas, R. [2007]. Computational fluid dynamics analysis of microbubble formation in microfluidic flow-focusing devices. *Microfluidics and Nanofluidics*, **3**(2):195–206.

White, F. M. [2002]. *Fluid Mechanics, 5th edn.* McGraw-Hill series in mechanical engineering. McGraw-Hill, Boston, 5th edition.

Wilson, S. D. R. [1988]. The slow dripping of a viscous fluid. *Journal of Fluid Mechanics*, **190**:561–570.

Wöner, M., Ghidersa, B., and Onea, A. [2007]. A model for the residence time distribution of bubble-train flow in a square mini-channel based on direct numerical simulation results. *International Journal of Heat and Fluid Flow*, **28**(1 SPEC. ISS.):83–94.

Xia, Y. and Whitesides, G. M. [1998]. Soft lithography. *Annual Review of Materials Science*, **28**(1):153–184.

Xu, Q., Liao, Y.-C., and Basaran, O. A. [2007]. Can surfactant be present at pinch-off of a liquid filament? *Physical Review Letters*, **98**(5):054503.

Xue, Z., Corvalan, C. M., Dravid, V., and Sojka, P. E. [2008]. Breakup of shear-thinning liquid jets with surfactants. *Chemical Engineering Science*, **63**(7):1842–1849.

Yabe, T., Xiao, F., and Utsumi, T. [2001]. The constrained interpolation profile method for multiphase analysis. *Journal of Computational Physics*, **169**(2):556–593.

Yeo, L. Y., Chang, H. C., Chan, P. P. Y., and Friend, J. R. [2011]. Microfluidic devices for bioapplications. *Small*, **7**(1):12–48.

Yildirim, O. E. and Basaran, O. A. [2001]. Deformation and breakup of stretching bridges of Newtonian and shear-thinning liquids: Comparison of one- and two-dimensional models. *Chemical Engineering Science*, **56**(1):211–233.

Zagnoni, M. and Cooper, J. M. [2009]. On-chip electrocoalescence of microdroplets as a function of voltage, frequency and droplet size. *Lab on a Chip*, **9**(18):2652.

Zhang, D. F. and Stone, H. A. [1997]. Drop formation in viscous flows at a vertical capillary tube. *Physics of Fluids*, **9**(8):2234–2242.

Zhang, X. [1999]. Dynamics of growth and breakup of viscous pendant drops into air. *Journal of Colloid and Interface Science*, **212**(1):107–122.

Zhang, X. and Basaran, O. A. [1996]. Dynamics of drop formation from a capillary in the presence of an electric field. *Journal of Fluid Mechanics*, **326**:239–263.

Zhao, B., Moore, J. S., and Beebe, D. J. [2001]. Surface-directed liquid flow inside microchannels. *Science*, **291**(5506):1023–1026.

Zhao, B., Moore, J. S., and Beebe, D. J. [2002]. Principles of Surface-Directed Liquid Flow in Microfluidic Channels. *Analytical Chemistry*, **74**(16):4259–4268.

Zheng, Y., Fujioka, H., and Grotberg, J. B. [2007]. Effects of gravity, inertia, and surfactant on steady plug propagation in a two-dimensional channel. *Physics of Fluids*, **19**(8):082107.

Zhou, C., Yue, P., and Feng, J. J. [2006]. Formation of simple and compound drops in microfluidic devices. *Physics of Fluids*, **18**(9):092105.